Journal of Electrical and Computer Engineering

Advances in Radar Technologies

Guest Editors: Sandra Costanzo, Alvaro Rocha, and Marcelo Sampaio de Alencar

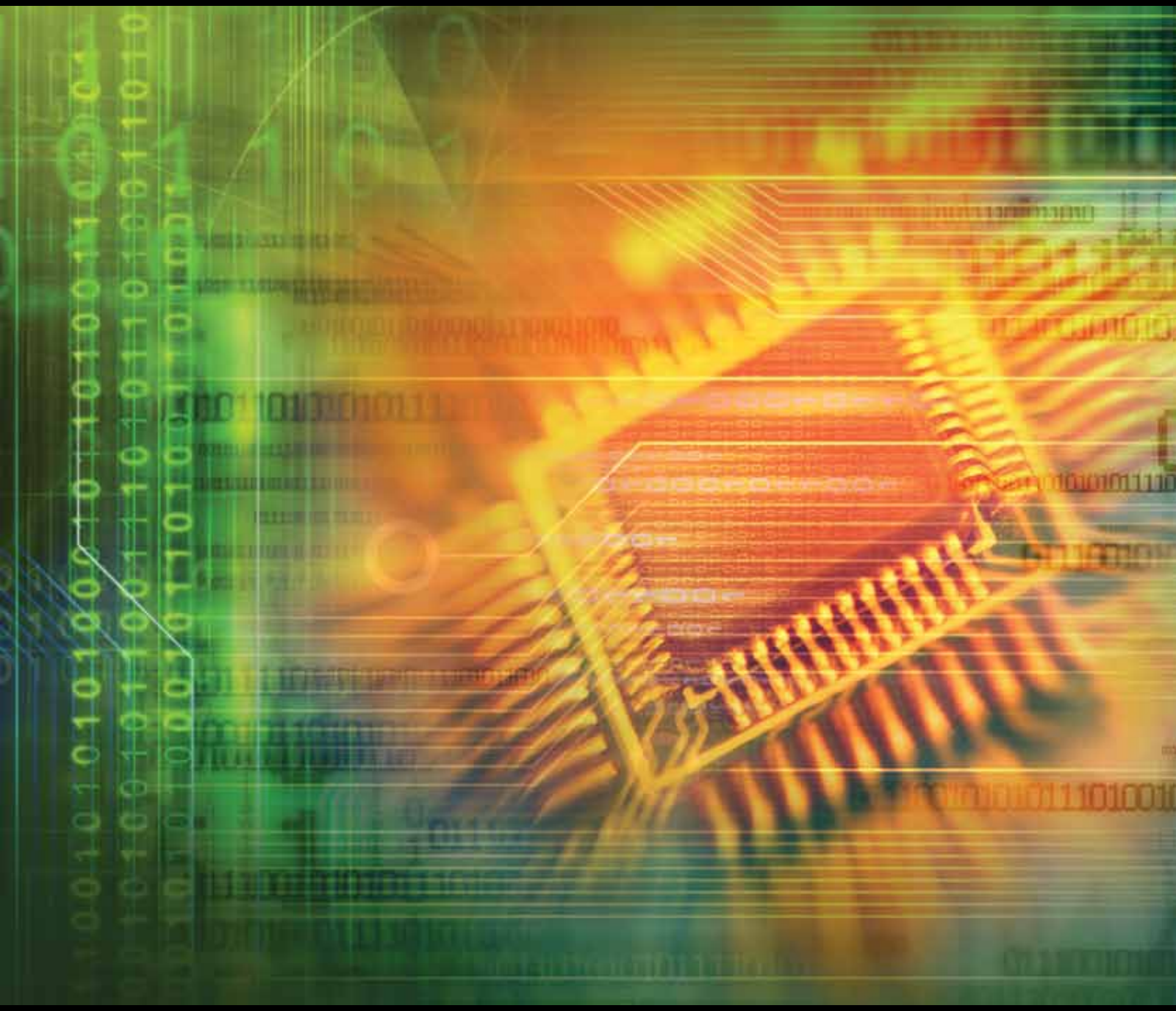

Advances in Radar Technologies

Journal of Electrical and Computer Engineering

Advances in Radar Technologies

Guest Editors: Sandra Costanzo, Alvaro Rocha,
and Marcelo Sampaio de Alencar

Copyright © 2014 Hindawi Publishing Corporation. All rights reserved.

This is a special issue published in "Journal of Electrical and Computer Engineering." All articles are open access articles distributed under the Creative Commons Attribution License, which permits unrestricted use, distribution, and reproduction in any medium, provided the original work is properly cited.

Editorial Board

The editorial board of the journal is organized into sections that correspond to the subject areas covered by the journal.

Circuits and Systems

M. T. Abuelma'atti, Saudi Arabia
Ishfaq Ahmad, USA
Dhamin Al-Khalili, Canada
Wael M. Badawy, Canada
Ivo Barbi, Brazil
Martin A. Brooke, USA
Y. W. Chang, Taiwan
Tian-Sheuan Chang, Taiwan
Chip Hong Chang, Singapore
Tzi-Dar Chiueh, Taiwan
M. Jamal Deen, Canada
A. El Wakil, UAE
Denis Flandre, Belgium
P. Franzon, USA
Andre Ivanov, Canada
Ebroul Izquierdo, UK
Wen-Ben Jone, USA
Yong-Bin Kim, USA
H. Kuntman, Turkey
Parag K. Lala, USA
Shen-Iuan Liu, Taiwan
Bin-Da Liu, Taiwan
Joafko Antonio Martino, Brazil
Pianki Mazumder, USA
Michel Nakhla, Canada
Sing Kiong Nguang, New Zealand
Shun-ichiro Ohmi, Japan
Mohamed A. Osman, USA
Ping Feng Pai, Taiwan
Marcelo Antonio Pavanello, Brazil
Marco Platzner, Germany
Massimo Poncino, Italy
Dhiraj K. Pradhan, UK
F. Ren, USA
Gabriel Robins, USA
Mohamad Sawan, Canada
Raj Senani, India
Gianluca Setti, Italy
Jose Silva-Martinez, USA
Nicolas Sklavos, Greece
Ahmed M. Soliman, Egypt
Dimitrios Soudris, Greece
Charles E. Stroud, USA
Ephraim Suhir, USA
Hannu Tenhunen, Sweden
George S. Tombras, Greece
Spyros Tragoudas, USA
Chi Kong Tse, Hong Kong
Chi-Ying Tsui, Hong Kong
Jan Van der Spiegel, USA
Chin-Long Wey, USA
Fei Yuan, Canada

Communications

Sofiène Affes, Canada
Dharma Agrawal, USA
H. Arslan, USA
Edward Au, China
Enzo Baccarelli, Italy
Stefano Basagni, USA
Jun Bi, China
Z. Chen, Singapore
René Cumplido, Mexico
Luca De Nardis, Italy
M.-Gabriella Di Benedetto, Italy
J. Fiorina, France
Lijia Ge, China
Z. Ghassemlooy, UK
K. Giridhar, India
Amoakoh Gyasi-Agyei, Ghana
Yaohui Jin, China
Mandeep Jit Singh, Malaysia
Peter Jung, Germany
Adnan Kavak, Turkey
Rajesh Khanna, India
Kiseon Kim, Republic of Korea
D. I. Laurenson, UK
Tho Le-Ngoc, Canada
C. Leung, Canada
Petri Mähönen, Germany
Mohammad A. Matin, Bangladesh
M. Nájar, Spain
M. S. Obaidat, USA
Adam Panagos, USA
Samuel Pierre, Canada
Nikos C. Sagias, Greece
John N. Sahalos, Greece
Christian Schlegel, Canada
Vinod Sharma, India
Iickho Song, Korea
Ioannis Tomkos, Greece
Chien Cheng Tseng, Taiwan
George Tsoulos, Greece
Laura Vanzago, Italy
Roberto Verdone, Italy
Guosen Yue, USA
Jian-Kang Zhang, Canada

Signal Processing

S. S. Agaian, USA
Panajotis Agathoklis, Canada
Jaakko Astola, Finland
Tamal Bose, USA
A. G. Constantinides, UK
Paul Dan Cristea, Romania
Petar M. Djuric, USA
Igor Djurović, Montenegro
Karen Egiazarian, Finland
W.-S. Gan, Singapore
Z. F. Ghassemlooy, UK
Ling Guan, Canada
Martin Haardt, Germany
Peter Handel, Sweden
Andreas Jakobsson, Sweden
Jiri Jan, Czech Republic
S. Jensen, Denmark
Chi Chung Ko, Singapore

M. A. Lagunas, Spain
J. Lam, Hong Kong
D. I. Laurenson, UK
Riccardo Leonardi, Italy
S. Marshall, UK
Antonio Napolitano, Italy
Sven Nordholm, Australia
S. Panchanathan, USA
Periasamy K. Rajan, USA
Cédric Richard, France
W. Sandham, UK
Ravi Sankar, USA
Dan Schonfeld, USA
Ling Shao, UK
John J. Shynk, USA
Andreas Spanias, USA
Yannis Stylianou, Greece
Ioan Tabus, Finland
Jarmo Henrik Takala, Finland
Clark N. Taylor, USA
A. H. Tewfik, USA
Jitendra Kumar Tugnait, USA
Vesa Valimaki, Finland
Luc Vandendorpe, Belgium
Ari J. Visa, Finland
Jar Ferr Yang, Taiwan

Contents

Advances in Radar Technologies, Sandra Costanzo, Alvaro Rocha, and Marcelo Sampaio de Alencar
Volume 2014, Article ID 818369, 2 pages

Multimode/Multifrequency Low Frequency Airborne Radar Design, Sandra Costanzo, Giuseppe Di Massa, Antonio Costanzo, Antonio Borgia, Claudio Papa, Giovanni Alberti, Giuseppe Salzillo, Gianfranco Palmese, Dario Califano, Luca Ciofanello, Maria Daniele, Claudia Facchinetti, Francesco Longo, and Roberto Formaro
Volume 2013, Article ID 857530, 9 pages

Radar Measurement of Human Polarimetric Micro-Doppler, David Tahmoush and Jerry Silvious
Volume 2013, Article ID 804954, 5 pages

Compact U-Slotted Antenna for Broadband Radar Applications, S. Costanzo and A. Costanzo
Volume 2013, Article ID 910146, 6 pages

High Resolution Software Defined Radar System for Target Detection, S. Costanzo, F. Spadafora, A. Borgia, H. O. Moreno, A. Costanzo, and G. Di Massa
Volume 2013, Article ID 573217, 7 pages

Space-Time Radar Waveforms: Circulating Codes, G. Babur, P. Aubry, and F. Le Chevalier
Volume 2013, Article ID 809691, 8 pages

Radar Array Diagnosis from Undersampled Data Using a Compressed Sensing/Sparse Recovery Technique, S. Costanzo, A. Borgia, G. Di Massa, D. Pinchera, and M. D. Migliore
Volume 2013, Article ID 627410, 5 pages

Performance of 2D Compressive Sensing on Wide-Beam Through-the-Wall Imaging, Edison Cristofani, Mathias Becquaert, and Marijke Vandewal
Volume 2013, Article ID 636972, 11 pages

Multiband Software Defined Radar for Soil Discontinuities Detection, S. Costanzo, F. Spadafora, O. H. Moreno, F. Scarcella, and G. Di Massa
Volume 2013, Article ID 379832, 6 pages

Noise Radar Technology as an Interference Prevention Method, Gaspare Galati and Gabriele Pavan
Volume 2013, Article ID 146986, 6 pages

Tunable Reflectarray Cell for Wide Angle Beam-Steering Radar Applications, F. Venneri, S. Costanzo, and G. Di Massa
Volume 2013, Article ID 325746, 7 pages

Bayesian Compressive Sensing as Applied to Directions-of-Arrival Estimation in Planar Arrays, Matteo Carlin, Paolo Rocca, Giacomo Oliveri, and Andrea Massa
Volume 2013, Article ID 245867, 12 pages

Modeling and Processing L-Band Ground Based Radar Data for Landslides Early Warning,
A. R. Laganà, M. T. Bevacqua, and T. Isernia
Volume 2013, Article ID 804615, 6 pages

Hindawi Publishing Corporation
Journal of Electrical and Computer Engineering
Volume 2014, Article ID 818369, 2 pages
http://dx.doi.org/10.1155/2014/818369

Editorial
Advances in Radar Technologies

Sandra Costanzo,[1] Alvaro Rocha,[2] and Marcelo Sampaio de Alencar[3]

[1] *Dipartimento di Ingegneria Informatica, Modellistica, Elettronica e Sistemistica, Università della Calabria, 87036 Rende, Italy*
[2] *Universidade Europeia & Universidade do Porto, LIACC, Portugal*
[3] *Federal University of Campina Grande, Campina Grande, PB, Brazil*

Correspondence should be addressed to Sandra Costanzo; costanzo@deis.unical.it

Received 21 November 2013; Accepted 21 November 2013; Published 9 January 2014

Copyright © 2014 Sandra Costanzo et al. This is an open access article distributed under the Creative Commons Attribution License, which permits unrestricted use, distribution, and reproduction in any medium, provided the original work is properly cited.

"As first shown by Hertz, electric waves can be completely reflected by conducting bodies. In some of my tests I have noticed the effects of reflection and detection of these waves by metallic objects miles away"
(Gugliemo Marconi, Radio Telegraphy, Proc. Inst. Radio Eng., vol. 10, 1922)
. . .the history of RADAR technology in Italy begun. . .
The Navy Officer (later on Professor at University of Pisa) Ugo Tiberio made a theoretical study on the detection of objects by electromagnetic waves and developed the radar equation
(Ugo Tiberio, "Misura di distanze per mezzo di onde ultracorte (Radiotelemetria)," Alta Frequenza, Maggio 1939, Torino, Italy)

Even after a century of research and study in the field, radar systems with enhanced features are in high demand for surveillance, tracking, and imaging applications, required for both civilian and military contexts. Advanced radar technologies are needed to face the problem of complex environments, with changing electromagnetic properties of targets, such as vehicles, ships, buildings, and terrain, for different frequencies, polarimetric modes, and configurations.

This special issue collects 12 papers from 37 authors belonging to different countries and institutions. It summarizes the most recent developments and ideas on emerging radar technologies, with particular focus addressed to the following issues:

(i) compressive sensing applied to large array diagnosis, directions-of-arrival estimation, and through-the-wall imaging,

(ii) software defined radar approach,

(iii) flexible, multimode radar solutions,

(iv) radar data processing techniques,

(v) compact and broadband antennas useful for sounder and imager radar,

(vi) usage of micro-Doppler radar signals for human detection,

(vii) circulating codes in space-time radar waveforms,

(viii) mitigation techniques for interference from a similar radar.

In the paper by S. Costanzo et al. entitled "*Radar array diagnosis from undersampled data using a compressed sensing/sparse recovery technique*", the problem of large arrays diagnosis is faced by adopting an equivalent sparse formulation to accurately detect fault elements from undersampled data.

M. Carlin et al. in the paper "*Bayesian compressive sensing as applied to directions-of-arrival estimation in planar arrays*"

adopted a probabilistic version of compressive sensing which is successfully applied for estimating the directions of arrival of multiple electromagnetic signals impinging on planar arrays.

The paper by E. Cristofani et al. entitled "*Performance of 2D compressive sensing on wide-beam through-the-wall imaging*" explores the application of compressive sensing to minimize the amount of data required for accurate reconstructions of through-the-wall imaging scenes.

In the paper by S. Costanzo et al., entitled "*High resolution software defined radar system for target detection*," a software defined approach is proposed to design a compact and low-cost L-band software defined radar system which is useful for landslides monitoring.

The same approach is adopted in the paper by S. Costanzo et al. entitled "*Multiband software defined radar for soil discontinuities detection*," which uses an orthogonal frequency-division multiplexing technique to perform the dielectric characterization of multilayer structures, such as soils with dispersive features.

The paper by S. Costanzo et al. entitled "*Multimode/multifrequency low frequency airborne radar design*" presents the design of a flexible and low cost airborne radar that is able to easily switch between two different operational modes, namely, a sounder or SAR imager.

In the paper by A. R. Laganà et al. entitled "*Modeling and processing L-band ground based radar data for landslides early warning*," the approaches commonly used in SAR data processing for deformations imaging are generalized to the case of ground-based, nonsynthetic radar operating in the L-band.

In the paper by F. Venneri et al. entitled "*Tunable reflectarray cell for wide angle beam-steering radar applications*," an electronically tunable reflectarray element is presented to design beam-steering arrays suitable for radar applications.

In the paper by S. Costanzo and A. Costanzo entitled "*Compact U-slotted antenna for broadband radar applications*," a modified U-shaped microstrip patch antenna with reduced size and broadband features is presented to be usefully applied for low-frequency penetrating radar.

In the paper by D. Tahmoush and J. Silvious entitled "*Radar measurement of human polarimetric micro-doppler*," extensive polarimetric micro-Doppler walking signatures are collected and analyzed to reveal different characteristics of human motions.

The paper by G. Babur et al. entitled "*Space-Time radar waveforms: circulating codes*" describes a novel solution to transmit only one waveform circulating from one antenna element to another (or from one subarray to another) with a very small relative time shift.

In the paper by G. Galati and G. Pavan entitled "*Noise radar technology as an interference prevention method*," mitigation techniques based on waveform diversity supplied by Noise Radar Technology are discussed to face the problem of interferences from several similar radar systems operating in a small environment with limited allocated bandwidths, such as in the marine radar context.

The focus theme treated in this special issue owns a particular multidisciplinary feature, so it is able to attract and integrate various different expertise, leading to scientific and economical returns of significant impact.

Sandra Costanzo
Alvaro Rocha
Marcelo Sampaio de Alencar

Hindawi Publishing Corporation
Journal of Electrical and Computer Engineering
Volume 2013, Article ID 857530, 9 pages
http://dx.doi.org/10.1155/2013/857530

Research Article

Multimode/Multifrequency Low Frequency Airborne Radar Design

Sandra Costanzo,[1] Giuseppe Di Massa,[1] Antonio Costanzo,[1] Antonio Borgia,[1] Claudio Papa,[2] Giovanni Alberti,[2] Giuseppe Salzillo,[2] Gianfranco Palmese,[2] Dario Califano,[2] Luca Ciofanello,[2] Maria Daniele,[2] Claudia Facchinetti,[3] Francesco Longo,[3] and Roberto Formaro[3]

[1] *Dipartimento di Ingegneria Informatica, Modellistica, Elettronica e Sistemistica, Università della Calabria, 87036 Rende, Italy*
[2] *Consortium of Research on Advanced Remote Sensing Systems (CO.RI.S.T.A.), 80125 Napoli, Italy*
[3] *Italian Space Agency (ASI), Rome, Italy*

Correspondence should be addressed to Sandra Costanzo; costanzo@deis.unical.it

Received 29 May 2013; Revised 16 September 2013; Accepted 17 September 2013

Academic Editor: Marcelo Sampaio de Alencar

Copyright © 2013 Sandra Costanzo et al. This is an open access article distributed under the Creative Commons Attribution License, which permits unrestricted use, distribution, and reproduction in any medium, provided the original work is properly cited.

This work deals with the design of multimode/multifrequency airborne radar suitable for imaging and subsurface sounding. The system operates at relatively low frequencies in the band ranging from VHF to UHF. It is able to work in two different modalities: (i) nadir-looking sounder in the VHF band (163 MHz) and (ii) side-looking imager (SAR) in the UHF band with two channels at 450 MHz and 860 MHz. The radar has been completely designed by CO.Ri.S.T.A. for what concerns the RF and the electronic aspect, and by the University of Calabria for what concerns the design, realization, and test of SAR antennas. The radar has been installed on a civil helicopter and its operation has been validated in flight in both sounder and imager modality. Preliminary surveys have been carried out over different areas of Campania region, South Italy.

1. Introduction

In recent years, great interest has been devoted to the development of airborne radars working in the frequency range from VHF to UHF bands (e.g., see [1–4]). The combination of low frequencies with high relative bandwidth of such systems allows several military and civilian applications. According to Table 1, these range from forestry applications, biomass measuring, and monitoring, archaeological and geological exploration, glaciers investigation, and detection and localization of buried targets. In addition, their extension to noncivil applications concerns subsurface target detection and foliage penetration. The development of this type of systems entails technological and scientific efforts in the design of antennas, low noise amplifiers, band-pass filters, and digital receiver technology, as well as in the field of data-processing algorithms.

In this framework, the Italian Space Agency (ASI) has promoted the development of a new multifunction/multimode airborne radar able to operate as a nadir-looking sounder in the VHF band and as side-looking imager in the UHF band. On one side, it constitutes a "proof of concept" for next Earth observation and planetary exploration space missions; from another perspective, the system can be seen as a validation tool for civil and non-low frequency radar terrestrial diagnostics, imaging, and monitoring applications. The radar system has been conceived and funded by ASI to be a growing laboratory to experiment and asses potentialities of low frequency radar bands (up to about 1 GHz). To this aim, three working frequency values have been chosen, namely, low, middle, and high ones. The low one (163 MHz), up to now, has been used in sounder mode, since ASI has a strong heritage in such systems for planetary exploration (MARSIS and SHARAD for Mars and future RIME for

Table 1: Applications for low frequency airborne radars.

Application	Scope	Observation technique
Forest classification and biomass retrieval	Biosphere and bioclimatology studies, especially for terrestrial carbon cycle evaluation	Side-looking SAR
Ice sheets sounding	Glaciology studies to better describe ice sheet dynamics, which is connected with climate changes and sea level modifications	Nadir-looking SAR or cross-track interferometric SAR
Subsurface geomorphology, soil moisture estimation, permafrost, and sea salinity analysis	Climate modeling	Side-looking SAR (subsurface analyses may require nadir-pointing geometry)
Target detection in forest areas	Military application	Side-looking SAR

Jovian icy moon), but it can also be used in off-nadir configuration as imager. On the contrary, the middle and high frequencies (450 MHz and 860 MHz) are currently used in SAR configuration, but pointing the antennas at nadir; also, sounder configuration is in principle possible.

Three frequencies packed into one system mean to observe the same scene at different penetration depths, and that is very powerful in tomographic applications.

Of course, this implies to have a radar system very flexible, easy to be installed on board of small airborne platform, easy to be configured in different modalities, and with low operational costs. These key points have driven the present radar development and, in our opinion, represent the actual novelty of the proposed instrument.

The research consortium CO.RI.S.T.A. was in charge of the design, realization, and in flight validation of the system. In particular, the development stage has benefited from the expertise made jointly by ASI and CO.RI.S.T.A. in a recent project concerning the design and realization of the SORA, a sounder installed on a stratospherical balloon. This was deployed during a mission on Svalbard Islands on 2009 with the aim to carry out a very large scale investigation of the glaciers stratigraphy. In the framework of the system development, the SAR antenna design and implementation are the responsibility of University of Calabria as CO.RI.S.T.A. subcontractor.

In this work, we present the complete radar system design, including the SAR antennas, and the full guidelines that have driven the system realization.

The paper is organized as follows. Section 2 describes the main features of the radar system. Section 3 deals with the description of the design and test of SAR antennas. Section 4 discusses the results of a first measurement campaign. Finally, conclusions and future works are outlined in Section 5.

2. Radar System Description

The radar exploits three different frequency bands: VHF channel with center frequency at 163 MHz and two UHF channels with center frequency at 450 MHz and 860 MHz, respectively, in such a way to achieve both subsurface and SAR imaging capabilities. The sounder operates with a 163 MHz carrier and the effective bandwidth is equal to 10 MHz. As regards the SAR modality, two frequency ranges are employed to obtain two imagers with lower and higher resolution. The lower resolution SAR (SAR-Low) imager works at 450 MHz with a 40 MHz bandwidth, whereas the higher resolution SAR (SAR-High) imager operates at 860 MHz with a bandwidth of 80 MHz.

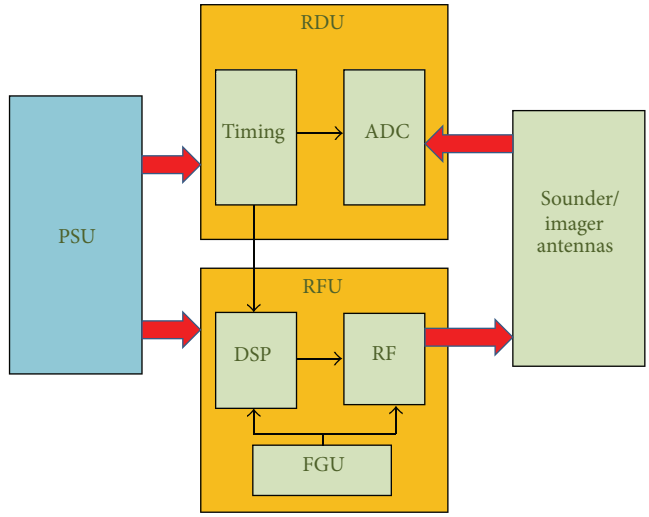

Figure 1: Block diagram of radar system.

In both the sounder and imager modalities, a linear frequency modulated signal is transmitted, where the bandwidth is synthesized in the imager mode by a stepped chirp and each bandwidth step is equal to 10 MHz, in order to achieve higher resolution products.

The entire system can be schematized as built by three main blocks (see Figure 1): Radar Digital Unit (RDU), Radio Frequency Unit (RFU), and Power supply Unit (PSU). The RDU is in charge of the parameters setting, timing generation, and data handling. It is a full programmable digital unit comprising the Analog to Digital Converter (ADC) and the data storage unit. The RFU embeds the Frequency Generation Unit (FGU), having the task to generate all synchronisms and RF signals, and the DSP, which generates the Low Frequency Modulated (LFM) signal chirp by means of digital synthesis. The PSU provides the power supply to the whole system by external 28 V DC voltage.

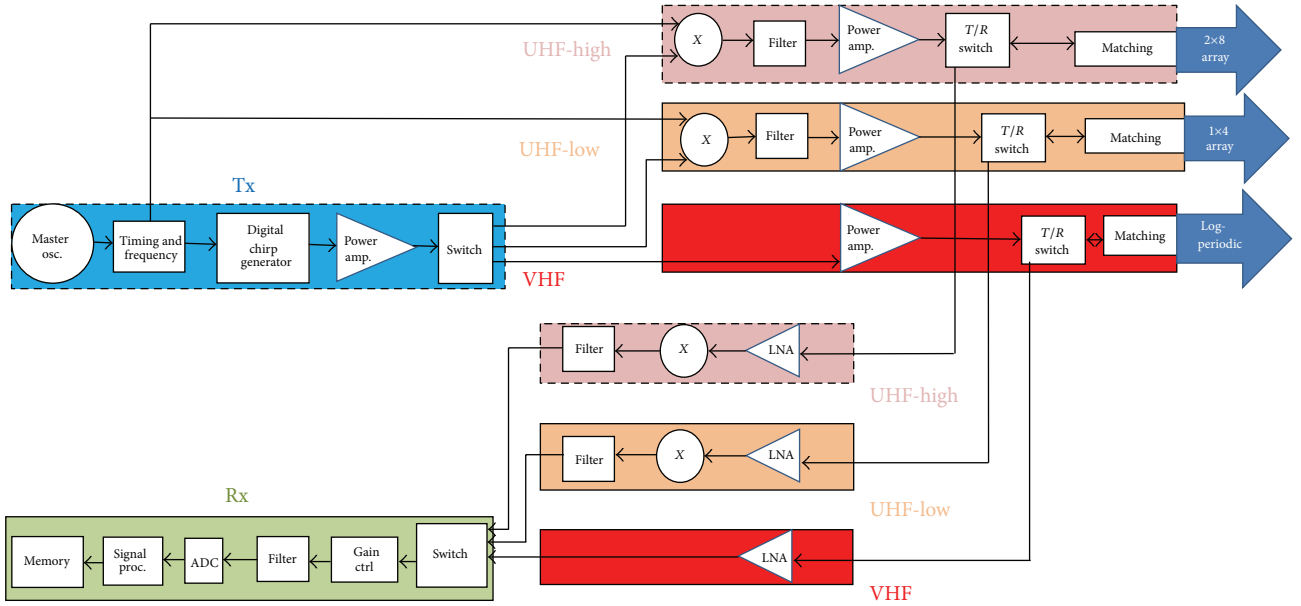

Figure 2: General system architecture.

The general architecture of the system is depicted in Figure 2. As it can be seen, the design is conceived so that most building blocks are shared by sounder and imager functionalities. In particular, base band signal generation, base band data sampling, and data handling are common to both sounder and imager operational mode. This represents the main feature of the entire system. The great advantage stands in the utilization of the same ADC, which is possible due to the adoption of an undersampling technique.

The system has been designed to be very flexible as far as timing and configuration parameters are concerned. Stepped frequencies and bandwidth are generated by means of DDS technology and all relevant parameters can be configured by the user before the flight. Therefore, the system has the capability of easily changing the frequency values and overlapping the bandwidth as well.

During the preliminary flights, stepped frequency technique was not used to increase geometric resolution (in this case a bandwidth overlap would help the processing) but only to produce multilooked images.

The system settings for the different functional modalities are described as follows.

Sounder Mode. Transmitted bandwidth of 10 MHz centered on a 163 MHz carrier. The transmitted signal is generated by FGU as LFM with the starting frequency at 158 MHz.

SAR-Low. Stepped 40 MHz transmitted bandwidth synthetized by four subbands of 10 MHz transmitted over four carriers. The carriers differ of 10 MHz each other, thus, no overlap arises between the transmitted subbands. By considering the four frequency subranges, the transmitted signal covers the frequency range (430–470) MHz.

SAR-High. Stepped 80 MHz transmitted bandwidth synthesized by eight subbands of 10 MHz transmitted over eight carriers. The carriers differ of 10 MHz each other, thus, no overlap arises between the transmitted subbands. By considering the four frequency subranges, the transmitted signal covers the overall frequency range (820–900) MHz.

As it can be seen from Figure 2, Tx and Rx blocks are common to either Sounder and Imager operative modes. Only the frequency up conversion modules are different. Tx block performs base band signal generation. The base band signal, as described before, is the Sounder signal itself. The chains depicted in Figure 2, UHF-Low, which means 450 MHz carrier, UHF-High, which means 860 MHz carrier, and VHF band, work in an exclusive way. VHF corresponds to Sounder operative mode and performs base band signal amplification only. UHF-High and UHF-Low blocks perform base band signal upconversion to working frequencies when relatives operational mode are selected. Rx block performs data antialiasing filtering and data sampling after frequency downconversion, taking place into Imager operative modes only.

The designed architecture allows a high flexibility to the system in terms of transmitted bandwidth; in fact, the radar can be easily upgraded to transmit a wider bandwidth.

As regards the Rx chain, after the downconversion is performed in the SAR-Low and SAR-High receiving chains, the IF signal is centered at 163 MHz, covering [158–168] MHz bandwidth. Hence, the incoming signal is sampled by the ADC at 100 MHz using the undersampling technique. In other words, the sampled spectrum is a replica at IF of the main one. This solution ensures the advantage to use the same ADC for different frequency carriers, such as 163 MHz, 450 MHz, and 860 MHz, thus allowing a hardware cost saving and avoiding the use of a critical (relative bandwidth approaching to unity) antialiasing filter. An auto check functional mode is implemented so to carry out an internal calibration. Specifically, a high speed and high

Table 2: System parameters.

	Sounder	SAR-Low	SAR-High
Altitude	>1300 m	>1000 m	>1000 m
Carrier	163 MHz	450 MHz	860 MHz
Tx bandwidth	10 MHz	40 MHz	80 MHz
Tx steps	1 × 10 MHz	4 × 10 MHz	8 × 10 MHz
PRF	500 Hz	2000 Hz	4000 Hz
Pulse width (single step)	3.3 μs for all operative modes		
Rx window width	10 μs	8.03 μs	8.03 μs
Antenna type	Periodic Log	Planar array of 1 × 4 patch	Planar array of 2 × 8 patch, dual polarization
Antenna gain	7 dB	17 dB	19 dB
Elevation pointing	Nadir	45° for both SAR operative mode	
Azimuth pointing	Nadir	0° for both SAR operative mode	
Range aperture	68°	75°	37°
Azimuth aperture	50°	20°	10°
ADC sampling frequency	50 MHz/100 MHz for all operative mode		
Peak power	200 W for all operative mode		

Table 3: Nominal performances.

	Sounder	SAR-Low	SAR-High
Across track resolution	10–100 m	N/A	N/A
Range resolution (free space)	15 m	3.75 m (stepped)	1.87 m (stepped)
Along track resolution	7–75 m @ 800 m 27–280 m @ 3000 m.	4.8 m @ 4 looks	2.5 m @ 2 looks
Penetration depth	100 m (moderate attenuation)	Foliage penetration	No penetration
Maximum swath (geometrical)	2000 m @ 800 m 7000 m @ 3000 m	7400 m @ 1000 m	1500 m @ 1000 m
NESZ	−95 dB @ 800 m −70 dB @ 3000 m	−80 dB −64 dB	−70 dB −54 dB
AASR	N/A	No appreciable at chosen PRF	No appreciable at chosen PRF
RASR	N/A	−55 dB	−62 dB

attenuation switch reroutes the transmitted signal on the Rx chain bypassing the antenna. The auto check mode may be switched on, manually, every time during the mission, with the exception of the acquisition stage.

Platform altitude and georeferencing are ensured by external GPS/INS linked by serial port to the RDU.

The nominal parameters of the three radars are listed in Table 2, whereas their performances are summarized in Table 3. Here, the noise equivalent sigma zero (NESZ), azimuth ambiguity ratio (AASR), and range ambiguity ratio (RASR) are also reported.

Three different antennas are adopted: one for the sounder and two for the imager modalities. The sounder antenna is a standard Log periodic with four radiating elements, having a 7 dB gain, a beam width of 68°, and a front-to-back ratio of 15–19 dB. The imager antennas are planar patch arrays designed and realized at the Microwave Laboratory of University of Calabria, Cosenza, Italy. A photo of the sounder and imager SAR-Low antenna installed on the civil helicopter (Eurocopter AS350) used for the surveys is shown in Figure 3.

Both data from the sounder and imager are preprocessed by *ad-hoc* configurable software. Prior interesting works in the sounder area can be found in [5–7]. Focusing is the core of the data processing and is based on the well assessed Chirp Scaling Algorithm (CSA) [5–15].

Due to Doppler bandwidth oversampling, a data presumming is performed in order to improve the signal to noise ratio. Other preprocessing features are related to interferences identification and suppression [16]. Furthermore, the Phase Gradient Autofocus (PGA) algorithm allows for a motion compensation [17–19]. This last feature is useful in imager data processing. The Doppler parameter estimation is necessary for data processing and is achieved by data together with

Figure 3: Sounder and imager antenna in flight configuration.

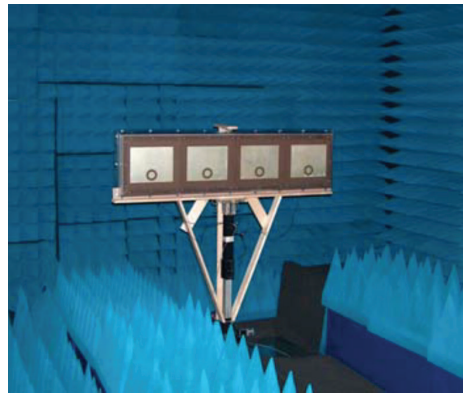

Figure 5: SAR-Low antenna mounted into the anechoic chamber at University of Calabria.

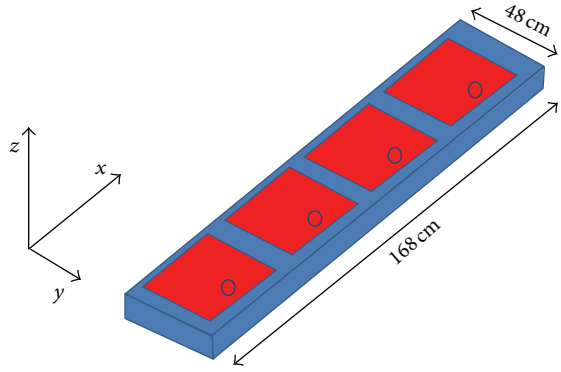

Figure 4: SAR antenna configuration.

auxiliary information from the GPS/INS navigation system. The data processing software is developed in Matlab environment. In this context, heritage gained during SHARAD mission has been used, because CO.RI.S.T.A. designed and developed data processing algorithms for this instrument [20]. For what concerns the nadir suppression technique, no particular implementation has been performed at the antenna level, where the reduced number of elements (the minimum one sufficient for the application and giving a compact structure) does not allow an efficient synthesis technique to properly reduce the sidelobes. However, nadir return is cut away from the scene with an appropriate selection of the PRF and the receiving window opening time values.

3. SAR Antenna: Design and Test

The antenna configuration adopted for the imager modality SAR-Low is composed of an array of 1×4 microstrip patches operating in linear vertical polarization (Figure 4). The single radiating element is given by a coaxial fed patch antenna and loaded with a capacitive ring, so to have a compact and wideband antenna [21, 22].

In particular, to realize a large operating bandwidth of about 80 MHz, even greater than that required by the application, a foam dielectric ($\varepsilon_r = 1.07$) having thickness equal to 6 cm is adopted as main substrate, and an upper thin (0.762 mm) layer of standard dielectric (Arlon Diclad 870, $\varepsilon_r = 2.33$) is inserted uniquely to guarantee a strong mechanical support. This gives a compact single-layer structure, with a strongly reduced thickness (compared to the wavelength), while similar performances are generally achieved by adopting much more complex configurations [23].

A photograph of the SAR-Low array mounted in the anechoic chamber of the Microwave Laboratory at University of Calabria is illustrated in Figure 5. A full experimental characterization of the array, having a weight approximately equal to 4 Kg, is performed in terms of both return loss and radiation pattern behavior. In particular, the wideband feature is well confirmed by the return loss illustrated in Figure 6, where a good agreement can be observed between simulations (Ansoft Designer) and measurements.

The measured radiation pattern in the $y = 0$ array plane (Figure 4) is reported in Figure 7 for the central design frequency equal to 450 MHz. A −3 dB beamwidth approximately equal to 22°, as imposed by the constraint on the azimuth resolution, is obtained in the copolar field.

Furthermore, the array shows an excellent performance in terms of cross polar component, which is significantly lower with respect to the copolar one. The radiation performances of the designed array is maintained all over the operating frequency range, as demonstrated by a very similar behavior of the measured radiation patterns at different frequencies, reported in Figure 8. Finally, the measured boresight gain, with a mean value properly equal to 17 dB (as declared in Table 2), is illustrated in Figure 9. A similar configuration is adopted for the SAR-High antenna, with the same basic radiating element, but working at dual linear polarization and assuming an array of 2×8 elements in order to increase the azimuth resolution.

A design very similar to that adopted in the case of SAR-Low antenna is assumed, but including two coaxial feeds, in order to have the dual polarization feature. A foam thickness equal to 3 cm, with an upper thin (0.762 mm) layer of Arlon Diclad 870 is considered, and the overall dimension of the

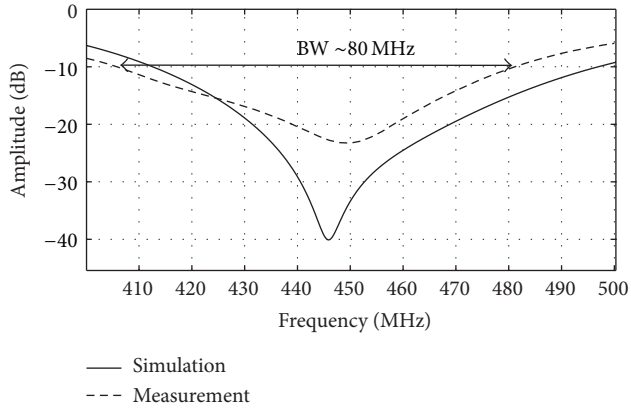

Figure 6: Return loss of SAR-Low antenna: comparison between simulation and measurement.

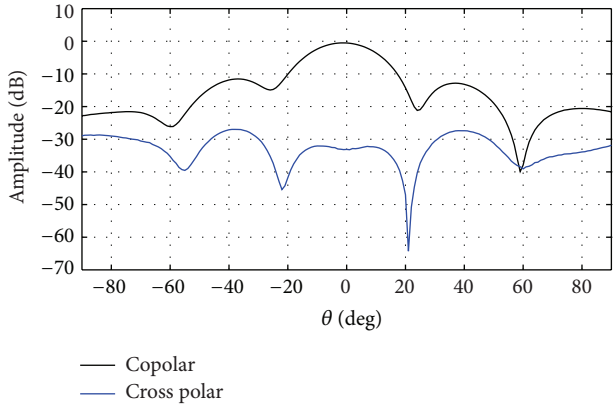

Figure 7: Measured radiation pattern of SAR-Low antenna: copolar and cross polar components @ 450 MHz.

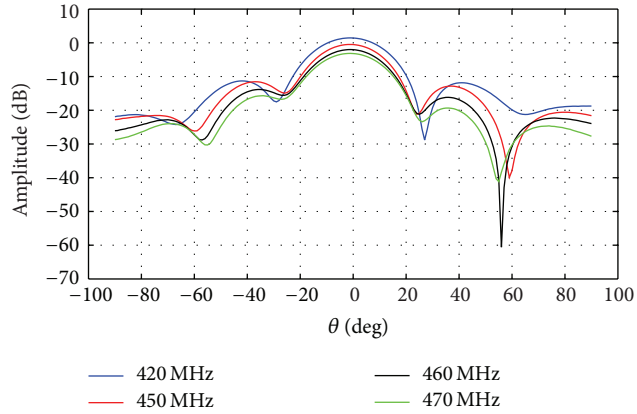

Figure 8: Measured radiation pattern of SAR-Low antenna: copolar component at different frequencies.

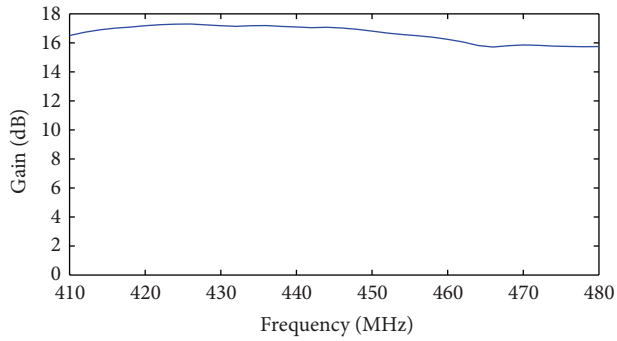

Figure 9: Measured gain of SAR-Low antenna versus frequency at boresight.

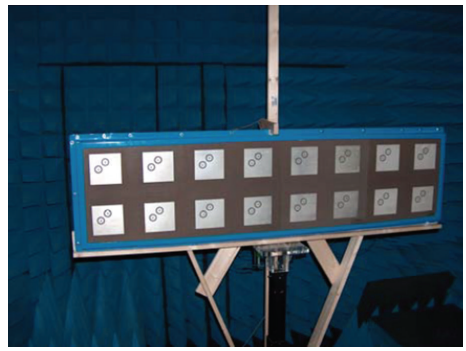

Figure 10: SAR-High antenna mounted into the anechoic chamber at University of Calabria.

SAR-High array is exactly equal to that relative to the SAR-Low case (Figure 4), so to adopt the same equipped slot on the helicopter. Experimental validations are again performed into the Microwave Laboratory at University of Calabria (Figure 10).

In particular, the return loss curves, reported in Figure 11, show a very similar behavior for the two linear polarizations, with an operating bandwidth approximately equal to 120 MHz, again greater than that imposed by the application. The measured pattern in the $y = 0$ array plane reported in Figure 12 for the central frequency of 900 MHz. A −3 dB beamwidth approximately equal to 12°, as imposed by the constraints on the azimuth resolution, can be observed in the copolar field, significantly above (~25 dB) the undesired cross polar component. Finally, the measured gain (at boresight) for the two polarizations, reported in Figure 13, show a mean value approximately equal to 19 dB, as indicated in Table 2.

4. Measurement Campaign Results

Two flight campaigns are performed with the aim to verify system functionality in operative conditions. Only the sounder antenna is mounted on board of a military helicopter during the first flight campaign. The relative performed tracks over an ancient volcanic hill located in the Roccamonfina site (South Italy) are reported in Figure 14, while the obtained radargram is shown in Figure 15. By observing the Figures, there are some evidence that the sounder is able to penetrate the hill terrain and intercept the bedrock at about 300 m depth.

During the second flight campaign, the 450 MHz antenna is also mounted on board of a commercial helicopter. An

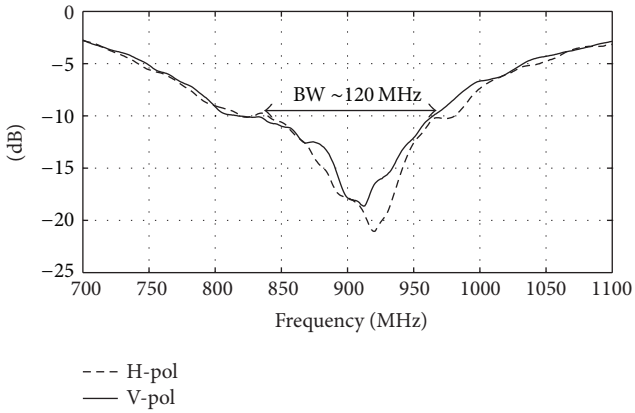

Figure 11: Return loss of SAR-High antenna: comparison between H and V polarizations.

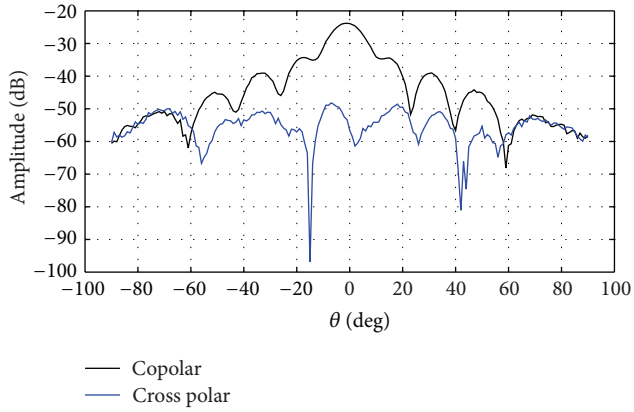

Figure 12: Measured radiation pattern of SAR-High antenna: copolar and cross polar components @ 900 MHz.

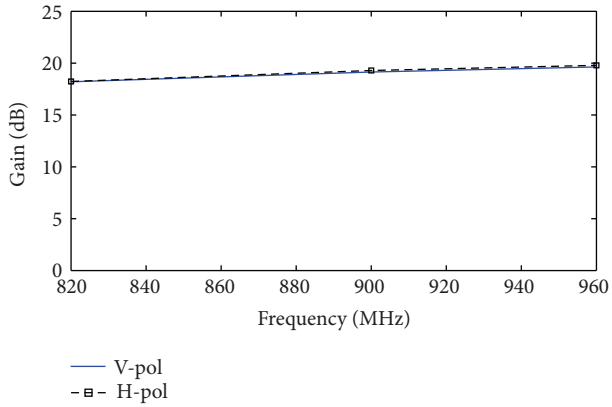

Figure 13: Measured gain of SAR-High antenna versus frequency at boresight: comparison between H and V polarizations.

example of the resulting SAR image over a coastal zone in Southern Italy (Paestum) is illustrated in Figure 16.

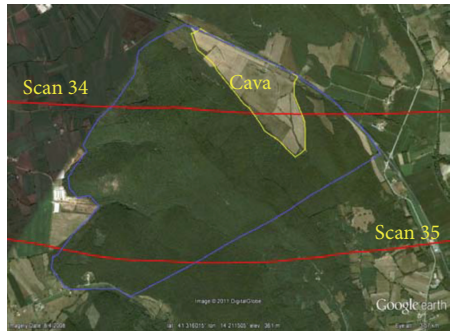

Figure 14: Performed tracks over an ancient volcanic hill located in the Roccamonfina site (South Italy).

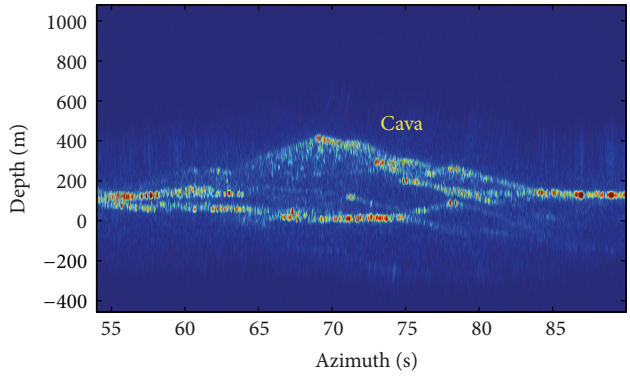

Figure 15: Obtained radargram on the Roccamonfina site (South Italy).

Figure 16: SAR image obtained over a coastal zone in Southern Italy (Paestum).

5. Conclusions and Future Works

The design of a flexible and low-cost airborne radar, able to easily switch between different operational modes (sounder as well as SAR imager) has been fully described in this work. The availability of more different frequency bands packaged into a unique system makes it strongly useful to obtain maps

with different penetration depths, thus specifically powerful in tomographic applications, as demonstrated by the first measurement campaigns. Actually, only two flight validations have been performed with the aim of verifying the overall system functionality.

No calibration flights have been performed to assess the true system performances, and this will be the focus of a future work. Furthermore, even if the proposed radar is conceived to be fully polarimetric, it is not currently equipped to receive the two polarizations simultaneously, because it contains only one receiving channel. Therefore, the full polarization can only be implemented in an "interleaved" configuration, that is, through 4 consecutive pulses (HH, HV, VH, and VV). The receiving channel duplication will be an upgrade foreseen in the next future.

Conflict of Interests Disclosure

We state there is no financial or competing interest which could influence the validity of the present research.

Acknowledgment

The authors would like to thank Mr. Ennio Marozzo for the precious technical support in the realization of the antenna prototypes.

References

[1] H. Hellsten, L. M. Ulander, A. Gustavsson, and B. Larsson, "Development of VHF CARABAS II SAR," in *Radar Sensor Technology*, vol. 2747 of *Proceedings of SPIE*, pp. 48–60, April 1996.

[2] E. G. Njoku, W. J. Wilson, S. H. Yueh et al., "Observations of soil moisture using a passive and active low-frequency microwave airborne sensor during SGP99," *IEEE Transactions on Geoscience and Remote Sensing*, vol. 40, no. 12, pp. 2659–2673, 2002.

[3] G. Smith-Jonforsen, L. M. H. Ulander, and X. Luo, "Low VHP-band backscatter from coniferous forests on sloping terrain," *IEEE Transactions on Geoscience and Remote Sensing*, vol. 43, no. 10, pp. 2246–2260, 2005.

[4] L. M. H. Ulander, M. Lundberg, W. Pierson, and A. Gustavsson, "Change detection for low-frequency SAR ground surveillance," *IEE Proceedings: Radar, Sonar and Navigation*, vol. 152, no. 6, pp. 413–420, 2005.

[5] M. E. Peters, D. D. Blankenship, S. P. Carter, S. D. Kempf, D. A. Young, and J. W. Holt, "Along-track focusing of airborne radar sounding data from west antarctica for improving basal reflection analysis and layer detection," *IEEE Transactions on Geoscience and Remote Sensing*, vol. 45, no. 9, pp. 2725–2736, 2007.

[6] R. Scheiber, P. Prats, and F. Hélière, "Surface clutter suppression techniques for ice sounding radars: analysis of airborne data," in *Proceedings of the 7th European Conference on Synthetic Aperture Radar (EUSAR '08)*, pp. 1–4, Friedrichshafen, Germany, June 2008.

[7] K. C. Jezek, S. Gogineni, X. Wu et al., "Two-frequency radar experiments for sounding glacier ice and mapping the topography of the glacier bed," *IEEE Transactions on Geoscience and Remote Sensing*, vol. 49, no. 3, pp. 920–929, 2011.

[8] K. Player, L. Shi, C. Allen et al., "A multi-channel depth-sounding radar with an improved power amplifier," *High-Frequency Electronics*, pp. 18–29, 2010.

[9] F. Rodriguez-Morales, P. Gogineni, C. Leuschen et al., "Development of a multi-frequency airborne radar instrumentation package for ice sheet mapping and imaging," in *Proceedings of the IEEE MTT-S International Microwave Symposium (MTT '10)*, pp. 157–160, Anaheim, Calif, USA, May 2010.

[10] L. Shi, C. T. Allen, J. R. Ledford et al., "Multichannel coherent radar depth sounder for NASA operation ice bridge," in *Proceedings of the 30th IEEE International Geoscience and Remote Sensing Symposium (IGARSS '10)*, pp. 1729–1732, Honolulu, Hawaii, USA, July 2010.

[11] L. M. H. Ulander, B. Flood, P. O. Frolind et al., "Bistatic VHF/UHF-band airborne SAR experiment," in *Proceedings of the IET International Conference on Radar Systems (Radar '12)*, pp. 22–25, Glasgow, UK, October 2012.

[12] A. Potsis, A. Reigber, and K. P. Papathanassiou, "Phase preserving method for RF interference suppression in P-band synthetic aperture radar interferometric data," in *Proceedings of the IEEE International Geoscience and Remote Sensing Symposium (IGARSS '99)*, pp. 2655–2657, Hamburg, Germany, July 1999.

[13] J. Dall, "A new frequency domain autofocus algorithm for SAR," in *Proceedings of the International Geoscience and Remote Sensing Symposium (IGARSS '91)*, pp. 1069–1072, Helsinki, Finland, June 1991.

[14] Y. Zhang, J. Wu, and H. Li, "Two simple and efficient approaches for compressing stepped chirp signals," in *Proceedings of the Asia-Pacific Microwave Conference (APMC '05)*, vol. 1, pp. 690–693, Suzhou, China, December 2005.

[15] G. I. Cumming and H. F. Wong, *Digital Processing of Synthetic Aperture Radar Data*, Artech House, Boston, Mass, USA, 2005.

[16] J. C. Curlander and R. N. McDonough, *Synthetic Aperture Radar*, John Wiley & Sons, New York, NY, USA, 1991.

[17] A. Moreira, J. Mittermayer, and R. Scheiber, "Extended chirp scaling algorithm for air- and spaceborne SAR data processing in stripmap and ScanSAR imaging modes," *IEEE Transactions on Geoscience and Remote Sensing*, vol. 34, no. 5, pp. 1123–1136, 1996.

[18] A. Moreira and Y. Huang, "Airborne SAR processing of highly squinted data using a chirp scaling approach with integrated motion compensation," *IEEE Transactions on Geoscience and Remote Sensing*, vol. 32, no. 5, pp. 1029–1040, 1994.

[19] A. Gallon and F. Impagnatiello, "Motion compensation in chirp scaling SAR processing using phase gradient autofocusing," in *Proceedings of the IEEE International Geoscience and Remote Sensing Symposium (IGARSS '98)*, pp. 633–635, Seattle, Wash, USA, July 1998.

[20] G. Alberti, S. Dinardo, S. Mattei, C. Papa, and M. R. Santovito, "SHARAD radar signal processing technique," in *Proceedings of the 4th International Workshop on Advanced Ground Penetrating Radar (IWAGPR '07)*, pp. 261–264, Naples, Italy, June 2007.

[21] S. Costanzo and A. Costanzo, "Compact slotted antenna for wideband radar applications," in *Advances in Information Systems and Technologies*, Á. Rocha, A. M. Correia, T. Wilson, and K. A. Stroetmann, Eds., vol. 206 of *Advances in Intelligent Systems and Computing*, pp. 989–996, 2013.

[22] S. Costanzo and A. Costanzo, "Compact U-slotted antenna for broadband radar applications," *Journal of Electrical and Computer Engineering*, vol. 2013, Article ID 910146, 6 pages, 2013.

[23] S. López-Peña, J.-F. Zürcher, R. Torres, A. G. Polimeridis, and J. R. Mosig, "Modeling and manufacturing of a series of identical antennas for a P-Band ice sounder," in *Proceedings of the 4th European Conference on Antennas and Propagation (EuCAP '10)*, Barcelona, Spain, April 2010.

Hindawi Publishing Corporation
Journal of Electrical and Computer Engineering
Volume 2013, Article ID 804954, 5 pages
http://dx.doi.org/10.1155/2013/804954

Research Article

Radar Measurement of Human Polarimetric Micro-Doppler

David Tahmoush and Jerry Silvious

U.S. Army Research Lab, Adelphi, MD 20783, USA

Correspondence should be addressed to David Tahmoush; david.tahmoush@us.army.mil

Received 24 May 2013; Accepted 4 September 2013

Academic Editor: Sandra Costanzo

Copyright © 2013 D. Tahmoush and J. Silvious. This is an open access article distributed under the Creative Commons Attribution License, which permits unrestricted use, distribution, and reproduction in any medium, provided the original work is properly cited.

We use polarimetric micro-Doppler for the detection of arm motion, especially for the classification of whether someone has their arms swinging and is thus unloaded. The arm is often bent at the elbow, providing a surface somewhat similar to a dihedral. This is distinct from the more planar surfaces of the body which allows us to isolate the signals of the arm (and knee). The dihedral produces a double bounce that can be seen in polarimetric radar data by measuring the phase difference between HH and VV. This measurement can then be used to determine whether the subject is unloaded.

1. Introduction

Detailed radar processing can reveal many characteristics of human motions and of the human body, including gait characteristics. Micro-Doppler signals refer to Doppler scattering returns produced by the motions of the target other than gross translation. Parts of the human body do not move with constant radial velocity; some of the small micro-Doppler signatures are periodic, and therefore analysis techniques can be used to obtain more characteristics [1, 2]. Micro-Doppler gives rise to many detailed radar image features in addition to those associated with the bulk target motions. Modulations of the radar return from arms, legs, and even body sway are being investigated by researchers [3–5]. There are also some tutorials on micro-Doppler phenomena [2, 6, 7].

The Doppler information measured by a radar arises from target motions. The equation for computing the nonrelativistic Doppler frequency shift, F_d, of a simple point scatterer moving with speed v with respect to a stationary transmitter is

$$F_d = F_t \frac{2v}{c} \cos\theta \cos\phi, \tag{1}$$

where F_t is the frequency of the transmitted signal, θ is the angle between the subject's velocity and the beam of the radar in the ground plane, and ϕ is the elevation angle between the subject's velocity and the radar beam. This assumes that the radar itself is stationary. Targets can be considered as collections of simple scatterers, though this is a rough approximation. The micromotion of the scatterers around the center frequency creates a micro-Doppler model that varies with time. Several micro-Doppler models have been developed which characterize and attempt to predict the human micro-Doppler response [8–10] using animated collections of simple scatterers as the foundation.

A short-time FT (STFT) is one way to explore the slow time-dependent behaviour of the Doppler spectrum by doing a Fourier transform over a small window in time, then sliding the window [11]. This avoids the loss of time information that occurs when applying a Fourier transform. The continuous form of the STFT is

$$\mathrm{STFT}\,(x(t)) = X(\tau,\omega) = \int_{-\infty}^{\infty} x(t)\, w(t-\tau)\, e^{-jwt} dt, \tag{2}$$

where $w(t)$ is the window function. Because human micro-Doppler varies slowly with time, we employ STFTs of the IQ radar data. The length of time used in the STFT is called coherent processing window, and this determines the resolution in Doppler frequency that can be measured. This can partially be overcome by superresolving methods. The spectrogram is the square modulus of the STFT and is then

$$\mathrm{spectrogram}\,(\tau,\omega) = 10\log_{10}|X(\tau,\omega)|^2 \tag{3}$$

which is often used to display micro-Doppler data in decibels. Much of the analysis in this report makes use of spectrograms for the display of micro-Doppler phenomenology.

The extraction of micro-Doppler features is typically performed in the joint time-frequency domain. Chirplet techniques [12] as well as linear FM basis decomposition [13] can be used to perform feature extraction. Independent component analysis (ICA) can be used to extract independent basis functions from the spectrogram to be used as features in a classifier [14]. Micro-Doppler signatures have been suggested as a biometric [15], and micro-Doppler features have been used in classification algorithms [15–18]. Micro-Doppler signatures have been extracted through a brick wall [19]. Fully polarimetric human radar signatures at different approach angles with respect to the radar have been collected [20]. Automatic target classification has also been done on data including multiple humans, wheeled vehicles, tracked vehicles, clutter, and animal classes [21]. Micro-Doppler phenomena have been investigated in frequencies as low as UHF [22]. A 77 GHz radar was used to observe micro-Doppler signatures of human gait to recognize multiple persons and attempt to identify whether the person is swinging their arms [23]. An ultrawide band (UWB) impulse radar was used to provide both high resolution range profiles and high resolution Doppler spectrogram, which helps to extract detailed micro-Doppler signatures like swinging arms [24]. The detailed signatures are used to recognize human activities, such as marching, walking, one-arm swinging, or two-arm swinging. A combination of micro-Doppler signatures with microrange features was also proposed [25].

2. Models

To understand the micro-Doppler presented by moving humans, a model was built using the human motion as a collection of simple scatterers. Several other micro-Doppler models have been developed that characterise and attempt to predict the human micro-Doppler response [8–10]. We use research on human gait to model the expected Doppler shifts measured over time by a radar system. We started with the measurements made on twenty men and twenty women whose ages ranged from 20 to 38 years with an average age of 26 years and had their motions captured on video and extracted then their characteristics analyzed [26]. The resulting motion information was extracted, and then animated. We took the animated gait and extracted the micro-Doppler velocities that would be created by differentiating the motions using a point-scatterer model for each separate part.

We neglected obscuration for these simulations because they were limited to frontal view, and we used a metallic skin approximation to simplify the calculations by neglecting the skin depth. The simulated micro-Doppler motions for different body parts are compared to measured data. These are calculated from the model and are calculated and measured at 17 GHz. The scaling for the images was set in order to simplify the comparison of images to demonstrate the variability of the human gait as viewed by the radar. The stride rate is also held fixed to simplify comparisons. We also do not simulate noise in the models. Highly accurate mesh-modeled simulations of the human micro-Doppler signature have also been done [27] at lower frequencies where the metallic skin approximation does not apply.

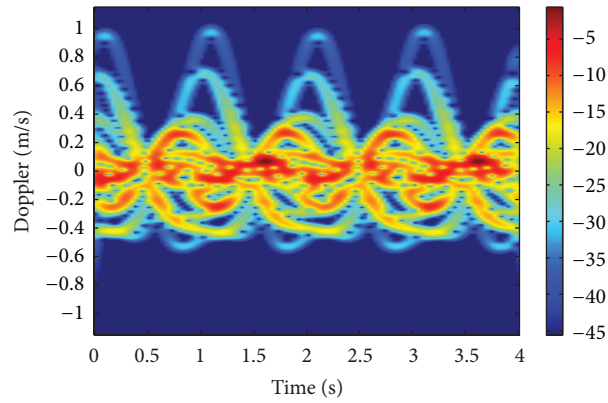

Figure 1: Simulated micro-Doppler for a man walking on a treadmill in the radial direction toward the radar at 17 GHz.

The usefulness of the simulations is in the ability to understand the measured effects seen in different radar scenarios. They also provide the ability to create a simulated database to test algorithms and approaches for feature extraction and classification. There is not a perfect agreement between simulated and actual measurements, but much of the qualitative signature aspects are in the simulations. The torso line, foot swing, and arm motions are all contained in the simulation. This compares well to other micro-Doppler simulations [9, 15]. We then added radar cross sections (RCS) to the simulations by modeling the human body as a set of elliptical shapes and calculated the resulting spectrogram as shown in Figure 1.

Now that we have a qualitatively validated model, we are going to use it to analyze the results of polarimetric human micro-Doppler measurements.

3. Polarimetric Micro-Doppler

Fully polarimetric radar data can potentially improve the separability of different parts of human motion. One of the techniques to determine whether someone is carrying a load is looking at their arm motion [28]. The arm is often bent at the elbow, providing a surface similar to a dihedral which could create a double bounce. This is distinct from the more planar surfaces of the body and allows us to separate the signals of the arm (and knee) motion from the rest of the body. The double bounce can be measured in polarimetric radar data by measuring the phase difference between HH and VV [29]. Measurements of humans were taken at an outdoor radar test range with realistic but low levels of clutter at Ka band. Further descriptions of the radar system, test range, clutter, and other parameters are available in [20].

A standard spectrogram model of the micro-Doppler of a human walking motion is shown in Figure 1. The dominant phases for a walking human similar to Figure 1 are measured and shown in Figure 2. Note that the characteristic foot swing is still somewhat discernible. There is a significant number of signals with a high (>150 or < −150 degrees) phase shift in the torso-line area of the motion. Figure 3 shows the dismount with the simulated motion of elbows superimposed, which

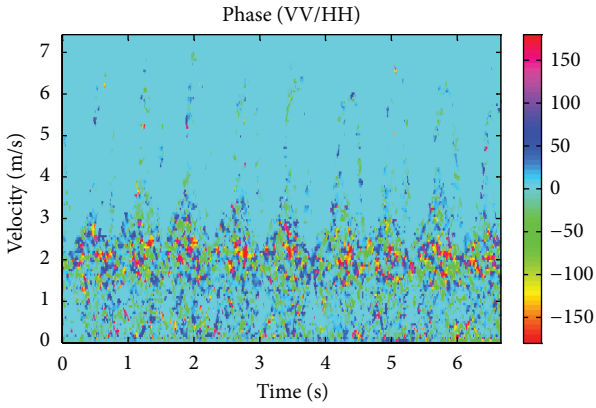

Figure 2: Polarimetric measurement of human walking toward the radar. The red (and yellow) double-bounce areas correspond to the elbow motion, while the blue (and green) single bounce is the rest of the body.

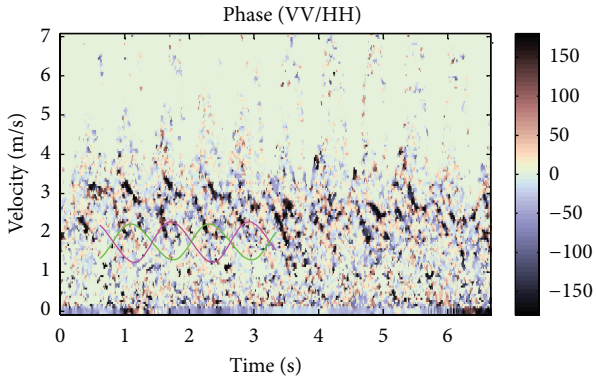

Figure 3: Polarimetric measurement of an unloaded human walking toward the radar at Ka band from Figure 2 with the simulated elbow movement superimposed as red and green lines roughly corresponding to the areas of significant phase offset from zero.

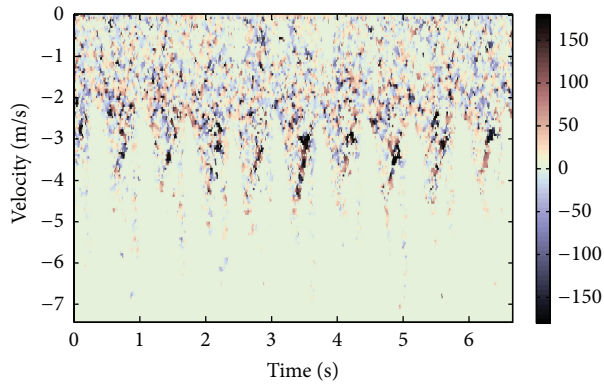

Figure 4: Polarimetric measurement of a human walking away from the radar at Ka band. The black double-bounce areas correspond to the elbow motion, while the white and grey single-bounce area is the rest of the body.

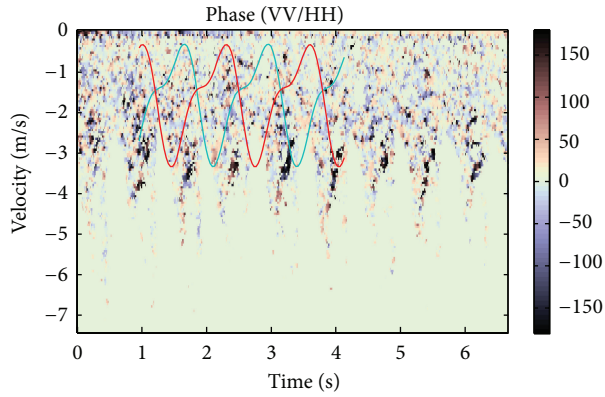

Figure 5: Repeated polarimetric measurement of a human walking away from the radar at Ka band. The black double-bounce areas correspond to the elbow motion, while the white and grey single-bounce area is the rest of the body. The simulated motions of the knee are superimposed on the image, showing a rough correspondence to areas of high doublebounce.

matched reasonably well the measured areas of high phase offset from zero. Note that the elbow maxima are simulated to be slightly before the foot maxima, as shown in Figure 1.

The repeatability of the measurement is an issue. Two measurements were made of an individual walking away from the radar, with the knees being highlighted instead of the elbows. This is shown in Figures 4 and 5 where a measurement of knee polarimetric response is repeated and the simulated motion is superimposed. An additional issue is the effect of angle on the measurement response. Polarimetric micro-Doppler with a double bounce was only clearly detectible at small offsets from the radial direction in azimuth or elevation. The arm is smaller in RCS than the torso or leg, so when both signals are present, the smaller arms signal is not as distinguishable. This meant that the angles where it is easy to view the double bounce returns from the elbow and knee are when the arm is readily discernible from other signals.

When a dismount is loaded, the arm motion is restricted so there is less opportunity to easily observe the double bounce. Figure 6 shows a loaded dismount which can be compared to Figure 2. It is clear from the differences in Figures 2 and 6 that there is potential in utilizing polarimetric radar in classifying dismounts as having their arms loaded or freely swinging. The simulated arm motion is overlaid in Figure 3. The polarimetric measurement of human walking toward the radar at Ka band while carrying a load in Figure 6 shows that the red double-bounce areas corresponding to the elbow motion are severely diminished because the dismount can no longer swing the arms freely. Dismounts carrying different objects can appear to have similar motion, though this was not true with the most common implements [28]. This study is not definitive because of the small amount of data with limited statistics, but the potential to utilize polarimetry to distinguish loaded versus unloaded dismounts is shown.

4. Conclusions

Extensive fully polarimetric outdoor radar human micro-Doppler walking signatures have been collected and analyzed. Micro-Doppler simulations were created and

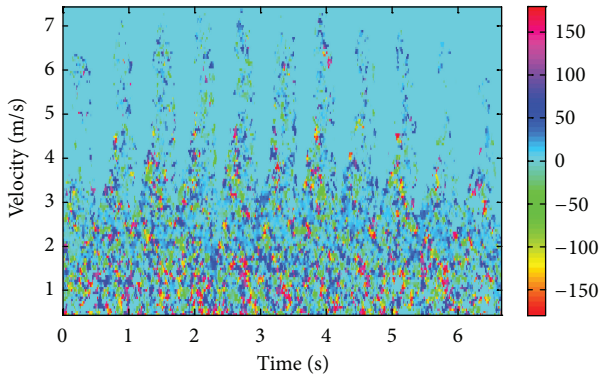

Figure 6: Polarimetric measurement of a loaded human walking toward the radar at Ka band. The red (and yellow) double-bounce areas correspond to the elbow motion, while the blue (and green) single bounce is the rest of the body. Comparison with Figure 2 shows a reduction in the arm motion.

qualitatively validated against the measured data, allowing the use of the simulations to analyze the polarimetric micro-Doppler returns. The motion of humans is shown to have measurable double-bounce returns from both the elbows and knees similar to a dihedral. These returns vary when the human is loaded versus unloaded, primarily in the double-bounce return from the freely swinging arms. Thus, the extraction of polarimetric micro-Doppler features from radar data has been shown to be feasible and potentially useful.

We discovered several important characteristics that should be considered for the measurement of human micro-Doppler. First, since the arm motion is important for the determination of whether a person could be loaded, polarimetric measurements can isolate and highlight the arm motion for a classification as being loaded or unloaded. Second, the azimuthal angle of the motion is a critical parameter to consider in ground-based systems. For choke-point observations where the direction of motion is more controlled, polarimetric radar could be used to determine who is unloaded and who should be checked.

References

[1] L. Cohen, *Time-Frequency Analysis*, Prentice-Hall, Englewood Cliffs, NJ, USA, 1995.

[2] V. C. Chen and H. Ling, *Time-Frequency Transforms for Radar Imaging and Signal Analysis*, Artech House, Norwood, Mass, USA, 2002.

[3] S. Z. Gürbüz, W. L. Melvin, and D. B. Williams, in *Proceedings of the SPIE Signal Processing, Sensor Fusion, and Target Recognition XVI*, vol. 6567, 2006.

[4] G. Greneker, "Very low cost stand-off suicide bomber detection system using human gait analysis to screen potential bomb carrying individuals," in *Proceedings of the Radar Sensor Technology IX*, vol. 5788, pp. 46–56, Orlando, Fla, USA, March 2005.

[5] J. L. Geisheimer, W. S. Marshall, and E. Greneker, "A continuous-wave (CW) radar for gait analysis," in *Proceedings of the 35th Asilomar Conference on Signals, Systems and Computers*, pp. 834–838, November 2001.

[6] V. C. Chen and R. Lipps, "Time-frequency signatures of micro-Doppler phenomenon for feature extraction," in *Proceedings of the Wavelet Applications VII*, pp. 220–226, April 2000.

[7] V. C. Chen, F. Li, S.-S. Ho, and H. Wechsler, "Micro-doppler effect in radar: phenomenon, model, and simulation study," *IEEE Transactions on Aerospace and Electronic Systems*, vol. 42, no. 1, pp. 2–21, 2006.

[8] D. Tahmoush and J. Silvious, "Radar microdoppler for security applications: modeling men versus women," in *Proceedings of the IEEE International Symposium on Antennas and Propagation and USNC/URSI National Radio Science Meeting (APSURSI '09)*, Charleston, SC, USA, June 2009.

[9] P. Van Dorp and F. C. A. Groen, "Human walking estimation with radar," *IEE Proceedings: Radar, Sonar and Navigation*, vol. 150, no. 5, pp. 356–366, 2003.

[10] D. Tahmoush and J. Silvious, "Angle, elevation, PRF, and illumination in radar microdoppler for security applications," in *Proceedings of the IEEE International Symposium on Antennas and Propagation and USNC/URSI National Radio Science Meeting (APSURSI '09)*, Charleston, SC, USA, June 2009.

[11] A. V. Oppenheim and R. W. Schafer, *Discrete-Time Signal Processing*, Prentice Hall, Englewood Cliffs, NJ, USA, 1989.

[12] J. Li and H. Ling, "Application of adaptive chirplet representation for ISAR feature extraction from targets with rotating parts," *IEE Proceedings: Radar, Sonar and Navigation*, vol. 150, no. 4, pp. 284–291, 2003.

[13] P. Setlur, M. Amin, and F. Ahmad, "Analysis of micro-doppler signals using linear FM basis decomposition," in *Proceedings of the Radar Sensor Technology X*, Orlando, Fla, USA, April 2006.

[14] V. C. Chen, "Spatial and temporal independent component analysis of micro-Doppler features," in *Proceedings of the IEEE Radar Conference*, pp. 348–353, May 2005.

[15] J. L. Geisheimer, E. F. Greneker, and W. S. Marshall, "A high-resolution doppler model of human gait," in *Proceedings of the Radar Sensor Technology and data Visualisation*, pp. 8–18, Orlando, Fla, USA, April 2002.

[16] Y. Yang, J. Lei, W. Zhang, and C. Lu, "Target classification and pattern recognition using micro-doppler radar signatures," in *Proceedings of the 7th ACIS International Conference on Software Engineering, Artificial Intelligence, Networking, and Parallel/Distributed Computing, SNPD 2006, including Second ACIS International Workshop on Self-Assembling Wireless Networks (SAWN '06)*, pp. 213–217, Las Vegas, Nev, USA, June 2006.

[17] P. G. Kealey and M. Jahangir, "Advances in Doppler recognition for ground moving target indication," in *Proceedings of the Automatic Target Recognition XVI*, Orlando, Fla, USA, April 2006.

[18] M. Otero, "Application of a continuous wave radar for human gait recognition," in *Proceedings of the Signal Processing, Sensor Fusion, and Target Recognition XIV*, pp. 538–548, Orlando, Fla, USA, March 2005.

[19] A. Lin and H. Ling, "Through-wall measurements of a Doppler and Direction-of-Arrival (DDOA) radar for tracking indoor movers," in *Proceedings of the IEEE Antennas and Propagation Society International Symposium and USNC/URSI Meeting*, vol. 3B, pp. 322–325, July 2005.

[20] R. Tan and R. Bender, "Analysis of Doppler Measurements of People," in *Proceedings of SPIE Targets and Backgrounds XII: Characterization and Representation*, R. Wendell Watkins and Dieter Clement, Eds., vol. 6239, pp. 623908–623901, 2006.

[21] I. Bilik, J. Tabrikian, and A. Cohen, "GMM-based target classification for ground surveillance Doppler radar," *IEEE*

Transactions on Aerospace and Electronic Systems, vol. 42, no. 1, pp. 267–278, 2006.

[22] J. Silvious, J. Clark, T. Pizzillo, and D. Tahmoush, "Micro-doppler phenomenology of humans at UHF and Ku-band for biometric characterization," in *Proceedings of the Radar Sensor Technology XIII*, Orlando, Fla, USA, April 2009.

[23] S. Björklund, H. Petersson, A. Nezirovic, M. B. Guldogan, and F. Gustafsson, "Millimeter-wave radar micro-Doppler signatures of human motion," in *Proceedings of the International Radar Symposium, (IRS '11)*, pp. 167–174, September 2011.

[24] Y. Wang and A. E. Fathy, "Micro-Doppler signatures for intelligent human gait recognition using a UWB impulse radar," in *Proceedings of the IEEE International Symposium on Antennas and Propagation and USNC/URSI National Radio Science Meeting (APSURSI '11)*, pp. 2103–2106, Spokane, Wash, USA, July 2011.

[25] O. R. Fogle and B. D. Rigling, "Micro-range/micro-Doppler decomposition of human radar signatures," *IEEE Transactions on Aerospace and Electronic Systems*, vol. 48, no. 4, pp. 3058–3072, 2012.

[26] N. F. Troje, "Decomposing biological motion: a framework for analysis and synthesis of human gait patterns," *Journal of Vision*, vol. 2, no. 5, pp. 371–387, 2002.

[27] T. Dogaru, C. Le, and G. Kirose, "Time-Frequency Analysis of a Moving Human Doppler Signature," ARL-TR-4728, 2009.

[28] D. Tahmoush, R. Wellman, and J. Silvious, "A compact persistent surveillance radar with micro-doppler capabilities," in *Proceedings of the MSS National Symposium*, Las Vegas, Nev, USA, August 2009.

[29] A. Freeman, "Fitting a two-component scattering model to polarimetric SAR data from forests," *IEEE Transactions on Geoscience and Remote Sensing*, vol. 45, no. 8, pp. 2583–2592, 2007.

Hindawi Publishing Corporation
Journal of Electrical and Computer Engineering
Volume 2013, Article ID 910146, 6 pages
http://dx.doi.org/10.1155/2013/910146

Research Article

Compact U-Slotted Antenna for Broadband Radar Applications

S. Costanzo and A. Costanzo

Dipartimento di Ingegneria Informatica, Modellistica, Elettronica e Sistemistica, Università della Calabria, 87036 Rende, Italy

Correspondence should be addressed to S. Costanzo; costanzo@deis.unical.it

Received 29 May 2013; Accepted 4 September 2013

Academic Editor: Alvaro Rocha

Copyright © 2013 S. Costanzo and A. Costanzo. This is an open access article distributed under the Creative Commons Attribution License, which permits unrestricted use, distribution, and reproduction in any medium, provided the original work is properly cited.

The original U-shaped patch antenna is properly modified in this work to provide a compact and broadband antenna configuration with reduced cross-polar effects, well suitable for modern radar applications. The proposed antenna layout is applied to design, realize, and test two different prototypes working at P-band and C-band, typically adopted for ground-penetrating radar. The experimental results successfully demonstrate a large operating bandwidth between 15% and 20%, a significant reduction of size (about half of the standard configuration), and a low cross-polarization level within the operating frequency range.

1. Introduction

The new generation radar systems require advanced components and materials [1–4] in order to properly exhibit their innovative features [5, 6]. For this motivation, in recent years, most of the classical hardware radar architecture functions have begun to be implemented via software, in order to reduce the costs and the complexity of the entire system [7–9]. Antennas often represent the most critical hardware component in the radar system, and the design of the radiating element needs to satisfy several constraints required by the novel applications, especially in terms of bandwidth [10–14] and quality of the radiation pattern, while guaranteeing, at the same time, a compact configuration. Microstrip patch antennas are largely employed in radar systems due to their low costs and easy manufacturing, low profile, light weight, and good strength, but the use of standard single-layer microstrip patch is not suitable for most radar applications, mainly due to its narrowband behavior. Additional resonant elements, such as slots, may be included in the radiating surface in order to enhance the bandwidth. The U-slot configuration is typically adopted at this aim, as the multiple resonances introduced by the slot allow it to produce a unique wideband response. Various examples exist in the literature for the standard U-slot patch antenna configuration. In [15], a compact U-slotted microstrip patch, performing a wideband behavior, has been presented, and in [16] an example of multiband U-slot antenna has been proposed. Even if all existing works show that U-slot configuration yields good results in terms of bandwidth and compactness, the additive resonances significantly disturb the main flow of the surface current, thus increasing the cross-polarization level. As a consequence of this, the useful radiation bandwidth of standard U-slot configuration is significantly reduced with respect to that achieved in terms of return loss behavior, thus preventing its application in modern broadband radar systems.

Most of the existing works in the literature for the standard U-slot antenna are focused on the achievement of a tradeoff between bandwidth and size reduction but not giving an effective procedure for reducing the cross-polar component.

Starting from the study of U-slot antenna behavior presented in [17], the original configuration is properly modified in this work to guarantee the wideband radiation feature, while reducing, at the same time, the cross-polarization effects due to the complex combination of the antenna and the slot modes. In the modified U-slot layout, the current path forced by the slot is properly constrained to provide a low cross-polarization effect, while achieving a significant reduction in the total size of the radiating element. To prove the effectiveness of the proposed antenna configuration, experimental validations on two different prototypes, useful for P-band and C-band radar applications, are successfully discussed. In particular, radiation bandwidths between 15% and 20% are demonstrated with reduced cross-polar levels and compact dimensions.

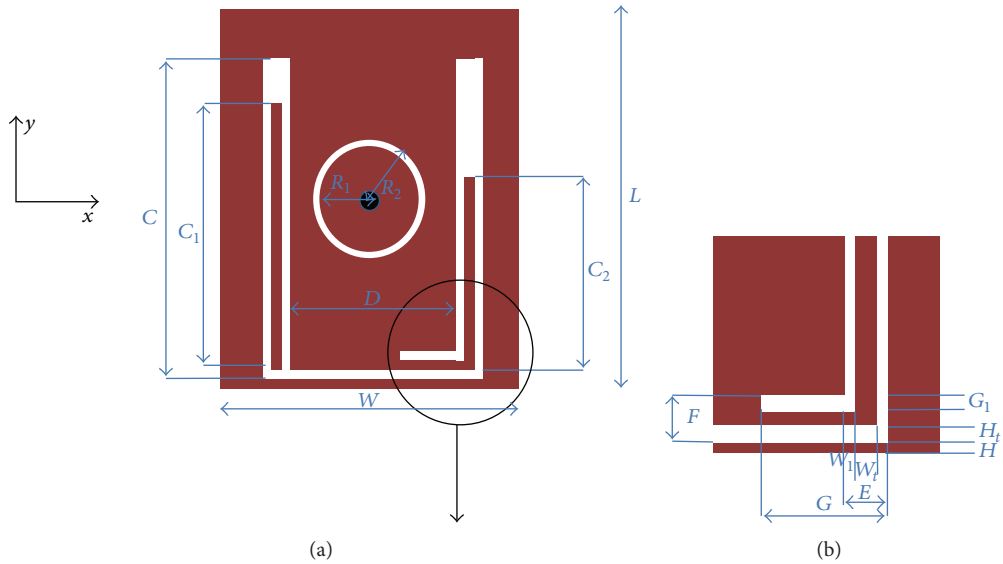

Figure 1: Layout of modified U-slot antenna: (a) top layer and (b) enlarged view of right corner.

2. Antenna Configuration

The technique based on the application of slot cuts in the radiating element is widely adopted in the literature to improve the bandwidth and/or reduce the antenna size [18–20]. In this paper, the basic U-slot shape is considered, properly modifying the layout as in Figure 1, in order to control the undesired current giving cross-polarization, but guaranteeing at the same time a compact structure with a large bandwidth behavior. Two main differences exist between the standard configuration and the proposed design, namely,

(i) asymmetrical strips introduced in the arms of the vertical U-shaped slots;

(ii) a further modification to the horizontal arm of the slot in order to introduce more degrees of freedom in the design, thus better controlling the current flow and the antenna resonance frequencies.

In the example shown in Figure 1, the polarization is vertical, so the layout is designed in order to avoid x-directed modal propagation.

As in classical U-slot antenna, a low permittivity substrate is used to reduce the antenna Q factor, thus increasing the bandwidth. In the proposed configuration, a ring slot is introduced around the central feeding point to compensate the large probe inductance due to the presence of the low permittivity substrate, which could worsen the impedance matching after a certain value of thickness. As discussed in [17], antenna and U-slot modes combinations, in the classical design, give undesired x-directed currents; hence, an unwanted increase of cross-polarization is produced. As a consequence of this, a particular ratio between the vertical and the horizontal arms needs to be considered to avoid this problem, but bandwidth requirements cannot always be satisfied according to this constraint.

The combination of the cuts in the proposed design allows a good tradeoff between bandwidth improvement and paths minimization of unwanted x-directed modes, avoiding a limiting constraint in the arms dimensions. The asymmetry in the vertical strip is necessary in order to achieve a better impedance matching, a significant size reduction, and a correct compensation of the x-directed currents. In the next section, the proposed antenna layout is successfully applied to design compact and wideband prototypes, with low cross-polarization effects, useful for P-band and C-band radar systems.

3. P-Band and C-Band Antenna Prototypes

Radar systems requiring a deep penetration into the monitoring scenario usually work in the relatively low region of the electromagnetic spectrum. For these applications, P-band operating frequencies are largely adopted. On the other hand, when high resolutions but lower waves penetrations are required, such as in short-range weather observation, C-band frequencies are usually considered.

In order to make the proposed antenna configuration well suitable for typical radar applications, two prototypes, respectively, working in P-band and C-band, are designed, realized, and tested. A low permittivity dielectric (foam, $\varepsilon_r = 1.07$) simulating an air filling is assumed as main substrate, while an upper thin (0.762 mm) standard layer of Arlon DiClad870 ($\varepsilon_r = 2.33$) is uniquely employed for robustness reasons, to better support the modified U-slot patch antenna. A thickness approximately equal to $\lambda_o/11$ is adopted in both cases for the foam substrate. An optimization procedure, based on the proper tuning of all geometrical parameters illustrated in Figure 1, is applied to derive, after a few iteration steps, the antennas dimensions, fully reported in Tables 1 and 2, respectively, for the P-band and the C-band prototypes.

The adopted design procedure assumes the study presented in [17] as a starting point, improving the configuration,

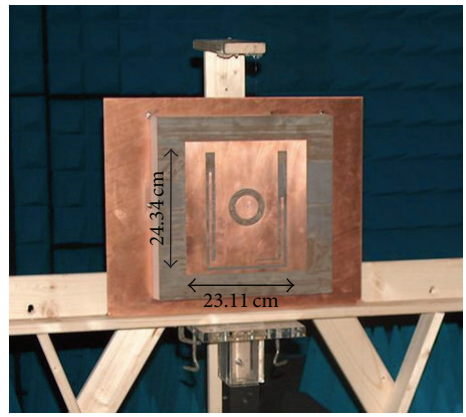

Figure 2: Photograph of P-band prototype into the anechoic chamber of Microwave Laboratory at University of Calabria.

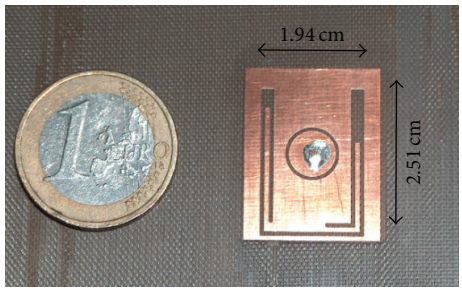

Figure 3: Photograph of C-band prototype.

in terms of compactness and wideband features, by assuming the following expressions for the patch width W, given as

$$W = \frac{c}{3.55 f_o}\sqrt{\varepsilon_r} \tag{1}$$

with c being the free-space velocity.

The inner and outer radii R_1, R_2 of the ring slot are chosen on the basis of the design procedure outlined in [21].

Finally, the parameters C_1, C_2, relative to the modified U-slot arms, are computed by the following expressions:

$$C_1 = \left(\frac{c}{4 f_o \sqrt{\varepsilon_r}} - \frac{E}{2}\right) \cdot \left(1 + \frac{D f_o \alpha}{c}\right),$$
$$C_2 = \left(\frac{c}{4 f_o \sqrt{\varepsilon_r}} - \frac{E}{2}\right) \cdot \left(1 - \frac{D f_o}{\alpha c}\right), \tag{2}$$

where the term α, assuming values in the range between 0.88 and 0.93, is adopted as tuning parameter to optimize, after a few iteration steps (typically two or three), the radiating structure in terms of impedance matching, achieving a bandwidth between 15% and 20%.

Both configurations reported in Tables 1 and 2 show a reduction of about 50% in the patch surface area, thus providing a significant compactness. As a matter of fact, a standard U-slot patch antenna [17] presents at P-band a width equal to 492.6 mm, while the proposed prototype in Table 1 (Figure 2) has a strongly reduced width equal to 231.1 mm. Similar features can be observed for the C-band prototype (Figure 3).

Table 1: Geometrical parameters of P-band prototype (centre frequency: 450 MHz).

Parameter	Dimension (mm)	Parameter	Dimension (mm)
L	243.4	R_1	22
W	231.1	F	18
D	156	W_t	6
E	18	G	59.2
C	218	R_2	35
C_1	181.5	W_1	6
H	6	G_1	5
C_2	231.1	H_t	5

Table 2: Geometrical parameters of C-band prototype (centre frequency: 4.25 GHz).

Parameter	Dimension (mm)	Parameter	Dimension (mm)
L	25.1	R_1	3.4
W	19.4	F	1.9
D	11.0	W_t	0.6
E	1.9	G	5.5
C	21.5	R_2	3.9
C_1	18.0	W_1	0.6
H	0.6	G_1	0.6
C_2	13.0	H_t	0.6

Experimental validations of prototypes in Figures 2 and 3 are performed into the anechoic chamber of the Microwave Laboratory at University of Calabria, equipped for both near-field [22–24] and far-field measurements.

For the P-band prototype, a bandwidth of about 15% is successfully demonstrated by the measured return loss behavior reported in Figure 4.

The operation bandwidth is further confirmed in terms of radiation features by the measured H-plane patterns illustrated in Figure 5 at different frequencies. As a matter of fact, it is straightforward to observe that the cross-polar component properly remains below the copolar field within the entire frequency band. This advantageous result is achieved by accurately minimizing the x-directed currents

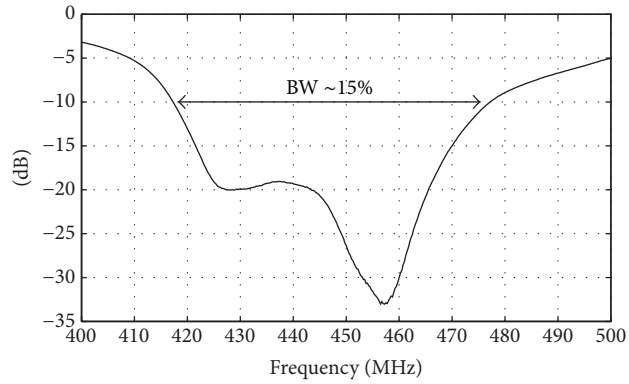

Figure 4: Measured return loss of P-band antenna prototype.

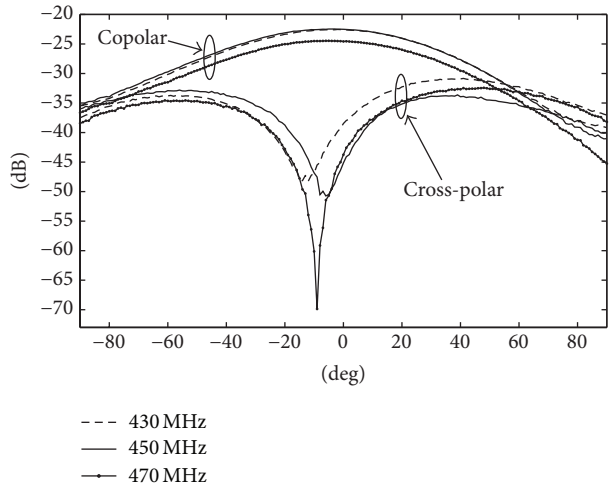

Figure 5: Measured radiation patterns of P-band antenna prototype at different frequencies.

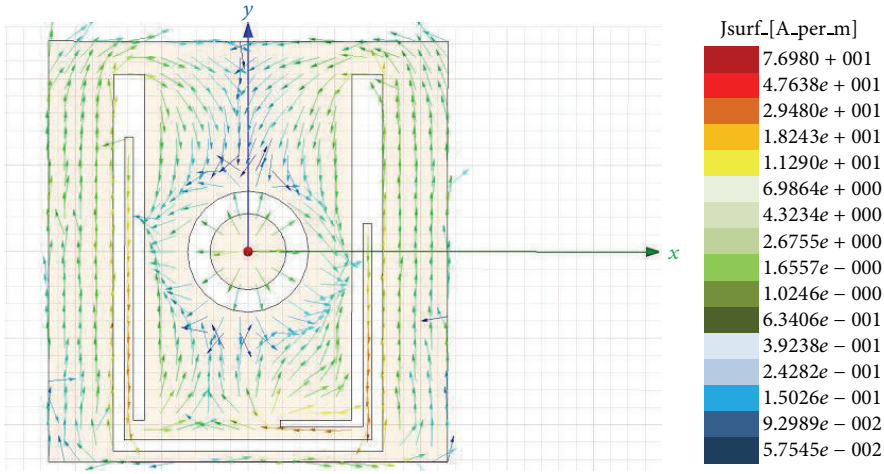

Figure 6: Simulated current distribution on the proposed P-band antenna prototype.

on the radiating elements, which are mainly dependent on the geometrical parameters D, C, G_1, and G_2 (Figure 1).

To demonstrate the proper reduction of the horizontal component of the current, a plot of the simulated current distribution on the P-band prototype at the central operating frequency of 450 MHz is reported in Figure 6. A strongly y-directed current can be observed in the strips inside the vertical arms of the U-slot, while no relevant x-directed current can be identified in the region outside the slot.

For comparison purpose, the simulated current distribution on a standard U-slot antenna [17] working at the same frequency is reported in Figure 7. In this case, a relevant

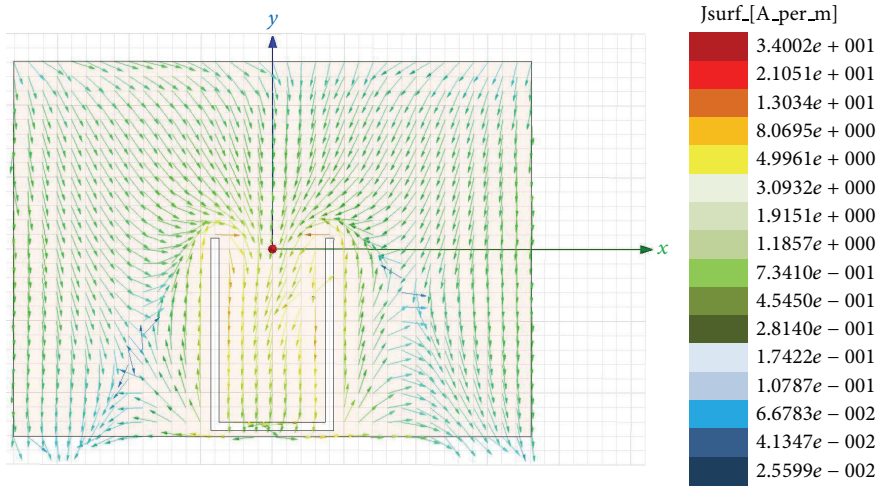

Figure 7: Simulated current distribution on a standard P-band U-slot antenna.

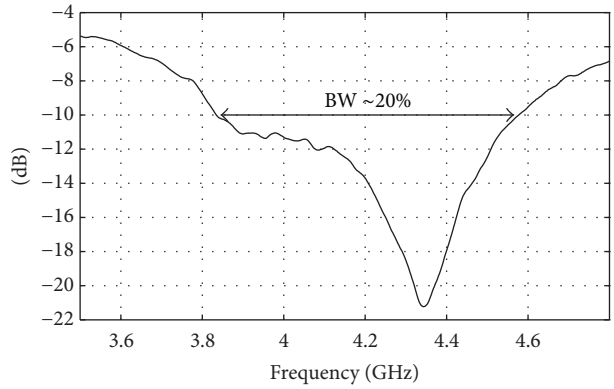

Figure 8: Measured return loss of C-band antenna prototype.

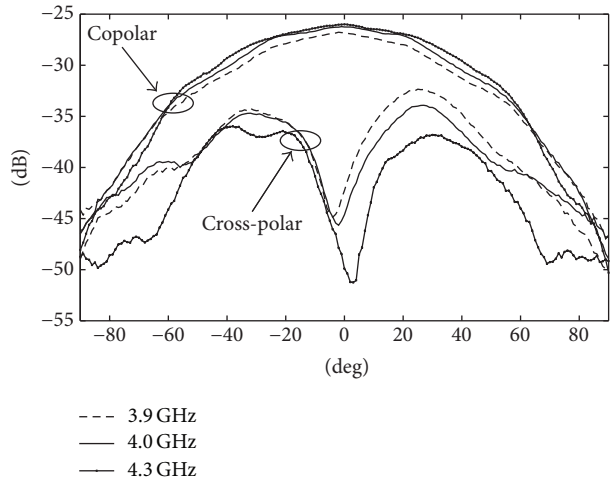

Figure 9: Measured radiation patterns of C-band antenna prototype at different frequencies.

x-directed current circulation can be observed, thus causing a more relevant cross-polar level with respect to the configuration proposed in this work.

Analogous experimental validations are performed on the C-band prototype (Figure 3), for which the measured return loss shows an operating bandwidth of about 20% (Figure 8). This is again confirmed by the measured radiation patterns of Figure 9, where the cross-polar fields are properly maintained below the copolar components when approaching the bandwidth extremes, thus overcoming the main limitation in terms of high cross-polarization effects, observed in [17] for the standard U-slot patch configuration.

4. Conclusion

An innovative U-shaped slot antenna has been discussed in this work to significantly overcome the limitations in terms of high cross-polar fields for the standard U-slot patch. The proposed slot design technique is able to provide a compact structure with a large operating bandwidth, without occurring in undesired cross-polarization effects strongly affecting the useful radiation frequency range. An effective broadband bandwidth between 15% and 20% has been successfully demonstrated by experimental validations on P-band and C-band prototypes, useful to be adopted as radiating elements into penetrating radar systems. As a matter of fact, the achieved broadband behavior assumes a great relevance at the radar system level, where wideband antennas are strongly necessary to support more demanding modes of operation, often condensing the received echo information into more channels, so as to enhance the radar capabilities in terms of target classification.

Acknowledgments

The authors would like to thank Mr. Ennio Marozzo for the precious technical support in the realization of the antenna prototypes. This work has been carried out under the framework of PON 01_01503 National Italian Project "Landslides Early Warning," financed by the Italian Ministry of University and Research.

References

[1] S. Costanzo, I. Venneri, G. D. Massa, and A. Borgia, "Benzocyclobutene as substrate material for planar millimeter-wave structures: dielectric characterization and application," *Journal of Infrared, Millimeter, and Terahertz Waves*, vol. 31, no. 1, pp. 66–77, 2010.

[2] S. Costanzo, F. Venneri, A. Borgia, I. Venneri, and G. di Massa, "60 GHz microstrip reflectarray on a benzocyclobutene dielectric substrate," *IET Science, Measurement and Technology*, vol. 5, no. 4, pp. 134–139, 2011.

[3] S. Costanzo, A. Borgia, I. Venneri, and G. di Massa, "Millimeter-waves structures on benzocyclobutene dielectric substrate," *Radioengineering*, vol. 20, no. 4, pp. 785–789, 2011.

[4] G. di Massa, S. Costanzo, and O. H. Moreno, "Accurate circuit model of open resonator system for dielectric material characterization," *Journal of Electromagnetic Waves and Applications*, vol. 26, no. 5-6, pp. 783–794, 2012.

[5] F. Venneri, S. Costanzo, and G. di Massa, "Tunable reflectarray cell for wide angle beam-steering radar applications," *Journal of Electrical and Computer Engineering*, vol. 2013, Article ID 325746, 7 pages, 2013.

[6] F. Venneri, S. Costanzo, and G. di Massa, "Design of a reconfigurable reflectarray unit cell for wide angle beam-steering radar applications," *Advances in Intelligent Systems and Computing*, vol. 206, pp. 1007–1013, 2013.

[7] S. Costanzo, F. Spadafora, A. Borgia, O. H. Moreno, A. Costanzo, and G. di Massa, "High resolution software defined radar system for target detection," *Advances in Intelligent Systems and Computing*, vol. 206, pp. 997–1005, 2013.

[8] S. Costanzo, F. Spadafora, O. H. Moreno, F. Scarcella, and G. di Massa, "Multiband software defined radar for soil discontinuities detection," *Journal of Electrical and Computer Engineering*, vol. 2013, Article ID 379832, 6 pages, 2013.

[9] S. Costanzo, F. Spadafora, G. di Massa et al., "Potentialities of USRP-based software defined radar systems," *Progress in Electromagnetics Research B*, vol. 53, pp. 417–435, 2013.

[10] S. Costanzo, F. Venneri, and G. di Massa, "Bandwidth enhancement of aperture-coupled reflectarrays," *Electronics Letters*, vol. 42, no. 23, pp. 1320–1322, 2006.

[11] S. Costanzo, G. di Massa, I. Venneri, and G. Arriendola, "Hybrid array antenna for broadband millimeter-wave applications," *Progress in Electromagnetics Research*, vol. 83, pp. 173–183, 2008.

[12] F. Venneri, S. Costanzo, G. di Massa, and G. Amendola, "Aperture-coupled reflectarrays with enhanced bandwidth features," *Journal of Electromagnetic Waves and Applications*, vol. 22, no. 11-12, pp. 1527–1537, 2008.

[13] S. Costanzo, I. Venneri, and G. di Massa, "Wideband hybrid array concept for millimeter-wave applications," *Journal of Infrared, Millimeter, and Terahertz Waves*, vol. 30, no. 4, pp. 374–380, 2009.

[14] F. Venneri, S. Costanzo, and G. di Massa, "Bandwidth behavior of closely spaced aperture-coupled reflectarrays," *International Journal of Antennas and Propagation*, vol. 2012, Article ID 846017, 11 pages, 2012.

[15] G. F. Khodaei, G. Nourinia, and C. Ghobadi, "A practical miniaturized U-slot patch antenna with enhanced bandwidth," *Progress in Electromagnetics Research B*, vol. 3, pp. 47–62, 2008.

[16] K. F. Lee, K. M. Luk, K. M. Mak, and S. L. S. Yang, "On the use of U-slots in the design of dual-and triple-band patch antennas," *IEEE Antennas and Propagation Magazine*, vol. 53, no. 3, pp. 60–74, 2011.

[17] S. Weigand, G. H. Huff, K. H. Pan, and J. T. Bernhard, "Analysis and design of broad-band single-layer rectangular U-slot microstrip patch antennas," *IEEE Transactions on Antennas and Propagation*, vol. 51, no. 3, pp. 457–468, 2003.

[18] F. Jolani and A. M. Dadgarpour, "Compact M-slot folded antenna for WLAN," *Progress in Electromagnetics Research Letters*, vol. 3, pp. 35–42, 2008.

[19] J. A. Ansari, P. Singh, S. K. Dubey, R. U. Khan, and B. R. Vishvakarma, "H-shaped stacked patch for dual-band operation," *Progress in Electromagnetics Research*, vol. B5, pp. 291–302, 2008.

[20] F. Yang, X. X. Zhang, X. Ye, and Y. Rahmat-Samii, "Wide-band E-shaped patch antennas for wireless communications," *IEEE Transactions on Antennas and Propagation*, vol. 49, no. 7, pp. 1094–1100, 2001.

[21] P. S. Hall, "Probe compensation in thick microstrip patches," *Electronics Letters*, vol. 23, no. 11, pp. 606–607, 1987.

[22] S. Costanzo and G. di Massa, "Far-field reconstruction from phaseless near-field data on a cylindrical helix," *Journal of Electromagnetic Waves and Applications*, vol. 18, no. 8, pp. 1057–1071, 2004.

[23] S. Costanzo and G. di Massa, "Direct far-field computation from bi-polar near-field samples," *Journal of Electromagnetic Waves and Applications*, vol. 20, no. 9, pp. 1137–1148, 2006.

[24] S. Costanzo and G. di Massa, "Near-field to far-field transformation with planar spiral scanning," *Progress in Electromagnetics Research*, vol. 73, pp. 49–59, 2007.

Hindawi Publishing Corporation
Journal of Electrical and Computer Engineering
Volume 2013, Article ID 573217, 7 pages
http://dx.doi.org/10.1155/2013/573217

Research Article

High Resolution Software Defined Radar System for Target Detection

S. Costanzo,[1] F. Spadafora,[1] A. Borgia,[1] H. O. Moreno,[2] A. Costanzo,[1] and G. Di Massa[1]

[1] *Dipartimento di Ingegneria Informatica, Modellistica, Elettronica e Sistemistica, Università della Calabria, 87036 Rende, Italy*
[2] *Facultad de Informatica y Electronica, Escuela Superior Politecnica de Chimborazo, Riobamba EC060155, Ecuador*

Correspondence should be addressed to S. Costanzo; costanzo@deis.unical.it

Received 10 May 2013; Revised 14 July 2013; Accepted 25 August 2013

Academic Editor: Alvaro Rocha

Copyright © 2013 S. Costanzo et al. This is an open access article distributed under the Creative Commons Attribution License, which permits unrestricted use, distribution, and reproduction in any medium, provided the original work is properly cited.

The Universal Software Radio Peripheral USRP NI2920, a software defined transceiver so far mainly used in Software Defined Radio applications, is adopted in this work to design a high resolution L-Band Software Defined Radar system. The enhanced available bandwidth, due to the Gigabit Ethernet interface, is exploited to obtain a higher slant-range resolution with respect to the existing Software Defined Radar implementations. A specific LabVIEW application, performing radar operations, is discussed, and successful validations are presented to demonstrate the accurate target detection capability of the proposed software radar architecture. In particular, outdoor and indoor test are performed by adopting a metal plate as reference structure located at different distances from the designed radar system, and results obtained from the measured echo are successfully processed to accurately reveal the correct target position, with the predicted slant-range resolution equal to 6 m.

1. Introduction

Radar systems have been employed for a long time mainly in military operation, like target detection, target recognition, surveillance, and other specific applications, such as meteorology and air-traffic control. However, especially in the last recent years, new kind of large-scale commercial applications is requiring the standard radar system operations, but according to significant cost reduction and strong adaptability. Medical diagnostics and automotives are just some examples of the possible application fields. According to this new operating context, Software Defined Radar (SDRadar) could represent a new challenge in radar technology due to the possibility of performing most of the basic operations (i.e., mixing, filtering, modulation, and demodulation) by simply employing software modules in order to strike out most of the specific hardware [1]. The main goal of a software defined approach is related not only to a clear cost reduction, but also to a significant increase of the versatility of the system, since signal generation and signal processing parameters may be easily adapted on the fly to the task under consideration. New researches are recently conducted to implement a SDRadar for target distance detection [2, 3], but they are based on the use of sophisticated FPGA and/or DSP, thus being not able to guarantee the required cost reduction.

A possible solution for a low cost SDRadar system development can be obtained by the adoption of the Universal Software Radio Peripheral (USRP) transceiver. A first attempt to apply USRP for target detection is performed in [4]; however, due to the bandwidth limitations imposed by the available USB connection, a limited slant-range resolution equal to 75 m is obtained. Interesting results are presented in [5–8], where different characterizations of the USRP N200 e N210 are employed as SDRadar systems. However, these transceivers are not able to easily design a compact device; moreover, a full adaptability of the software code on the fly for different scenarios can be scarcely achieved. National Instruments (NI) has recently manufactured two new generation devices, the USRP NI2920 and USRP NI2921, successfully combining the NI LabVIEW software and the USRP hardware to deliver an affordable and easy-to-use software-reconfigurable RF platform potentially suitable for experimentation, research, and rapid prototyping [9]. These devices, as yet used for teaching, communication, and mainly

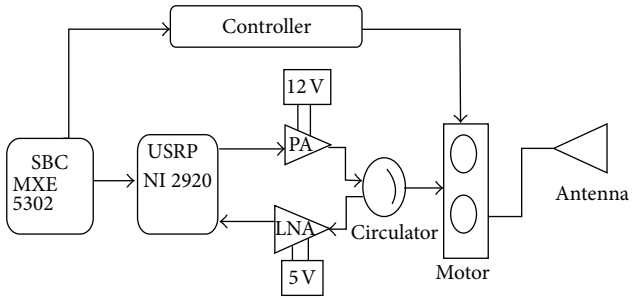

Figure 1: Block diagram of the proposed SDRadar system.

in Software Defined Radio applications [10], are considered in this work as a potential transceiver for a compact and versatile SDRadar. In particular, as described in Section 2, USRP NI2920 is employed in a SDRadar design for target detection.

Since one of the most relevant problems of SDRadar developing is related to a low slant-range resolution, due to the low speed of its interface, the main goal of this work is to explore the potentialities of the NI new generation USRP in order to enhance this specific parameter, taking advantage of the Gigabit Ethernet Interface. A LabVIEW code is developed to both control the features of the SDRadar system as well as to perform a signal processing compression technique (not completely suitable for the first generation USRP interface capabilities), thus achieving a strongly enhanced slant-range resolution with respect to the previous systems. Furthermore, experimental indoor and outdoor tests are performed in order to validate the system behavior in terms of target detection capability. A possible application scenario of the designed L-Band SDRadar system can be represented by the landslides monitoring in the presence of vegetated areas.

2. Proposed SDRadar System

The software radar architecture proposed in this work is developed to create a low cost, compact, and flexible solution for an accurate target detection; potentially, this scheme can be easily adopted in different scenarios without significant hardware modification, thus leading to create a multipurpose radar system. The complete block diagram of the proposed SDRadar system is reported in Figure 1. The USRP 2920 platform is used to transmit and receive data by a linear array antenna with specific bandwidth and directivity features useful for the prescribed application [11–16].

One of the main motivations for the choice of the USRP NI2920 is due to the enhanced available bandwidth (25 MHz), when compared to the first version (2 MHz), with the possibility to significantly enhance the radar slant-range resolution. The whole system is controlled by a LabVIEW application running on a compact single board computer (SBC). It is able to perform the required processing for target detection, but it is designed also to control a motor system guaranteeing the antenna, thus giving a scanning feature useful for an accurate surface monitoring in different directions. A power amplifier (PA) and a low noise amplifier (LNA) increase the signal power along both the transmission and the receiving paths, and a circulator can also be adopted to use a single antenna in both the transmission and the receiving paths, thus further reducing the total hardware costs and the size of the entire device.

3. Signal Processing Algorithm

A stretch processor (SP) approach [17], according to the diagram scheme of Figure 2, is adopted to implement the signal processing stage. First, the radar echo signal is mixed with a replica (reference signal) of the transmitted waveform. Then, a low pass filtering (LPF) and a coherent detection are performed in order to avoid the high frequency response coming from the mixer output. Analog to digital (A/D) conversion is subsequently applied, and a bank of narrow band filters is adopted to extract the tones proportional to the target range. Finally, a Fast Fourier Transform (FFT) is applied to derive the amplitude spectrum, whose peaks are related to the targets positions.

The adopted transmitted signal is a linear frequency modulated waveform expressed by the following equation:

$$s(t) = \cos\left[2\pi\left(f_0 t + \frac{\mu}{2}t^2\right)\right], \quad 0 < t < \tau', \tag{1}$$

where $\mu = B/\tau'$ is the LFM coefficient, B gives the bandwidth, f_0 is the chirp start frequency, and τ' is the chirp duration.

The slant-range resolution ΔR is then provided by the expression [17]

$$\Delta R = \frac{c}{2B}, \tag{2}$$

thus being strictly related to the system bandwidth B.

As imposed by (2), the use of USRP NI 2920 offers a maximum available bandwidth of 25 MHz, leading to have a slant-range resolution $\Delta R = 6$ m, which is significantly enhanced when compared to the value $\Delta R = 75$ m achieved with the first generation USRP, having a bandwidth $B = 2$ MHz [4].

On the basis of the outlined SP technique, a sophisticated algorithm implementing both the signal processing code and the motor control operations is developed in LabVIEW code (Figure 3) to obtain the proposed scanning SDRadar in Figure 1. In particular, the radar system is designed to perform N distinct scannings on different frames of the area under analysis (e.g., mountain, landslide, topography surfaces, and glaciers) through the controlled rotation of the radar antenna (Figure 4).

The main steps of SDRadar algorithm, whose block diagram is given in Figure 5, can be summarized as follows.

(1) Parameters definition:

(i) *Footprint* (antenna illuminating area) of each scan, defined in terms of distance between the radar antenna and the analyzed area, azimuth and elevation antenna beamwidths, grazing angle, and operating frequency;

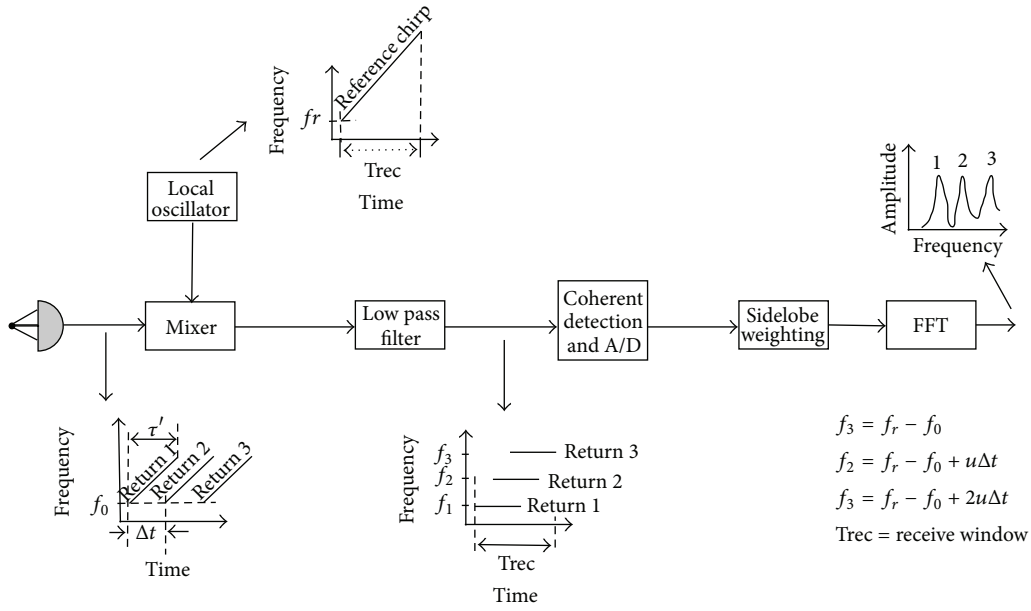

Figure 2: Block diagram of the Stretch Processor technique.

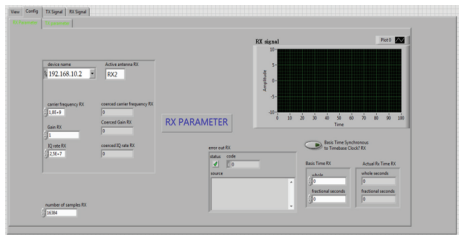

Figure 3: LabVIEW SDRadar application window.

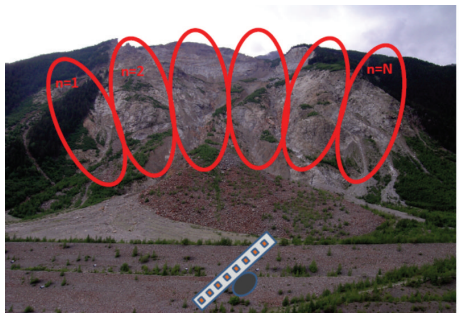

Figure 4: Schematic view of SDRadar antenna scanning.

(ii) *Receiving window* that ensures the correct recognition of any type of topology relative to the surface under analysis, defined by R_{min} and R_{max} (minimum and maximum required target range);

(iii) *Total area size*, giving the exact number N of radar scannings necessary to retrieve the total topology.

(2) Matrix definitions:

The Matrix is composed by N rows, corresponding to the N produced scanning, and M columns, depending on the receiving angular windows.

(3) Main loop implementing the SP algorithm and the motor control operations.

Once completing the matrix, a color assignment is performed like in a radar gram [18]. Colors are helpful for the remote view of the overall topology.

4. Experimental Validations

The performance of the SDRadar system proposed in Section 2 is tested in order to verify the proper distance detection between the radar device and a test metal plate, with dimensions equal to 1.22 m × 0.91 m, placed orthogonally to the direction of propagation of the radar transmitted waves. In this particular scenario, antennas are linearly polarized and the operating central frequency is equal 1.8 GHz, so the device operates as an L-band radar.

Specific outdoor tests are performed on the basic system, composed by a PC, USRP 2920, and two antennas, in order to validate the correct behavior of the transceiver in this scenario, and further indoor tests are performed on the complete system, described in Figure 1, with the adoption of the same test target, in order to confirm the enhanced radar resolution.

4.1. Outdoor Tests. A scheme of the outdoor test setup is reported in Figure 6. A broadband ridged horn is adopted as transmitting antenna, while a broadband logarithmic

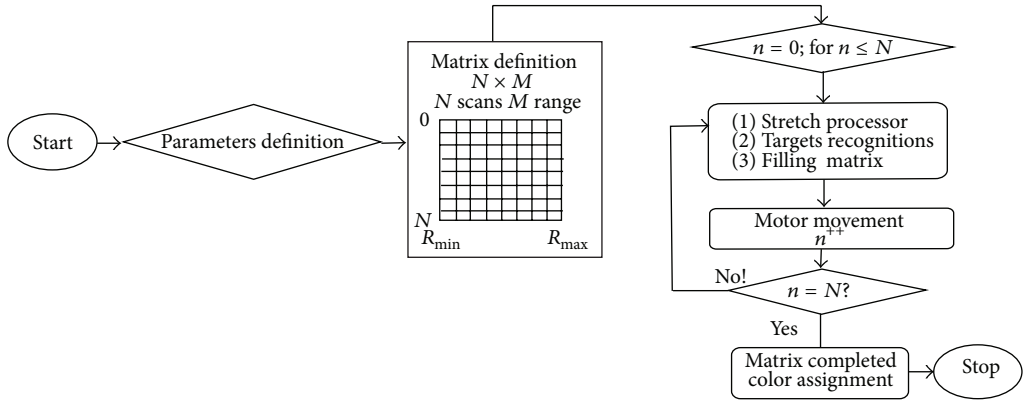

Figure 5: Block diagram of the scanning SDRadar algorithm.

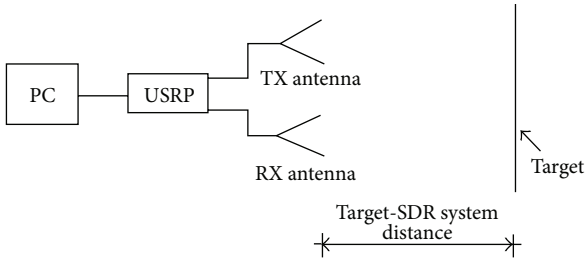

Figure 6: Scheme of the basic system for outdoor test.

Figure 7: Photograph of outdoor test setup.

antenna, with the same linear polarization, is used in the receiving path.

With reference to the general block diagram of Figure 1, the circulator, the amplifiers, and SBC are excluded in this first validation case, in order to test only the USRP behavior in terms of radar capabilities. A calibration step is preliminarily performed in the absence of the test target, in order to characterize and subsequently remove the undesired reflections due to the open measurement environment, otherwise producing "false" peaks. The test metal plate is subsequently placed at three different reference distances (6 m, 12 m, and 18 m) from the transmitting/receiving platform, in order to test the SDRadar slant-range resolution. A noncongested pedestrian zone (Figure 7) is chosen as test location, in order to have negligible contribution of multipath. The results of the FFT processing on the receiving echo for different target positions are illustrated in Figure 8, while a comparison between the true and the software retrieved target positions is summarized in Table 1.

Table 1: Real and retrieved target positions with the NI-USRP 2920.

Real target position [m]	Retrieved target position [m]
0 ÷ 6	6
6 ÷ 12	12
12 ÷ 18	18

The results relative to the reconstruction of the three targets positions are represented in terms of SDRadar map described in Section 4, but assuming for simplicity $N = 1$ (single scan). The corresponding radar gram, reported in Figure 9, properly displays the targets positions at 6 m, 12 m, and 18 m, with three different colors in a gray scale.

The results shown in Figures 8 and 9 confirm the proper distance detection capabilities and a resolution equal to 6 m, thus being 12 times less with respect to that obtained by using the first generation USRP in a SDRadar system.

4.2. Indoor Tests. Similar measurements are performed into the anechoic chamber of the Microwave Laboratory at University of Calabria, in order to test the correct behavior of the entire compact system illustrated in Figure 1. A broadband logarithmic antenna is adopted as both transmitting and receiving device, so the two paths are separated through the use of a circulator. A scheme of the relative test setup is shown in Figure 10. As in the outdoor tests, a preliminary calibration step is performed to avoid false peaks due to reflections in the path between circulator and antenna, power amplifier and circulator, and USRP and power amplifier. Again, a copper sheet is assumed as reference target and positioned at various distances, multiple of the theoretical range resolution, equal to 6 m.

The results of FFT performed on the received signal are illustrated in Figures 11 and 12 for target positions equal to 6 m and 12 m, respectively.

In both cases, the relative amplitude peaks can be properly distinguished in the diagrams, thus confirming the correct value of the slant-range resolution.

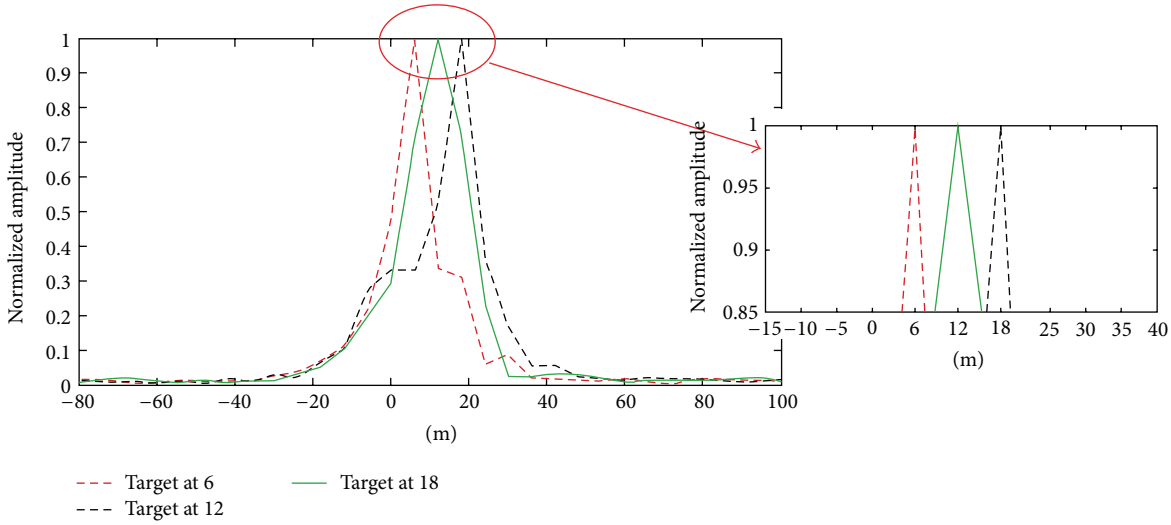

Figure 8: Retrieved signal peaks for different target positions.

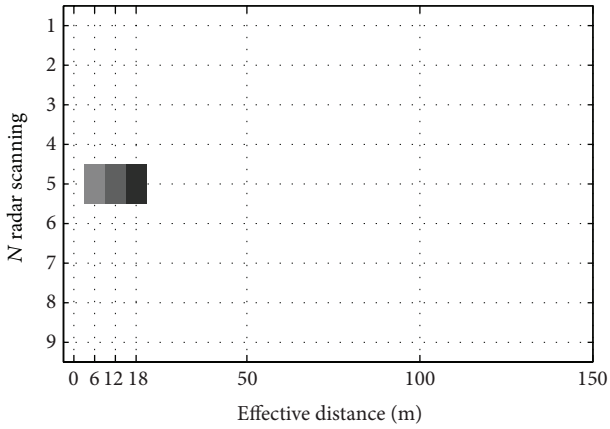

Figure 9: SDRadar map for a single scanning.

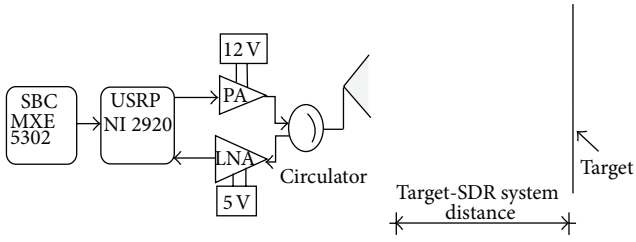

Figure 10: Scheme of indoor test setup.

Finally, two identical metal plates are both placed in the test zone, the first one at a distance between 0 m and 6 m and the second one between 6 m and 12 m.

Both relative target positions are accurately identified by the two main peaks corresponding to 6 m and 12 m (Figure 13). Other lower peaks, in correspondence with higher distances multiple of the slant-range resolution, represent multipaths of the radar signal between the two metallic plates. However, the low signal corresponding to multipaths does

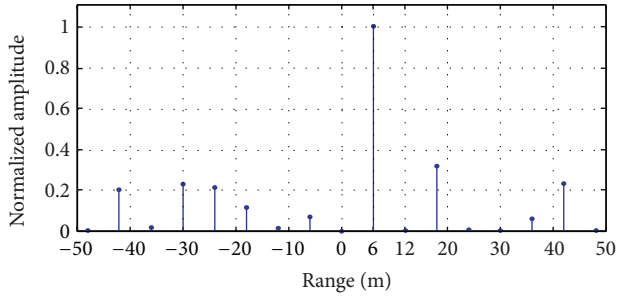

Figure 11: Retrieved signal peaks with the target placed at 6 m.

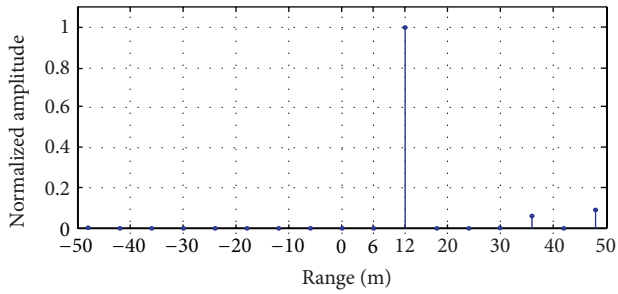

Figure 12: Retrieved signal peaks with the target placed at 12 m.

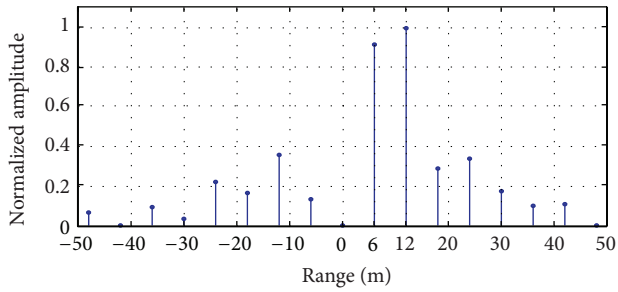

Figure 13: Retrieved signal peaks with two targets placed between 0 and 12 m.

not prevent the correct interpretation of the scene, so indoor tests on the entire compact device confirm the validity of proposed approach.

5. Final Discussion

The strong limitation in terms of slant-range resolution, due to the low data rate available at the interface of the first generation USRP and the low adaptability of similar transmitter-receiver devices into a compact device, strongly prevent the potential use of SDRadar in several new applications; as a consequence of this, the resolution enhancement, along with compactness and low costs, is becoming key factor in the SDRadar research. In this work, the use of the new generation NI 2920 USRP has been investigated to design a compact and low-cost SDRadar system able to provide appealing slant-range resolutions with a strong improvement (from 12 m to 6 m) when compared to the solutions existing in the literature. The effectiveness of the proposed approach has been successfully proven by indoor and outdoor tests, thus leading to the attractive possibility of creating multipurpose and adaptive low cost radar systems to be applied in different contexts.

6. Conclusions and Future Works

A low cost, flexible, compact, and versatile solution to create an L-Band SDRadar system has been proposed in this work. The USRP NI2920 platform has been adopted for the first time to realize a SDRadar system for target detection. The main result of integrating NI2920 in the proposed SDRadar system is related to the significant enhancing of slant-range resolution (6 m) with respect to that achieved in the existing SDRadar solutions. A specific LabVIEW application has been developed to implement the radar processing algorithm as well as to control the various components of the system. A stretch processing approach has been implemented in the system to fully take advantage of the benefit of the available enhanced bandwidth. Outdoor tests, using a basic version of the proposed SDRadar scheme, have been performed, correct distance measurements between the SDRadar platform and some metallic sheets have been obtained, and the expected slant-range resolution has been achieved. Indoor experimental validations have been also performed to demonstrate the correct working of the entire proposed system, in the case of single and multiple targets. As a future extension of this work, the proposed design will be updated by implementing supplementary signal processing features on the proposed SDRadar; for instance, a Doppler shift frequency analysis will be performed for movement detection, so new functions will be added to the proposed platform, with no changes in the hardware design, in order to create, step by step, a simple, low cost, and multipurpose radar.

Conflict of Interests

The authors state that there are no financial or competing interests which could influence the validity of the present research.

Acknowledgment

This work has been carried out under the framework of PON 01_01503 National Italian Project "Landslides Early Warning," financed by the Italian Ministry of University and Research.

References

[1] T. Debatty, "Software defined RADAR a state of the art," in *Proceedings of the 2nd International Workshop on Cognitive Information Processing (CIP '10)*, pp. 253–257, Brussels, Belgium, June 2010.

[2] Z. Hui, L. Lin, and W. Ke, "24 GHz software-defined radar system for automotive applications," in *Proceedings of the 10th European Conference on Wireless Technology (ECWT '07)*, pp. 138–141, Munich, Germany, October 2007.

[3] D. Garmatyuk, J. Schuerger, and K. Kauffman, "Multifunctional software-defined radar sensor and data communication system," *IEEE Sensors Journal*, vol. 11, no. 1, pp. 99–106, 2011.

[4] G. Aloi, A. Borgia, S. Costanzo et al., "Software defined radar: synchronization issues and practical implementation," in *Proceedings of the 4th International Conference on Cognitive Radio and Advanced Spectrum Management (CogART '11)*, Barcelona, Spain, October 2011.

[5] C. Prathyusha, S. N. Sowmiya, S. Ramanathan et al., "Implementation of a low cost synthetic aperture radar using software defined radio," in *Proceedings of the 2nd International Conference on Computing, Communication and Networking Technologies (ICCCNT '10)*, Karur, India, July 2010.

[6] M. Fuhr, M. Braun, C. Sturmz, L. Reichardtz, and F. K. Jondral, "An SDR-based Experimental Setup for OFDM-based radar," in *Proceedings of the 7th Karlsruhe Workshop on Software Radio*, Karlsruhe, Germany, March 2012.

[7] M. Muller, M. Braun, M. Fuhr, and F. K. Jondral, "A USRP-based testbed for OFDM-based radar and communication systems," in *Proceedings of the 22nd Virginia Tech Symposium on Wireless Communications*, Blacksburg, Va, USA, June 2012.

[8] V. Fernandes, "Implementation of a RADAR System using MATLAB and the USRP," CSUN ScholarWorks, 2012.

[9] National Instruments Data-sheet, NI USRP-2920, NI USRP-2921, http://arabia.ni.com/.

[10] U. Pesovic, D. Gliech, P. Planinsiz, Z. Stamenkovic, and S. Randic, "Implementation of IEEE 802.15.4 transceiver on software defined radio platform," in *20th Telecommunications Forum (TELFOR '12)*, Belgrade, Serbia, November 2012.

[11] S. Costanzo and A. Costanzo, "Compact slotted antenna for wideband radar applications," *Advances in Intelligent Systems and Computing*, vol. 206, pp. 989–996, 2013.

[12] S. Costanzo, G. A. Casula, A. Borgia et al., "Synthesis of slot arrays on integrated waveguides," *IEEE Antennas and Wireless Propagation Letters*, vol. 9, pp. 962–965, 2010.

[13] S. Costanzo, I. Venneri, G. Di Massa, and G. Arriendola, "Hybrid array antenna for broadband millimeter-wave applications," *Progress in Electromagnetics Research*, vol. 83, pp. 173–183, 2008.

[14] F. Venneri, S. Costanzo, G. Di Massa, and G. Amendola, "Aperture-coupled reflectarrays with enhanced bandwidth features," *Journal of Electromagnetic Waves and Applications*, vol. 22, no. 11-12, pp. 1527–1537, 2008.

[15] F. Venneri, S. Costanzo, and G. Di Massa, "Tunable reflectarray cell for wide angle beam-steering radar applications," *Journal*

of Electrical and Computer Engineering, vol. 2013, Article ID 325746, 7 pages, 2013.

[16] F. Venneri, S. Costanzo, and G. Di Massa, "Design of a reconfigurable reflectarray unit cell for wide angle beam-steering radar applications," *Advances in Intelligent Systems and Computing*, vol. 206, pp. 1007–1013, 2013.

[17] B. R. Mahafza and A. Z. Elsherbeni, *Simulations for Radar Systems Design*, Chapman & Hall/CRC, New York, NY, USA, 1999.

[18] M. Skolnik, *Radar Handbook*, McGraw Hill, San Francisco, Calif, USA, 3rd edition, 2008.

Hindawi Publishing Corporation
Journal of Electrical and Computer Engineering
Volume 2013, Article ID 809691, 8 pages
http://dx.doi.org/10.1155/2013/809691

Research Article

Space-Time Radar Waveforms: Circulating Codes

G. Babur, P. Aubry, and F. Le Chevalier

Microwave Sensing, Systems and Signals (MS3), Delft University of Technology, 2628 CD Delft, The Netherlands

Correspondence should be addressed to G. Babur; g.babur@tudelft.nl

Received 18 May 2013; Accepted 1 August 2013

Academic Editor: Sandra Costanzo

Copyright © 2013 G. Babur et al. This is an open access article distributed under the Creative Commons Attribution License, which permits unrestricted use, distribution, and reproduction in any medium, provided the original work is properly cited.

This paper describes a concept of the circulating codes covering the whole class of the space-time codes. The circulating codes do not narrow the radiated pattern of the antenna array, thus providing a wide angular coverage, possibly tunable. In turn, the beam-forming on transmit is achievable by means of the signal processing in one (or each) receiver channel. The modelling results demonstrate the efficiency of the circulating codes based on their multidimensional ambiguity functions.

1. Introduction

In many modern radar applications, pulse compression is a key element to achieve the required performance. The codes to be used must possess appropriate properties of auto- and cross-correlations. In turn, beam-forming is another well-known signal processing technique used in sensor arrays for directional signal transmission or reception [1].

Many engineers have noted that if one were able to form truly simultaneous transmit beams in independent directions, then a flexible radar system could be build that would be capable of true simultaneous multifunction operation [2]. Moreover, since digital array MIMO radars can be operated in either the MIMO or the more conventional transmit modes (as needed), a great deal of flexibility can be provided.

Until recently, radar transmitters have not enjoyed the same degree of software-driven agility as radar receivers [3]. Nowadays radar transmitters incorporate highly agile, software-driven waveform generators. In principle, the radar designer's choice of beam shape and waveform can be used to spread energy over space and time in many interesting and different ways [2].

The coloured transmission principles have been presented in [4]. They allow the transmission of the sounding signals in a wide angular angle, and, at the same time, to perform the beam-forming on transmit in one (or each) of the receiving channels. They allow for an effective monitoring of any number of beams formed on transmit by means of signal processing on receive. The technique, describing application of the digital beam-forming processing with a single receiver channel, can be found, for example, in [5]. At the same time, the amount of measurements stays the same as for one beam, with some increase of the computational cost in the receiver. So, the coloured waveform transmission offers vastly increased transmitter agility to identify ways to exploit agile transmitter capabilities in practice.

In the literature on MIMO radar, it is often assumed that the transmitted waveforms associated with each transmit antenna or subarray are orthogonal and have perfect waveform cross-correlation properties. In practice, this is hardly achievable, when the transmitted signals occupy the same time interval within the same bandwidth. When we consider the same waveform circulating through each antenna element with a very small relative time shift, as presented in this paper, it seems that achievement of good cross-correlation properties is simply impossible. However, the received results demonstrate the opposite. Consequently, the circulating codes for coherent MIMO deserve careful consideration and analysis.

Implicit in the waveform design is that the observed radar scene should be estimated accurately. The scattering response of the clutter and targets must be disentangled by the receiver. A commonly used measure for assessing waveform selection in radar systems is the ambiguity function, which will be used here for analyzing the properties of the proposed code. In conventional radar systems, Woodward's ambiguity function is used to characterize waveform resolution performance [6, 7]. For analysis of space-time radar waveforms, such as

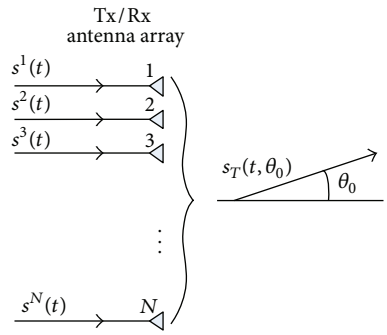

Figure 1: MIMO transmission.

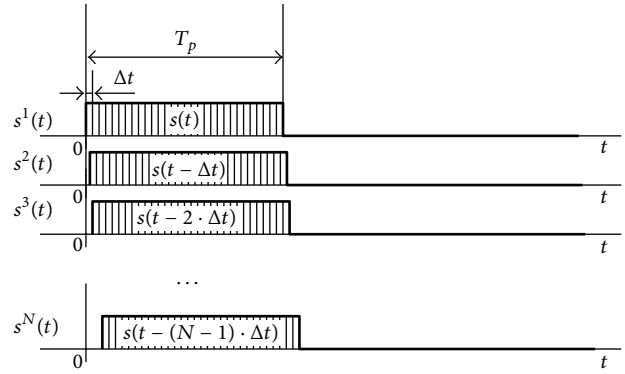

Figure 2: Circulating signals.

the circulating codes presented in this paper, the multidimensional ambiguity function should be employed [8, 9].

This paper describes a solution for the proposed waveforms based on the use of a novel and technically simple solution of transmitting only one waveform circulating from one antenna element to another (or from one subarray to another) with a very small relative time shift. In this way the radiated signals have exactly the same coding complex envelope, highly overlapping both in the time and frequency domains.

The paper is organized as follows. In Section 2 the concept of the circulating space-time codes, which applies to all possible waveforms having good autocorrelation properties, is introduced. Section 3 describes the multidimensional ambiguity function used for the space-time signals analysis. Section 4 gives the examples of the ambiguity functions for a number of circulating codes examples. The capabilities of the waveforms for the beam-forming on transmit and pulse compression are shown. Section 5 contains the conclusions.

2. Circulating Codes Concept

The transmitted waveforms are assumed to be encoded by the same waveform $s(t)$ circulating with a relative time shift through N MIMO transmitter channels (see Figure 1). The waveform $s^n(t)$ circulating through the nth channel can be written as

$$s^n(t) = a_n \cdot s(t - (n-1) \cdot \Delta t), \quad (1)$$

where the index n represents both the number of the transmitting channels and the number of the transmitted waveforms. The relative time shift Δt between the circulating signals is equal to 1-sample time, $\Delta t = 1/\Delta F$, where ΔF is the signal bandwidth. For waveforms with a large BT-product (compression ratio), the relative time shift is very small compared to the pulse duration T_p because, in fact, $\mathrm{BT} = T_p/\Delta t$. For the sake of simplicity, the amplitudes a_n are assumed to be the same and equal to one and will be omitted further.

The simplicity of implementation of the circulating codes should be emphasized. Because of the use of only one waveform, only one complex signal with a large BT product should be generated; and then it circulates in all the transmitter channels with a small relative offset.

Figure 2 shows the circulating signals $s^n(t)$, $n = 1 \cdots N$. The total radiated signal $s_T(t)$ has the following properties. It has the same duration T as the signal $s(t)$. This is explained by the fact that the envelope of the sum signal has a trapezium shape with duration T at −3 dB level. The relative time delay of the signal $s_T(t)$ compared to $s(t)$ is equal to the half of the relative time shift between the first and the last circulating signals. This time delay is constant and it is equal to $(N - 1) \cdot \Delta t/2$. It can be compensated at the signal generation stage in the MIMO radar transmitter by the equal shift of all the radiated signals or by compensation of this known time delay at the signal processing stage in the MIMO radar receiver.

The time offset used in the circulating signal can be looked at as a time-delay beam-steering (see, e.g., [10]). The time-delay steering of array antennas is used to steer the narrow main beam of the antenna array physically. When the circulating signals are used for sounding, the radiated beam is not steered, and the signals are radiated within the wide angle. The time shifts within the circulating codes are used not to steer the beam but to keep it as wide as possible. The beam-forming on transmit (narrowing of the main beam) is implemented by the signal processing means on receive.

Array theory tends to discuss things in phase rather than delay, so we can convert the delay experienced by the circulating signal into a phase shift, between adjacent antenna elements, at a given frequency:

$$\Delta\varphi = 2\pi \cdot f \cdot \Delta t = \frac{2\pi \cdot f}{\Delta F}, \quad (2)$$

where f is the radiated signal's frequency. Since the radiated signal bandwidth ΔF is not equal to zero, the phase shift is not fixed. The phase shift is a function of the frequency $\Delta\varphi(f)$ where the radiated signal's frequency belongs to the following interval: $f \in [(f_0 - \Delta F/2) \cdots (f_0 + \Delta F/2)]$, where f_0 is the radiated signal's central frequency. Therefore, the range of the phase shift described by (2) can be written as

$$(\Delta\varphi_{\min} \cdots \Delta\varphi_{\max}) = ((\Delta\varphi_0 - \pi) \cdots (\Delta\varphi_0 + \pi)), \quad (3)$$

where $\Delta\varphi_0$ is the phase shift provided by the central radiated frequency. Equation (3) shows that the phase shift within the radiated signal's bandwidth changes by 2π, which characterizes the full angular coverage.

The uniformly spaced linear array can be steered by applying a phase shift such as $\Delta\varphi = 0$ at the angle of interest [11]:

$$\Delta\varphi_0 = 2\pi \cdot \frac{d}{c} \cdot f \cdot \sin\theta_0, \tag{4}$$

where d is the spacing between the antenna elements and c is the speed of light. However, for the circulating signals the phase shift varies by 2π along the array for any θ_0. It means that, regardless of the value of $\Delta\varphi_0$ or on the steering direction, the physically radiated circulating signals provide the full angular coverage, in practice, limited only by the radiated patterns of the antenna elements. So, in fact, the signals are radiated within a wide angular range, and the beam-forming on transmit (forming of multiple beams) is performed on receive by the signal processing means, which is explained further in the paper.

The group transmitted signal (see Figure 1) is angular dependent. For ease of exposition, let us make the usual narrowband assumption; this is not a requirement, but simplifies the discussion. So, in a given direction θ_0 the aggregate transmitted signal can be written as the sum of all transmitted signals, with appropriate phase shifts for this direction defined by the wavenumber $\vec{k}(\theta_0)$:

$$s_T(t,\theta_0) = \sum_{n=1}^{N} e^{j\vec{k}(\theta_0)\cdot\vec{x}(n)} \cdot s^n(t), \tag{5}$$

where $\overline{k}$ is a wave-vector, $\overline{x}(n)$ is the position vector of the nth radiating element, and $s^n(t)$ is a circulating signal described by (1).

The signal received by one receiver channel r is written as

$$s_R^r(t,\theta_0) = e^{-j\overline{k}(\theta_0)\cdot\overline{x}(r)} \cdot \dot{A} \cdot s_T(t-\tau_0,\theta_0) + e(t), \tag{6}$$

where $\dot{A}$ is the complex scattering coefficient of an observed target, τ_0 is a time delay defined by the travelling distance of the signal, and $e(t)$ is noise at time t. In this work, we assume that within one pulse the phase variance due to the Doppler shift is negligible and the Doppler shift becomes just a constant phase term. The multidimensional transmit ambiguity function presented in the next section is calculated for one pulse as a squared modulus of the matched filter output (see the end of Section 3). Since we take the modulus, we neglect the phase term defined by the Doppler shift imposed on the pulse. So, the use of the bank of Doppler filters together with the sounding circulating signals makes the observation of moving objects possible and, at the same time, provides a wide angular coverage with possibility of the beam-forming on transmit performed in radar receiver.

3. Transmit Ambiguity Function: Circulating Codes

As known, the matched filter is the solution for maximizing the output signal-to-noise ratio (SNR). So, the beam-forming on transmit is performed on the received signals in the rth channel as the filtering matched with the transmitted signal $s_T(t,\theta_0)$:

$$R_{\theta_0}^r(\tau,\theta') = \int s_T(t-\tau,\theta') \cdot \left(s_R^r(t,\theta_0)\right)^* dt, \tag{7}$$

where θ' is a hypothesis about the arrival direction. The superscript "$*$" means complex conjugation. The extended form of the compressed signal is

$$R_{\theta_0}^r(\tau,\theta') = \dot{A}^* \cdot e^{+j\cdot\overline{k}(\theta_0)\cdot\overline{x}(r)} \cdot \int s_T(t-\tau,\theta') \cdot \left(s_T(t-\tau_0,\theta_0)\right)^* dt. \tag{8}$$

Omitting the constant phase term characteristic for the rth receiving channel and changing the time variables $t' = (t-\tau_0)$, $\tau' = (\tau_0 - \tau)$, we receive

$$R_{\theta_0}(\tau',\theta') = \int s_T(t'+\tau',\theta') \cdot \left(s_T(t',\theta_0)\right)^* dt', \tag{9}$$

which can be rewritten as

$$R_{\theta_0}(\tau',\theta') = \int \left(\sum_{n=1}^{N} e^{j\cdot\overline{k}(\theta')\cdot\overline{x}(n)} \cdot s(t'+\tau'-n\cdot\Delta t+\Delta t)\right) \cdot \left(\sum_{n'=1}^{N} e^{j\cdot\overline{k}(\theta_0)\cdot\overline{x}(n')} \cdot s(t'-n'\cdot\Delta t+\Delta t)\right)^* dt', \tag{10}$$

where, as we remember, n is the index for the transmitted signal and n' is the index for its replica.

$$R_{\theta_0}(\tau',\theta') = \sum_{n=1}^{N}\sum_{n'=1}^{N} e^{j\cdot(\overline{k}(\theta')\cdot\overline{x}(n)-\overline{k}(\theta_0)\cdot\overline{x}(n'))} \cdot \int s(t'+\tau'-(n-1)\cdot\Delta t) \cdot s^*(t'-(n'-1)\cdot\Delta t)\, dt'. \tag{11}$$

As was defined before, Δt is a 1-sample time shift between the replicas of $s(t)$ in the circulating code. At the same time, Δt is the width of the autocorrelation function $\mathrm{ACF}_S(\tau')$ of the signal $s(t')$ taking into account the time variables' change:

$$R_{\theta_0}(\tau',\theta') = \sum_{n=1}^{N}\sum_{n'=1}^{N} e^{j\cdot(\overline{k}(\theta')\cdot\overline{x}(n)-\overline{k}(\theta_0)\cdot\overline{x}(n'))} \cdot \mathrm{ACF}_S(\tau'-(n-1)\cdot\Delta t+(n'-1)\cdot\Delta t). \tag{12}$$

The normalized value of the autocorrelation function is equal to 1 within 1-sample time interval $\Delta t = 1/\Delta F$ around $\tau' = 0$. For the rest, the ACF is described by its side-lobe level (SLL). The SLL for signals having large BT

products and providing good autocorrelation properties can be approximated as 0. So, (12) can be written as

$$R_{\theta_0}\left(\tau', \theta'\right) = \sum_{n=1}^{N}\sum_{n'=1}^{N} e^{j\cdot\left(\bar{k}(\theta')\cdot\bar{x}(n)-\bar{k}(\theta_0)\cdot\bar{x}(n')\right)} \cdot 1\left(\tau' - (n-1)\cdot\Delta t + \left(n'-1\right)\cdot\Delta t\right). \tag{13}$$

The function $1(\tau')$ is equal to 1 within 1-sample time interval around $\tau' = 0$ and zero for the rest. Consider

$$R_{\theta_0}\left(\tau', \theta'\right) = \sum_{n=1}^{N} \operatorname{rect}\left(\tau' - (n-1)\cdot\Delta t\right) \sum_{n'=1}^{N} e^{j\cdot\left(\bar{k}(\theta')\cdot\bar{x}(n)-\bar{k}(\theta_0)\cdot\bar{x}(n')\right)}, \tag{14}$$

where

$$\operatorname{rect}\left(\tau'\right) = \begin{cases} 1 & \text{for } -(N-1)\cdot\Delta t \le \tau' \le 0, \\ 0 & \text{for elsewhere } \tau'. \end{cases} \tag{15}$$

We note that the function $\operatorname{rect}(\tau')$ for the circulating signals is N times wider than the achievable range resolution provided by one waveform, which is equal to 1 bit or Δt. This gives the proper width of its autocorrelation function (ACF) introduced below, and, therefore, the proper widening of the ambiguity function along ranges.

Equation (14) can be simplified as follows:

$$R_{\theta_0}\left(\tau', \theta'\right) = \begin{cases} \operatorname{ACF}_{\text{rect}}\left(\tau'\right)\cdot \sum_{n=1}^{N}\sum_{n'=1}^{N} e^{j\cdot\left(\bar{k}(\theta')\cdot\bar{x}(n)-\bar{k}(\theta_0)\cdot\bar{x}(n')\right)} & \text{for } \left|\tau'\right| \le \dfrac{N\cdot\Delta t}{2}, \\ 0 & \text{for elsewhere } \tau'. \end{cases} \tag{16}$$

Equation (16) is an adequate approximation in case of an ideal autocorrelation function of the signal $s(t)$ with one peak and zero side-lobe level (SLL).

The mathematical expression of the multiparameter signal $R_{\theta_0}(\tau', \theta')$ shows its dependency on the transmitted waveforms $s^n(t)$ (see (1)). The ambiguity function $|R_{\theta_0}(\tau', \theta')|^2$ is thus a 3-dimensional function (or 4-dimensional, if the amplitude is considered as a dimension as well), giving for each aiming direction θ_0 the delay-angle ambiguity. $R_{\theta_0}(\tau', \theta')$, being a 3-parameters function, cannot be visualized easily; a preferred way is to look at the angle-angle cut, for $\tau = 0$, and at the range-angle ambiguity, for a specific θ_0:

(i) $|R_{\theta_0}(0, \sin\theta)|^2 = D(\theta, \theta_0)$, is the angular transmit diagram (at the exact range of the target, $\tau' = \tau_0$), as a function of the angular aiming position θ_0.

(ii) $|R_{\theta_0}((c\tau')/2, \theta')|^2$, where θ_0 is constant, is the range-angle ambiguity function, for boresight aiming direction—ideally, this range angle ambiguity function should also be analyzed for each possible aiming direction θ_0.

4. Modeling Results

Four very different complex waveforms have been chosen for operation in the circulating space-time mode as follows.

(1) Quadratic Alltop code, as a representative of the distinct complex-valued sequences constructed for the minimization of the magnitudes of autocorrelation side lobes and cross-correlations [12].

(2) M-sequence or a maximum length sequence, as a type of widely used pseudorandom binary sequences, which are inexpensive to implement in hardware or software. The autocorrelation function has a uniform side-lobe level.

(3) LFM signal, which is a very common radar waveform to realize pulse compression for its fairly ready generation and easy processing. However, without weighting, the autocorrelation function experiences a high side-lobe level.

(4) Nonlinear LFM signal (NLFM). Nonlinear frequency modulation can advantageously shape the "rectangular" energy spectrum of an LFM signals, such that the autocorrelation function exhibits substantially reduced side lobes. The NLFM signal with the tangent-based frequency variation law [13] has been chosen for modeling.

It is known that the number of orthogonal LFM signals within the same bandwidth and time interval is limited by a number of 2. In case an LFM signal is used according to the principle presented in this paper, all the signals circulating through the transmitting channels have the same shape, as can be seen in (1). The important conclusion for all waveforms, not necessarily having LFM modulation, is that the number of circulated signals (transmitters/antenna elements) is not really limited, and it can be definitely more than 2. What is really needed is the good autocorrelation properties of the circulating waveform to make the approximation (13) viable.

The pulse duration is equal to 100 μs. The carrier frequency is 10 GHz. The BT product of all the modelled signals was chosen relatively small, 255, for better visibility of the results. The antenna array is made of $N = 8$ elementary omnidirectional antennas spaced $\lambda/2$ from each other. For demonstrating the possibilities of the beam-forming on transmit for the analysed waveforms, only one element of the array was used on receive.

In Figure 3, four angle-angle cuts of the ambiguity function calculated for four considered types of circulating waveforms are shown. They are angle versus aiming (beamformed on transmit) angle taken at the contingently zero range $\tau' = 0$ ($\tau = \tau_0$). These cuts demonstrate the possibilities of the considered signals to implement beam-forming on transmit implemented in one (or each) of the receiving radar channels. Every single vertical slice for a definite possible angular direction θ_0 describes the array patterns formed on transmit by the signal processing means in the receiver, while physically the radiation pattern on transmit stays wide (omnidirectional for the presented modelling results). This is illustrated by eight vertical slices of the ambiguity function

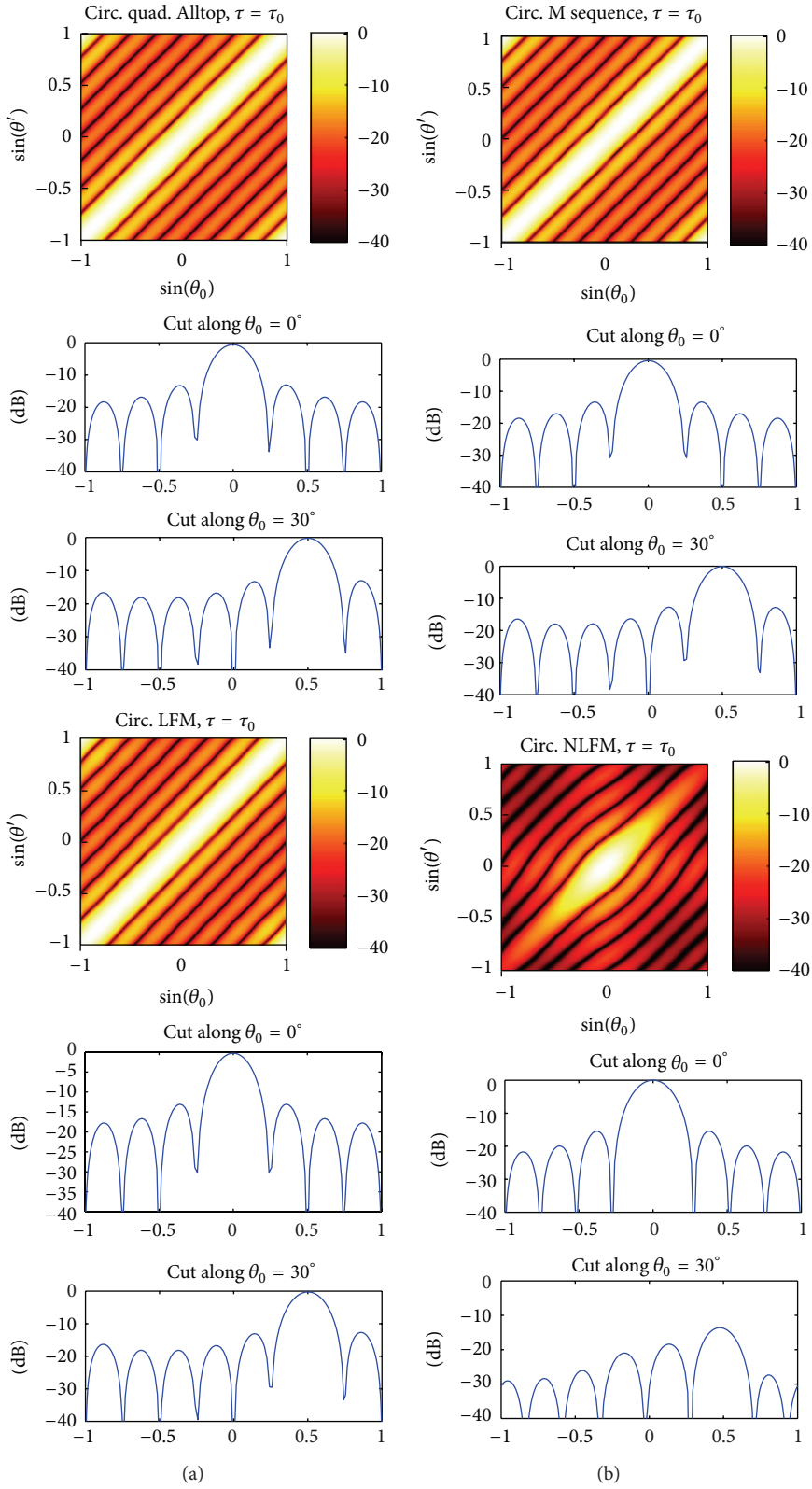

FIGURE 3: Angle-angle cuts of the ambiguity function $|R^0_{\theta_0}(\tau', \theta')|^2$ at $\tau' = 0$ in dB.

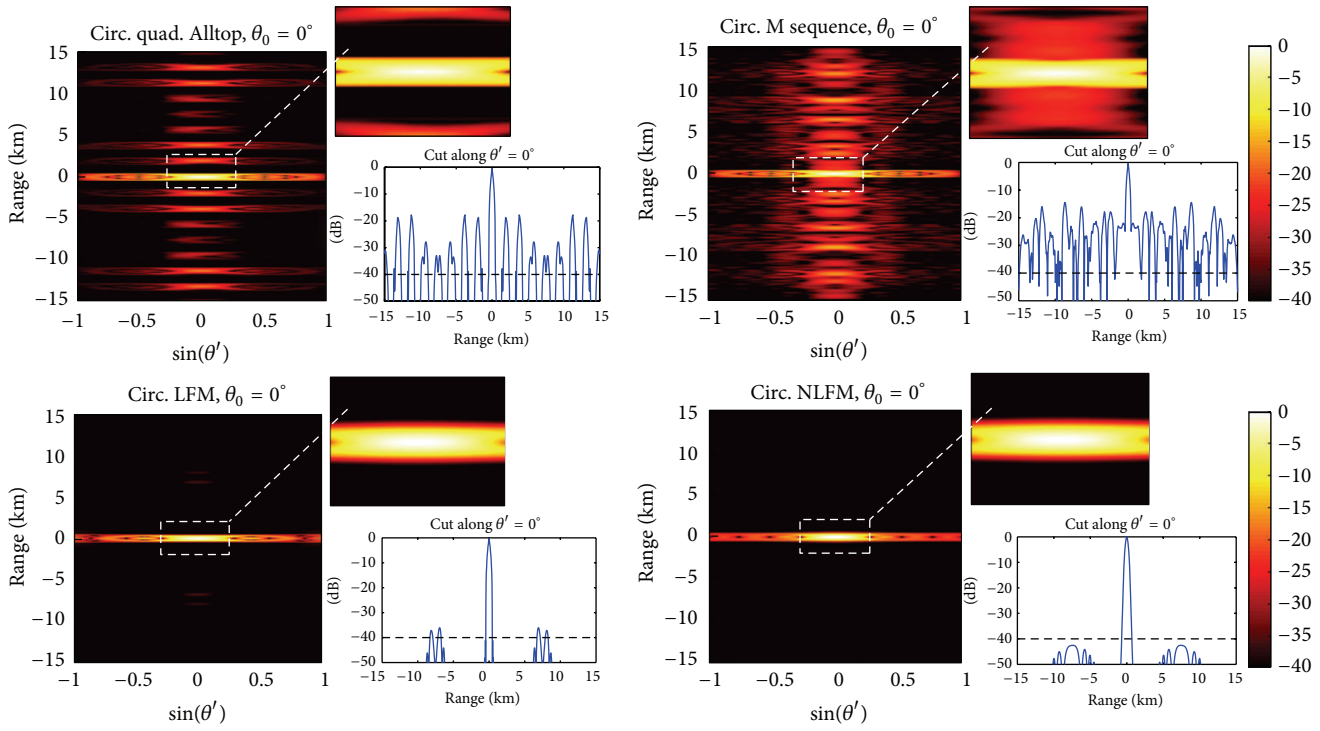

FIGURE 4: Range-angle cuts of the ambiguity function $|R^0_{\theta_0}(\tau', \theta')|^2$ at $\theta_0 = 0^\circ$ in dB.

cuts, namely, by eight antenna patterns, presented for the considered signals in two possible aiming angular directions, $\theta_0 = 0^\circ, 30^\circ$ in Figure 3. The angle-angle cuts demonstrate the uniform radiation for all the considered angular directions θ' for the circulating quadratic Alltop signal, M-sequence, and LFM-signal. There are no fluctuations along the diagonal, which means that the antenna array gain is constant with respect to the aiming angle. This is a clear demonstration of the fact that by circulating one waveform through the transmitting radar channels, the orthogonality of the radiated signals can be achieved.

As for the circulating NLFM signal, the beam-formed patterns have maximal amplitude, the main beam-width increases in the zero angular direction, and the gradual amplitude degrades for farther angles. The amplitude degradation is in order of 14 dB, which is certainly not negligible. The amplitude degradation is explained by the reduced equivalent bandwidth of the NLFM signal compared to the total occupied bandwidth and, therefore, by the inappropriate definition of the bandwidth dependent offset Δt. This problem can be solved by recalculation of the relative time shift Δt between the circulating signals $s^n(t)$ according to the reduced equivalent bandwidth of the NLFM signal. The reduced angular coverage for the circulating NLFM signal means also that the angular coverage of the antenna can be adapted by reducing the time shift between adjacent transmitters; this is also a valuable property of circulating codes, for use in different operational uses, requiring different angular coverages. In this work, for fair comparison, the relative time shifts are preserved equal.

We note that the results presented in Figure 3 indicate the inherent properties of the considered signals for beamforming because they have been obtained with the assumption of omnidirectional radiation patterns of the antenna array elements.

One of the important properties of transmitted circulating signals is the ability to detect weak (with small radar cross-sections) targets against strong targets or clutter. This property is normally illustrated by the range side lobes of the ambiguity function. Figures 4 and 5 demonstrate, as an example, this property for two aiming directions, while not changing the transmitted waveforms or array geometry.

Figure 4 presents four range-angle cuts of the ambiguity function. They are angle versus range taken at the aiming (beam-formed) angle $\theta_0 = 0^\circ$. The zoomed figures display the main lobe of the ambiguity functions for four analysed signals. In turn, the vertical slices demonstrate the obtained main lobe and range side lobes for one chosen observed angular direction $\theta' = 0^\circ$. In this way these vertical slices received for the space-time radar waveforms can be considered as an analogue of the traditional autocorrelation function obtained, however, for each observed angular direction.

The range side lobes are maximal for the observed direction which is equal to the aiming direction. The side-lobe level between the considered signals is maximal, about −15 dB, for the circulating M-sequence; and it is rather homogeneous

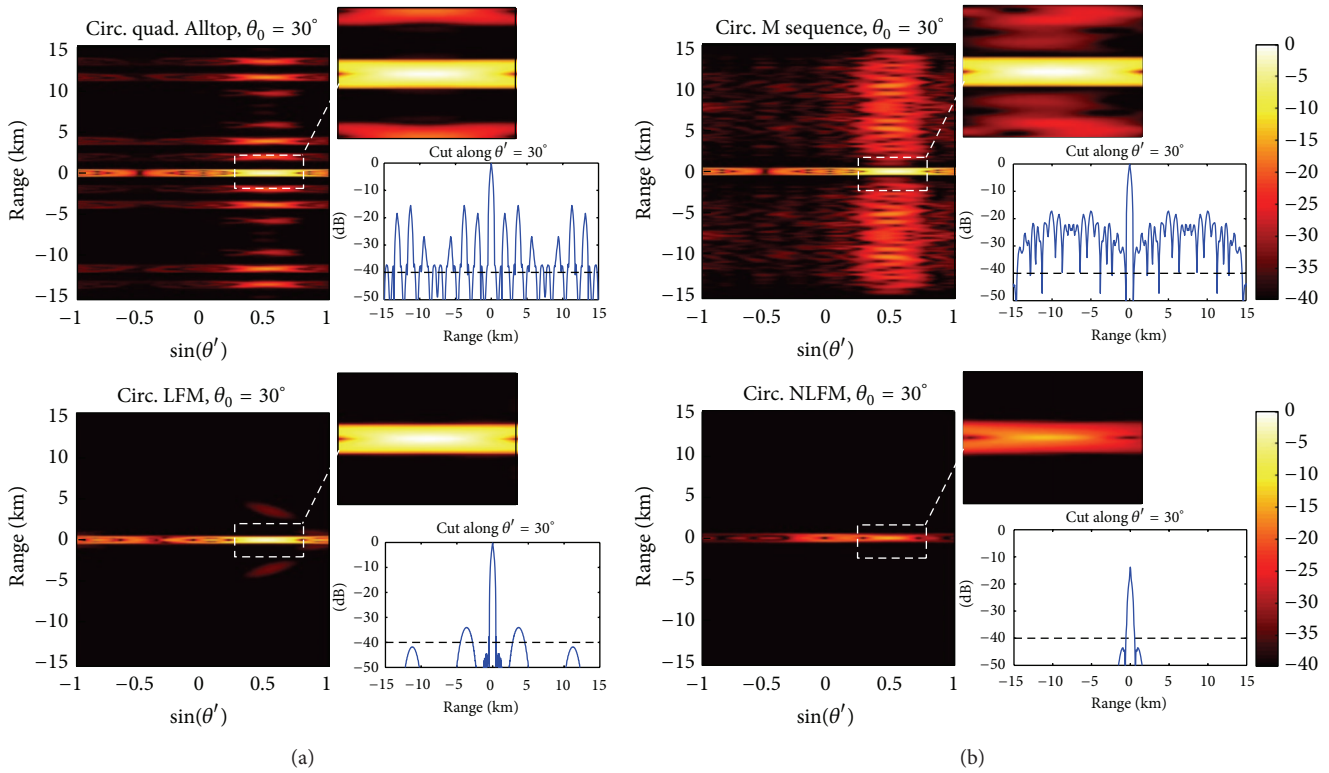

FIGURE 5: Range-angle cuts of the ambiguity function $|R^0_{\theta_0}(\tau', \theta')|^2$ at $\theta_0 = 30^\circ$ in dB.

in each chosen observation direction. Such side-lobe levels would certainly be detrimental in case of multiple targets situations. The minimal side-lobe level, about −42 dB, has been obtained for the circulating NLFM signal. Both, the circulating LFM and NLFM signals, are characterized by a very low side-lobe level for all the observed directions θ'. We remind that the BT product of all the signals has been chosen pretty small, 255. The main lobe is widened in range for the NLFM signal, which is visible in the corresponding zoomed figure in Figure 4. This is explained by the widened main beam of the antenna array for the circulating NLFM signal case in the aiming direction $\theta_0 = 0^\circ$; see the corresponding angle-angle cut of the ambiguity function in Figure 3.

Figure 5 shows another cut of the ambiguity function $|R^0_{\theta_0}(\tau', \theta')|^2$ obtained by means of the signal processing for the aiming angle $\theta_0 = 30^\circ$ in one of the receiving channels. Now the main lobe of the ambiguity function is shifted in the proper angular direction. The peak of the ambiguity function along the observed angular directions is located at the aiming angle. The zoomed figures display the main lobe of the ambiguity functions for four analysed signals, as in the previous figure. The vertical slices demonstrate the obtained main lobe and range side lobes for one observed angular direction $\theta' = 30^\circ$, which is equal to the aiming angle. The range side-lobes are maximal for the aiming directions for all the analysed waveforms. This time the range side-lobes are maximal for the circulating quadratic Alltop code, −15.6 dB, and lower for the M-sequence, −17 dB. The circulating LFM and NLFM signals are still providing very low side-lobe level in range for all the observed angles. In the aimed direction, the maximal values are −34 dB and −44 dB, respectively. It is quite impressive, taking into account the small BT-product of the waveforms. For the circulating NLFM signal, the normalized amplitude of the main lobe drops to −14 dB. This is caused by the amplitude degradation with the angle increase appropriate for the circulating NLFM signal (see the proper angle-angle function in Figure 3).

5. Conclusions

A concept of the circulating space-time code has been described. Basically the presented concept describes the whole class of space-time codes employing a selected type of a waveform having a large BT product. The circulating codes do not narrow the radiated pattern of the antenna array, thus providing a wide angular coverage, possibly tunable. In turn, the beam-forming on transmit is achievable by means of the signal processing in one (or each) receiver channel.

Four types of circulating codes have been analysed in the paper using their ambiguity functions. The circulating LFM and NLFM signals demonstrated a very clean range-angle ambiguity function, with some angular-dependent amplitude degradation of the latter.

This paper describes a novel and technically simple solution of transmitting only one waveform circulating with a very small offset from one antenna element to another

(or from one subarray to another). The signals can be uniformly radiated in free space, providing the beam-forming on transmit implemented in radar receiver.

References

[1] B. D. Van Veen and K. M. Buckley, "Beamforming: a versatile approach to spatial filtering," *IEEE ASSP Magazine*, vol. 5, no. 2, pp. 4–24, 1988.

[2] D. J. Rabideau and P. A. Parker, *Ubiquitous MIMO Multifunction Digital Array Radar and the Role of Time-Energy, Management in Radar*, Massachusetts Institute of Technology, Lincoln Laboratory, 2004.

[3] D. Cochran, S. Suvorova, S. D. Howard, and B. Moran, "Waveform libraries and measures of effectiveness for radar scheduling," *IEEE Signal Processing Magazine*, vol. 26, no. 1, pp. 12–21, 2009.

[4] F. Le Chevalier, "Space-time transmission and coding for airborne radars," *Radar Science and Technology*, vol. 6, no. 6, pp. 411–421, 2008.

[5] P. Calvary and D. Janer, "Spatio-temporal coding for radar array processing," in *Proceedings of the IEEE International Conference on Acoustics, Speech and Signal Processing (ICASSP '98)*, vol. 4, pp. 2509–2512, Seattle, Wash, USA, May 1998.

[6] P. Woodward, "Radar ambiguity analysis," RRE Technical Note 731, 1967.

[7] H. L. Van Trees, *Detection, Estimation, and Modulation Theory*, Part III, John Wiley & Sons, 1971.

[8] G. S. Antonio, D. R. Fuhrmann, and F. C. Robey, "MIMO radar ambiguity functions," in *Proceeding of the 40th Asilomar Conference on Signals, Systems, and Computers (ACSSC '06)*, pp. 36–40, IEEE, Pacific Grove, Calif, USA, November 2006.

[9] J. Li and P. Stoica, *MIMO Radar Signal Processing*, Wiley-IEEE Press, 2008.

[10] M. I. Skolnik, *Introduction To Radar Systems*, McGraw-Hill, New York, NY, USA, 3rd edition, 2001.

[11] M. Longbrake, "True time-delay beamsteering for radar," in *Proceedings of the IEEE National Aerospace and Electronics Conference (NAECON '12)*, pp. 246–249, 2012.

[12] W. O. Alltop, "Complex sequences with low periodic correlations," *IEEE Transactions on Information Theory*, vol. 26, no. 3, pp. 350–354, 1980.

[13] S. Boukeffa, Y. Jiang, and T. Jiang, "Sidelobe reduction with nonlinear frequency modulated waveforms," in *Proceedings of the IEEE 7th International Colloquium on Signal Processing and Its Applications (CSPA '11)*, pp. 399–403, Penang, Malaysia, March 2011.

Hindawi Publishing Corporation
Journal of Electrical and Computer Engineering
Volume 2013, Article ID 627410, 5 pages
http://dx.doi.org/10.1155/2013/627410

Research Article

Radar Array Diagnosis from Undersampled Data Using a Compressed Sensing/Sparse Recovery Technique

S. Costanzo,[1] A. Borgia,[1] G. Di Massa,[1] D. Pinchera,[2] and M. D. Migliore[2]

[1] *DIMES, Università della Calabria, 87036 Rende, Italy*
[2] *DIEI, Università di Cassino e del Lazio Meridionale, Via Di Biasio 43, 03043 Cassino, Italy*

Correspondence should be addressed to S. Costanzo; costanzo@deis.unical.it

Received 24 May 2013; Accepted 20 August 2013

Academic Editor: Alvaro Rocha

Copyright © 2013 S. Costanzo et al. This is an open access article distributed under the Creative Commons Attribution License, which permits unrestricted use, distribution, and reproduction in any medium, provided the original work is properly cited.

A Compressed Sensing/Sparse Recovery approach is adopted in this paper for the accurate diagnosis of fault array elements from undersampled data. Experimental validations on a slotted waveguide test array are discussed to demonstrate the effectiveness of the proposed procedure in the failures retrieval from a small set of measurements with respect to the number of radiating elements. Due to the sparsity feature of the proposed formulation, the method is particularly appealing for the diagnostics of large arrays, typically adopted for radar applications.

1. Introduction

The identification of failures in array antennas is an important problem that have addressed large attention both in academies and industries. It is well known that the presence of fault elements in arrays causes a performance degradation in terms of both gain and sidelobe levels. This is particulary important in case of high performance arrays with very low sidelobes, largely adopted in radar applications.

The back-propagation algorithm [1] is the most widely adopted approach to detect fault array elements. It is based on the Fourier relationship between the fields on the array aperture and the measurement plane, with a number of samples satisfying the Nyquist theorem. However, using the standard half-wavelength sampling step, the number of measurement points and consequently the time required for data acquisition turns out to be very large.

Broadly speaking, it is possible to obtain a data reduction by introducing tighter a priori information on the source. For example, in the last couple of decades, an effective theory to reduce the set of data in antenna measurements under a priori knowledge of the antenna shape [2] has been successfully applied to near-field measurements [3, 4]. Using different a priori information, for example, on the spatial correlation of the sources, a further decrease in the number of measurements can be achieved [5]. Efficient algorithms have been also introduced in the literature to obtain accurate antenna far-field characterization from near-field measurements performed on strategic scanning surfaces with reduced acquisition points [6–8].

The approach proposed in [9], and based on the matrix inversion method, can be also adopted to obtain a reduction of data by introducing a proper model of the source. However, it generally requires a set of measurements not smaller than the number of array elements.

Recently, Compressed Sensing/Sparse Recovery (CS/SR) techniques [10, 11] have been proposed in antenna diagnosis, first from near-field data [12] and more recently from far-field measurements [13]. The application of CS/SR techniques potentially allows a number of data that increases linearly with the number of failures but only logarithmically with the number of radiating elements, thus allowing a large reduction in the amount of measured data as well as in the acquisition time.

In this paper, an experimental validation of the CS approach proposed in [12] for a proper detection of fault array elements is provided for the first time. For illustrative purpose, a small linear array well known in the literature, namely, a slotted waveguide array, is assumed as a test structure. Near-field measurements on a reduced number of points

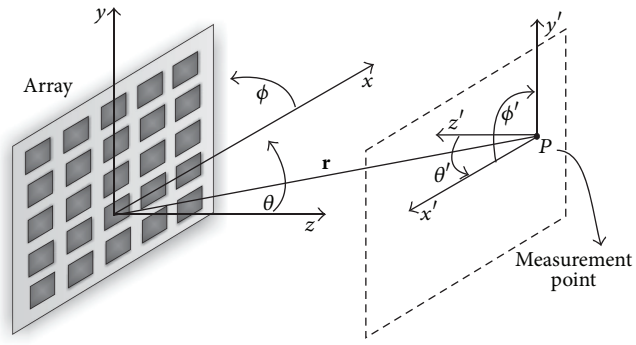

Figure 1: Problem geometry.

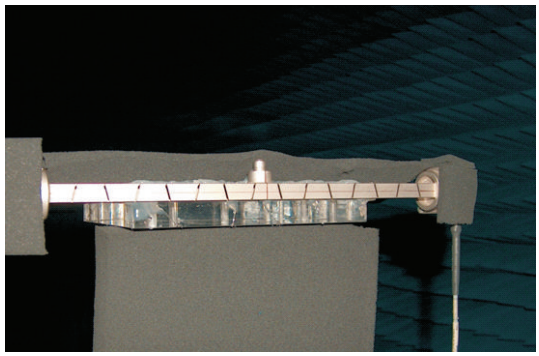

Figure 2: Photograph of slotted waveguide array (AUT) into anechoic chamber at the University of Calabria.

with respect to the number of array elements are successfully adopted to accurately identify the failures positions, thus demonstrating the effectiveness of the proposed CS approach on undersampled data.

2. Outline of the Method

Let us consider (Figure 1) an array under test (AUT) consisting of N radiating elements located at known positions $\mathbf{r}_n$. Let x_n and $\mathbf{f}_n(\theta, \phi)$ be the excitation coefficient and the electric-field radiation pattern of the nth radiating element, respectively. A probe having effective height $\mathbf{h}(\theta, \phi)$ is placed into M spatial points $\mathbf{r}_m$, $m = 1, \ldots, M$. The voltage at the probe output can be expressed by a linear system of the kind:

$$\mathbf{Ax} = \mathbf{y}, \tag{1}$$

wherein $\mathbf{y} = (\mathbf{y}_1, \mathbf{y}_2, \ldots, \mathbf{y}_n)^{\mathbf{T}} \in \mathbf{C}^{\mathbf{M}}$, y_m is the probe voltage measured at point $\mathbf{r}_m$, $\mathbf{x} = (\mathbf{x}_1, \ldots, \mathbf{x}_N)^{\mathbf{T}} \in \mathbf{C}^{\mathbf{N}}$, $\mathbf{A} \in \mathbf{C}^{\mathbf{M\times N}}$ is a matrix whose (m, n) element is equal to $\exp(-j\beta r_{m,n})/(4\pi r_{m,n})\mathbf{f}(\theta_{m,n}, \phi_{m,n}) \cdot \mathbf{h}(\theta'_{m,n}, \phi'_{m,n})$, $r_{m,n} = |\mathbf{r}_m - \mathbf{r}_n|$, and $\theta_{m,n}$ and $\phi_{m,n}$ are the relative angles between the mth measurement point and the nth element position in a reference system centered on the nth array radiating element.

In the present work, the problem of identification of fault elements into array antennas is considered. If assuming a number S of failures, this goal can be achieved by inverting

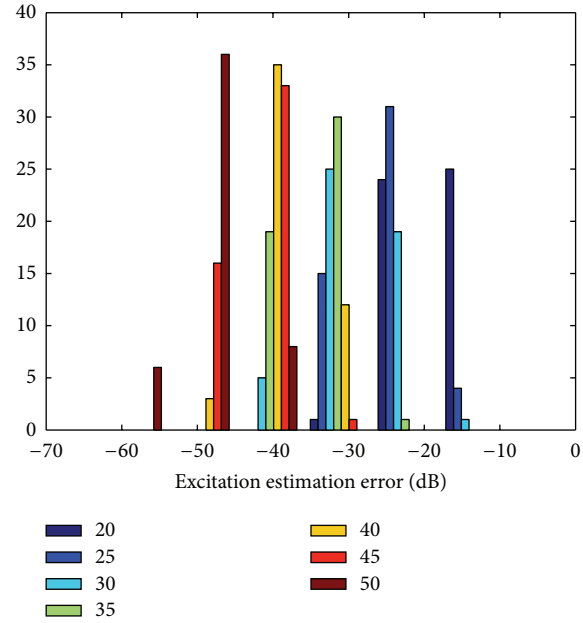

Figure 3: Histogram (simulations) of MSE of the ℓ_1 solution: $S = 2$, $M = 11$, and SNR ranging from 20 dB up to 50 dB.

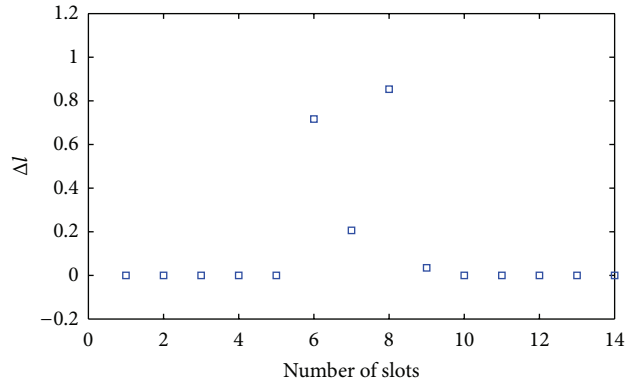

Figure 4: The difference between exact and estimated excitations (simulations) with failures at positions $n = 6$ and $n = 8$: $S = 2$, $M = 11$, and MSE = 20 dB.

the system (1), as proposed in [9], but requiring that $M \geq N$. Let us suppose $S \ll N$, as usually happens.

As first step, we suppose to know (by measurements or available model/simulation) the field radiated by the failure-free array into M measurement points, thus obtaining a reference data vector $\mathbf{y}^r$. The relative excitations of the reference (failure-free) array are denoted by vector $\mathbf{x}^r$. In a successive step, we collect the field radiated by the array with fault elements, thus obtaining a second vector $\mathbf{y}^d$ with associated excitations $\mathbf{x}^d$. Now, let us consider the linear system (1), with

$$\begin{aligned} \mathbf{x} &= \mathbf{x}^r - \mathbf{x}^d, \\ \mathbf{y} &= \mathbf{y}^r - \mathbf{y}^d; \end{aligned} \tag{2}$$

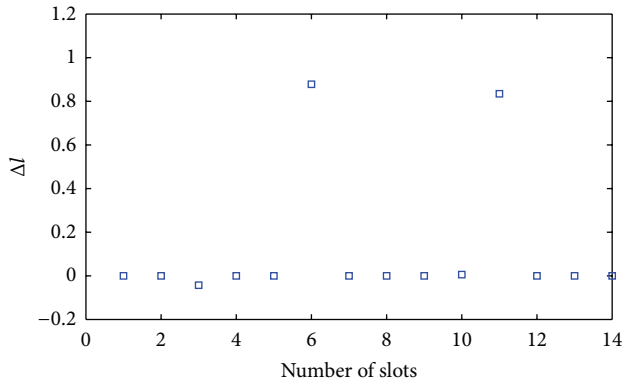

FIGURE 5: The difference between exact and estimated excitations (simulations) with failures at positions $n = 6$ and $n = 11$: $S = 2$, $M = 11$, and MSE = 25 dB.

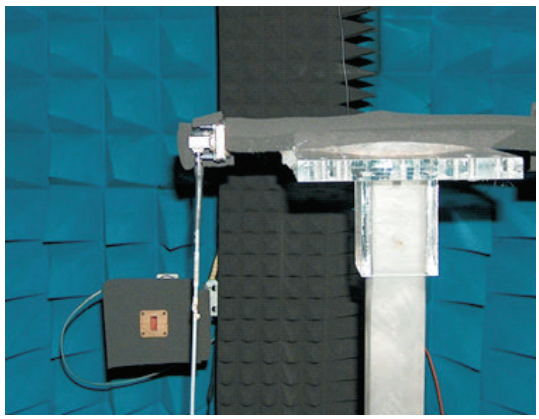

FIGURE 6: Photograph of measuring probe into anechoic chamber at the University of Calabria.

x and **y** are named as "innovation" vectors. Since $S \ll N$, we have an equivalent problem involving a highly sparse array.

Accordingly, the problem is *sparse*; that is, the unknown vector has only a small number of not null entries, and it can be solved by the following constraint minimization:

$$\begin{aligned} &\min_{\mathbf{x}} \quad \|\mathbf{x}\|_1 \\ &\text{subject to} \quad \|\mathbf{A}\mathbf{x} - \mathbf{y}\|_2 \leq \epsilon, \end{aligned} \tag{3}$$

wherein ϵ is related to the noise affecting the data.

3. Numerical Results

As a preliminary step, extensive numerical simulations are performed to check the performance of the failure detection algorithm, by assuming a slotted-waveguide array well characterized in the literature to be AUT [14], with $N = 14$ radiating elements (Figure 2). The slotted array is terminated into a matched load, thus working as a nonresonant array and producing a main lobe tilted with respect to the broadside direction [15].

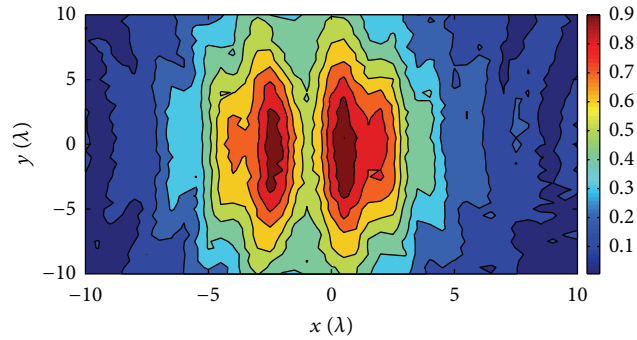

FIGURE 7: Measured near-field amplitude on the failure-free slotted waveguide array.

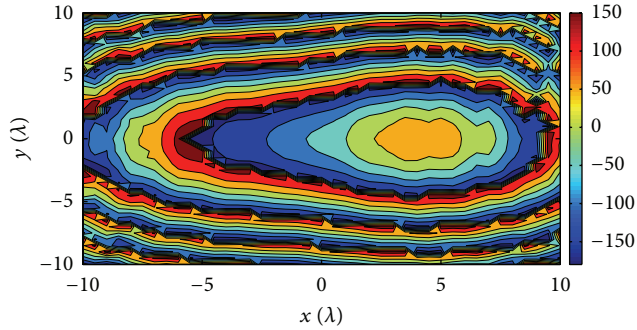

FIGURE 8: Measured near-field phase on the failure-free slotted waveguide array.

To check the robustness of the CS technique, various simulations are initially performed by considering different numbers of failures and data affected by Gaussian noise. As an example, the histogram of the Mean Square Error (MSE) in the reconstruction of the array excitations is reported in Figure 3, by considering 50 trials in the presence of $S = 2$ failures randomly chosen among the $N = 14$ elements and assuming $M = 11$ measurements affected by a Signal-to-Noise Ratio (SNR) ranging from 20 dB up to 50 dB.

In order to have a qualitative information on the value of MSE required to accurately identify the failures, an example of faults reconstruction is reported in Figures 4 and 5 by assuming a MSE equal to 20 dB and 25 dB, respectively. The plots indicate that a value of MSE equal to 20 dB is not sufficient for an accurate failures identification, while a value of 25 dB gives good results. Accordingly, results depicted in Figure 3 indicate that $M = 11$ measurements assure an accurate detection of failures with high probability in the case of SNR greater than 30 db. Such a noise level is easily reached in near-field measurements.

4. Setup Description and Experimental Results

In order to validate the CS approach for fault-arrays diagnosis, a planar near-field setup is assumed by adopting a slotted-waveguide array (Figure 2) as AUT and a standard X-band rectangular waveguide (Figure 6) as measuring probe.

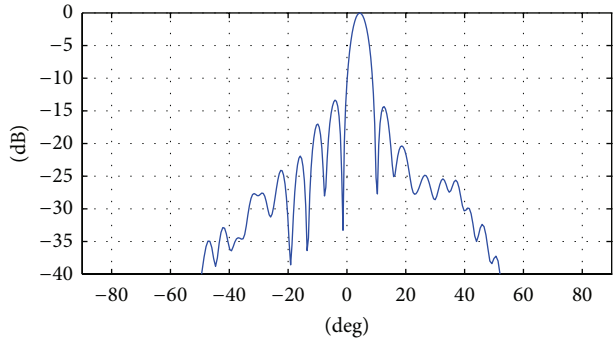

FIGURE 9: Far-field pattern of failure-free slotted waveguide array (result from planar near-field to far-field transformation).

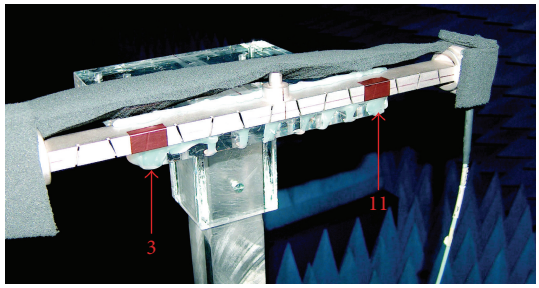

FIGURE 10: Photograph of slotted waveguide array with failures at positions $n = 3$ and $n = 11$.

The proper operation of the test array is first verified by performing near-field measurements on a planar grid of 41×41 $\lambda/2$ spaced points and then applying the standard planar near-field to far-field transformation. An operating frequency $f = 10$ GHz is chosen. The contour plots of near-field amplitude and phase on the measurement plane placed 40 cm away from the AUT are reported in Figures 7 and 8, respectively. The corresponding far-field pattern along the array plane, illustrated in Figure 9, shows a main lobe properly pointing at an angle approximately equals 5°, as imposed by the array theory [15].

To apply the proposed CS technique, a second set of near-field data is collected on the slotted array by assuming the presence of two failures (namely, with the 3rd and 11th slots covered by a conductive material), as illustrated in Figure 10. The measured near-field amplitudes on the failure-free and two-fault arrays are reported in Figure 11 along the central line of the acquisition domain.

To perform the experimental validation, only a subset of near-field data illustrated in Figure 11 is adopted. In particular, $M = 11$ points are assumed, which are equivalent to a field undersampling at a 2λ spacing. As outlined in the previous section, the ℓ_1 minimization is applied to the difference of the fields plotted in Figure 11, and the corresponding result of Figure 12, giving the difference between the excitation coefficients of the failure-free and the two-faults array, clearly identifies the failures at positions $n = 3$ and $n = 11$. It is worth stressing that we use only $M = 11$ measurements to estimate $N = 14$ excitations. As a comparison, the result obtained

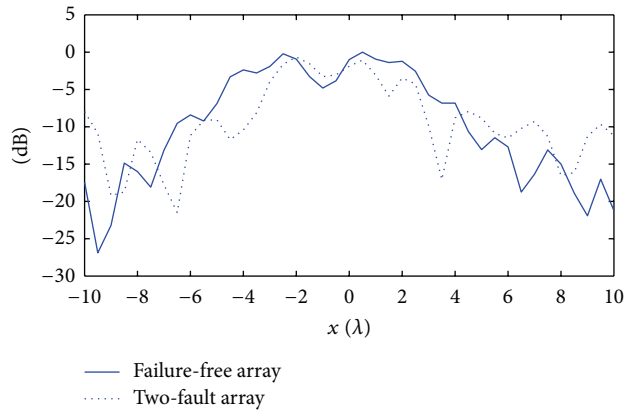

FIGURE 11: Measured near-field amplitude [dB] in the absence and presence of failures (slots 3 and 11 closed).

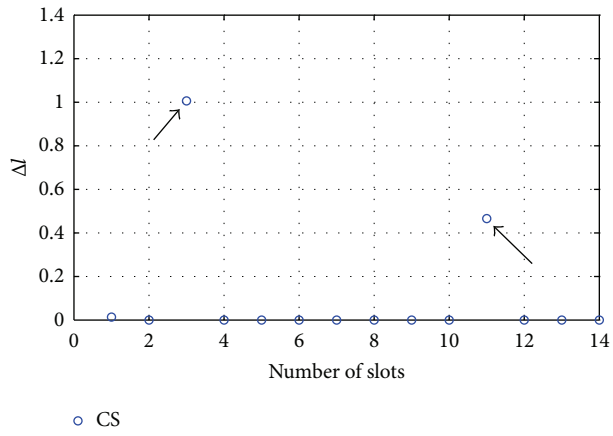

FIGURE 12: ℓ_1 minization: the difference of excitations in the absence and the presence of failures (slots 3 and 11 closed).

using the linear inversion method by pseudoinverse [16] is plotted in Figure 13, showing a poor identification of the fault elements in this case.

5. Conclusion

The problem of arrays diagnostics has been faced in this work by adopting a Compressed Sensing/Sparse Recovery approach able to give an equivalent sparse formulation of the problem relative to the identification of fault elements.

Due to the sparsity feature, the method is able to detect arrays failures from a set of largely undersampled data compared to the one obtained using standard Nyquist sapling step.

The validity of the approach has been tested on a standard slotted waveguide array, by artificially creating critical configurations, and results have demonstrated an accurate identification of the failure positions using a number of measured data smaller than the number of the radiating elements of the array.

In the experimental example, the reduction of the measurements compared to the standard $\lambda/2$ sampling step

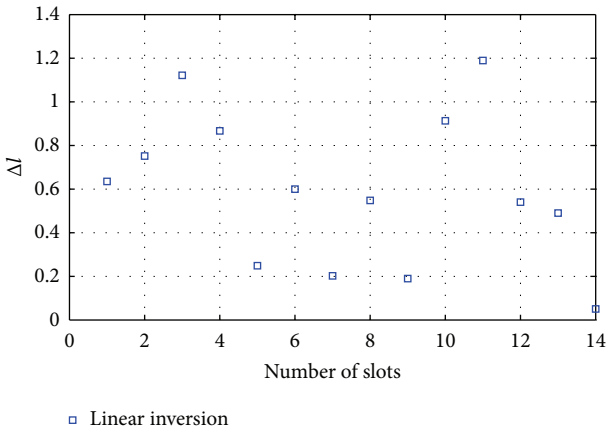

FIGURE 13: ℓ_2 minization: the difference of excitations in the absence and the presence of failures (slots 3 and 11 closed).

adopted in near-field measurements is relatively modest, that is, 4 times. However, it is worth recalling that, broadly speaking, the number of measurements required by the proposed technique mainly depends on the number of failures, while other techniques not based on Sparse Recovery require a number of measurements that depend on the electrical dimensions of the antenna under test. Consequently, the small dimensions of the array here adopted for the experimental validations do not make so clear the advantages of the technique when testing high-performance radar antennas with thousands of elements distributed on 2D surfaces, for which a much more significant reduction in the number of measurements is expected [12].

References

[1] J. J. Lee, E. M. Ferren, D. P. Woollen, and K. M. Lee, "Near-field probe used as a diagnostic tool to locate defective elements in an array antenna," *IEEE Transactions on Antennas and Propagation*, vol. 36, no. 6, pp. 884–889, 1988.

[2] O. M. Bucci, C. Gennarelli, and C. Savarese, "Representation of electromagnetic fields over arbitrary surfaces by a finite and non redundant number of samples," *IEEE Transactions on Antennas and Propagation*, vol. 46, pp. 361–369, 1998.

[3] O. M. Bucci and M. D. Migliore, "A new method for avoiding the truncation error in near-field antennas measurements," *IEEE Transactions on Antennas and Propagation*, vol. 54, no. 10, pp. 2940–2952, 2006.

[4] S. Costanzo, G. Di Massa, and M. D. Migliore, "A novel hybrid approach for far-field characterization from near-field amplitude-only measurements on arbitrary scanning surfaces," *IEEE Transactions on Antennas and Propagation*, vol. 53, no. 6, pp. 1866–1874, 2005.

[5] M. D. Migliore, "An informational theoretic approach to the microwave tomography," in *Proceedings of the IEEE International Symposium on Antennas and Propagation and USNC/URSI National Radio Science Meeting (APSURSI '08)*, San Diego, Calif, USA, July 2008.

[6] S. Costanzo and G. Di Massa, "Far-field reconstruction from phaseless near-field data on a cylindrical helix," *Journal of Electromagnetic Waves and Applications*, vol. 18, no. 8, pp. 1057–1071, 2004.

[7] S. Costanzo and G. Di Massa, "Direct far-field computation from bi-polar near-field samples," *Journal of Electromagnetic Waves and Applications*, vol. 20, no. 9, pp. 1137–1148, 2006.

[8] S. Costanzo and G. Di Massa, "Near-field to far-field transformation with planar spiral scanning," *Progress in Electromagnetics Research*, vol. 73, pp. 49–59, 2007.

[9] O. M. Bucci, M. D. Migliore, G. Panariello, and P. Sgambato, "Accurate diagnosis of conformal arrays from near-field data using the matrix method," *IEEE Transactions on Antennas and Propagation*, vol. 53, no. 3, pp. 1114–1120, 2005.

[10] E. J. Candes and T. Tao, "Near-optimal signal recovery from random projections: universal encoding strategies?" *IEEE Transactions on Information Theory*, vol. 52, no. 12, pp. 5406–5425, 2006.

[11] D. L. Donoho, "Compressed sensing," *IEEE Transactions on Information Theory*, vol. 52, no. 4, pp. 1289–1306, 2006.

[12] M. D. Migliore, "A compressed sensing approach for array diagnosis from a small set of near-field measurements," *IEEE Transactions on Antennas and Propagation*, vol. 59, no. 6, pp. 2127–2133, 2011.

[13] G. Oliveri, P. Rocca, and A. Massa, "Reliable diagnosis of large linear arrays: a bayesian compressive sensing approach," *IEEE Transactions on Antennas and Propagation*, vol. 60, no. 10, pp. 4627–4636, 2012.

[14] S. Silver, *Microwave Antenna Theory and Design*, McGraw-Hill, New York, NY, USA, 1949.

[15] R. E. Collin, *Antennas and Radiowave Propagation*, McGraw-Hill, New York, NY, USA, 1987.

[16] G. Golub and C. F. Van Loan, *Matrix Computation*, John Hopkins University Press, Baltimore, Md, USA.

Hindawi Publishing Corporation
Journal of Electrical and Computer Engineering
Volume 2013, Article ID 636972, 11 pages
http://dx.doi.org/10.1155/2013/636972

Research Article

Performance of 2D Compressive Sensing on Wide-Beam Through-the-Wall Imaging

Edison Cristofani, Mathias Becquaert, and Marijke Vandewal

CISS Department, Royal Military Academy, 30 Avenue de la Renaissance, 1000 Brussels, Belgium

Correspondence should be addressed to Edison Cristofani; edison.cristofani@elec.rma.ac.be

Received 27 May 2013; Revised 18 July 2013; Accepted 24 July 2013

Academic Editor: Sandra Costanzo

Copyright © 2013 Edison Cristofani et al. This is an open access article distributed under the Creative Commons Attribution License, which permits unrestricted use, distribution, and reproduction in any medium, provided the original work is properly cited.

Compressive sensing has become an accepted and powerful alternative to conventional data sampling schemes. Hardware simplicity, data, and measurement time reduction and simplified imagery are some of its most attractive strengths. This work aims at exploring the possibilities of using sparse vector recovery theory for actual engineering and defense- and security-oriented applications. Conventional through-the-wall imaging using a synthetic aperture configuration can also take advantage of compressive sensing by reducing data acquisition rates and omitting certain azimuth scanning positions. An ultra-wideband stepped frequency system carrying wide beam antennas performs through-the-wall imaging of a real scene, including a hollow concrete block wall and a corner reflector behind it. Random downsampling rates lower than those announced by Nyquist's theorem both in the fast-time and azimuth domains are studied, as well as downsampling limitations for accurate imaging. Separate dictionaries are considered and modeled depending on the objects to be reconstructed: walls or point targets. Results show that an easy interpretation of through-the-wall scenes using the l_1-norm and orthogonal matching pursuit algorithms is possible thanks to the simplification of the reconstructed scene, for which only as low as 25% of the conventional SAR data are needed.

1. Introduction

Previous research studies have explored numerous applications of through-the-wall imaging (TWI) in domains which can exploit the convenient penetration capabilities of the 1–5 GHz frequency band in most nonmetal building construction materials [1, 2]. Indeed, being able to perform nondestructive inspection of objects behind a solid wall is a noteworthy application. The literature on TWI widely copes with object or human detection—either moving [3–5] or static [6, 7]. Among others, military, law enforcement, and security operations have already taken profit of the satisfactory performance of TWI. Although most of the studies suggest using an active TWI approach wherever needed, some authors opt for adequately processing opportunistic signals in the surroundings of the scene such as widespread GSM [8] or wireless networks [9]. Despite presenting interesting wall penetration properties, the noncooperative—thus passive—nature of these approaches cannot assure complete reliability and availability, and consequently, an active approach is preferred.

Synthetic Aperture Radar (SAR) allows competitive TWI using rather common antennas with wide beams and simple out-of-focus data acquisition. Thanks to coherent signal integration along a known measurement path, these data are focused on postprocessing, yielding an improved lateral resolution which remains constant at all ranges [10]. Given a measurement path, sufficient data both in the azimuth and fast-time directions must be obtained in order to perform SAR focusing and to satisfy the Nyquist-Shannon anti-aliasing criterion. This, generally, implies using complex hardware which generates amounts of data which can become unbearable when fine resolution imagery is needed.

Compressive Sensing (CS) introduces the possibility of reducing the amount of sensed signals for further digital reconstruction and, likewise, to perform accurate TWI. First used to solve sparse vector recovery problems within mathematical applications, CS has been recently used in a growing list of fields for sparse signal reconstruction, including TWI applications [11–14]. CS is able to reconstruct signals with high probability provided random sampling and sufficient

sparsity levels are satisfied [15]. Since CS announces a convex function optimization problem, solutions can be found by using the l_1-norm minimization or, in a less demanding approach, the Orthogonal Matching Pursuit (OMP) greedy algorithm, among an endless list of possibilities.

Actual TWI experiments were conducted for this study. Hollow concrete stretcher blocks were used to build up a solid wall, replicating load-bearing foundation walls used in most permanent constructions. A corner reflector, serving as an object of interest, was placed behind the wall. Scene reconstruction using an ultra-wideband moving sensor was achieved, both in conventional SAR and CS approaches. This study will explore the possibilities of random sampling, with a focus on minimizing the amount of data required to produce accurate enough reconstructions of simple TWI scenes. This action will lead to a significant simplification in hardware, as well as reducing processing complexity and data handling. The remaining of this document is divided into four further sections: Section 2 describes the used experimental setup, as well as signal processing concepts that will be used throughout the work. Section 3 formulates the CS problem to sparse data recovery, and strategies for creating dictionaries are described. Section 4 presents conventional and CS results obtained from actual TWI measurements. Finally, Section 5 details conclusions drawn and future work.

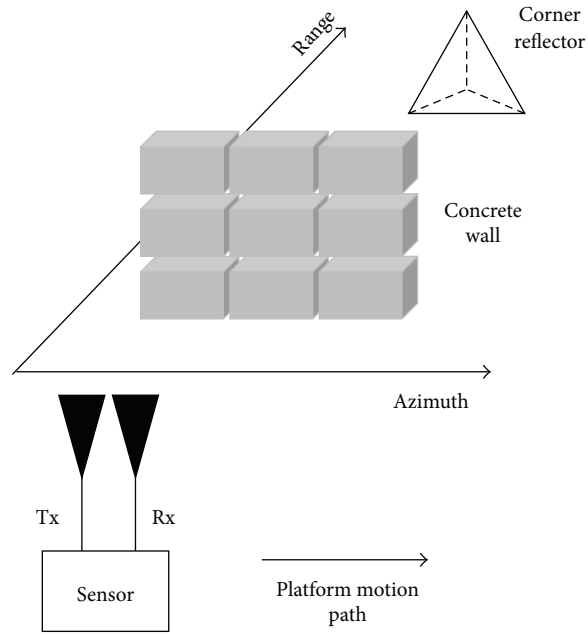

Figure 1: Schematic representation of the proposed experimental setup.

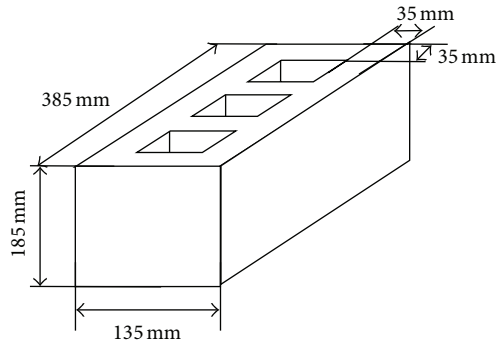

Figure 2: Dimensions of a hollow concrete stretcher block are 385 mm × 185 mm × 135 mm (length, height, and width, resp.). The outer structure is 35 mm thick.

2. Conventional TWI Measurements

2.1. TWI and the Measurement Site. The sensor used for the presented TWI comprises two Schwarzbeck BBHA 9120 D horn antennas [16] (for transmitting and receiving, providing gain stability in the 1–5 GHz band) on a stepped frequency (SF) SAR moving scanner, which translates for 1500 mm following an equispaced azimuth sampling scheme. The sensor used is an Anritsu 37169A Vector Network Analyzer (VNA). A concrete wall was built up for this study in order to obtain results comparable to those of a real TWI situation (see Figure 1). The wall was located at 950 mm from the antennas, in the far-field region for the entire sensor's frequency band, and a corner reflector was placed at 1240 mm behind the wall.

Hollow concrete stretcher blocks were used (see Figure 2 for shape and dimensions), commonly found in masonry and especially in load-bearing foundation walls.

Range estimation is greatly affected by the change of relative permittivity occurring in the air-material interfaces. Consequently, imaged targets and walls will appear further away and wider than in reality. Given a material with relative permittivity $\epsilon_r > 1$, any transmitted electromagnetic wave through it will propagate at a speed $v = c/\sqrt{\epsilon_r}$, being c the speed of light in vacuum. For an air-concrete-air interface of 35 mm, and considering $\epsilon_r \sim 4$ approximately [17], the second interface would be located at $d = +70$ mm, or $\Delta d = +35$ mm further away. As depicted in Figure 3, any object behind a concrete wall will suffer from this phenomenon, whereas its actual location is closer than shown by TWI. Waves traveling through hollow concrete blocks, as those used in the proposed experiments, will encounter two 35-mm air-concrete-air transitions, and therefore the expected range of the corner reflector would be shifted to ca. $2\Delta d = +70$ mm.

2.2. The SF Sensor and Signal Model. The SAR scanner operated in this study is based on an SF ultra-wideband sensor in the 1–5 GHz band. Using such SF sensor guarantees low hardware requirements, since the instantaneous bandwidth is kept narrow, while achieving a remarkable range resolution and power output. Instead of transmitting a linear frequency modulated chirp using a continuous or pulsed approach, the SF sensor produces signals by sequentially generating N carrier frequencies covering an effective system bandwidth B. These frequencies pulses are described by

$$f_n = f_0 + n\Delta f \quad \text{being } n = 1, \ldots, N-1, \tag{1}$$

where f_n is the nth frequency generated, f_0 is the starting frequency (i.e., 1 GHz for this setup), and $\Delta f = B/(N-1)$

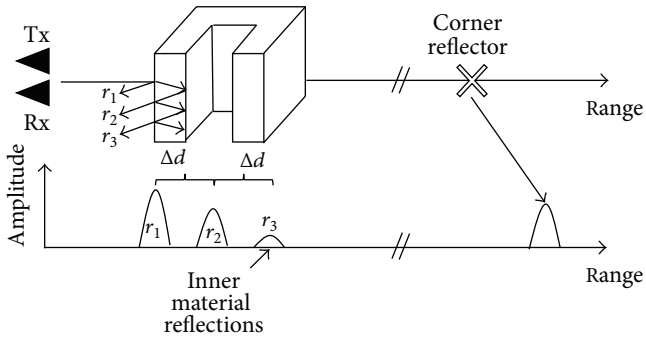

Figure 3: The ranging information is altered due to the different transmission media in the wall. Objects will appear further away.

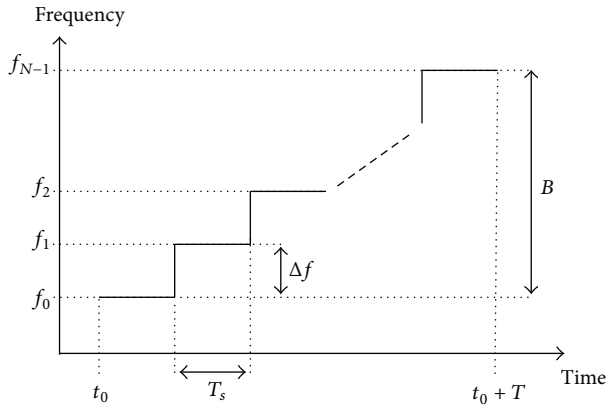

Figure 4: Waveform generation scheme of an SF sensor.

is the frequency step. Figure 4 depicts how the transmitted signals are generated.

For any SF systems, the maximum unambiguous range and range resolution parameters are respectively obtained as follows:

$$R_{\max} = \frac{c}{2\Delta f}, \qquad \Delta r = \frac{c}{2(N-1)\Delta f} = \frac{c}{2B}. \tag{2}$$

In Table 1, the most important parameters of the available experimental setup are shown. During the waveform generation phase, each frequency pulse f_n is transmitted for a given time T_s. Averaging is performed in detection in order to reduce noise and spurious contributions to the signal of interest.

The signal model of the transmitted waveform s_t for a given f_n can be described as

$$s_t(f_n, t) \propto \exp(j2\pi f_n t), \tag{3}$$

where t corresponds to the fast-time dimension. The sensor will actually transmit a series of N individual frequencies

Table 1: Descriptive parameters of the TWI experiment.

VNA model	Anritsu 37169A
Start frequency	1 GHz
End frequency	5 GHz
N	101
Averaging	10
Antenna opening angle	14°
$R_{\max}$	3750 mm
Δf	40 MHz
B	4 GHz
Tx power	+10 dBm
Tx/RX antennas	Schwarzbeck BBHA 9120 D
Typ. ant. gain	11 dBi
Scene size	1500 mm × 2500 mm
Δr	37.5 mm

which will cover the whole bandwidth. The detected signal model can be described as follows:

$$s_d(t) \propto \sum_{k=0}^{K-1} \sum_{n=0}^{N-1} \exp\left(j2\pi f_n (t - \tau_k)\right), \tag{4}$$

where $\tau_k = 2r_k/c$ corresponds to the delay caused by the round-trip propagation time of a given kth scatterer in the scene located at a distance r_k from the sensor. Distance r_k is simply obtained as the sensor-to-scatterer Euclidean distance. The VNA performs a homogeneous demodulation of the detected signal, which is known as beat signal and is modeled as

$$s_b(t) = s(t) \cdot \exp(-j2\pi f_n t) \propto \sum_{k=0}^{K-1} \sum_{n=0}^{N-1} \exp(-j2\pi f_n \tau_k). \tag{5}$$

2.3. SAR Imaging. SAR measurements use relatively simple antennas with a small aperture length and, therefore, poor azimuth resolution. By translating the sensor as shown in Figure 5 appropriately and coherently combining received signals from the different azimuth positions, the equivalent physical length of the aperture can be increased. An antenna of a theoretically unlimited aperture length could be synthesized yielding very fine azimuth resolutions. Building such antenna would not be feasible in practice; therefore, SAR processing results in a useful tool.

Collected unfocused SAR data must be combined coherently using an SAR focusing algorithm. These algorithms perform range/azimuth compression in order to compact received energy, whether in the time or frequency domains, and are mostly based on the matched filter [18–20] assuming the prior knowledge of the transmitted signal model. Figure 6 shows a simplified representation of a range-compressed SAR measurement based on the experimental setup described in Section 2.1.

The distance between the sensor's positions along the azimuth measurement track and any point in the scene is computed using the Euclidean distance and will follow a hyperbolic function. The collected energy from any given

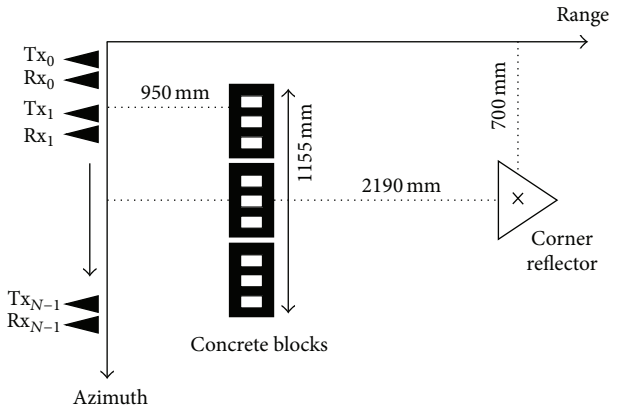

Figure 5: Experimental scene description. The SAR sensor moves in azimuth illuminating the scene with a wide-beam antenna.

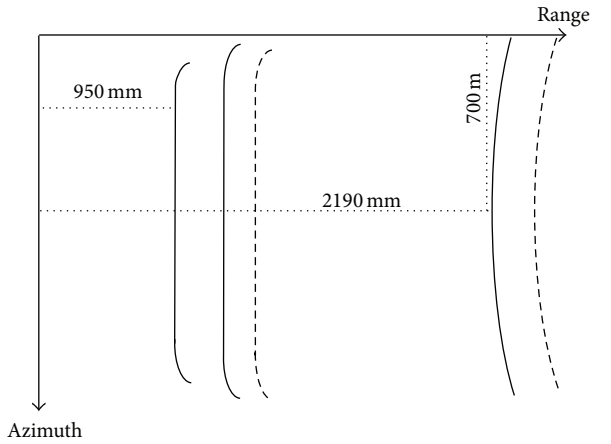

Figure 6: Expected results after an SAR measurement. Energy is spread in azimuth following a hyperbolic function. Certain elements will be shifted in range (dashed lines).

point target will present such hyperbolic shape and an amplitude variation in function of the antenna radiation diagram (both transmitting and receiving antennas).

Produced SAR images achieve interesting improved azimuth resolutions, which can be theoretically computed as

$$\delta_{az} \cong \frac{c}{2 f_c \sin(\theta_A)}, \tag{6}$$

where f_c is the carrier or center frequency of the sensor and θ_A is the opening angle of the antenna. According to the used sensor described in Table 1, expected resolutions range and azimuth are $\delta_r = 37.5$ mm and $\delta_{az} = 207$ mm, respectively.

3. Compressive Sensing

3.1. Conventional Sensing. In signal acquisition and processing, the Nyquist-Shannon theorem [21] specifies that any signal can be perfectly reconstructed only after being uniformly sampled at, at least, twice the maximum frequency or bandwidth describing it. Consider

$$f_s \geq 2 f_{\max} = 2B, \tag{7}$$

where f_s and $f_{\max}$ are the sampling and maximum frequencies, respectively. This condition can be a remarkable burden for certain systems, where challenging amounts of data are needed when large areas must be measured, high bandwidth is needed, or a combination of both. Handling, storing, or transmitting large amounts of data are onerous tasks, and SAR imaging systems are affected. Complexity of analog-to-digital converters would increase if fine-resolution SAR imagery was needed.

3.2. Problem Formulation. Data recovery of sparse vectors is extensively described in the literature [15, 22, 23]. Let $x \in \mathbb{C}^N$ be an arbitrary N-dimensional vector or complete measurement, and let $y \in \mathbb{C}^P$ be an incomplete observation of x, being $P \ll N$. Vectors x and y are related to the linear expression

$$y = \mathbf{A}x, \tag{8}$$

where $\mathbf{A} \in \mathbb{R}^{PxN}$ is a measurement matrix containing a plausible observation scheme. Illustratively, the nth element of x would be stored in the pth element of y if $a_{pn} \neq 0$. A perfect recovery of vector x can be obtained from y if two conditions are fulfilled: vector x must be sufficiently sparse and matrix $\mathbf{A}$ must satisfy the Restricted Isometry Property (RIP) [15, 22]. Vector x is said to be S-sparse if the l_0-norm of x satisfies $\|x\|_0 \leq S$ that is, the maximum number of nonzero elements describing x must be S. Nevertheless, having such a vector satisfying the S-sparsity condition or demonstrating the RIP for all the possible combinations can be cumbersome tasks, if not implausible. This latter requirement can be relaxed by defining matrix $\mathbf{A}$ following a random distribution which satisfies the RIP with high probability [24].

In radar imaging, vector x is defined as the full observation of the returns from an illuminated scene. Provided that the signal model is known (refer to Section 2.2), vector x can be expressed as

$$x = \mathbf{\Psi}\sigma, \tag{9}$$

where for all L positions in the scene, $\sigma \in \mathbb{C}^L$ describes the reflectivity coefficients, being $P \leq L \ll N$, whereas matrix $\mathbf{\Psi} \in \mathbb{C}^{NxL}$, an over complete dictionary, contains fully sampled received signals as described by the theoretical signal model. Therefore, $\mathbf{\Psi}$ is populated column wise as

$$\mathbf{\Psi} = \left[s_0, s_1, \ldots, s_{L-1}\right]. \tag{10}$$

Let then $\mathbf{\Phi} \in \mathbb{R}^{PxN}$ be a matrix containing either zeros or ones, in perfect analogy to matrix $\mathbf{A}$, describing a certain sampling scheme. Let a sensor obey such scheme; the sensed signal y for a given σ is now defined as

$$y = \mathbf{\Phi}x = \mathbf{\Phi}\mathbf{\Psi}\sigma = \mathbf{\Theta}\sigma. \tag{11}$$

Inputs:
(i) measured incomplete signal y and matrix $\boldsymbol{\Theta}$, populated with simulated wall or point-target model data
(ii) maximum number of iterations K
Output: reconstructed scene vector $\widehat{\sigma}$
(1) Initialize residual r_0 to the measured signal vector y and secondary matrix $\boldsymbol{\Theta}^{\dagger}$ to zero

$$r_0 = y, \qquad \boldsymbol{\Theta}^{\dagger} = 0$$

(2) Increase k. Find the column-vector of Θ that provides highest correlation with the residual

$$c_k = \arg\max \left|\langle r_{k-1}, \boldsymbol{\Theta}_n \rangle\right|$$

(3) Add column c_k of $\boldsymbol{\Theta}$ to $\boldsymbol{\Theta}^{\dagger}$ and zero c_k from $\boldsymbol{\Theta}$
(4) Solve

$$\widehat{\sigma} = \arg\min_{\sigma} \|\sigma\|_2 \quad \text{s.t. } y = \boldsymbol{\Theta}^{\dagger}\sigma$$

and update residual with $\boldsymbol{\Theta}$

$$r_k = y - \boldsymbol{\Theta}\widehat{\sigma}$$

(5) Go to step 2 until k reaches stop condition ($k = K$)

Algorithm 1: OMP algorithm description. Adapted from [26].

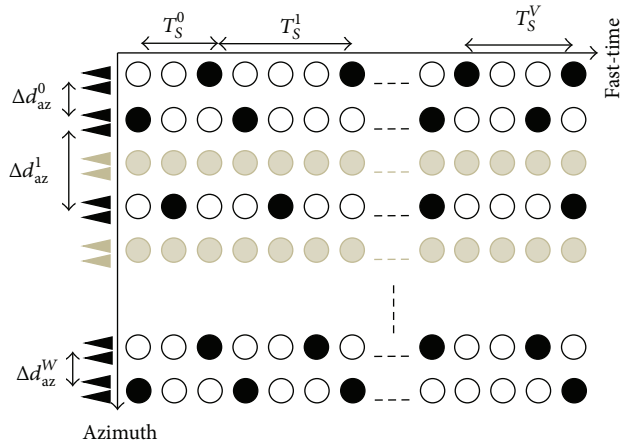

Figure 7: Sample selection scheme on full SAR data simulating a real CS sensor. Fast-time samples in white and azimuth measurements in grey are skipped.

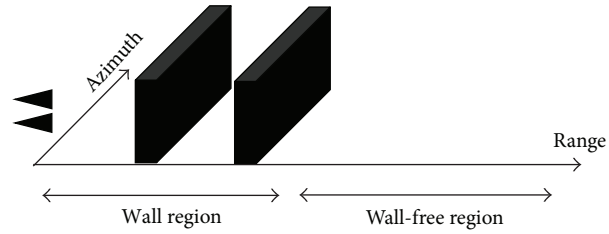

Figure 8: Two regions are described and will be treated differently. Walls may appear closer to the sensor. Further away only point targets are expected.

For the application proposed in this study, only the scene reflectivity coefficients in σ are needed and not the original measurement vector x. The recovery problem to be solved can then be formulated as

$$\widehat{\sigma} = \arg\min_{\sigma} \|\sigma\|_0 \quad \text{s.t. } y = \boldsymbol{\Theta}\sigma, \tag{12}$$

being $\|\sigma\|_0$ the l_0-norm of vector σ. However, the l_0-norm is an NP-hard problem and solutions may not exist. Since matrix $\boldsymbol{\Theta}$ sufficiently satisfies the RIP condition, the l_1-norm can be used as a viable alternative to noise-free convex optimization problems

$$\widehat{\sigma} = \arg\min_{\sigma} \|\sigma\|_1 \quad \text{s.t. } y = \boldsymbol{\Theta}\sigma. \tag{13}$$

Optimization of noisy measurements must be approximated since a perfect reconstruction will not be possible [22]. A tolerance threshold ε related to the data noise level or accepted reconstruction error must be imposed as follows:

$$\widehat{\sigma} = \arg\min_{\sigma} \|\sigma\|_1 \quad \text{s.t. } \left\|\boldsymbol{\Theta}\sigma - y\right\|_2 < \varepsilon. \tag{14}$$

Several categories different from convex optimization or basis pursuit can be found, each one offering multiple algorithms and variations. One of the most popular in terms of simplicity and efficiency is Orthogonal Matching Pursuit (OMP) [25] and its variations [26]. Being a greedy and simple algorithm (see Algorithm 1), OMP requires a prior knowledge or estimation of the sparsity in order to recover a sparse vector. Assessing the sparsity of a scene is not always possible especially in TWI. A relatively performing solution is implementing a stop condition to avoid the algorithm iterating more than what required by the scene. l_1-norm and OPM will be used in Section 4.

3.3. CS Random Sampling and Dictionary Structure. Random downsampling in the fast-time and azimuth dimensions implies a substantial reduction in data collection, in measurement time (less azimuth scans), and sensor complexity (fast-time sampling is less demanding). Random sampling schemes must be cautiously imitated when constructing the CS dictionary $\boldsymbol{\Theta}$ with the known signal model. Figure 7 describes how azimuth and fast-time random samplings are generated using the conventional SAR approach as a reference. Sampling intervals T_S^v and azimuth steps Δd_{az}^w follow adjustable random statistical distributions.

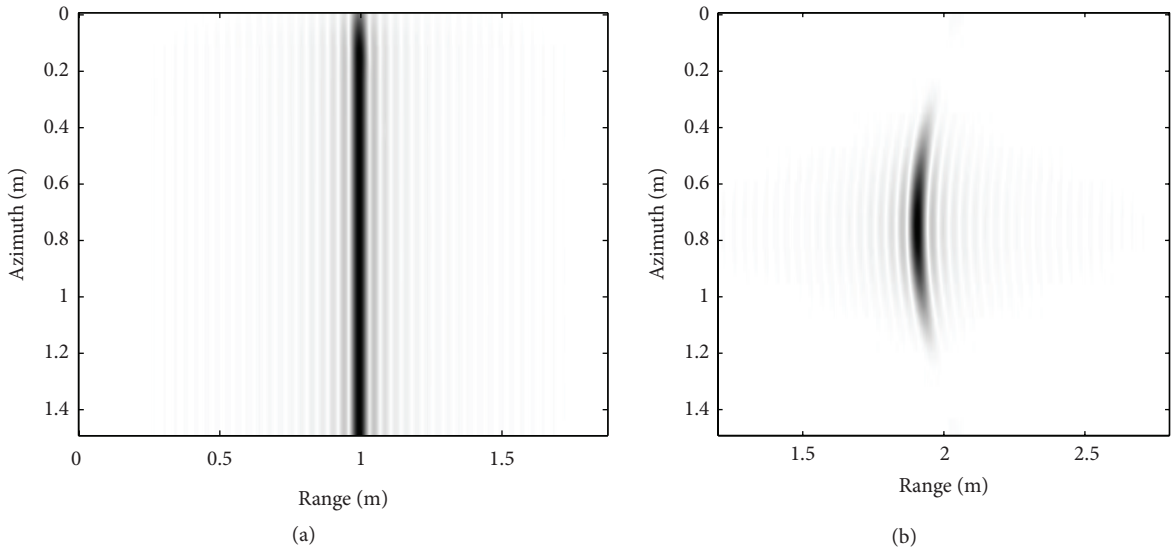

Figure 9: Range-compressed images of a simulated stepped frequency SAR system. (a) a scene containing scatterers modeling a simple wall model located at 0.99 m in range, used to populate the wall dictionary. (b) a scene containing one-single point target located at range 1.9 m and azimuth 0.75 m, used to populate the point-target dictionary.

3.4. Modeling CS Dictionaries. CS dictionaries can be modeled according to the type of scene that must be reconstructed. A possible solution for the problem here addressed is considering two regions in the measurement (Figure 8), which also add complexity scalability to CS on TWI scenes as follows.

(i) A region closer to the sensor (wall region) where only walls parallel to the sensors' motion path are expected to appear. Since walls present very strong azimuth redundancies in SAR measurements, the wall region can be reconstructed forcing coarse azimuth and range resolutions in the final imagery. For every possible range in the scene, the wall dictionary will contain in its columns simulated received SAR data based on a simple infinite wall model (Figure 9(a)).

(ii) A second region is defined further away from the sensor, where scatterers other than walls are expected. This region is known as the wall-free region. Sufficient azimuth information is necessary to characterize point targets in the scene, and reducing the number of azimuth positions is not a sound option. For each position of a point target in the scene, received SAR signals are simulated and included in the columns of the point-target dictionary (Figure 9(b)).

3.5. Random Sampling Limitations. Estimating the number of required random samples for CS reconstruction is a complex task since scene sparsity cannot be easily assessed prior to the measurement. However, an approximate expertise can be gained by systematically testing out several random downsampling possibilities. As discussed in Section 3.3, the main restriction will be established by the wall-dictionary reconstruction. Figure 10 shows Peak Signal-to-Noise Ratio (PSNR) reconstruction values, in which from 10% to 90%

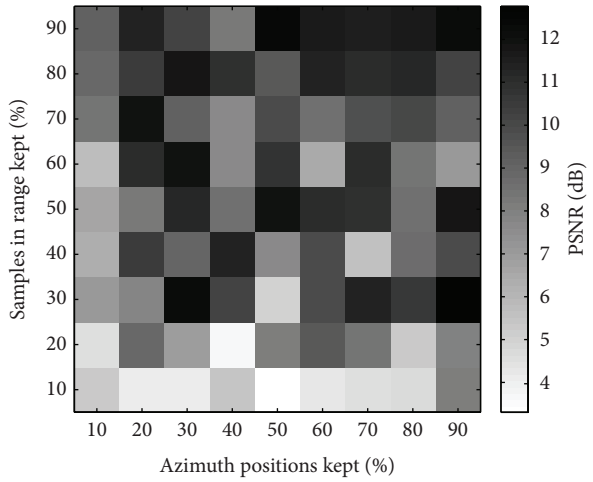

Figure 10: PSNR values in dB for different random downsampling possibilities in fast time and azimuth. A time-domain signal model was used to create the dictionary.

of the azimuth and fast-time samples of a complete SAR TWI measurement were randomly selected. The underlying purpose of the experiment is determining how accurate the image of a wall can be reconstructed if low, medium, or severe downsampling happens and selecting an adequate working point. Analysis of results suggests, as expected, that using severe random downsampling in any dimension impedes an accurate data reconstruction. Using higher values produces an evident improvement in the reconstructions, but those would not yield hardware or computational time reductions. Based on the compromise between accuracy and simplicity, random sampling should range between 20% and 50% in the fast time and between 20% and 50% for azimuth.

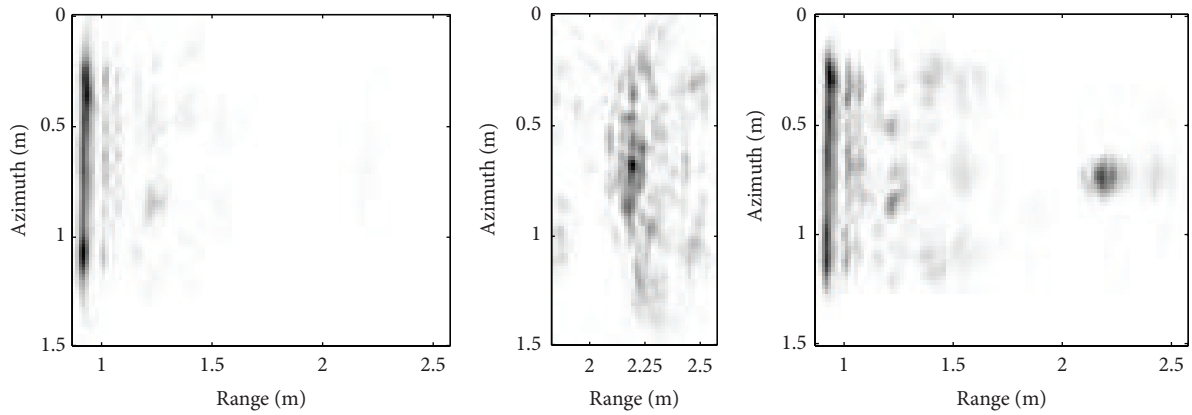

Figure 11: (a) A range-compressed SAR image. The wall is clearly seen. (b) The energy of the corner reflector is spread in azimuth at approximate range 2.25 m. (c) A fully processed SAR image where the presence of a corner reflector is clearly spotted at range 2.25 m.

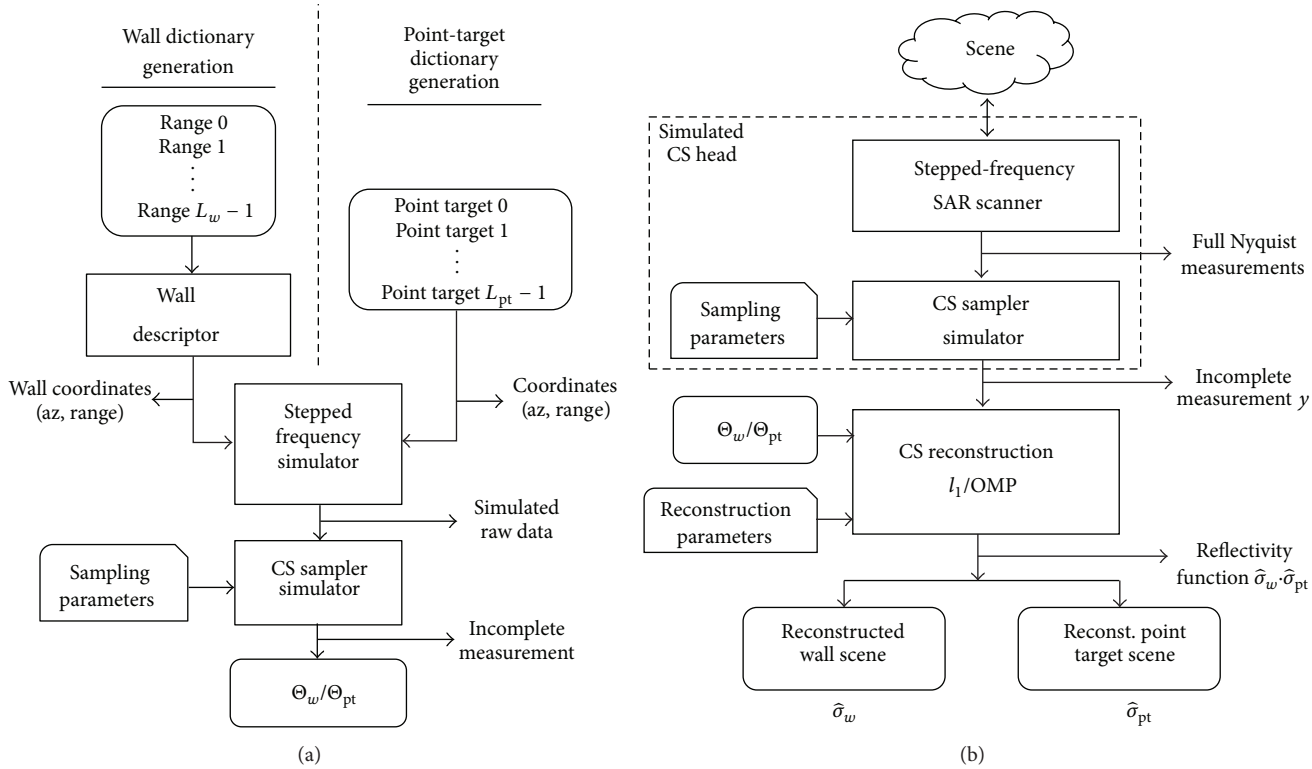

Figure 12: Block diagrams of the (a) wall and point-target dictionary generation and (b) scene reconstruction from actual incomplete measurements.

Given the presented results, this study will use a random downsampling of 50% of the usual samples for both fast-time and azimuth dimensions in the wall-free region, which implies keeping only 25% of the necessary samples for conventional SAR processing. Additionally, decimation by two of the azimuth measurements can be safely applied for the wall region, yielding 12.5% of the original data.

3.6. Practical Experimental Details. The experimental TWI setup uses a conventional SAR system, and original CS measurements cannot be obtained. A full SAR measurement is performed with the presented SF SAR system in order to obtain sufficient fast-time and azimuth information for further random downsampling. The SAR simulator used to model the expected scatterers operates likewise.

4. Results and Discussion

4.1. Conventional SAR TWI Results. The experimental setup depicted in Figures 1 and 5 was measured using the sensor described in Table 1, and conventional time-domain SAR processing was applied. In Figure 11(a), in a range-compressed image of the acquired SAR signals, the wall is clearly visible in the leftmost side due to the strong reflections generated. In the center image, the received energy from corner reflector behind the wall is greatly spread in azimuth following the hyperbolic structure depicted in Figure 6.

After having taken into account azimuth information, the fully compressed SAR image is reconstructed as shown in Figure 11(c). Indeed, the wall is clearly seen as well as several artifacts in adjacent ranges further from the sensor. Such artifacts correspond to low returns from the second layer of the hollow concrete blocks as well as multiple internal reflections which appear in object-free ranges, as predicted in Section 2.1.

4.2. CS Experimental Results. A CS head and processor are imitated in software following the considerations explained in Sections 2 and 3. Raw SAR data shown in Section 4.1 are sampled at different random sampling rates and reconstructed assuming scene sparsity. In this section, presented results were obtained according to the methodology described in Section 3.4 for efficient wall reconstruction and ranging and behind-the-wall accurate reconstruction. The reconstruction dictionaries are built up using simple wall and point-target models and a stepped-frequency SAR simulator.

Figure 12(a) describes how the signal simulator is fed with coordinates produced by the models, which follows to a CS sampler simulator which downsamples the simulated data in range and azimuth according to the provided sampling parameters. The resulting downsampled data are vectorized and stored in the columns of the wall or point-target dictionary, $\boldsymbol{\Theta}_w$ or $\boldsymbol{\Theta}_{\text{pt}}$, respectively. Scene reconstruction of actual measurements is depicted in Figure 12(b). A CS head is partially simulated in software, downsampling the measured signals following a given random sampling scheme identical to that used during the dictionary generation. The CS reconstruction block is fed with the incomplete measurements and the previously generated dictionaries and operational parameters for reconstruction, which may vary depending on the reconstruction algorithms (OMP or the l_1-norm).

Figure 13 shows the reconstruction of the wall reflectivity coefficients vector σ_w using OMP and a wall-only dictionary coarsely modeled for efficient processing purposes. The range of maximum reflectivity, 0.95 m, corresponds to the imaged wall, which satisfies expected results.

A more accurate CS dictionary is then used for point-target reflectivity coefficients reconstruction, or vector σ_{pt}. Based on σ_w, it is assumed that one-single wall was present in the scene. A guard range is kept to avoid the clutter region in ranges immediately after the wall (refer to Figures 3, 6, and 8). Figures 14–16 present reconstructed scenes, where a corner reflector is expected to appear at range 2.25 m, for several range downsampling options (60%, 50%, and 40%). OMP generates simplified but correct reconstructions of σ_{pt} two or three orders of magnitude faster, on average, than the l_1-norm algorithm.

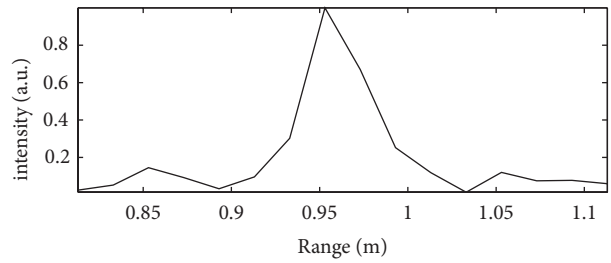

Figure 13: CS reconstruction of the scene using a coarse wall dictionary for wall ranging. The actual wall was located at 0.95 m.

Figure 14 depicts results using downsampling factors of 50% and 60% for azimuth and fast time, respectively. Accurate ranging of the corner reflector is obtained (2.25 m) and comparable to that of the conventional SAR imagery shown in Figure 10 right. Results generated by the l_1-norm clearly indicate where the corner reflector is located, while OPM extracts the most significant reflectivity coefficients. Given the theoretical range resolution of 37.5 mm, the two targets extracted using OMP can be assumed to be in the same resolution cell. As the number of fast-time samples kept is reduced (Figures 15 and 16), inaccuracies in the corner reflector's positioning and false alarms appear, although a general agreement can be reached on the presence of a strong reflector in the scene.

5. Conclusions and Future Work

In this work, CS has been successfully applied to TWI of a real concrete wall. SAR measurements were preprocessed in software to simulate a CS sensor which would perform random sampling in the fast-time and azimuth dimensions. The particular considerations regarding the application of CS onto SAR measurements for TWI were addressed. By using CS, any kind of SAR processing was avoided. A conceptually simple procedure was designed to automatically distinguish between wall and wall-free regions, which exploits the possibilities that CS can offer and reduces computational complexity and avoids having to treat wall clutter. A systematic investigation was performed to determine the minimum random downsampling with respect to conventional SAR TWI without compromising reconstruction accuracy. Data volume was reduced to as low as 25% of the usual required samples, enabling measurement time and hardware complexity reduction.

Future work is focused on finding alternatives to further exploit the CS capabilities for TWI. Some of the lines of investigation the authors are following related to signal processing and CS are as follows.

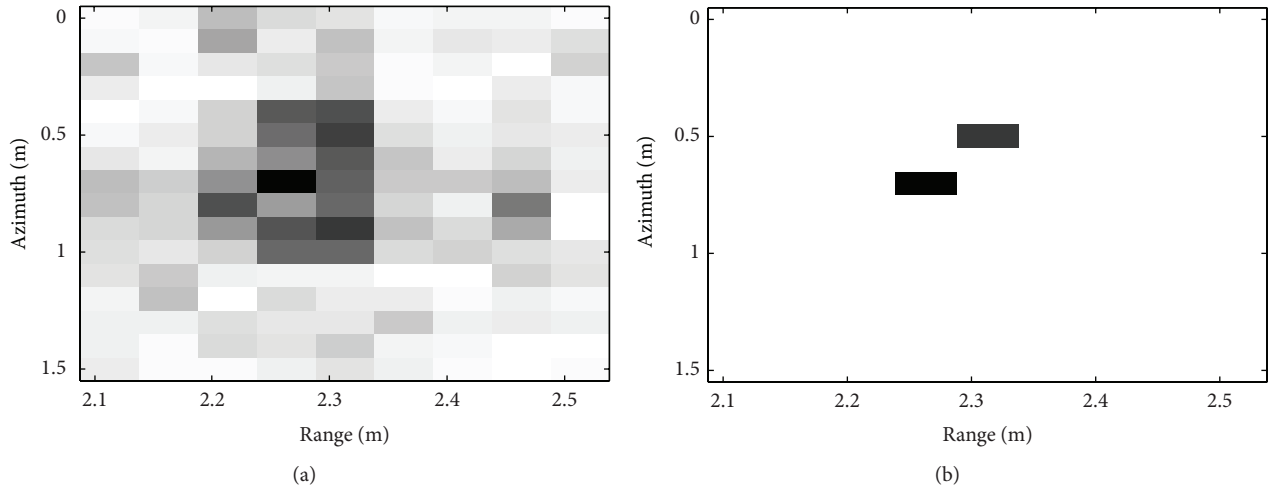

Figure 14: CS reconstructions of the behind-the-wall scene using a point-target dictionary. Downsampling factors were set to 60% for fast-time and 50% for azimuth. (a) l_1-norm; (b) OMP.

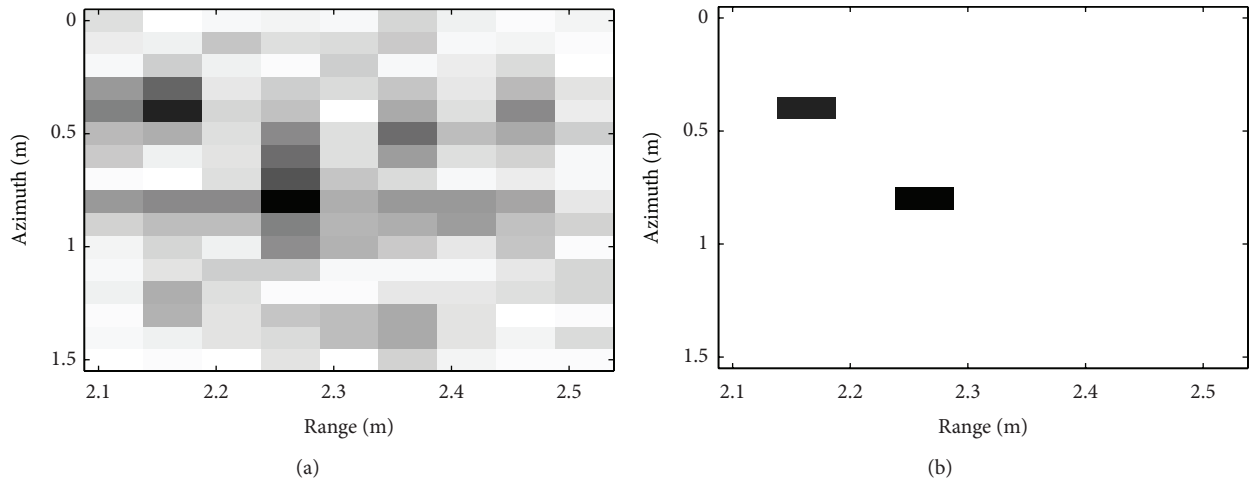

Figure 15: CS reconstructions of the behind-the-wall scene using a point-target dictionary. Downsampling factors were set to 50% for fast-time and 50% for azimuth. (a) l_1-norm; (b) OMP.

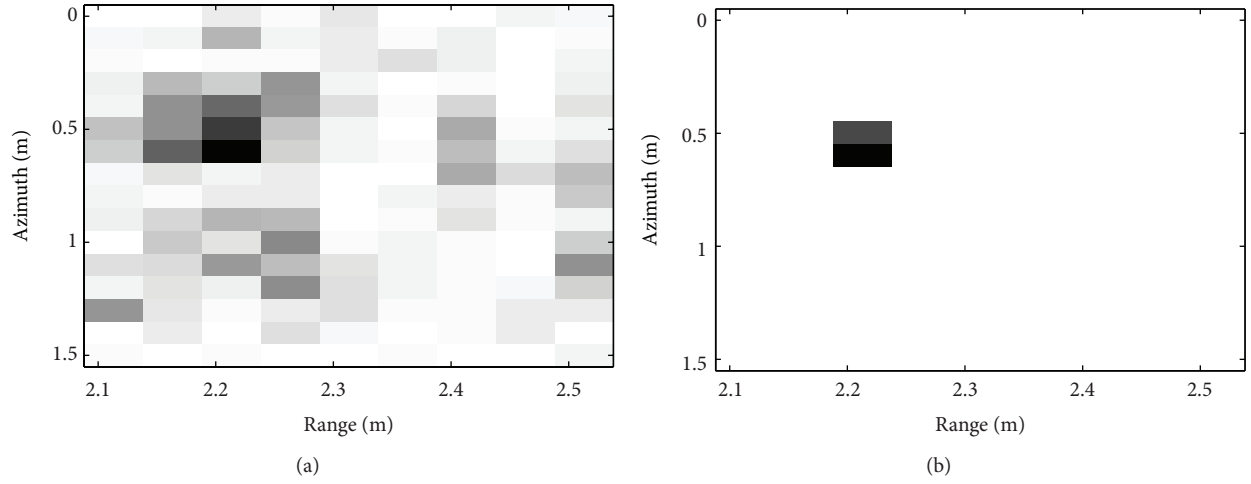

Figure 16: CS reconstructions of the behind-the-wall scene using a point-target dictionary. Downsampling factors were set to 40% for fast-time and 50% for azimuth. (a) l_1-norm; (b) OMP.

(i) Reducing the effects of strong reflections from the wall introduces the reconstruction of point-target regions and improves the accuracy of detection. The authors currently are working on strategies to overcome these negative effects.

(ii) Multiple echoes and patterns due to the wall structure appear in further adjacent ranges. Using a complete SAR model of a wall will help identify which scatterers can be considered as wall clutter or targets of interest behind the wall.

(iii) Range inaccuracies due to inhomogeneous transmission media will be corrected to provide a correct range estimation. A complete wall model will be developed based on existing publications.

(iv) The SF system used in the experiments as well as the antennas has a frequency-dependent performance. A complete SAR signal model must be developed to create CS dictionaries as accurate as possible. Moreover, the mutual interaction between both adjacent antennas modifies their radiation patterns. The antennas will be measured in an anechoic chamber to include this effect in the complete signal model.

(v) CS applied to 3D SAR imaging proposes challenging open questions regarding sparsity assessment and strategies to guarantee the viability the of proposed methodologies in this work.

(vi) Data transformation bases will be studied to enhance data sparsity and facilitate accurate scene reconstructions with even less random samples and simpler hardware.

(vii) Other efficient sparse data reconstruction algorithms will be explored and modified to the TWI needs where applicable.

Acknowledgments

The authors of this study would like to show their gratitude to the OMRA and LEMA laboratories of the Royal Military Academy, Belgium, for providing both technical support and logistic support during construction and measurement of the presented experimental scenes.

References

[1] O. Landron, M. J. Feuerstein, and T. S. Rappaport, "A comparison of theoretical and empirical reflection coefficients for typical exterior wall surfaces in a mobile radio environment," *IEEE Transactions on Antennas and Propagation*, vol. 44, no. 3, pp. 341–351, 1996.

[2] A. Muqaibel, A. Safaai-Jazi, A. Bayram, A. M. Attiya, and S. M. Riad, "Ultra-wideband through-the-wall propagation," *IEE Proceedings*, pp. 581–588, 2005.

[3] T. S. Ralston, G. L. Charvat, and J. E. Peabody, "Real-time through-wall imaging using an ultrawideband multiple-input multiple-output (MIMO) phased array radar system," in *Proceedings of the 4th IEEE International Symposium on Phased Array Systems and Technology (Array '10)*, pp. 551–558, October 2010.

[4] F. Ahmad, M. G. Amin, and P. Setlur, "Through-the-wall target localization using dual-frequency CW radars," in *Proceedings of the Sensors, and Command, Control, Communications, and Intelligence (C3I) Technologies for Homeland Security and Homeland Defense V*, vol. 6201 of *Proceedings of SPIE, 62010H*, May 2006.

[5] Y. Yoon and M. G. Amin, "Spatial filtering for wall-clutter mitigation in through-the-wall radar imaging," *IEEE Transactions on Geoscience and Remote Sensing*, vol. 47, no. 9, pp. 3192–3208, 2009.

[6] R. Solimene, F. Soldovieri, G. Prisco, and R. Pierri, "Three-dimensional through-wall imaging under ambiguous wall parameters," *IEEE Transactions on Geoscience and Remote Sensing*, vol. 47, no. 5, pp. 1310–1317, 2009.

[7] W. Zhang, L. Li, and F. Li, "Autofocusing imaging through the unknown building walls," in *Proceedings of the Asia Pacific Microwave Conference (APMC '08)*, pp. 1–5, December 2008.

[8] D. K. P. Tan, M. Lesturgie, H. Sun, W. Li, and Y. Lu, "Gsm based through-the-wall passive radar demonstrator for motion sensing," in *Proceedings of the New Trends for Environmental Monitoring Using Passive Systems (PASSIVE '08)*, pp. 1–4, Hyères, France, October 2008.

[9] K. Chetty, G. E. Smith, and K. Woodbridge, "Through-the-wall sensing of personnel using passive bistatic wifi radar at standoff distances," *IEEE Transactions on Geoscience and Remote Sensing*, vol. 50, no. 4, pp. 1218–1226, 2012.

[10] I. G. Cumming and F. H. Wong, *Digital Processing of Synthetic Aperture Radar Data: Algorithms and Implementation*, Artech House, Norwood, Mass, USA, 2005.

[11] M. Leigsnering, C. Debes, and A. M. Zoubir, "Compressive sensing in through-the-wall radar imaging," in *Proceedings of the 36th IEEE International Conference on Acoustics, Speech, and Signal Processing (ICASSP '11)*, pp. 4008–4011, May 2011.

[12] F. Ahmad and M. G. Amin, "Partially sparse reconstruction of behind-the-wall scenes," in *Proceedings of the SPIE Symposium on Defense, Security, and Sensing, Compressive Sensing Conference*, Baltimore, Md, USA, April 2012.

[13] Q. Huang, L. Qu, B. Wu, and G. Fang, "UWB through-wall imaging based on compressive sensing," *IEEE Transactions on Geoscience and Remote Sensing*, vol. 48, no. 3, pp. 1408–1415, 2010.

[14] E. Lagunas, M. G. Amin, F. Ahmad, and M. Najar, "Compressive sensing for through wall radar imaging of stationary scenes using arbitrary data measurements," in *Proceedings of the 11th International Conference on Information Science, Signal Processing and their Applications (ISSPA '12)*, pp. 1347–1352, July 2012.

[15] D. L. Donoho, "Compressed sensing," *IEEE Transactions on Information Theory*, vol. 52, no. 4, pp. 1289–1306, 2006.

[16] (n. d.), Schwarzbeck Mess—Elektronik, Double Ridged Broadband Horn BBHA, 9120 D, http://www.schwarzbeck.de/Datenblatt/k9120d.pdf.

[17] C. Thajudeen, A. Hoorfar, F. Ahmad, and T. Dogaru, "Measured complex permittivity of walls with different hydration levels and the effect on power estimation of twri target returns," *Progress in Electromagnetics Research B*, vol. 30, pp. 177–199, 2011.

[18] R. Bamler, "A comparison of range-Doppler and wavenumber domain SAR focusing algorithms," *IEEE Transactions on Geoscience and Remote Sensing*, vol. 30, no. 4, pp. 706–713, 1992.

[19] I. G. Cumming, Y. L. Neo, and F. H. Wong, "Interpretations of the omega-K algorithm and comparisons with other algorithms," in *Proceedings of the IEEE International Geoscience and*

Remote Sensing Symposium (IGARSS '03), pp. 1455–1458, July 2003.

[20] H. L. Van Trees, "Detection of signals—estimation of signal parameters," in *Detection, Estimation, and Modulation Theory: Detection, Estimation, and Linear Modulation Theory*, John Wiley & Sons, New York, NY, USA, 2002.

[21] C. E. Shannon, "A mathematical theory of communication," *The Bell Systems Technical Journal*, vol. 27, pp. 379–423, 623–656, 1948.

[22] E. J. Candès, J. K. Romberg, and T. Tao, "Stable signal recovery from incomplete and inaccurate measurements," *Communications on Pure and Applied Mathematics*, vol. 59, no. 8, pp. 1207–1223, 2006.

[23] E. J. Candès, J. Romberg, and T. Tao, "Robust uncertainty principles: exact signal reconstruction from highly incomplete frequency information," *IEEE Transactions on Information Theory*, vol. 52, no. 2, pp. 489–509, 2006.

[24] H. Rauhut, "Compressive sensing and structured random matrices," in *Theoretical Foundations and Numerical Methods for Sparse Recovery*, M. Fornasier, Ed., vol. 9 of *Radon Series on Computational and Applied Mathematics*, pp. 1–92, deGruyter, Berlin, Germany, 2010.

[25] T. Blumensath and M. E. Davies, "In greedy pursuit of new directions: (nearly) orthogonal matching pursuit by directional optimisation," in *Proceedings of the 15th European Signal Processing Conference (EUSIPCO '07)*, Poznan, Poland, September 2007.

[26] J. A. Tropp and D. Needell, "CoSaMP: iterative signal recovery from incomplete and inaccurate samples," presented at CoRR, 2008.

Hindawi Publishing Corporation
Journal of Electrical and Computer Engineering
Volume 2013, Article ID 379832, 6 pages
http://dx.doi.org/10.1155/2013/379832

Research Article

Multiband Software Defined Radar for Soil Discontinuities Detection

S. Costanzo,[1] F. Spadafora,[1] O. H. Moreno,[2] F. Scarcella,[1] and G. Di Massa[1]

[1] *Dipartimento di Ingegneria Informatica, Modellistica, Elettronica e Sistemistica, Università della Calabria, 87036 Rende (CS), Italy*
[2] *Facultad de Informatica y Electronica, Escuela Superior Politecnica de Chimborazo, Riobamba, EC060155, Ecuador*

Correspondence should be addressed to S. Costanzo; costanzo@deis.unical.it

Received 30 May 2013; Accepted 24 June 2013

Academic Editor: Alvaro Rocha

Copyright © 2013 S. Costanzo et al. This is an open access article distributed under the Creative Commons Attribution License, which permits unrestricted use, distribution, and reproduction in any medium, provided the original work is properly cited.

A multiband Software Defined Radar based on orthogonal frequency-division multiplexing technique is proposed in this work for an accurate soil discontinuities detection, taking into account also the dispersive behavior of media. A multilayer soil structure is assumed as a validation test to demonstrate the effectiveness of the proposed approach, by accurately retrieving the unknown thicknesses and permittivities of the soil layers.

1. Introduction

Electromagnetic sensors such as ground penetrating radar (GPR) are largely adopted for the detection of buried land mines, unexploded ordnance, and soil discontinuities. The performance of these sensors strongly depends on the dielectric properties of the soil, which in turn are related to specific parameters, such as texture, bulk density, and water content. The accurate knowledge of soil dielectric constant is of primary importance in this kind of radar application and is particularly difficult to achieve in the presence of dispersive media, where the dielectric properties vary with frequency. The use of a multiband radar technique can be strongly helpful in this case, thus an approach in terms of Software Defined Radar (SDR) system can be adopted to face the problem. As a matter of fact, the use of SDR technology leads to significant advantages in terms of lowcost, compactness, easy implementation of radar functions, and in particular signal processing techniques. The potentialities of SDR systems have been discussed by the authors in [1, 2] for the case of single-band applications. In this work, a multiband SDR technology is proposed to implement a GPR system, in order to perform an accurate soil discontinuities detection. For the considered multiband application, the adoption of SDR concept provides strong advantages with respect to classical radars, due to the easy software implementation of all required hardware modules, such as mixers, filters, modulators/demodulators, and the easier integration into a unique compact system of all necessary signal processing operations. In particular, in the present work, the adoption of an orthogonal frequency-division multiplexing (OFDM) signal processing technique [3–7] is discussed to implement a multiband radar system able to retrieve the frequency variations of soil permittivity.

The benefit of multicarrier radar signaling [8] has been well established in various application fields, such as remote sensing of wheatear forecasting [9], detection of buried objects [10], and interpretation of urban scenes [11]. In these works, the strong advantages of OFDM in terms of robustness against multipath fading, easy synchronization and equalization, and a high flexibility in the system design are clearly outlined.

Alternative multiband signal methods also exist in literature. For example, ultrashort pulses (USP) are often used to accomplish a good radar range resolution. However, the main problem of these signals is related to the strong attenuation of the average transmitted power, which can hinder the radar's normal operation modes. The attenuation issue can be controlled by the adoption of chirp waveforms [12], but in this case a nonregular signal (typically frequency modulated) is applied, while the main advantage of OFDM radar systems is just related to the adoption of regular signals leading to a potential primary active radar system available at zero additional spectrum usage [13].

In synthesis, apart from the aforementioned features, the main advantages deriving from the adoption of an OFDM radar can be summarized as follows:

(i) digital waveforms generation with the possibility of pulse-to-pulse shape variation;

(ii) narrowband jamming/interference possibility mitigation by simply turning off specific subbands;

(iii) noise-like waveforms for increased low probability of intercept/detection;

(iv) high resolution and good robustness against multipath;

(v) high spectral efficiency;

(vi) ability to transmit large amounts of image data in real time;

(vii) flexible usage of subbands to be adopted and used for Doppler/location/voice communication.

In order to validate the proposed multiband OFDM-based SDR approach, a test of multilayer structure is considered in this work and a multiband OFDM algorithm is applied to accurately reconstruct the thickness and the permittivities of the soil layers [14–16]. As reference simulations, the empirical models described in [14, 15] are adopted to predict the permittivity behavior in the frequency range between 0.3 GHz and 18 GHz.

2. Empirical Models of Soil Electrical Properties

The dielectric properties of a soil depend on a number of factors, such as bulk density, sand percentage, clay and silt particles, density of soil particles, volumetric water content, temperature, and frequency of interest [14–16].

In this section, we summarize the results obtained from the two empirical models [14, 15] largely adopted in the literature for an accurate soil simulation.

The first model is tuned for the frequency range between 0.3 GHz and 1.3 GHz [14], while the second one [15] is calibrated between 1.4 GHz and 18 GHz. In these models, a dielectric constant as a function of frequency can be retrieved by setting the sand and clay fraction and the volumetric water content.

The models calculate the real and the imaginary parts of the dielectric constant ε of a particular soil, on the base of the following inputs:

(i) θ: volumetric soil water content;

(ii) f: operating frequency;

(iii) S: fraction of sand particles;

(iv) C: fraction of clay particles;

(v) ρ_s: density of soil particles (typically 2.66 g/cm^3);

(vi) ρ_b: bulk density of the soil (typically 1.66 g/cm^3);

(vii) $\varepsilon_{fw} = \varepsilon'_{fw} + j\varepsilon''_{fw}$: dielectric constant of free water.

The real and imaginary parts ε', ε'' of soil dielectric constant ε are given by the following:

$$\varepsilon' = \left[1 + \frac{\rho_B}{\rho_s}\left(\varepsilon_s^{\alpha} - 1\right) + \theta^{\beta'}\varepsilon_{fw}'^{\alpha} - \theta\right]^{1/\alpha},$$
$$\varepsilon'' = \left[\theta^{\beta''}\varepsilon_{fw}''^{\alpha}\right]^{1/\alpha}, \tag{1}$$

where

$$\alpha = 0.65,$$
$$\beta' = 1.2748 - 0.519S - 0.152C, \tag{2}$$
$$\beta'' = 1.33797 - 0.603S - 0.166C,$$

$$\varepsilon'_{fw} = \varepsilon_{w\,\inf} + \frac{\varepsilon_{w\infty} - \varepsilon_{w0}}{1 + \left(2\pi f\tau_w\right)^2},$$
$$\varepsilon''_{fw} = \frac{2\pi f\tau_w\left(\varepsilon_{w0} - \varepsilon_{w\infty}\right)}{1 + \left(2\pi f\tau_w\right)^2} + \frac{\sigma_{\text{eff}}}{2\pi\varepsilon_0 f}\frac{\left(\rho_s - \rho_B\right)}{\rho_s^{\theta}}. \tag{3}$$

In (3), ε_0 is the free-space permittivity, ε_{w0} gives the dielectric constant of the water equal to 20.1 at 20°C, $\varepsilon_{w\infty}$ is the high frequency limit of ε'_{fw} equal to 4.9, and τ_w is the relaxation time of the water equal to 9.23×10^{-12} s at 20°C. The dielectric constant of the soil particles ε_s and the effective soil conductivity σ_{eff} are given by the following empirical formulas:

$$\varepsilon_s = \left(1.01 + 0.44\rho_s\right)^2 - 0.062,$$
$$\sigma_{\text{eff}}^{1.3\,\text{GHz}}{}_{18\,\text{GHz}} = -1.645 + 1.939\rho_B - 2.013S + 1.594C, \tag{4}$$
$$\sigma_{\text{eff}}^{0.3\,\text{GHz}}{}_{1.3\,\text{GHz}} = 0.0467 + 0.2204\rho_B - 0.4111S + 0.6614C.$$

In Figure 1, the behavior of the real and imaginary parts for the soil dielectric constant ε is reported versus frequency. Discontinuities in the graphs can be observed as due to the combinations of the two empirical models. In the following sections, these will be adopted to simulate a multilayer soil as validation test for the OFDM multiband algorithm.

3. OFDM Signal Processing Method

OFDM is a combination of modulation and multiplexing techniques, which allows the transmission of complex modulation symbols obtained through discrete phase modulation (e.g., BPSK). The block diagram of the OFDM principle is schematically illustrated in Figure 2.

The symbols use orthogonal subcarriers with duration T, which are frequency spaced by the interval:

$$\Delta f = \frac{1}{T}, \tag{5}$$

in order to avoid intercarrier interference. Each complex modulation symbol is expressed by the following:

$$\Psi_k(t) = S_k(t)\, e^{-j2\pi(f_k)t}, \tag{6}$$

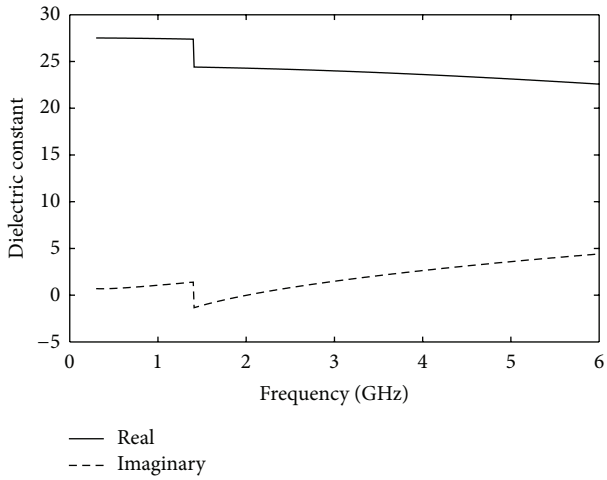

Figure 1: Dielectric constant versus frequency for a soil with $S = 0.95$, $C = 0.02$, and $\theta = 0.27$.

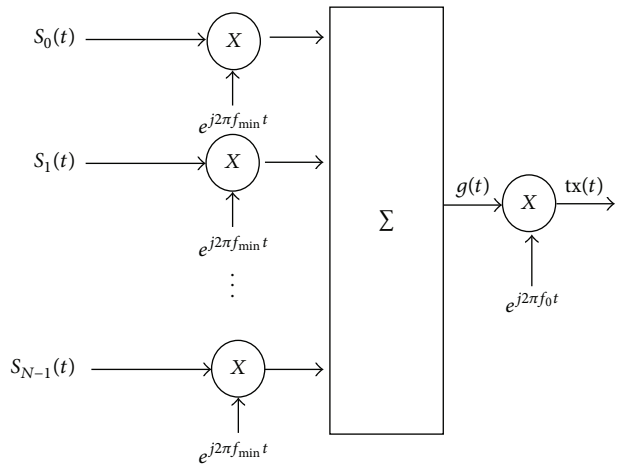

Figure 2: OFDM block diagram.

where $S_k(t)$ is a complex symbol (e.g., in BPSK it can be equal to 1 or −1 with duration T), and f_k is the individual subcarrier frequency, given as

$$f_k = f_{\min} + k\Delta f, \quad k = 0, 1, 2, \ldots, N-1, \tag{7}$$

with $f_{\min}$ giving the minimum frequency with an arbitrary value.

The multiplexed signal is represented as

$$g(t) = \begin{cases} \sum_{k=0}^{N-1} S_k(t)\, e^{-j2\pi(f_{\min}+k\Delta f)t}, & 0 < t < T \\ 0, & \text{otherwise.} \end{cases} \tag{8}$$

It is modulated with a carrier frequency f_0 to obtain the OFDM signal, which is equal to

$$\text{tx}(t) = g(t)\, e^{j2\pi f_0 t}. \tag{9}$$

OFDM radar works as a static system, by transmitting a signal of kind (9) and receiving reflections of this signal from objects in the path of the signal's wavefront. It is important that transmitter and receiver are synchronized in order to avoid time or frequency offset. The received signal, in the absence of Doppler effect, can be expressed as

$$\text{rx}(t) = \sum_{h=0}^{H-1} b_h g\left(t - \tau_h\right) e^{j2\pi f_0 (t-\tau_h)}, \tag{10}$$

where H is the number of reflecting targets. Every target at a distance d_h is represented by a delay τ_h of the corresponding signal. The term b_h represents the attenuation for each target which depends on the material characteristics and the radar cross-section.

The OFDM signal processing technique gives a maximum measurement distance defined as

$$d_{\max} = \frac{c}{2\Delta f} = \frac{Tc}{2}, \tag{11}$$

where c is free-space velocity.

The radar slant range resolution depends on the total bandwidth B occupied by the transmitted signal, so it is given by

$$\Delta r = \frac{c}{2B} = \frac{c}{2N\Delta f}. \tag{12}$$

Figure 3 shows the block diagram for an OFDM radar, where the transmitted signal is composed by N symbols $S = [S_0, S_1, S_2, \ldots, S_{N-1}]^T$ modulated with N orthogonal frequencies $f = [f_{\min}, f_{\min} + \Delta f, f_{\min} + 2\Delta f, \ldots, f_{\min} + (N-1)\Delta f]^T$ using OFDM technique. The total time T_t for an OFDM symbol considers the symbol duration T and a guard interval T_G, that is, the time to avoid intersymbol interference between subsequent OFDM symbols.

The received signal rx is demodulated, and a vector $Y = [Y_0, Y_1, Y_2, \ldots Y_1]$, containing the values of received symbols, is retrieved.

The target position is then obtained by applying the IFFT on the result of the wise division between the symbols received Y and that transmitted S.

4. Multiband OFDM SDR

The scheme reported in Figure 2 is relative to a single band OFDM system. In order to obtain a multiband configuration, the original block diagram is modified as in Figure 4, with the adoption of M carrier frequencies, namely, $f_{01}, f_{02}, \ldots, f_{0M}$.

There are two possibilities for obtaining an OFDM multiband signal tx. The first one consists in transmitting all the OFDM waves at the same time, using only one shoot of T_t seconds, while in the second approach just one OFDM signal is transmitted each T_t seconds, with a total time signal of $M * T_t$ seconds. The second option is the simplest one for processing and analysis, so it is adopted in this work for the reconstruction of multilayer soil permittivity. As an example, the spectrum of the a multiband OFDM signal with $M = 5$ carriers is illustrated in Figure 5.

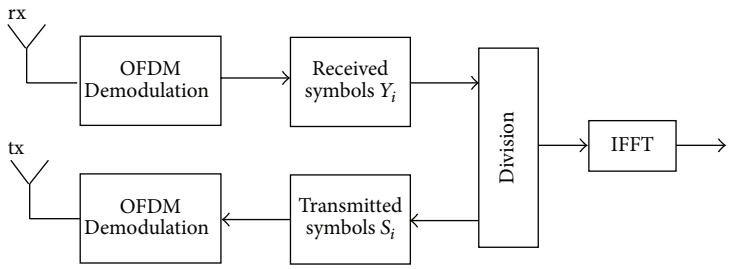

Figure 3: OFDM radar block diagram.

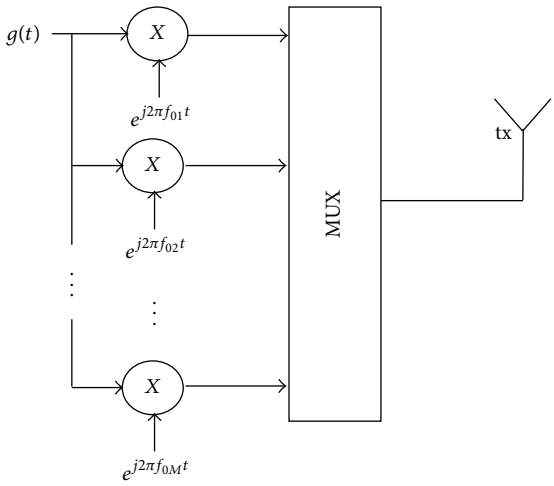

Figure 4: Block diagram of OFDM multiband radar system.

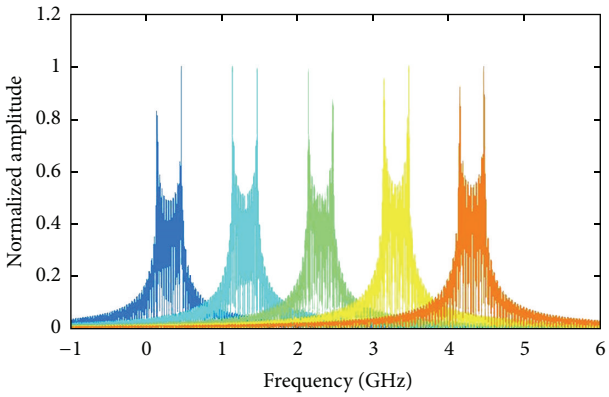

Figure 5: Spectrum of OFDM multiband signal with $M = 5$ carriers.

5. Dielectric Characterization Algorithm

Let us consider a simple structure with 2 homogeneous materials having thickness d_1 and d_2, respectively (Figure 6). A radar signal from a distance $d_0 > 2D^2/\lambda_{f_{\min}}$ ($\lambda_{f_{\min}}$ being the wavelength for the minimum frequency $f_{\min}$ under analysis) is assumed to impinge on the multilayer structure.

As a first case, we assume non-dispersive dielectric media, characterized by constant permittivities versus frequency. In this situation, we can use a single band OFDM signal tx(t) to

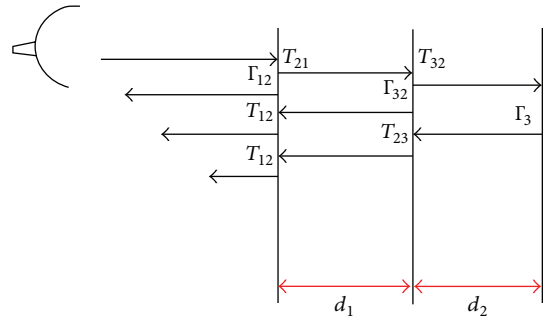

Figure 6: Multilayer test structure.

retrieve the permittivity values ϵ_{r1} and ϵ_{r2} of the two layers. The corresponding signal detected by the receiver is given by the following expression:

$$\begin{aligned} \mathrm{rx}(t) = {} & b_0 g(t-\tau_0) e^{j2\pi f_0 (t-\tau_0)} \\ & + b_1 g(t-\tau_1) e^{j2\pi f_0 (t-\tau_1)} \\ & + b_2 g(t-\tau_2) e^{j2\pi f_0 (t-\tau_2)}, \end{aligned} \tag{13}$$

where

(i) b_0 is directly related to the reflection coefficient Γ_{01} of the first reflection from the first substrate, and τ_0 is the associated delay time;

(ii) b_1 is related to the expression $(1 - {\Gamma_{01}}^2)\,\Gamma_{12}$ of the second reflection from the second substrate, and τ_1 is the associated delay time;

(iii) b_2 is related to the expression $(1 - {\Gamma_{12}}^2)\,\Gamma_{23}$ of the third reflection from the third substrate, and τ_2 is the associated delay time.

The terms Γ_{01}, Γ_{12}, and Γ_{23} are well known in the literature [17].

The result of OFDM signal processing on the received signal (13) is illustrated in Figure 7, where the three peaks corresponding to the reflections from the three interfaces can be observed. In the same figure, the result obtained from a preliminary system calibration, performed with a perfect conductor surface covering the test structure, is also reported.

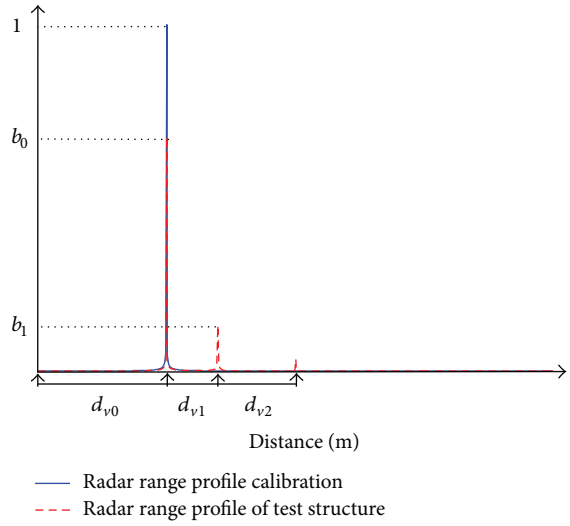

Figure 7: Radar range profile.

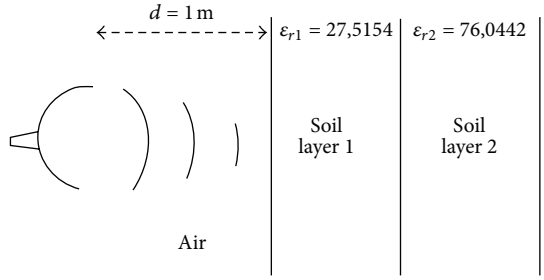

Figure 8: Simulated scenario.

A recursive algorithm is applied to retrieve the permittivity values ϵ_{r1} and ϵ_{r2}. In particular, we have

$$b_0 = \Gamma_{01} = \frac{1 - \sqrt{\epsilon_{r1}}}{1 + \sqrt{\epsilon_{r1}}}, \tag{14}$$

from which it is straightforward to retrieve the value of ϵ_{r1}. Then, we can use the following expression:

$$\frac{b_1}{b_0} = \frac{\left(1 - \Gamma_{01}{}^2\right)}{\Gamma_{01}}\Gamma_{12}, \tag{15}$$

to retrieve the value of ϵ_{r2} directly from Γ_{12} and so on for the successive substrate:

$$\frac{b_2}{b_1} = \frac{\left(1 - \Gamma_{12}{}^2\right)}{\Gamma_{12}}\Gamma_{23}. \tag{16}$$

A generalized equation for the algorithm can be expressed as

$$\frac{b_n}{b_{n-1}} = \frac{\left(1 - \Gamma_{n-1,n}{}^2\right)}{\Gamma_{n-1,n}}\Gamma_{n,n+1}. \tag{17}$$

Once the values of the permittivity values ϵ_{r1} and ϵ_{r2} are known, the next step is to calculate the thicknesses d_1 and d_2 of the two layers. In particular, the distances d_{v0}, d_{v1}, and d_{v2} highlighted in Figure 7 are related to the real distances d_i by the following relationship:

$$d_i = \frac{dvi}{\sqrt{\epsilon_{ri}}} \tag{18}$$

Let us assume, now, that layers in Figure 7 are composed by dispersive media, with a variation of permittivities versus frequency. In this case, a multiband OFDM technique can be adopted to retrieve the variation profile of dielectric constants. In particular, by considering M different carriers as in Figure 4, the algorithm previously described for the case of single band OFDM must be repeated for every carrier frequency, thus obtaining M graphs similar to that of Figure 7 but presenting a shift Δd, variable versus frequency, for the distances d_{v1} and d_{v2}. It is in turn related to the permittivity shift $\Delta\varepsilon_r$, which can be expressed as

$$\Delta\varepsilon_r = \left(\frac{d_{vi}}{d_{vi} - \Delta d}\right)^2. \tag{19}$$

Table 1: Input soil electrical model.

	Soil layer 1	Soil layer 2
θ	0.27	0.8
S	0.95	0.70
C	0.02	0.01
ε_r	**27.5154**	**76.0442**

Table 2: Retrieved permittivities and thicknesses.

	Soil layer 1	Soil layer 2
Retrieved ε_r	26.8856	72.1654
Retrieved layer thickness m	0.3934	0.4453

Table 3: Permittivity variation for each carrier frequency.

Frequency GHz	Retrieved $\Delta\varepsilon_{r1}$	Retrieved $\Delta\varepsilon_{r2}$
2.3	1.0314	1.0503
3.3	1.0314	1.0503
4.3	1.0481	1.0726

6. Numerical Results

In order to validate the proposed multiband SDR technique, the multilayer soil structure in Figure 8 is assumed as a test scenario. The empirical models outlined in Section 2 are applied by assuming parameters C (clay fraction), S (sand fraction), and θ (water content) as reported in Table 1, where the simulated relative dielectric constants of the two layers are also indicated. As a first task, a single-band OFDM radar signal with f_0 = 2.3 GHz (Figure 2) is assumed to retrieve the values of ϵ_{r1}, ϵ_{r2} and the thicknesses d_1, d_2 of the two layers (Table 2). In a successive step, a multiband OFDM signal with M = 3 carriers is considered, thus obtaining the curves reported in Figure 9, for a frequency variation from 2.3 GHz up to 4.3 GHz. The relative detected values of Δd, variable with carrier frequency (Figure 9), are then used to obtain the variation profile of the permittivity as a function of frequency, for the two soil layers (Table 3).

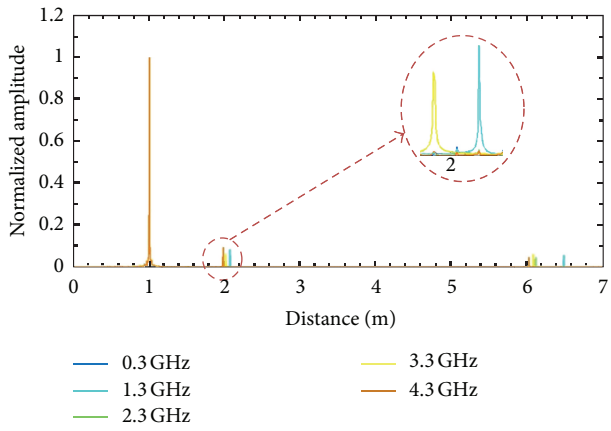

Figure 9: Shift effect on the retrieved signal peaks.

7. Conclusion and Future Development

The adoption of a Software Defined Radar system, used in conjunction with an orthogonal frequency-division multiplexing technique, has been discussed in this work. The advantageous features of Software Defined Radar technology, in terms of lowcost and easy implementation of signal processing algorithms, exploited together the adoption of multicarriers in the orthogonal frequency-division multiplexing method, to implement a multiband Software Defined Radar system able to accurately retrieve the geometrical and dielectric profiles of multilayer soils, with the further capability to reconstruct the frequency variation of permittivity. The proposed approach has been successfully validated on a two-layer soil structure. As a future work, a further extension of the method to a full dielectric characterization of media, including also the reconstruction of the imaginary part of the dielectric constant, will be developed. At this purpose, more accurate models for the multilayer structures and more efficient inversion algorithms for the dielectric characterization will be considered.

Acknowledgment

This work has been carried out under the framework of PON 01_01503 National Italian Project "Landslides Early Warning," financed by the Italian Ministry of Education, University and Research.

References

[1] G. Aloi, A. Borgia, S. Costanzo et al., "Software defined radar: synchronization issues and practical implementation," in *Proceedings of the 4th International Conference on Cognitive Radio and Advanced Spectrum Management (CogART '11)*, Barcelona, Spain, October 2011.

[2] S. Costanzo, F. Spadafora, A. Borgia, O. H. Moreno, A. Costanzo, and G. Di Massa, "High resolution software defined radar system for target detection," *Advances in Intelligent Systems and Computing*, vol. 206, pp. 997–1005, 2013.

[3] S. Sen, M. Hurtado, and A. Nehorai, "Adaptive OFDM radar for detecting a moving target in urban scenarios," in *Proceedings of the International Waveform Diversity and Design Conference (WDD '09)*, pp. 268–272, February 2009.

[4] S. Bausson and P. Forster, "Detection and pulse compression In passive radar with OFDM radio signals," in *Proceedings of the 16th European Signal Processing Conference (EUSIPCO '08)*, Lausanne, Switzerland, 2008.

[5] M. Braun, C. Sturm, and F. K. Jondral, "Maximum likelihood speed and distance estimation for OFDM radar," in *Proceedings of the IEEE International Radar Conference (RADAR '10)*, pp. 256–261, May 2010.

[6] C. Sturm, T. Zwick, and W. Wiesbeck, "An OFDM system concept for joint radar and communications operations," in *Proceedings of the 69th IEEE Vehicular Technology Conference (VTC '09)*, April 2009.

[7] M. Fuhr, M. Braun, C. Sturmz, L. Reichardtz, and F. K. Jondral, "An SDR-based experimental setup for OFDM-based radar," in *Proceedings of the Virginia Tech Symposium on Wireless Communications*, Blacksburg, Va, USA, June 2012.

[8] S. Sen and A. Nehorai, "Adaptive design of OFDM radar signal with improved wideband ambiguity function," *IEEE Transactions on Signal Processing*, vol. 58, no. 2, pp. 928–933, 2010.

[9] N. Majurec, S. M. Sekelsky, S. J. Frasier, and S. A. Rutledge, "The advanced multi-frequency radar (AMFR) for remote sensing of clouds and precipitation," in *Proceedings of the 11th Conference on Mesoscale Processes and the 32nd Conference on Radar Meteorology*, pp. 1051–1057, Albuquerque, NM, USA, October 2005, paper no. P1R.6.

[10] P. V. Genderen, P. Hakkaart, J. V. Heijenoort, and G. P. Hermans, "A multi frequency radar for detecting landmines: design aspects and electrical performance," in *Proceedings of the 31st European Microwave Conference*, vol. 2, pp. 249–252, 2001.

[11] M. L. Bryan, "Interpretation of an urban scene using multichannel radar imagery," *Remote Sensing of Environment*, vol. 4, no. 1, pp. 49–66, 1975.

[12] B. R. Mahafza and A. Z. Elsherbeni, *Simulations for Radar Systems Design*, Chapman and Hall/CRC, 2003.

[13] C. Sturm, T. Zwick, and W. Wiesbeck, "Spectral estimation-based OFDM radar algorithms for IEEE 802.11a signals," in *Proceedings of the IEEE Vehicular Technology Conference (VTC '12)*, 2012.

[14] N. R. Peplinski, F. T. Ulaby, and M. C. Dobson, "Dielectric properties of soils in the 0.3–1.3-GHz range," *IEEE Transactions on Geoscience and Remote Sensing*, vol. 33, no. 3, pp. 803–807, 1995.

[15] T. W. Miller, B. Borchers, J. M. H. Hendrickx, S. Hong, L. W. Dekker, and C. J. Ritsema, "Effects of soil physical properties on GPR for landmine detection," in *Proceedings of the 5th International Symposium on Technology and the Mine Problem*, 2002.

[16] M. C. Dobson, F. T. Ulaby, M. T. Hallikainen, and M. A. El-Rayes, "Microwave dielectric behavior of wet soil—part II: dielectric mixing models," *IEEE Transactions on Geoscience and Remote Sensing*, vol. 23, no. 1, pp. 35–46, 1985.

[17] C. A. Balanis, *Advanced Engineering Electromagnetics*, John Wiley & Sons, 1989.

Hindawi Publishing Corporation
Journal of Electrical and Computer Engineering
Volume 2013, Article ID 146986, 6 pages
http://dx.doi.org/10.1155/2013/146986

Research Article

Noise Radar Technology as an Interference Prevention Method

Gaspare Galati and Gabriele Pavan

Department of Electronic Engineering, Tor Vergata University, Via del Politecnico, 1-00133 Rome, Italy

Correspondence should be addressed to Gaspare Galati; gaspare.galati@uniroma2.it

Received 6 June 2013; Accepted 6 July 2013

Academic Editor: Sandra Costanzo

Copyright © 2013 G. Galati and G. Pavan. This is an open access article distributed under the Creative Commons Attribution License, which permits unrestricted use, distribution, and reproduction in any medium, provided the original work is properly cited.

In some applications, such as automotive and marine/navigation, hundreds of radars may operate in a small environment (e.g., a road complex or a strait) and in an allocated frequency band with limited width. Therefore, a compatibility problem between different radars arises that is not easily solved by time, frequency, space, or polarization diversity. The advent of fast digital signal processing and signal generation techniques makes it possible to use waveform diversity to solve this problem that will be exacerbated in the next future. Ideal waveforms for the diversity are supplied by Noise Radar Technology (NRT), whose application is promising in some military applications as well as in the civilian applications considered in this paper. In addition to being orthogonal as much as possible, the random signals to be transmitted have to satisfy requirements concerning side lobe level and crest factor, calling for novel, original design and generation processes.

1. Introduction

In spite of its military origin, dated back to the 1930s, radar technology is being more and more applied in the civilian domain for the safety of air, sea, and land traffic. In sea and road applications, this technology is entering the mass market with a significant yearly reduction of costs, mainly due to the larger and larger integration of the hardware and to the scale economy. For example in the automotive radar the factory cost has fallen by one order of magnitude (from hundreds to tens of dollars) in a few years. A similar situation is to be expected in the field of marine radar [1, 2], present in most vessels, as they (X-band radar) are mandatory for all passenger vessels and for all vessels above 500 tons GT (Gross Tonnage), with a double-band requirement (X-band radar + S-band radar) above 3000 tons GT. The allocated bands are 9.3 to 9.5 GHz (X) and 2.9 to 3.1 GHz. Most marine radars use the simple and cheap magnetron transmitter, a 1940s technology, generating short pulses (from 50–80 ns in the short-range mode to 800–1000 ns in the long-range mode, up to 96 NM) and peak power from a very few kW to 12.5–25 kW (and 50 kW in coastal applications for Vessel Traffic Systems).

The large number of marine radars in a given area, simultaneously present above the horizon, makes the mutual interference a very likely event. For a general overview of potential solution to this problem, see [3, 4]. In marine radars the most used solution is based on their relatively short pulses that can be suppressed (video blanking or thresholding) because they are received asynchronously with respect to the transmission from the victim (the own) radar. Such a suppression causes tolerable detection losses for small targets and negligible losses for large targets.

As in many other radar applications, for example, in Air Traffic Control (ATC), solid-state transmitter technology is attractive for marine radars. It permits (i) the implementation of highly stable, coherent Rx-Tx chains compatible with Doppler processing, (ii) the transmission of sophisticated waveforms [5], (iii) a better availability, and (iv) the absence of high voltages. Unlike ATC radars that have been using solid state transmitters for over two decades, solid-state marine radars are appearing on the market just now, most of them, in the S-band. While maintaining approximately the same average transmitted power as magnetron transmitters, these new (or experimental) solid-state marine radars have three orders of magnitude larger duty cycle, that is, in the range of 10%–12%. These long pulses (about 10 or 20 microseconds, in some cases up to 100 microseconds) are not compatible with the current interference suppression techniques. In

the remaining part of this paper a new technique is proposed to solve this interference problem, whose general framework is synopsized in the appendix.

2. Signal Requirements and Advantages of Noise Radar Technology (NRT)

Mitigation techniques for interferences from similar radars can be based on diversity in (i) frequency, (ii) polarization, (iii) direction (antenna pattern adaptation), and (iv) waveform. In the marine radar context, as considered here, the limited allocated bandwidth (only 200 MHz in X-band and the same in the S-band) and the use of standard antennae with fixed polarization prevent the use of (i), (ii), and (iii). Therefore a possible solution has to be based on waveform diversity, that is, the transmission (by the various radars in potential interference conditions) of pairwise orthogonal waveforms, such that the matched filter output is mainly due to the "own" waveform, with a noise floor due to the "other radars" waveforms. The large number of radars in busy maritime environments such as straits and sea areas around harbors, makes it necessary to exploit a large number of orthogonal waveforms, which can only be obtained by polyphase codes [3] or, as proposed here, by suitable processing of samples of random processes, leading to Noise Radar Technology.

The main requirements for a pair of signals with complex envelope $s_i(t)$ and $s_j(t)$ with $i, j = 1, \ldots, M$, pulsewidth T, and the same power are defined by the following:

(i) Peak Side Lobe Ratio (< −30 dB):

$$\mathrm{PSLR} = \frac{\max_i (s_i)}{\max_k (m_k)}, \tag{1}$$

where s_i = side lobe samples and m_k = main lobe samples.

(ii) Crest Factor (C) or Peak-to-Average Ratio (PAR), that is, the peak amplitude of the waveform divided by the rms value of the waveform $s(t)$:

$$C = \frac{\max (|s(t)|)}{\sqrt{(1/T)\int_0^T |s(t)|^2 dt}}. \tag{2}$$

(iii) Mean Envelope-to-Peak Power Ratio:

$$\mathrm{MEPPR} = \frac{(1/T)\int_0^T |s(t)|^2 dt}{\max\left(|s(t)|^2\right)}. \tag{3}$$

It results in EPPR = $1/C^2$.

(iv) Normalized cross-correlation:

$$r_{ij}(t) = \frac{\left|R_{ij}(t)\right|}{\left|R_{i(j)}(0)\right|}, \tag{4}$$

where $R_{ij}(t) = \int s_i^*(\theta) s_j(t+\theta) d\theta$, $i \neq j$; it measures the orthogonality, and the desired value is $r_{ij}(t) < -30$ dB.

(v) Spectral band occupancy: sometimes this item is overlooked, especially when noise-like waveforms are concerned, but it is of paramount importance in most real-world radars; see [4] and the appendix.

Good candidate deterministic signals that satisfy the orthogonality requirements are the well-known "up" and "down" chirps (Linear-FM and Non-LFM) [3, 5], but in this case only pairs of signals (not the needed multiplicity M) can be obtained. To obtain M signals Costas codes, All top sequences can be considered, and polyphase codes represent a possible solution [3, 6, 7]. More recent research on orthogonal signals proposed the use of normal or interleaved OFDM techniques [8]. The main limitation of the OFDM approach is due to the nonconstant envelope of the signals, that is, MEPPR < 1, which means that the transmitter does not work at its maximum power.

Another class of waveforms, that is, the phase noise signals [9], has two main advantages as compared to the signals introduced before. The former is the possibility to generate a large number of orthogonal signals, which is of great importance in the present case. The latter, applicable to defense applications (e.g., to the navigation radars of military vessels), is about the detectability; in fact they are random signals so they limit the detection, the identification, and the eventual spoofing of the signal. Such a limitation is of great importance in many military applications which require low detectability of the active system. Finally the MEPPR (and the crest factor) can be very close to the unity.

3. Methods for Generating Noise Radar Signals

For a phase noise signal the complex envelope can be written as

$$s(t) = A \cdot \exp\{j\varphi(t)\} \cdot \mathrm{rect}_T(t), \tag{5}$$

where A is the constant amplitude, $\mathrm{rect}_T(t)$ is 0 outside the interval $[-T/2, +T/2]$ and 1 inside it (with T being the pulse length), and $\varphi(t)$ is the phase process modulating the noise signal $s(t)$. In the following we present three methods to generate the phase noise signals highlighting their strengths and weaknesses.

3.1. Random Phase Modulation. In [9] Axelsson supposed for $\varphi(t)$ a zero-mean Gaussian process with root mean square (rms) σ and a given power with density spectrum within the band b. He showed that the normalized autocorrelation function of the signal $s(t)$ can be written in a closed-form expression as

$$R(\tau) = \exp\left\{-\sigma^2 [1 - \rho(\tau)]\right\}, \tag{6}$$

where $\rho(\tau)$ is the correlation coefficient of $\varphi(t)$. For example, $\rho(\tau) = \sin(\pi b\tau)/(\pi b\tau)$ for a constant spectrum within the band b. Of course, $R(\tau)$ depends on the bandwidth b, on the pulse length T, and on the rms phase fluctuation σ. The bandwidth b is related to the width of the main peak and defines the range resolution. An increase of T, and

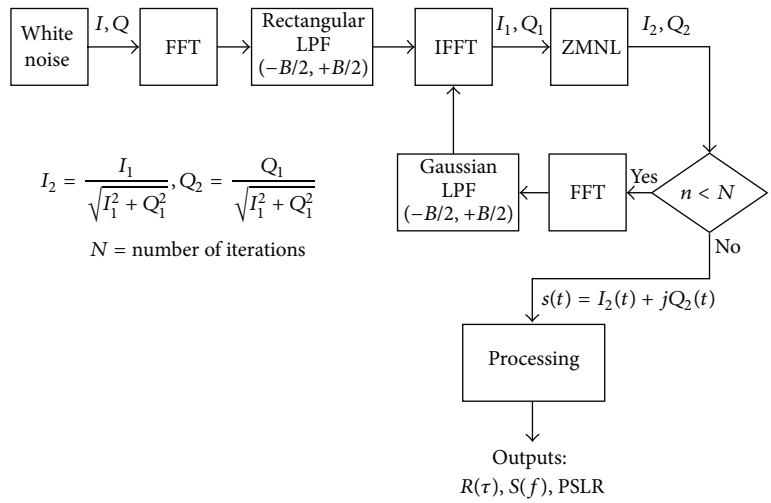

Figure 1: Block diagram of the iterative algorithm.

consequently of the compression ratio (the time-bandwidth product of the generated signal), causes a reduction in the range side lobe level, whereas the main lobe width remains fixed being independent of T. Finally the rms σ has two different effects. The former is on the side lobe level: an increase of σ causes a decrease of the side lobe level with improvement in the PSLR. The latter concerns the resolution. The rms value in fact establishes a connection between the bandwidth of the modulated signal and the bandwidth of the modulating signal. That is, when σ increases the final bandwidth increases too. In [9] a simple relation between the rms bandwidth of the phase modulated signal (B_{rms}) and the rms bandwidth of the phase modulating noise (b_{rms}) has been found:

$$B_{\text{rms}} = \sigma \cdot b_{\text{rms}}. \tag{7}$$

On the other hand, concerning the side lobe suppression, the expression of the autocorrelation function introduced in [9] would show a progressive improvement of the side lobe suppression as σ increases. However the periodic nature of $\varphi(t)$ with a folding in the $[-\pi, +\pi]$ interval has been neglected in [9], and in reality the model can be used only for values of σ significantly smaller than π. The Gaussian noise, used to modulate the signal phase, is to be compared with an *uniform* distribution in the range $[-\pi, +\pi]$ with a standard deviation of $(\pi/\sqrt{3}) \cong 1.8$ rad. Therefore, if σ is large ($\sigma > (\pi/\sqrt{3})$), the resultant phase is not Gaussian distributed and the mathematical formulation introduced in [9] does not apply. On the other hand, in connection with a potential real application, it would be better to generate the signal through a white Gaussian process with its *in phase* and *in quadrature* components (I, Q) that are band limited as desired. This is described in the following.

3.2. An Iterative Algorithm to Generate Phase Noise Signals. To control the spectral width and to reduce the Peak Side Lobe Ratio (PSLR) of the generated phase noise signals, we propose an iterative algorithm based on alternative projections in frequency and in time domain (Figure 1). The input to the algorithm is a zero-mean white complex Gaussian process $(I + jQ)$. The filtering is implemented in frequency domain. First the input is band limited using a rectangular Low Pass Filter of band B. The output from this filter is projected in time domain by IFFT, and the complex signal (I_1, Q_1) is amplitude limited using a Zero-Memory-Non-Linearity (ZMNL). The output in time (I_2, Q_2) is reprojected in frequency and filtered through a Gaussian LPF of band B. The output is again re-projected in time, and the procedure is iterated for a predefined value of N. Typically to achieve the optimum (minimum) PSLR, some tens of iterations are needed (it depends on the input white noise sequence).

Considering for ZMNL a hard limiter, that is,

$$I_2 = \frac{I_1}{\sqrt{I_1^2 + Q_1^2}}, \qquad Q_2 = \frac{Q_1}{\sqrt{I_1^2 + Q_1^2}}, \tag{8}$$

the signal (I_2, Q_2) shows a unitary amplitude and its randomness is only due to the random phase of the signal. Averaging different autocorrelations we have computed the mean normalized autocorrelation and its standard deviation (Figure 2 for BT = 10000).

Varying the compression ratio up to 30000, in Figure 3 the mean PSLR is shown.

To reach PSLR lower than −30 dB, compression ratios over 5000 are needed. However for BT = 30000 the PSLR is −36 dB, less, for example, than the one obtained with Non-LFM using Hamming weighting (−42.8 dB). Figure 4 shows the mean spectrum for BT = 10000 (B = 100 MHz). It shows a good control of the spectral width due to the rectangular LPF. Finally in Figure 5 the cross-correlation (it measures the orthogonality) for a pair of generated phase noise signals is shown with BT = 10000. It is lower than −30 dB (as compared with the same compression ratio, for a pair of up and down chirps the cross-correlation is −43 dB for LFM and −40 dB for Non-LFM).

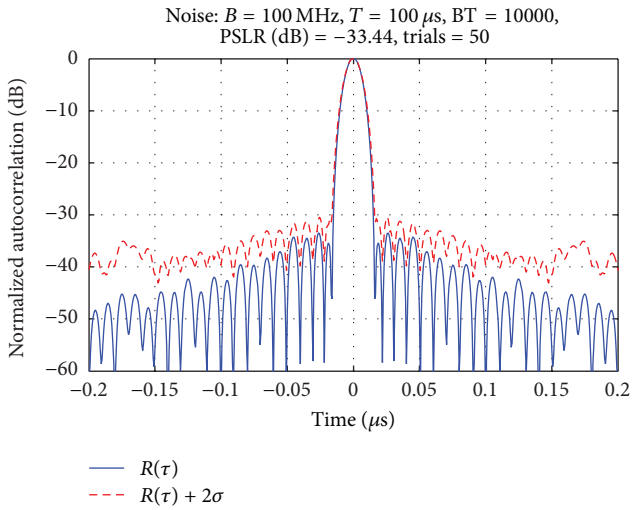

Figure 2: Mean normalized autocorrelation (obtained averaging 50 different autocorrelations). Dashed line: fluctuation at 2σ (σ denotes the standard deviation). Compression ratio BT = 10000, and the ZMNL is a hard limiter.

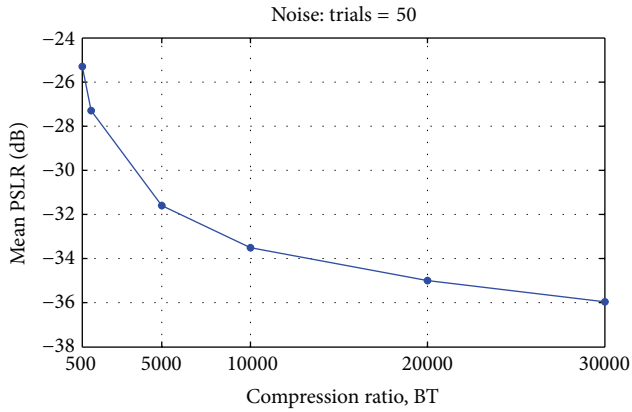

Figure 3: Mean PSLR (obtained averaging 50 different autocorrelations) versus the compression ratio BT, considering for ZMNL a hard limiter.

From the database of generated waveforms [10] a part is selected after analysis of the compliance with the required characteristics in terms of spectral occupancy and autocorrelation and cross-correlation functions. In order to further reduce the side lobe level (which is likely needed, especially for smaller values of the compression ratio BT), a mismatched filtering in reception may be needed [11, 12]. The filter coefficients must be computed for every selected waveform and associated with it for the ensuing usage. While permitting a significant suppression of the range side lobes, this technique calls for increased computation costs (the mismatched filter is typically three times longer than the matched filter) and larger memory requirements.

3.3. Closed Form by Inversion. A different, closed form generation approach is based on the following considerations.

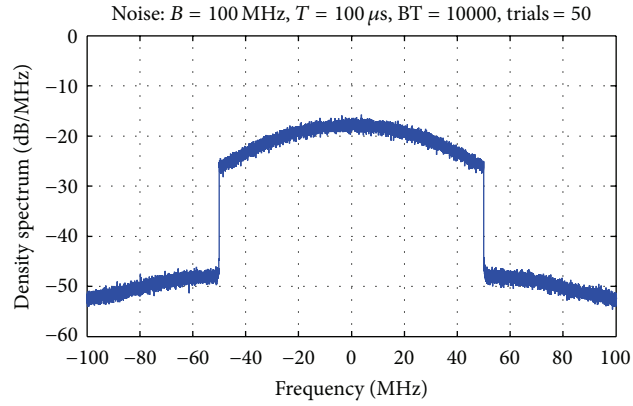

Figure 4: Mean density spectrum (obtained averaging 50 different spectra) for a pair of phase noise signals. Compression ratio 10000, considering for ZMNL a hard limiter.

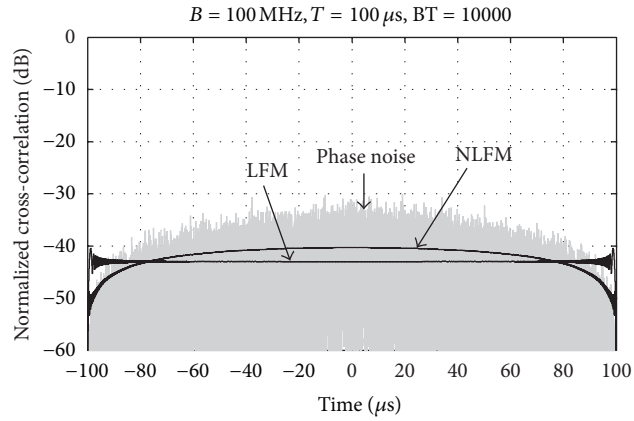

Figure 5: Normalized cross-correlation for a pair of generated noise phase signals by the iterative algorithm considering for ZMNL a hard limiter. Compression 10000.

For a real Gaussian process Van Vleck and Middleton [13] have shown that the autocorrelation coefficient (R_t with $t = t_2 - t_1$) of the output from a hard limiter is related with the input autocorrelation coefficient (here denoted r) by the well-known *arcsine law*:

$$R_t = \frac{2}{\pi} \cdot \arcsin(r). \tag{9}$$

Considering a complex Gaussian process, the correlation R_t after the hard limiter, that is, between

$$\frac{z_1^*}{|z_1|} = \frac{x_1 - jy_1}{\sqrt{x_1^2 + y_1^2}},$$
$$\frac{z_2}{|z_2|} = \frac{x_2 + jy_2}{\sqrt{x_2^2 + y_2^2}}, \tag{10}$$

is

$$R_t = E\left\{\frac{z_1^* z_2}{|z_1|\,|z_2|}\right\} = E\left\{\frac{x_1x_2 + y_1y_2 + j\left(x_1y_2 - x_2y_1\right)}{\sqrt{x_1^2 + y_1^2}\sqrt{x_2^2 + y_2^2}}\right\} = u + jv, \tag{11}$$

where $E\{\cdot\}$ is the statistical mean operator. Supposing a symmetrical power density spectrum with respect to the origin, the correlation is real and $v = 0$. Equation (11) has been evaluated, and it results in

$$R_t = b_0 r + \sum_{n=1}^{\infty} b_n \cdot r^{2n+1} \tag{12}$$

with

$$b_n = \frac{(2n-1)^2}{4n\,(n+1)} \cdot b_{n-1}, \quad b_0 = \frac{\pi}{4}, \quad n = 1, 2, 3, \ldots. \tag{13}$$

Then R_t can be expressed as a sum of odd powers of r, where the coefficients b_n are very similar to those evaluated for the *arcsine law*:

$$b_n = \frac{(2n-1)^2}{2n\,(2n+1)} \cdot b_{n-1}, \quad b_0 = \frac{2}{\pi}, \quad n = 1, 2, 3, \ldots. \tag{14}$$

Figure 6 shows R_t versus the input correlation r for real and complex Gaussian process. Inverting (12) it is possible to predistort the input autocorrelation to the hard limiter to obtain a desired R_t.

In such a way the requirements of Sections I and II can be met with no need for iterations. In fact, (a) the output autocorrelation is chosen in order to satisfy the PSLR requirement and the spectral band requirement; (b) the MEPPR requirement is satisfied by the hard limiter, and (c) the orthogonality is obtained by the randomness of the white Gaussian input sequence; and may be enhanced by proper choices of the generated output sequences.

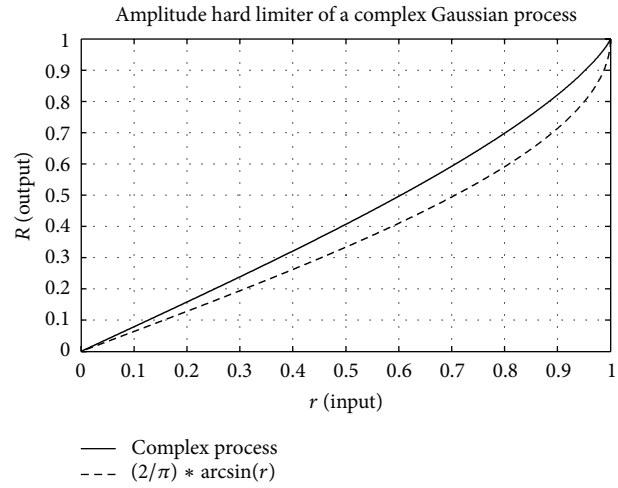

Figure 6: Output autocorrelation (R) from a hard limiter versus the input autocorrelation (r).

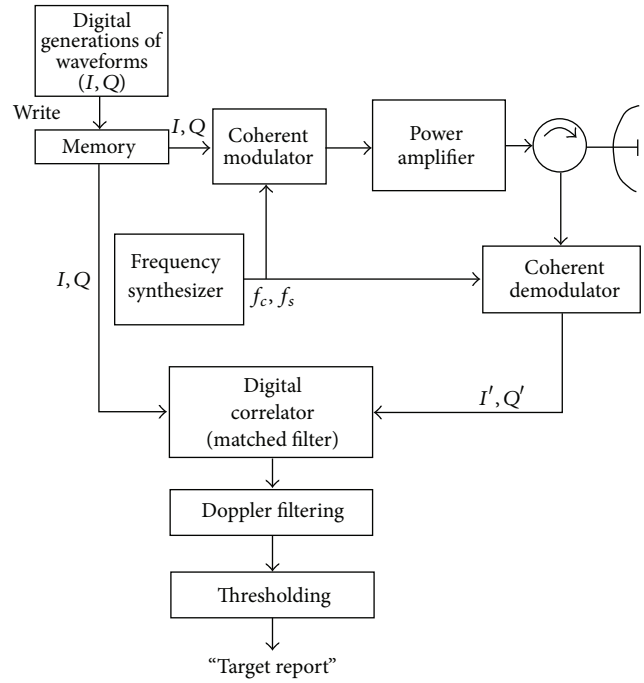

Figure 7: General architecture of solid-state, coherent, NRT-based marine radar.

4. An Architecture for Next Generation Marine Radar Based on NRT

The general architecture of a proposed, novel class of solid-state, coherent, NRT-based marine radar is shown in Figure 7, from [10]. Basically, this is a coherent radar transmitting preregistered pseudorandom signals and using a correlation receiver (or a mismatched, range-side lobe suppression receiver). In order to reduce the interference level between these marine radars exploiting the orthogonality of the transmitted waveforms, each radar must have a large number of them (order of hundreds of millions) stored in a mass memory; see Figure 7.

These waveforms are result of a generating procedure shown in Figure 1, as explained before. Thanks to this procedure, all of them have a crest factor close to the unity and their power spectral density (PSD) respects the spectral mask of the international regulations (see the appendix). For instance, let us consider a waveform, with a bandwidth of 80 MHz and a centre frequency of 9410 MHz, that is, a spectrum from 9.37 to 9.45 GHz with EIRP per MHz equal to 75 dBm. Outside the interval (the "Necessary Band") from 9.37 to 9.45 GHz its PSD will have to decay at 20 dB/dec, arriving at 35 dBm EIRP below 9.17 GHz and above 9.64 GHz. Only a part of the generated waveforms, that is, those with an acceptable PSR, is selected to be stored in the mass memory.

As in solid-state marine radar using deterministic waveforms and pulse compression, [14, 15], in the proposed marine

noise radar three sets of length will be used: a short pulse for sort range, a medium-duration waveform for medium range, and a long waveform for the maximum range of 96 NM.

5. Plans for Future Work and Conclusion

It has been recognized (see for instance [14]) that the long pulses of solid-state marine radar will create formidable problems of electromagnetic comparability to (a) traditional magnetron radar as well as to (b) other solid-state marine radars. Usage of pseudorandom, orthogonal signals will alleviate case (b) by a figure close to the value of the compression factor (the BT product). Further analysis is needed for case (a). For example, in [14] it is stated that "*characteristic pulsed interference was observed, caused by the long pulses disabling pulse cancellation logic in the magnetron radar. Such interference on established radar systems raised concerns to the system's further development …*," and "*A novel 3 pulse waveform has been designed and tested for solid-state marine radar. The waveform's spectral and range performance are excellent, … However the interference effects that such a radar might cause on existing marine radars may be catastrophic. Some of these effects could be reduced by techniques that were investigated, however no techniques were found that gave confidence to proceed with a solid state marine radar product based on this waveform.*" The damaging signals are of two types: direct (antenna to antenna) and indirect or bistatic clutter (antenna to reflecting surfaces to antenna). Summing up, further analysis, simulation, and trials are needed to establish the cost-effectiveness of solid-state S- and X-bands marine radars to be used in crowded environments as well as the electromagnetic compatibility between them and, presently more important, with legacy marine radar. The Noise Radar Technology is a promising tool to solve these problems.

Appendix

Interference in Marine Radar

Recommendations and rules for avoiding and/or mitigating the interferences related to radar systems have been issued by the International Electro Technical Committee [16] and by the International Telecommunication Union [17, 18]. Generally, distinction is made between (i) the "Necessary Band," related to the shape and modulation of the radar signal as designed to satisfy the radar performance, (ii) the "Out of Band" (OoB) domain that contains the spectral residuals of the modulation process for the radar signal, and (iii) the "spurious" domain that contains the harmonic, parasitic, intermodulation and frequency conversion effects. Methods are suggested to compute the Necessary Band from the pulse length and its rise and fall time or from the frequency span in the cases of linear or nonlinear frequency modulation (chirp signals). Roughly, the Necessary Band for a simple rectangular pulse of duration T is about $1.8/T$, and for a linear chirp of frequency deviation Δf is about $2\Delta f$. A −40 dB band is defined in the radar emission mask; in some significant cases, it results in $B_{-40} = 2.5B_{\text{Necessary}}$ and the transition between them has a 20 dB/decade roll-off.

References

[1] A. Bole, B. Dineley, and A. Wall, *Radar and ARPA Manual*, Elsevier, New York, NY, USA, 2nd edition, 2005.

[2] J. N. Briggs, *Target Detection by Marine Radar*, vol. 16 of *IEE Radar, Sonar and Navigation Series*, The Institute of Electrical Engineers, London, UK, 2004.

[3] S. Harman, "Spectral sharing with radar," in *Principles of Waveform Diversity and Design*, M. Wicks, M. Wicks, E. Mokole, S. Blunt, R. Schneible, and V. Amuso, Eds., Part 6: Spectrum Management, Chapter 35, SciTech, Edison, NJ, USA, 2010.

[4] J. T. Ascroft, "A study into techniques for improving radar spectrum utilization," Project AY, 4490, 2004, http://citeseerx.ist.psu.edu/viewdoc/download?doi=10.1.1.127.6876&rep=rep1&type=pdf.

[5] N. Levanon and E. Mozeson, *Radar Signals*, IEEE Press, Wiley-Interscience, Jhon Wiley & Sons, New York, NY, USA, 2004.

[6] J. P. Costas, "A study of detection waveforms having nearly ideal range-doppler ambiguity properties," *Proceedings of the IEEE*, vol. 72, no. 8, pp. 996–1009, 1984.

[7] W. O. Alltop, "Complex sequences with low periodic correlations," *IEEE Transactions on Information Theory*, vol. 26, no. 3, pp. 350–354, 1980.

[8] P. van Genderen, O. A. Krasnov, Z. Wanga, and R. F. Tigrek, "Some OFDM waveforms for a fully polarimetric weather radar," *International Journal of Microwave and Wireless Technologies*, vol. 4, no. 02, pp. 163–169, 2012.

[9] S. R. J. Axelsson, "Noise radar using random phase and frequency modulation," *IEEE Transactions on Geoscience and Remote Sensing*, vol. 42, no. 11, pp. 2370–2384, 2004.

[10] G. Galati, "Radar coerente," Patent Application N. RM, 2013 A000290, Roma, Italy, 2013.

[11] A. S. Mudukutore, V. Chandrasekar, and R. Jeffrey Keeler, "Pulse compression for weather radars," *IEEE Transactions on Geoscience and Remote Sensing*, vol. 36, no. 1, pp. 125–142, 1998.

[12] H. Urkowitz and N. J. Bucci, "Doppler-Tolerant range sidelobe suppression for meteorological radar," *IEEE Transactions on Geoscience Electronics*, vol. 4, pp. 206–208.

[13] J. H. Van Vleck and D. Middleton, "The cpectrum of clipped noise," *Proceeding of the IEEE*, vol. 54, pp. 2–19, 1966.

[14] S. Harman, "The performance of a novel Three-Pulse radar waveform for marine radar systems," in *Proceedings of the 5th European Radar Conference (EuRAD '08)*, pp. 160–163, Amsterdam, The Netherlands, October 2008.

[15] A. Nelander and Z. Tóth-Pál, "Modular system design for a new S-band marine radar," in *Proceedings of the International Radar Conference Surveillance for a Safer World (RADAR '09)*, Bordeaux, France, December 2009.

[16] International Electro Technical Commission, "Shipborne radar," IEC, 62388 Ed. 1. 0, 2007.

[17] ITU International Telecommunication Union, "Unwanted emission in the out of band domain," Recommendation ITU-R SM, 1541, 2001.

[18] ITU International Telecommunication Union, "Efficient use of the radio spectrum by radar stations," Recommendation ITU-R M, 1327-1, 1998–2003.

Hindawi Publishing Corporation
Journal of Electrical and Computer Engineering
Volume 2013, Article ID 325746, 7 pages
http://dx.doi.org/10.1155/2013/325746

Research Article

Tunable Reflectarray Cell for Wide Angle Beam-Steering Radar Applications

F. Venneri, S. Costanzo, and G. Di Massa

Dipartimento di Ingegneria Informatica, Modellistica, Elettronica e Sistemistica, Università della Calabria, 87036 Rende (CS), Italy

Correspondence should be addressed to S. Costanzo; costanzo@deis.unical.it

Received 10 May 2013; Accepted 1 July 2013

Academic Editor: Alvaro Rocha

Copyright © 2013 F. Venneri et al. This is an open access article distributed under the Creative Commons Attribution License, which permits unrestricted use, distribution, and reproduction in any medium, provided the original work is properly cited.

An electronically tunable reflectarray element is proposed in this work to design beam-steering antennas useful for radar applications. A reduced size reflectarray unit cell is properly synthesized in order to extend the antenna beam scanning capabilities within a wider angular region. The radiating structure is accurately optimized to provide a full phase tuning range by adopting a single varactor load as phase shifter element. A 0.46λ-reflectarray cell is designed at the frequency of 11.5 GHz, obtaining a phase agility of about 330°. The cell is successfully adopted for the design of a 21×21 reconfigurable reflectarray. The antenna is numerically tested for different configurations of the varactors capacitance values, and good beam-steering performances are demonstrated within a wide angular range.

1. Introduction

Modern radar systems usually adopt phased array antennas as transmission/reception modules. Phased arrays integrate the actual radiating structures, consisting of an array of elementary antennas, with phase shifter components, tunable power amplifiers, and switches [1]. These additional devices allow to control the input signal of each radiating element, thus offering the capabilities to electronically steer the radiated main beam. Phased arrays offer many advantages with respect to mechanically scanned antennas, such as low profile, agile beams, and scalability. Furthermore, electronically scanned antennas offer increased data rates, instantaneous positioning of the radar beam, avoiding also mechanical vibrations, and errors associated with mechanically scanned systems.

An attractive alternative to traditional phased array antennas is offered by the reflectarray antenna concept [2]. As a matter of fact, reflectarrays may be specifically designed also for applications requiring pattern reconfigurability or beam-scanning capabilities. Reconfigurable reflectarrays may offer many advantages over conventional phased arrays, such as reduced costs and volume, a simpler architecture due to the absence of complicated beam-forming networks, and increased efficiencies due to the adoption of spatial feeding. They consist of an array of microstrip elements illuminated by a feed antenna (Figure 1(a)). Each radiator is properly designed to compensate for the phase delay in the path coming from the feed and to introduce a phase contribution able to create a total reradiated field with some desired features, such as prescribed beam directions and/or shapes.

Many different reflectarray configurations have been proposed in the literature [2] also for mm waves applications [3], and recently, many efforts have been spent in the design of reconfigurable reflectarray elements, which are usually based on the use of tunable components and/or materials, such as MEMs, varactor diodes, and liquid crystal substrates [4–6].

Recently, the authors have proposed a novel tunable reflectarray element based on the use of an aperture-coupled patch electronically driven by a single varactor diode [7–10]. The radiating patch is coupled to a microstrip line printed onto a different substrate and loaded by a varactor (Figure 1(b)). By changing the bias voltage across the diode, the phase response of each element can be dynamically modified. A detailed description of the proposed phase control mechanism is reported in [10].

The phase tuning capabilities of the proposed reflectarray configuration have been already demonstrated in [7], while in [8–10] a reflectarray prototype composed by 3×15 elements,

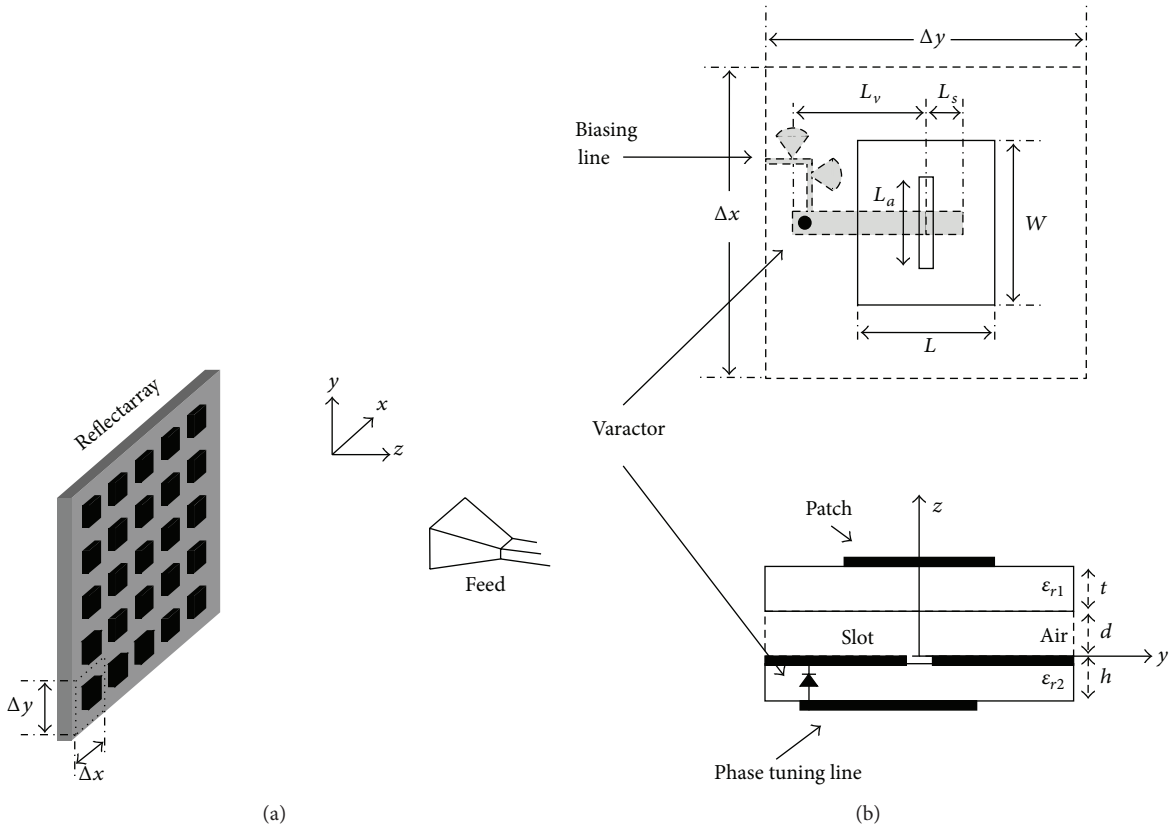

Figure 1: (a) Reflectarray antenna and (b) aperture-coupled reconfigurable reflectarray cell.

with a unit cell with equal to $\Delta x \times \Delta y = 0.7\lambda_0 \times 0.7\lambda_0$, has been successful designed at the frequency of 11.5 GHz. The synthesis approach described in [11, 12] has been adopted in order to compute the desired voltages distributions across the diodes. The antenna has been tested into the Microwave Laboratory at the University of Calabria, equipped with both near-field [13, 14] and far-field facilities. Various measurements of its radiation pattern for different configurations of the varactors biasing voltages have been performed, thus demonstrating in [10] the reconfiguration capabilities of the fabricated reflectarray prototype. In particular, good beam-steering performances have been obtained within an angular region going from -25° up to 25°. In this work, the reflectarray cell proposed in [7–10] is properly redesigned in order to enlarge the allowable beam scanning area, so to give the opportunity for designing wide-angle beam-steering antennas, suitable for radar applications. Pointing out that a large scan angle requires a close element spacing, less than or equal to half wavelength at the operating frequency [15], a reflectarray unit cell with a reduced size equal to $0.46\lambda_0 \times 0.46\lambda_0$ ($f_0 = 11.5$ GHz) is proposed. In order to accommodate the phasing circuitries inside the reduced available area embedded in the unit cell, the antenna stratification layers are properly modified by choosing a higher permittivity for the phasing line substrate. According to the considerations reported in [10], the varactor loaded line is accurately resized in order to maximize the antenna phase agility. A phase tuning range of about 330° is numerically demonstrated, by varying the capacitance of the varactor diode within the values ranging from 0.2 pF up to 2 pF.

The designed cell is adopted to synthesize a 21×21 reflectarray antenna able to steer the main beam up to 65°, as assessed numerically.

2. Design of a Reconfigurable Reflectarray Element Embedded into a Unit Cell with Reduced Size

2.1. Performance Limitations of Beam-Steering Arrays. The angular displacement of an electronically scanned radar beam is practically limited by two main factors, namely, the element pattern and the array elements spacing. As a matter of fact, the radiation pattern of an array of identical radiators is given by the product of the array factor and the element pattern. If the single array radiator is isotropic, that is, the array elements radiate an electric field quite uniform along those directions belonging to the scanning plane, only the array factor will affect the total radiation pattern.

However, practical array element patterns are not omnidirectional, showing an amplitude that decays when moving away from the broadside direction. In these cases, the single element will significantly reduce the amplitude of the scanned beam, except in the zone where it is nearly isotropic [15].

The second limitation, namely, the array elements spacing, is more relevant. As a matter of fact, it is well known that a large scan angle requires a close element spacing, in order to avoid grating lobes appearance. The maximum scan angle, that a linear phased array can achieve, may be derived from the well-known relation [15]:

$$\theta_{s\,\max} = \sin^{-1}\left(\frac{\lambda}{d} - 1\right), \quad (1)$$

where $\theta_{s\,\max}$ is the maximum scan angle from broadside direction, d is the spacing between two adjacent elements, and λ is the operating wavelength. Equation (1) is derived from the array factor expression of a linear array placed along the x-axis or y-axis, and its validity can be extended to the principal cuts of a planar array placed in the x-y plane [15]. If the array scan angle exceeds the value imposed by (1), grating lobes will appear along other directions. This last behavior is clearly illustrated in Figure 2, which shows the scanning limitations of a 0.7λ-spaced array. In this case, if the scan angle θ_s is greater than $\theta_{s\,\max} = 25^\circ$, as given by (1), the array factor will show a grating lobe having the same amplitude of the scanned main beam (Figure 2(c)).

Equation (1) also states that half wavelength spaced arrays will have a complete theoretical scan range of $\pm 90^\circ$, as illustrated in Figure 3.

The maximum scan angle achievable by a phased array is also a function of the array length and the desired half-power beam width [15]; however, the condition imposed by (1) is necessary for the design of an array with prescribed beam-steering capabilities.

2.2. Reflectarray Element Design. In order to improve the scanning capabilities of the reconfigurable reflectarray configuration proposed in [7–10], the single reflectarray element is properly redesigned by reducing the unit cell size. In fact, as discussed in the previous paragraph, a closer array elements spacing assures a larger scanning region.

The unit cell dimension is fixed to a value less than half wavelength at the operating frequency $f_0 = 11.5$ GHz. In particular, the array grid size $\Delta x \times \Delta y$ is set to $0.46\lambda_0 \times 0.46\lambda_0$. Furthermore, as demonstrated in [16–18], a reduced unit cell size allows to improve the bandwidth performances of reflectarray antennas. This last aspect is not considered in the present paper, but the relative analysis will be performed in a future work.

In order to allow the accommodation of the tuning circuitries in the smaller area embedded into the unit cell, the phasing line substrate adopted in [7] is properly substituted with a dielectric layer with $\varepsilon_r = 6$ and thickness $h = 0.762$ mm (see Table 1). As a matter of fact, the use of a substrate with a higher permittivity allows to reduce the wavelength inside the printed lines, thus providing the possibility to design a shorter phase tuning line. As reported in Table 1, the other layers composing the antenna stratification are equal to those adopted in [7].

The reflectarray unit cell is synthesized through a full-wave simulation code (Ansoft Designer) based on the method of moments. The infinite array approach is adopted in order to take into account the mutual coupling effects, relevant for the assigned reduced interelement spacing.

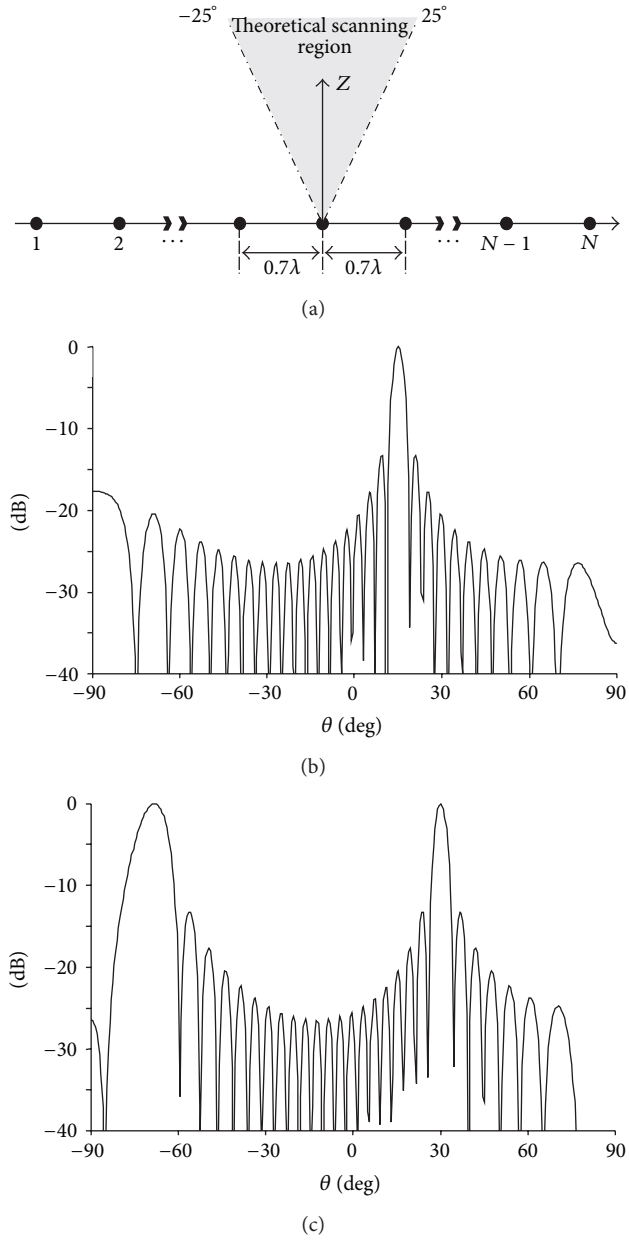

Figure 2: Scanning performances of an N-elements linear array with spacing equal to 0.7λ: (a) allowable scanning area given by relation (1); (b) array factor for a scan angle $\theta_s = 15^\circ$ and $N = 21$; (c) array factor for a scan angle $\theta_s = 30^\circ$ and $N = 21$.

The radiating structure design is performed by a proper tuning of patch and slot sizes, with the aim to satisfy the resonance condition as well as the matching between the patch and the phasing line, at the operating frequency of 11.5 GHz.

A varactor diode, with a tunable capacitance C_v ranging from 0.2 pF to 2 pF, is integrated to the microstrip line in order to obtain the required reconfiguration capabilities. The varactor diode is modeled with the equivalent circuit

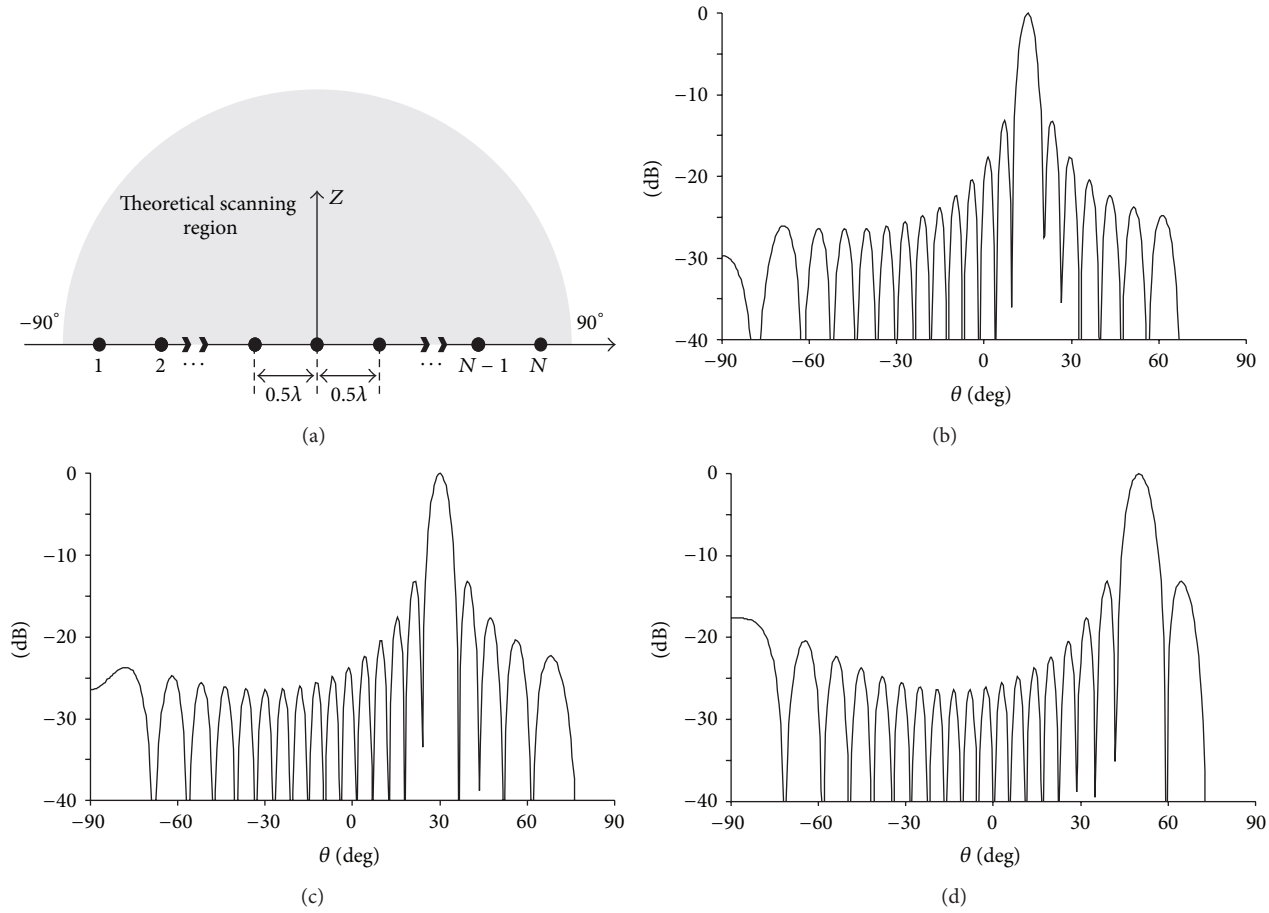

Figure 3: Scanning performances of an N-elements linear array with spacing equal to 0.5λ: (a) allowable scanning area given by relation (1); (b) array factor for a scan angle $\theta_s = 15^\circ$ and $N = 21$; (c) array factor for a scan angle $\theta_s = 30^\circ$ and $N = 21$; (d) array factor for a scan angle $\theta_s = 50^\circ$ and $N = 21$.

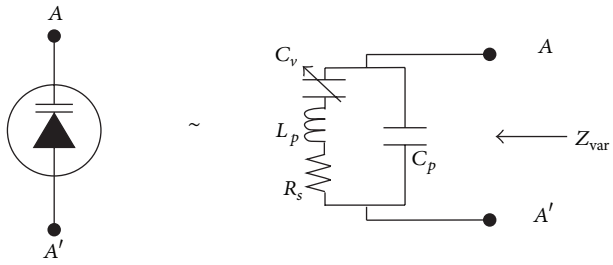

Figure 4: Equivalent circuit model of a varactor diode.

illustrated in Figure 4, which takes into account the package parasitic effects (L_p, C_p) and the diode losses (R_s). The varactor lumped parameters are fixed to the following values, derived by the Microsemi MV31011-89 diode datasheet: $L_p = 0.2$ nH, $C_p = 0.15$ pF, and $R_s = 1.36\ \Omega$.

As described in [10], the two line sections L_v and L_s (see Figure 1(b)) are optimized in order to maximize the phase agility of the element for the assigned varactor capacitance range. At this purpose, a parametric analysis of the reflectarray element is performed with respect to the lengths L_v and L_s, by assuming a normally incident plane wave. Figure 5 shows the reflection phase curves versus the varactor capacitance, computed for different values of the line length.

It can be observed that by increasing L_s, for a fixed value of L_v (Figure 5(a)), a higher phase tuning range is obtained. As accurately demonstrated in [10], this last result is due to the introduction of a proper inductive effect, which is directly related to the stub length. As a proof of this concept, the input impedance $Z_{t'}$ of the designed aperture coupled patch, evaluated at the slot center, is reported under Figure 6, for different values of the stub length L_s ranging from 1.05 mm (the matched case) up to 5.2 mm. It can be observed that for an increased input reactance a wider phase tuning range is achieved (Figure 5(a)). In particular, a phase tuning of about 330° is obtained for $L_s = 5.2$ mm. On the other hand the length L_v is tuned in order to match the maximum phase variation with the available varactor capacitance range [10]. As a matter of fact, Figure 5(b) shows that for any fixed value of L_s, the section L_v can be chosen to shift the phase curve within the capacitance range with the aim to increase the allowable phase tuning range, so obtaining a phasing line acting as a 360° phase shifter.

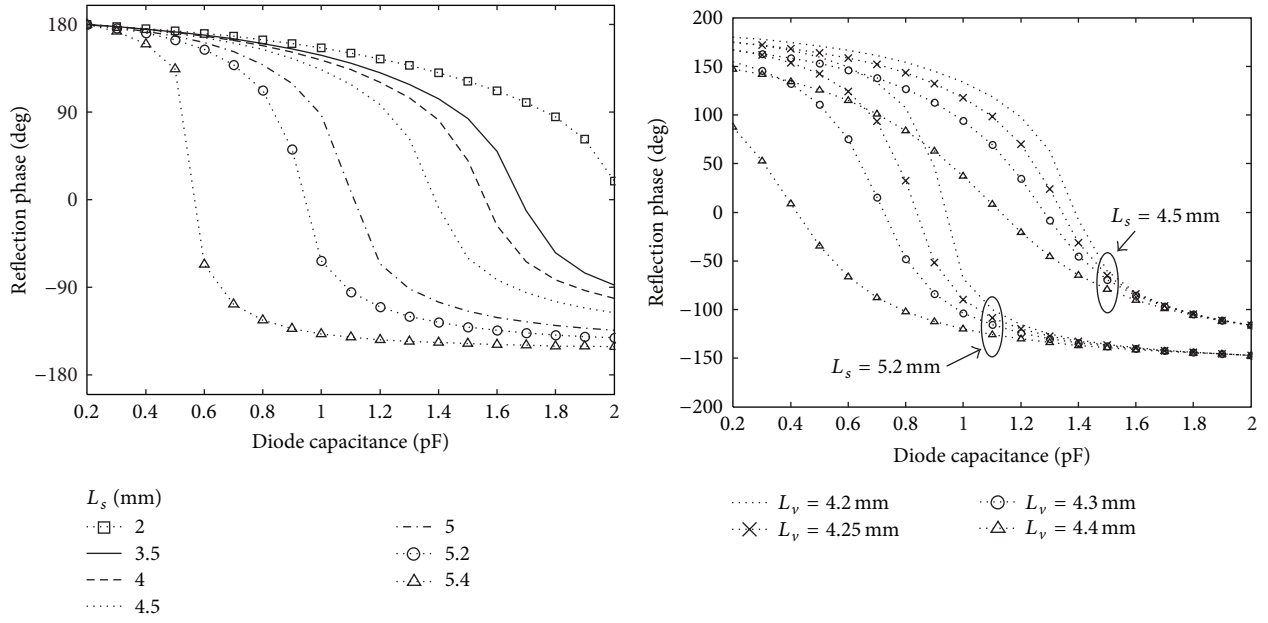

Figure 5: Phase curves versus diode capacitance for different line lengths: (a) $L_v = 4.2$ mm and L_s ranging from 2 mm up to 5.4 mm; (b) L_v ranging from 4.2 mm up to 4.4 mm for some fixed values of L_s.

Table 1: Element stratification.

Layer	Element designed in [7] $\Delta x \times \Delta y = 0.7\lambda_0 \times 0.7\lambda_0$		Element designed in this work $\Delta x \times \Delta y = 0.46\lambda_0 \times 0.46\lambda_0$	
	Material	Thickness	Material	Thickness
Patch	Copper	35 μm	Copper	35 μm
Antenna substrate	$\varepsilon_{r1} = 2.33$	$t = 0.762$ mm	$\varepsilon_{r1} = 2.33$	$t = 0.762$ mm
	Air	$d = 0.762$ mm	Air	$d = 0.762$ mm
Ground plane with slot	Copper	35 μm	Copper	35 μm
Phasing line substrate	$\varepsilon_{r2} = 2.33$	$h = 0.762$ mm	$\varepsilon_{r2} = 6$	$h = 0.762$ mm
Phasing line	Copper	35 μm	Copper	35 μm

The dimensions of the optimized reflectarray element are reported in Table 2.

Furthermore, the same table shows that the designed tuning line is shorter than the line controlling the reflectarray element described in [7]. In particular, a 35% length reduction is obtained, thus allowing the allocation of the tuning circuitries inside the smaller $0.46\lambda_0 \times 0.46\lambda_0$ cell (12 mm × 12 mm at 11.5 GHz).

The simulated element pattern of the designed unit cell is reported in Figure 7. The depicted diagrams refer to the reflectarray element with a phasing line having dimensions $L_v = 4.2$ mm and $L_s = 5.2$ mm. The radiation patterns computed in the two principal planes show a nearly isotropic behavior within the range from −45° up to 45°, as in the case of a typical $\cos(\theta)$ source.

In conclusion, the proposed unit cell could be suitable for the design of reflectarray antennas with improved beam-steering capabilities, as the main beam could be scanned within a quite large angular region ranging from −45° up to 45°, without occurring in the grating lobes phenomena. Furthermore, within this scanning range the main lobe will have at most a 3 dB amplitude reduction, as demonstrated by the simulated element pattern (Figure 7).

3. Design of a Beam-Steering Reflectarray

In order to prove the effectiveness of the proposed cell, a 21 × 21 reflectarray is designed at the frequency of 11.5 GHz. The array is illuminated by a broadside feed placed at a distance of 34 cm. A synthesis algorithm [11] is adopted in order to compute the varactor capacitance values which allow to steer the radiated main beam from 0° up to 65° in the H-plane. The computed radiation patterns depicted in Figure 8 show the validity of the proposed approach, as the main beam is successfully moved along the desired directions. As expected by the array theory, Figure 8 shows that the main beam amplitude decreases when moving away from the broadside direction. In particular, it can be observed that

Table 2: Element dimension.

	Element designed in [7] $\Delta x \times \Delta y = 0.7\lambda_0 \times 0.7\lambda_0$	Element designed in this work $\Delta x \times \Delta y = 0.46\lambda_0 \times 0.46\lambda_0$
Patch size	$W \times L = 8.2\,\text{mm} \times 9.3\,\text{mm}$	$W \times L = 7.75\,\text{mm} \times 7.75\,\text{mm}$
Slot size	$L_a \times W_a = 5.8\,\text{mm} \times 0.6\,\text{mm}$	$L_a \times W_a = 5.7\,\text{mm} \times 0.5\,\text{mm}$
Phase tuning line	$L_v = 6.5\,\text{mm} + L_s = 7.8\,\text{mm}$, $W_s = 3.07\,\text{mm}$	$L_v = 4.2\,\text{mm} + L_s = 5.2\,\text{mm}$ $W_s = 1.6\,\text{mm}$

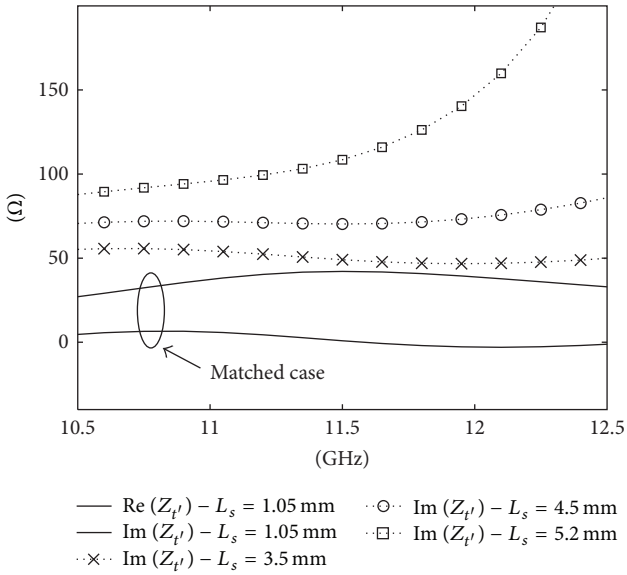

Figure 6: Input impedance $Z_{t'}$ for different stub lengths.

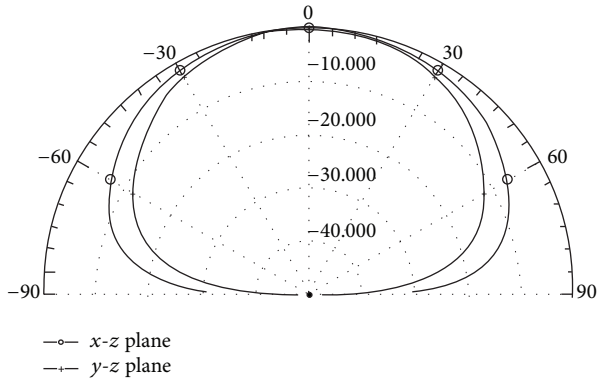

Figure 7: Element pattern of designed reflectarray element.

the scan loss increases away from broadside by following the cosine behavior of the element pattern. Thus, an acceptable 3 dB scan loss is obtained when the main lobe is pointed along the direction $\theta_s = 45^\circ$, while for $\theta_s = 65^\circ$ a greater scan loss of about 7 dB is observed. Furthermore, Figure 8 shows a broader main lobe for greater scan angles. Despite limitations imposed by the array theory (i.e., scan losses and main lobe broadening), the obtained numerical results demonstrate wide angle beam-steering capabilities of the designed antenna, without occurring in grating lobes appearance.

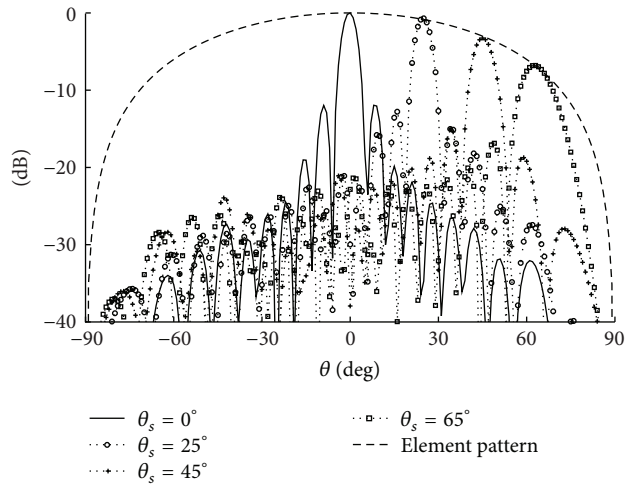

Figure 8: Computed radiation patterns for different configurations of the varactors capacitance values.

4. Conclusion

The reflectarray concept has been applied in this work to design beam-steering antennas suitable for radar applications. A reflectarray unit cell based on the use of a single varactor diode has been proposed and optimized to provide wide angle steering capabilities. At this purpose, the antenna has been properly designed by reducing the unit cell size, in order to achieve a large angular scanning. As a specific numerical example, a varactor loaded reflectarray element, embedded into a $0.46\lambda_0 \times 0.46\lambda_0$ cell at $f_0 = 11.5\,\text{GHz}$, has been synthesized, obtaining a full phase tuning range of about 330°. The designed unit cell has been adopted to design a 21 × 21 reconfigurable reflectarray. The antenna has been numerically tested showing good beam-steering performances within a wide angular range from −45° up to 45°.

Acknowledgment

This work has been carried out under the framework of PON 01_01503 National Italian Project "Landslides Early Warning," financed by the Italian Ministry of University and Research.

References

[1] A. J. Fenn, D. H. Temme, W. P. Delaney, and W. E. Courtney, "The development of phased-array radar technology," *Lincoln Laboratory Journal*, vol. 12, pp. 321–340, 2000.

[2] J. Huang and J. Encinar, *Reflectarray Antennas*, Wiley-IEEE Press, 2008.

[3] S. Costanzo, F. Venneri, A. Borgia, I. Venneri, and G. Di Massa, "60 GHz microstrip reflectarray on a benzocyclobutene dielectric substrate," *IET Science, Measurement and Technology*, vol. 5, no. 4, pp. 134–139, 2011.

[4] R. Sorrentino, R. V. Gatti, L. Marcaccioli, and B. Mencagli, "Electronic steerable mems antennas," in *Proceedings of the 1st European Conference on Antennas and Propagation (EuCAP '06)*, pp. 1–8, Nice, France, November 2006.

[5] S. V. Hum, M. Okoniewski, and R. J. Davies, "Realizing an electronically tunable reflectarray using varactor diode-tuned elements," *IEEE Microwave and Wireless Components Letters*, vol. 15, no. 6, pp. 422–424, 2005.

[6] M. Riel and J. J. Laurin, "Design of an electronically beam scanning reflectarray using aperture-coupled elements," *IEEE Transactions on Antennas and Propagation*, vol. 55, no. 5, pp. 1260–1266, 2007.

[7] F. Venneri, S. Costanzo, and G. Di Massa, "Reconfigurable aperture-coupled reflectarray element tuned by single varactor diode," *Electronics Letters*, vol. 48, no. 2, pp. 68–69, 2012.

[8] F. Venneri, S. Costanzo, G. Di Massa, A. Borgia, P. Corsonello, and M. Salzano, "Design of a reconfigurable reflectarray based on a varactor tuned element," in *Proceedings of the 6th European Conference on Antennas and Propagation (EUCAP '12)*, pp. 2628–2631, Prague, Czech Republic, March 2012.

[9] F. Venneri, S. Costanzo, G. Di Massa et al., "Beam-scanning reflectarray based on a single varactor-tuned element," *International Journal of Antennas and Propagation*, vol. 2012, Article ID 290285, 5 pages, 2012.

[10] F. Venneri, S. Costanzo, and G. Di Massa, "Design and validation of a reconfigurable single varactor-tuned reflectarray," *IEEE Transactions on Antennas and Propagation*, vol. 61, no. 2, pp. 635–645, 2013.

[11] F. Venneri, S. Costanzo, G. Di Massa, and G. Angiulli, "An improved synthesis algorithm for reflectarrays design," *IEEE Antennas and Wireless Propagation Letters*, vol. 4, no. 1, pp. 258–261, 2005.

[12] S. Costanzo, F. Venneri, G. Di Massa, and G. Angiulli, "Synthesis of microstrip reflectarrays as planar scatterers for SAR interferometry," *Electronics Letters*, vol. 39, no. 3, pp. 266–267, 2003.

[13] S. Costanzo and G. Di Massa, "Direct far-field computation from bi-polar near-field samples," *Journal of Electromagnetic Waves and Applications*, vol. 20, no. 9, pp. 1137–1148, 2006.

[14] S. Costanzo and G. Di Massa, "Near-field to far-field transformation with planar spiral scanning," *Progress in Electromagnetics Research*, vol. 73, pp. 49–59, 2007.

[15] C. A. Balanis, *Antenna Theory: Analysis and Design*, John Wiley & Sons, New York, NY, USA, 2nd edition, 1997.

[16] S. Costanzo, F. Venneri, and G. Di Massa, "Bandwidth enhancement of aperture-coupled reflectarrays," *Electronics Letters*, vol. 42, no. 23, pp. 1320–1321, 2006.

[17] F. Venneri, S. Costanzo, G. Di Massa, and G. Amendola, "Aperture-coupled reflectarrays with enhanced bandwidth features," *Journal of Electromagnetic Waves and Applications*, vol. 22, no. 11-12, pp. 1527–1537, 2008.

[18] F. Venneri, S. Costanzo, and G. Di Massa, "Bandwidth behavior of closely spaced aperture-coupled reflectarrays," *International Journal of Antennas and Propagation*, vol. 2012, Article ID 846017, 11 pages, 2012.

Hindawi Publishing Corporation
Journal of Electrical and Computer Engineering
Volume 2013, Article ID 245867, 12 pages
http://dx.doi.org/10.1155/2013/245867

Research Article

Bayesian Compressive Sensing as Applied to Directions-of-Arrival Estimation in Planar Arrays

Matteo Carlin, Paolo Rocca, Giacomo Oliveri, and Andrea Massa

ELEDIA Research Center @ DISI, University of Trento, Via Sommarive 5, 38123 Trento, Italy

Correspondence should be addressed to Andrea Massa; andrea.massa@ing.unitn.it

Received 19 May 2013; Accepted 19 June 2013

Academic Editor: Sandra Costanzo

Copyright © 2013 Matteo Carlin et al. This is an open access article distributed under the Creative Commons Attribution License, which permits unrestricted use, distribution, and reproduction in any medium, provided the original work is properly cited.

The Bayesian compressive sensing (BCS) is applied to estimate the directions of arrival (DoAs) of narrow-band electromagnetic signals impinging on planar antenna arrangements. Starting from the measurement of the voltages induced at the output of the array elements, the performance of the BCS-based approach is evaluated when data are acquired at a single time instant and at consecutive time instants, respectively. Different signal configurations, planar array geometries, and noise conditions are taken into account, as well.

1. Introduction

In the last few years, we assisted to an extraordinary and still growing development and use of compressive sensing (CS)-based methods [1] in a wide number of applicative contexts such as communications [2], biomedicine [3], radar [4], and microwave imaging [5, 6]. CS has proven to be a very effective resolution tool when the relationship between the problem data and the unknowns is linear, and these latter are sparse (or they can be sparsified) with respect to some representation bases.

In this paper, a probabilistic version of the CS, namely, the Bayesian compressive sensing (BCS) [7], is used for estimating the directions of arrival (DoAs) of electromagnetic signals impinging on an array of sensors in a planar arrangement. Since the DoAs of the incoming signals are few with respect to the whole set of angular directions, they can be modeled as a sparse vector. Accordingly, the estimation problem at hand can be reformulated as the retrieval of such a sparse signal vector whose nonnull entries are related to the unknown angular directions of the signals.

Compared to the state-of-the-art estimation methods (e.g., the multiple signal classification (MUSIC) [8], the signal parameters via rotational invariance technique (ESPRIT) [9], the maximum likelihood (ML) DoAs estimators [10], and the class of techniques based on learning-by-examples (LBE) strategies [11–13]), CS-based approaches have shown several interesting advantages. Likewise LBE-based methods, the computationally expensive calculation of the covariance matrix is not necessary since the voltages measured at the output of the array elements can be directly processed. CS-based methods turn out to be fast and also work with single time-instant (snapshot) data acquisitions. Moreover, unlike MUSIC and ESPRIT that require the incoherence of the impinging signals and a set of measurements larger than the number of signals, careful DoA estimates can be yielded also when the number of arriving signals is greater than the array sensors as well as in the presence of highly correlated sources.

Within the class of CS-based approaches, deterministic strategies recover the signal vector by enforcing the sparsity constraints through the l_1-norm, while the l_2-norm is adopted to quantify the mismatch between measured and estimated data as shown in [14] for the localization of narrowband sources when using a circular array. Hybrid l_1-norm and l_2-norm formulations have been considered [15, 16], as well. Other CS-based methods have been proposed [17–19] also dealing with the DoAs estimation of correlated sources [20]. Unfortunately, common formulations of the CS (i.e., based on deterministic strategies) require a minimum number of measurements equal to twice the number of impinging signals to satisfy the necessary condition for the well posedness of the problem (i.e., the restricted isometry property of the sapling matrix). To overcome such an issue,

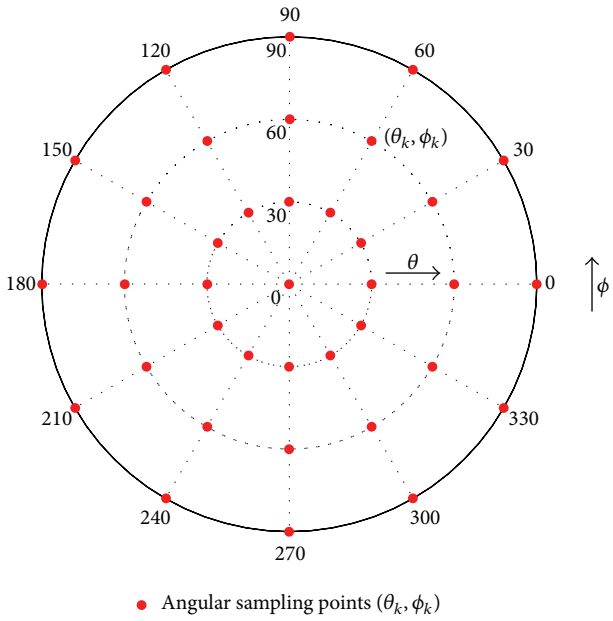

Figure 1: Sketch of the discretized observation domain for CS-based DoAs estimations.

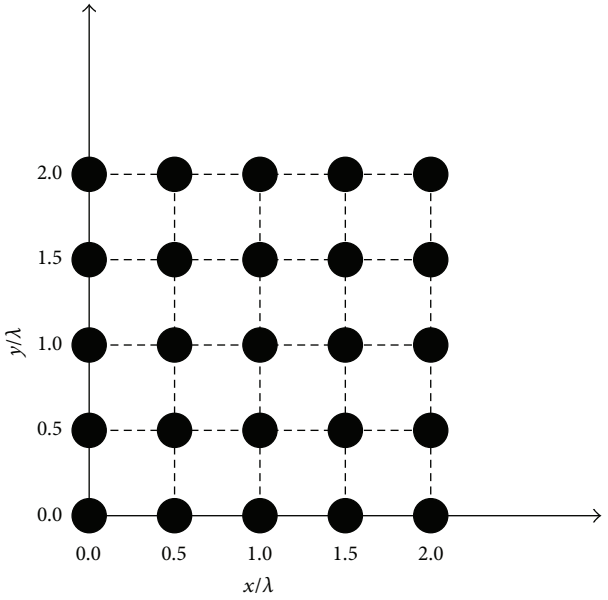

Figure 2: Geometry of the receiving fully populated array ($N = 25$).

probabilistic CS-based approaches have been taken into account [21–23] as the one considered in this work.

The outline of the paper is as follows. The DoAs estimation problem, its sparse reformulation, and the BCS-based DoAs estimation approach are presented in Section 2. A selected set of representative numerical results is reported in Section 3 to discuss, in a comparative fashion, the performance of the single and multiple snapshot implementations of the two-dimensional extension of the BCS method [24] for different array architectures. Eventually, some conclusions are drawn (Section 4).

Table 1: Fully populated array—($N = 25$; $d_x = d_y = 0.5\lambda$; $I \in [2 : 8]$; SNR = 10 dB; $C = 50$)—actual DoAs of the impinging signals.

I	$\{\Psi_i = (\theta_i, \phi_i), i = 1, \ldots, I\}$
2	$\{(25, 60);\ (60, 140)\}$
4	$\{(25, 60);\ (60, 140);\ (70, 210);\ (60, 300)\}$
8	$\{(25, 60);\ (60, 140);\ (70, 210);\ (60, 300);\ (40, 210);\ (80, 45);$ $(15, 5);\ (30, 350)\}$

2. Mathematical Formulation

Let us consider a planar antenna array made of N isotropic sensors located on the $x - y$ plane. An unknown set of I signals $\mathbf{s}_i(\mathbf{r}, t) = \alpha_i(t) e^{j(2\pi f_0 t + \mathbf{k}_i \cdot \mathbf{r})}$, $i = 1, \ldots, I$, is supposed to impinge on the array from the unknown directions $\Psi_i = (\theta_i, \phi_i)$, $i = 1, \ldots, I$, being $0^\circ \leq \theta_i \leq 90^\circ$ and $0^\circ \leq \phi_i \leq 360^\circ$. Such signals are modeled as narrowband electromagnetic plane waves (i.e., $\alpha_i(t) \simeq \alpha_i$, $i = 1, \ldots, I$) at the carrier frequency f_0, with $\mathbf{k}_i$ ($i = 1, \ldots, I$) being the ith wave vector having amplitude $k = |\mathbf{k}_i| = 2\pi/\lambda$, for all $i = 1, \ldots, I$, where λ is the free space wavelength.

By modelling the background noise as an additive Gaussian process with zero mean and variance σ^2, the phasor voltage measured at the nth element is equal to

$$v_n(\tau) = \sum_{i=1}^{I} v_{i,n}(\tau) + \eta_n(\tau), \tag{1}$$

where τ is the measurement time-instant/snapshot and $\eta_n(\tau)$ is the noise sample at the same instant. Moreover,

$$v_{i,n}(\tau) = \alpha_i(\tau)\, e^{j(2\pi/\lambda)(x_n \sin\theta_i \cos\phi_i + y_n \sin\theta_i \sin\phi_i)} \tag{2}$$

is the open circuit voltage induced by the ith impinging wave at the nth planar array element located in the position $\mathbf{r}_n = (x_n, y_n)$.

The relationship between the measured data (i.e., $v_n(\tau)$, $n = 1, \ldots, N$, $\tau = 1, \ldots, T$) and the unknown DoAs [i.e., $\Psi_i = (\theta_i, \phi_i)$, $i = 1, \ldots, I$] can be then represented in a compact matrix form as follows:

$$\boldsymbol{v}(\tau) = \mathbf{H}(\boldsymbol{\Psi})\, \mathbf{s}(\tau) + \boldsymbol{\eta}(\tau), \qquad \tau = 1, \ldots, T, \tag{3}$$

where $\boldsymbol{v}(\tau) = [v_1(\tau), v_2(\tau), \ldots, v_N(\tau)]^*$ is the complex measurement vector, with $*$ denoting the transpose operation, and $\mathbf{H}(\boldsymbol{\Psi}) = [\mathbf{h}(\Psi_1), \mathbf{h}(\Psi_2), \ldots, \mathbf{h}(\Psi_I)]$ is the steering vector matrix where $\mathbf{h}(\Psi_i) = [h_{i,1}, h_{i,2}, \ldots, h_{i,N}]^*$ being $h_{i,n} = e^{j(2\pi/\lambda)(x_n \sin\theta_i \cos\phi_i + y_n \sin\theta_i \sin\phi_i)}$. Moreover, $\mathbf{s}(\tau) = [\alpha_1(\tau), \alpha_2(\tau), \ldots, \alpha_I(\tau)]^*$ is the signal vector, and $\boldsymbol{\eta}(\tau) = [\eta_1(\tau), \eta_2(\tau), \ldots, \eta_N(\tau)]^*$ is the noise vector.

It is simple to observe that the solution of (3) is neither linear nor sparse with respect to the problem unknowns $\Psi_i = (\theta_i, \phi_i)$, $i = 1, \ldots, I$, while it is linear versus $\mathbf{s}(\tau)$, for all τ. In order to apply the BCS to the DoAs estimation in planar arrays, the method in [24] for linear arrays has been exploited and here suitably customized to the dimensionality (2D) at hand.

To reformulate the original problem as a sparse one, the observation domain composed by all angular directions $0^\circ \leq$

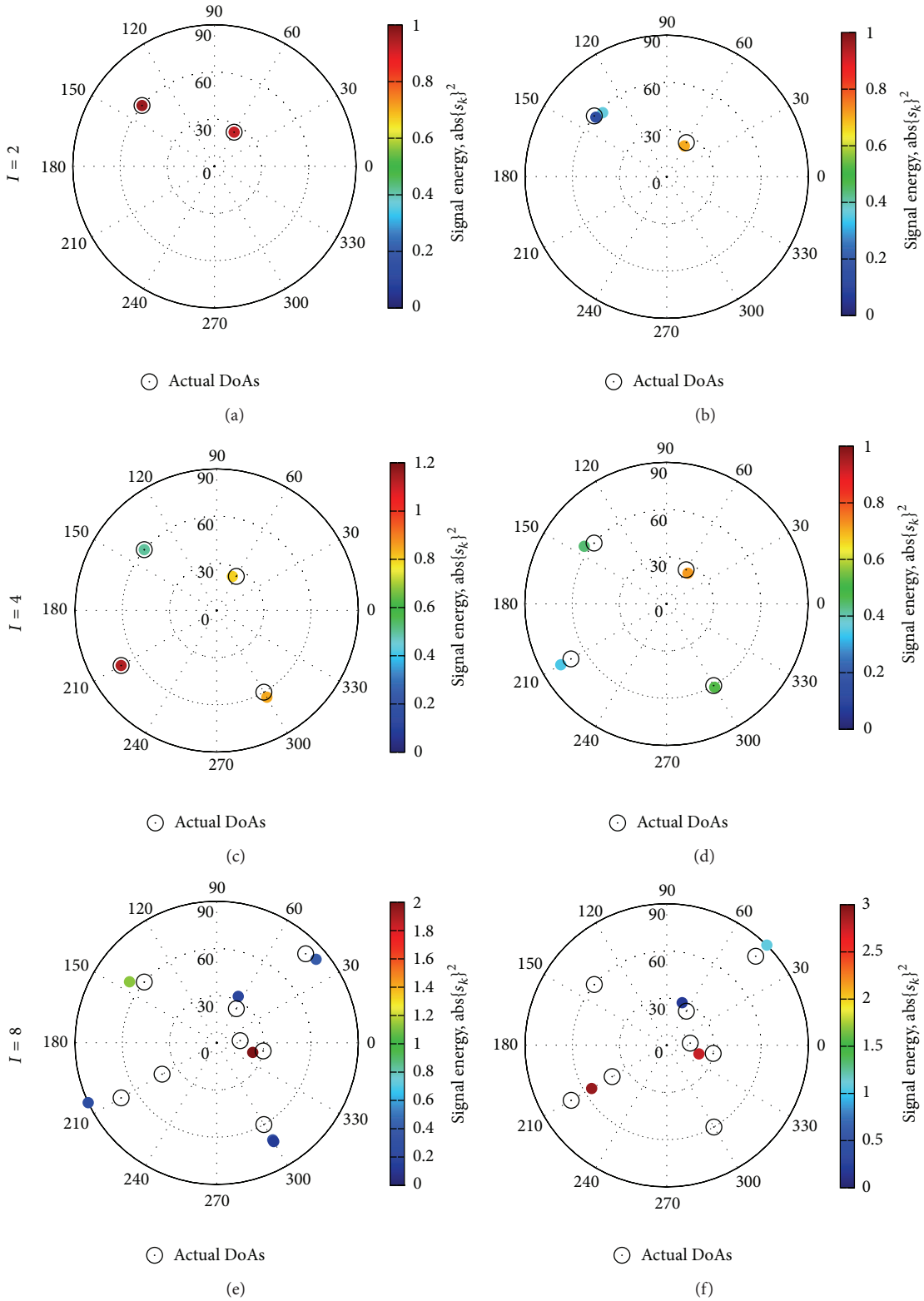

FIGURE 3: Fully populated array—($N = 25$; $d_x = d_y = 0.5\lambda$; $I \in [2 : 8]$; SNR = 10 dB; $T = 1$; $C = 50$)—plot of the best (left column) and worst (right column) estimations obtained by means of the ST-BCS among the C different noisy scenarios when (a) (b) $I = 2$, (c) (d) $I = 4$, and (e) (f) $I = 8$.

Table 2: Fully populated array—($N = 25$; $d_x = d_y = 0.5\lambda$; $I \in [2:8]$; SNR = 10 dB; $T = 1$; $C = 50$)—values of the DoAs for the best and worst estimation obtained by means of the ST-BCS among the C different noisy scenarios.

I	$\widehat{I}^{(\mathrm{bst})}$	$\left\{\widehat{\Psi}_i^{(\mathrm{bst})} = \left(\widehat{\theta}_i^{(\mathrm{bst})}, \widehat{\phi}_i^{(\mathrm{bst})}\right), i = 1, \ldots, I\right\}$
2	2	{(25, 60); (60, 140)}
4	4	{(23.75, 65); (60, 140); (63.75, 300); (70, 210)}
8	7	{(23.75, 345); (32.5, 65); (67.5, 145), (71.25, 300), (72.5, 300), (82.5, 40), (90, 205)}
I	$\widehat{I}^{(\mathrm{wst})}$	$\left\{\widehat{\Psi}_i^{(\mathrm{wst})} = \left(\widehat{\theta}_i^{(\mathrm{wst})}, \widehat{\phi}_i^{(\mathrm{wst})}\right), i = 1, \ldots, I\right\}$
2	3	{(22.5, 60); (57.5, 135); (58.75, 137.5)}
4	4	{(23.75, 55); (63.75, 145); (61.25, 300); (77.5, 210)}
8	4	{(21.25, 345); (28.75, 70); (55, 210); (90, 45)}

Table 3: Fully populated array—($N = 25$; $d_x = d_y = 0.5\lambda$; $I \in [2:8]$; SNR = 10 dB; $T = \{1, 2\}$; $C = 50$)—statistics (minimum, maximum, average, and variance) of the location index ξ among C different noisy scenarios when using the ST-BCS ($T = 1$) and the MT-BCS ($T = 2$).

I	$\xi^{(\min)}$	$\xi^{(\max)}$	$\xi^{(\mathrm{avg})}$	$\xi^{(\mathrm{var})}$	$t^{(\mathrm{avg})}$ [sec]
			ST-BCS		
2	0.00	3.80	1.36	1.24	4.48×10^{-1}
4	1.34	3.70	2.07	6.02×10^{-1}	1.37
8	3.02×10^{1}	8.23×10^{1}	6.06×10^{1}	2.96×10^{2}	1.77
			MT-BCS		
2	0.00	2.18	8.01×10^{-1}	4.06×10^{-1}	3.97
4	5.45×10^{-1}	1.91	1.37	1.19×10^{-1}	6.44
8	5.27	3.31×10^{1}	1.81×10^{1}	5.94×10^{1}	7.80

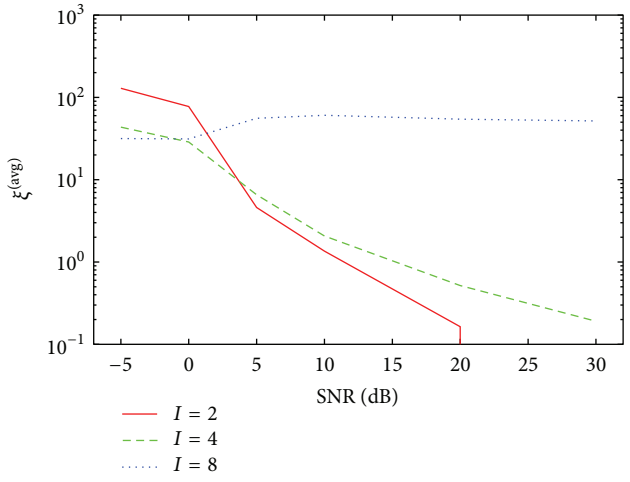

Figure 4: Fully populated array—($N = 25$; $d_x = d_y = 0.5\lambda$; $I \in [2:8]$; SNR$\in$ [−5 : 30] dB; $T = 1$; $C = 50$)—behavior of the location index $\xi^{(\mathrm{ave})}$ averaged among C different noisy scenarios versus the SNR when using the ST-BCS.

$\theta \leq 90^\circ$ and $0^\circ \leq \phi \leq 360^\circ$ is partitioned (Figure 1) in a fine grid of K samples satisfying the condition $K \gg I$. Therefore, the terms $\mathbf{H}(\boldsymbol{\Psi})$ and $\mathbf{s}(\tau)$ in (3) turn out being equal to

$$\begin{aligned} \breve{\mathbf{H}}\left(\breve{\boldsymbol{\Psi}}\right) &= \left[\breve{\mathbf{h}}\left(\breve{\Psi}_1\right), \breve{\mathbf{h}}\left(\breve{\Psi}_2\right), \ldots, \breve{\mathbf{h}}\left(\breve{\Psi}_k\right), \ldots, \breve{\mathbf{h}}\left(\breve{\Psi}_K\right)\right], \\ \breve{\mathbf{s}}(\tau) &= \left[\breve{\alpha}_1(\tau), \breve{\alpha}_2(\tau), \ldots, \breve{\alpha}_k(\tau), \ldots, \breve{\alpha}_K(\tau)\right]^*. \end{aligned} \tag{4}$$

By substituting (4) in (3), the problem is still linear with respect to also $\breve{\mathbf{s}}(\tau)$, but $\breve{\mathbf{s}}(\tau)$ [unlike $\mathbf{s}(\tau)$] is now sparse since $K \gg I$. Accordingly, only few coefficients $\breve{\alpha}_k(\tau)$, $k = 1, \ldots, K$ are expected to differ from zero and exactly in correspondence with the steering vectors $\breve{\mathbf{h}}(\breve{\Psi}_k)$ at the angular direction $\breve{\Psi}_k$ where the wave is estimated to impinge on the array. Accordingly, the original problem of determining the DoAs, $\Psi_i = (\theta_i, \phi_i)$, $i = 1, \ldots, I$, is reformulated as the estimation of the (sparse) signal vector $\widehat{\mathbf{s}}(\tau)$. The signal DoAs are then retrieved as the directions $\widehat{\Psi}_k = (\widehat{\theta}_k, \widehat{\phi}_k)$ whose corresponding signal amplitudes $\widehat{\alpha}_k(\tau)$ are nonnull.

For single time-instant ($T = 1$) acquisitions, the single-task bayesian compressive sensing (ST-BCS) is used, and the sparsest vector $\widehat{\mathbf{s}}(\tau)$ is retrieved by maximizing the posterior probability [24, 25]:

$$\mathscr{P}\left(\left[\widehat{\mathbf{s}}(\tau), \widehat{\sigma}^2, \mathbf{a}(\tau)\right] \mid \boldsymbol{\upsilon}(\tau)\right), \tag{5}$$

where $\widehat{\sigma}^2$ is the estimate of the noise power, supposed to be not varying in time, and $\mathbf{a}(\tau)$ is the hyperparameter vector [26] enforcing the sparseness of the solution $\widehat{\mathbf{s}}(\tau)$ at the τth snapshot. Accordingly, the analytic form of the solution turns out to be

$$\widehat{\mathbf{s}}(\tau) = \frac{1}{\widehat{\sigma}^2}\left(\frac{\widehat{\mathbf{H}}\left(\breve{\boldsymbol{\Psi}}\right)^* \widehat{\mathbf{H}}\left(\breve{\boldsymbol{\Psi}}\right)}{\widehat{\sigma}^2} + \mathrm{diag}\left(\mathbf{a}(\tau)\right)\right)^{-1} \widehat{\mathbf{H}}\left(\breve{\boldsymbol{\Psi}}\right)^* \widehat{\boldsymbol{\upsilon}}(\tau), \tag{6}$$

where all terms are real since the BCS works only with real numbers. The signal vector, $\widehat{\mathbf{s}}(\tau) = [\mathrm{Re}\{\widehat{\mathbf{s}}(\tau)\}; \mathrm{Im}\{\widehat{\mathbf{s}}(\tau)\}]^*$, has

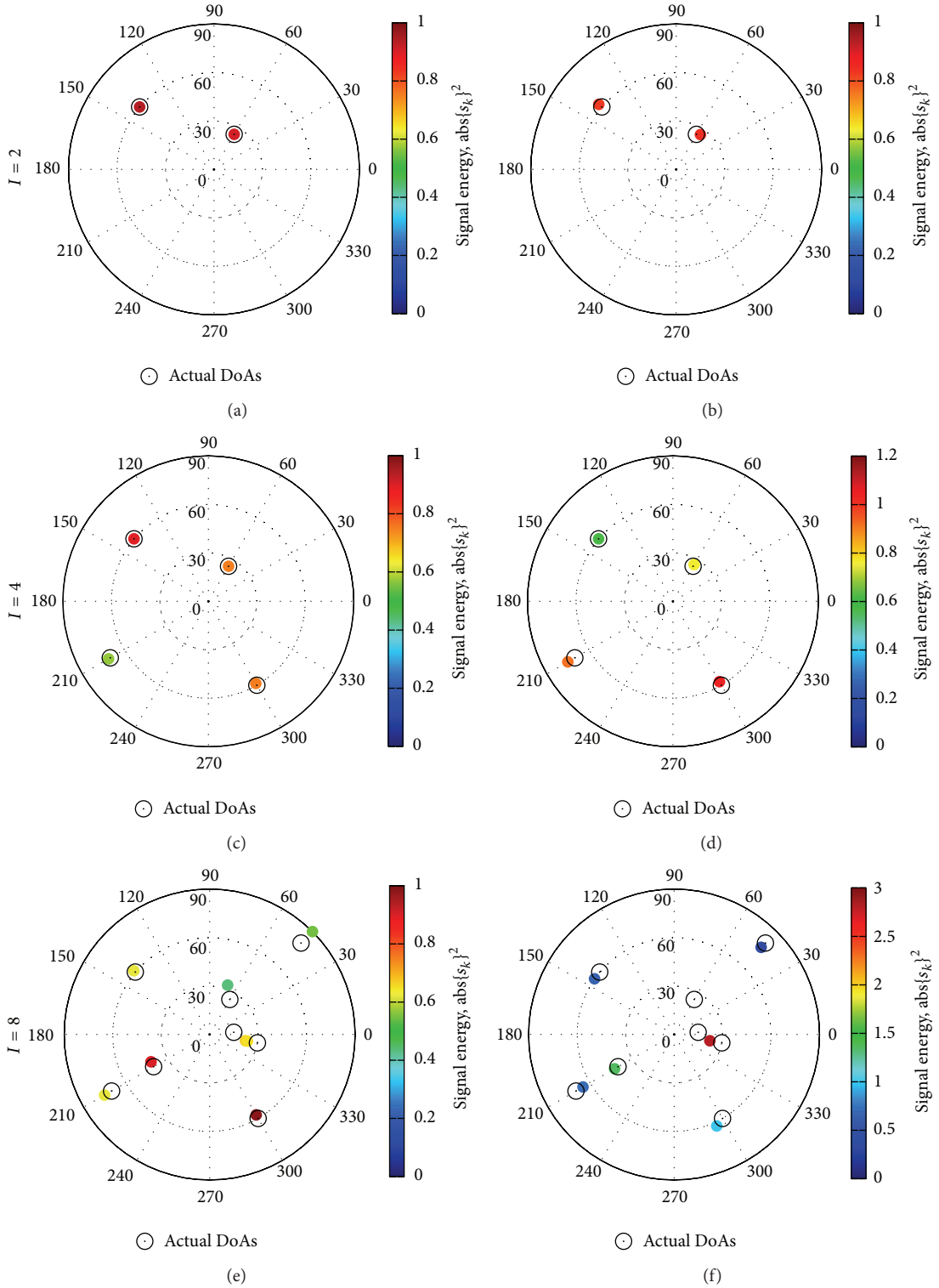

FIGURE 5: Fully populated array—($N = 25$; $d_x = d_y = 0.5\lambda$; $I \in [2:8]$; SNR = 10 dB; $T = 2$; $C = 50$)—plot of the best (left column) and worst (right column) estimations obtained by means of the MT-BCS among the C different noisy scenarios when (a) (b) $I = 2$, (c) (d) $I = 4$, and (e) (f) $I = 8$.

Table 4: Fully populated array—($N = 25$; $d_x = d_y = 0.5\lambda$; $I \in [2:8]$; SNR = 10 dB; $T = 2$; $C = 50$)—values of the DoAs for the best and worst estimation obtained by means of the MT-BCS among the C different noisy scenarios.

I	$\widehat{I}^{(\mathrm{bst})}$	$\left\{\widehat{\Psi}_i^{(\mathrm{bst})} = \left(\widehat{\theta}_i^{(\mathrm{bst})}, \widehat{\phi}_i^{(\mathrm{bst})}\right), i = 1, \ldots, I\right\}$
2	2	{(25, 60); (60, 140)}
4	4	{(25, 60); (58.75, 300); (60, 140); (71.25, 210)}
8	8	{(22.5, 350); (23.75, 350); (32.5, 70); (40, 205); (57.5, 300); (61.25, 140); (75, 210); (90, 45)}
I	$\widehat{I}^{(\mathrm{wst})}$	$\left\{\widehat{\Psi}_i^{(\mathrm{wst})} = \left(\widehat{\theta}_i^{(\mathrm{wst})}, \widehat{\phi}_i^{(\mathrm{wst})}\right), i = 1, \ldots, I\right\}$
2	2	{(26.25, 55); (62.5, 140)}
4	4	{(26.25, 60); (57.5, 300); (60, 140); (75, 210)}
8	6	{(22.5, 350); (42.5, 210); (60, 145); (62.5, 295); (65, 210); (76.25, 45)}

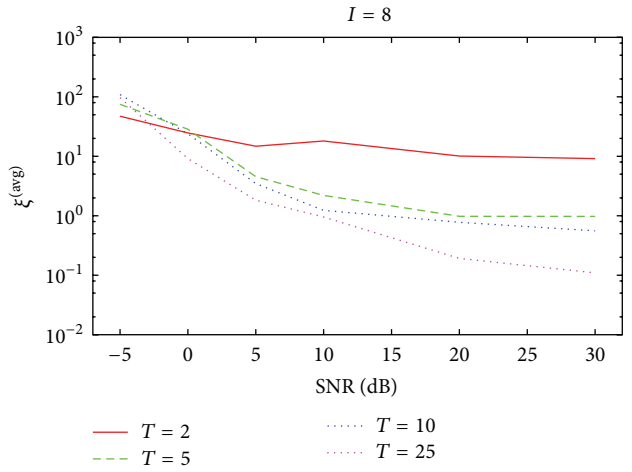

Figure 6: Fully populated array—($N = 25$; $d_x = d_y = 0.5\lambda$; $I = 8$; SNR$\in [-5:30]$ dB; $T \in [2:25]$; $C = 50$)—behavior of the location index $\xi^{(\mathrm{ave})}$ averaged among C different noisy scenarios versus the SNR when using the MT-BCS with different number of available snapshots T.

the dimension $2K \times 1$, and $\widehat{\boldsymbol{v}}(\tau) = [\mathrm{Re}\{\widehat{\boldsymbol{v}}(\tau)\}; \mathrm{Im}\{\widehat{\boldsymbol{v}}(\tau)\}]^*$ is a $2N \times 1$ vector, while

$$\widehat{\mathbf{H}}\left(\breve{\boldsymbol{\Psi}}\right) = \begin{bmatrix} \mathrm{Re}\left\{\breve{\mathbf{H}}\left(\breve{\boldsymbol{\Psi}}\right)\right\} & -\mathrm{Im}\left\{\breve{\mathbf{H}}\left(\breve{\boldsymbol{\Psi}}\right)\right\} \\ \mathrm{Im}\left\{\breve{\mathbf{H}}\left(\breve{\boldsymbol{\Psi}}\right)\right\} & \mathrm{Re}\left\{\breve{\mathbf{H}}\left(\breve{\boldsymbol{\Psi}}\right)\right\} \end{bmatrix} \tag{7}$$

is $2N \times 2K$ matrix, with Re{·} and Im{·} being the real and imaginary parts, respectively. The two control parameters in (6), $\mathbf{a}(\tau)$ and $\widehat{\sigma}^2$, are obtained through the maximization of the function

$$\Pi_{\mathrm{ST}}\left(\widehat{\sigma}^2, \mathbf{a}(\tau)\right) = K \log\left(\frac{1}{2\pi}\right) - \frac{\log|\boldsymbol{\Omega}(\tau)| + (\widehat{\boldsymbol{v}}(\tau))^* (\boldsymbol{\Omega}(\tau))^{-1} \widehat{\boldsymbol{v}}(\tau)}{2} \tag{8}$$

by means of the relevance vector machine (RVM). In (6), $\boldsymbol{\Omega}(\tau) \triangleq \widehat{\sigma}^2 \mathbf{I} + \widehat{\mathbf{H}}(\breve{\boldsymbol{\Psi}}) \operatorname{diag}(\mathbf{a}(\tau))^{-1} \widehat{\mathbf{H}}(\breve{\boldsymbol{\Psi}})^*$ where $\mathbf{I}$ is the identity matrix.

When a set of consecutive snapshots is available, the multitask BCS (MT-BCS) implementation is used to statistically correlate the estimates derived for each snapshot by setting a common hyperparameter vector: $\mathbf{a}(\tau) = \mathbf{a}$, for all $\tau = 1, \ldots, T$. Hence, the final MT-BCS solution is given by [24, 27]:

$$\widehat{\mathbf{s}} = \frac{1}{T} \sum_{\tau=1}^{T} \left\{ \left[\widehat{\mathbf{H}}\left(\breve{\boldsymbol{\Psi}}\right)^* \widehat{\mathbf{H}}\left(\breve{\boldsymbol{\Psi}}\right) + \operatorname{diag}(\mathbf{a}) \right]^{-1} \widehat{\mathbf{H}}\left(\breve{\boldsymbol{\Psi}}\right)^* \widehat{\boldsymbol{v}}(\tau) \right\}, \tag{9}$$

where $\mathbf{a}$ is computed through the RVM maximization of the following function:

$$\Pi_{\mathrm{MT}}(\mathbf{a}) = -\frac{1}{2} \sum_{\tau=1}^{T} \left\{ \log(|\boldsymbol{\Omega}|) + (K + 2\beta_1) \log\left[(\widehat{\boldsymbol{v}}(\tau))^* \boldsymbol{\Omega} \widehat{\boldsymbol{v}}(\tau) + 2\beta_2 \right] \right\}, \tag{10}$$

where $\boldsymbol{\Omega} \triangleq \mathbf{I} + \widehat{\mathbf{H}}(\breve{\boldsymbol{\Psi}}) \operatorname{diag}(\mathbf{a})^{-1} \widehat{\mathbf{H}}(\breve{\boldsymbol{\Psi}})^*$ and β_1 and β_2 are two user-defined parameters [28].

Although the condition $\widehat{\alpha}_k(\tau) \simeq 0$ or $\widehat{\alpha}_k \simeq 0$ usually holds true, the number of nonnull coefficients in either $\widehat{\mathbf{s}}(\tau)$ (ST-BCS) or $\widehat{\mathbf{s}}$ (MT-BCS) could be larger because of the presence of the noise. Hence, the energy thresholding techniques in [24] are exploited to firstly count the number of arriving signals, $\widehat{I}$, and then to estimate the corresponding DoAs. More in detail, the coefficients $\widehat{\alpha}_k(\tau)$ (or $\widehat{\alpha}_k$) are firstly sorted according to their magnitude, and then only the first $\widehat{I}$ coefficients whose cumulative power content is lower than a percentage χ of the totally received signal power, namely, $\|\widehat{\mathbf{s}}(\tau)\| = \sum_{k=1}^{K} (\widehat{\alpha}_k(\tau))^2$ (or $\|\widehat{\mathbf{s}}\| = \sum_{k=1}^{K} (\widehat{\alpha}_k)^2$), are preserved. Hence, $\widehat{I}$ is selected such that $\sum_{i=1}^{\widehat{I}} (\widehat{\alpha}_i(\tau))^2 < \chi \|\widehat{\mathbf{s}}(\tau)\|$ (or $\sum_{i=1}^{\widehat{I}} (\widehat{\alpha}_i)^2 < \chi \|\widehat{\mathbf{s}}\|$).

3. Numerical Results

The planar array BCS-based estimation method is assessed by means of the following analysis devoted to evaluate (a) the performance of its different implementations in correspondence with single snapshot ($T = 1$) or multiple-snapshots ($T > 1$) acquisitions and (b) the impact of different array configurations. Throughout the numerical assessment, the array elements have been assumed uniformly spaced of $d_x = \lambda/2$ and $d_x = \lambda/2$ along the x-axis and y-axis, respectively, and all signals have been characterized with the same amplitude $\alpha_i(\tau) = \alpha_{i+1}(\tau)$, $i = 1, \ldots, I-1$. The

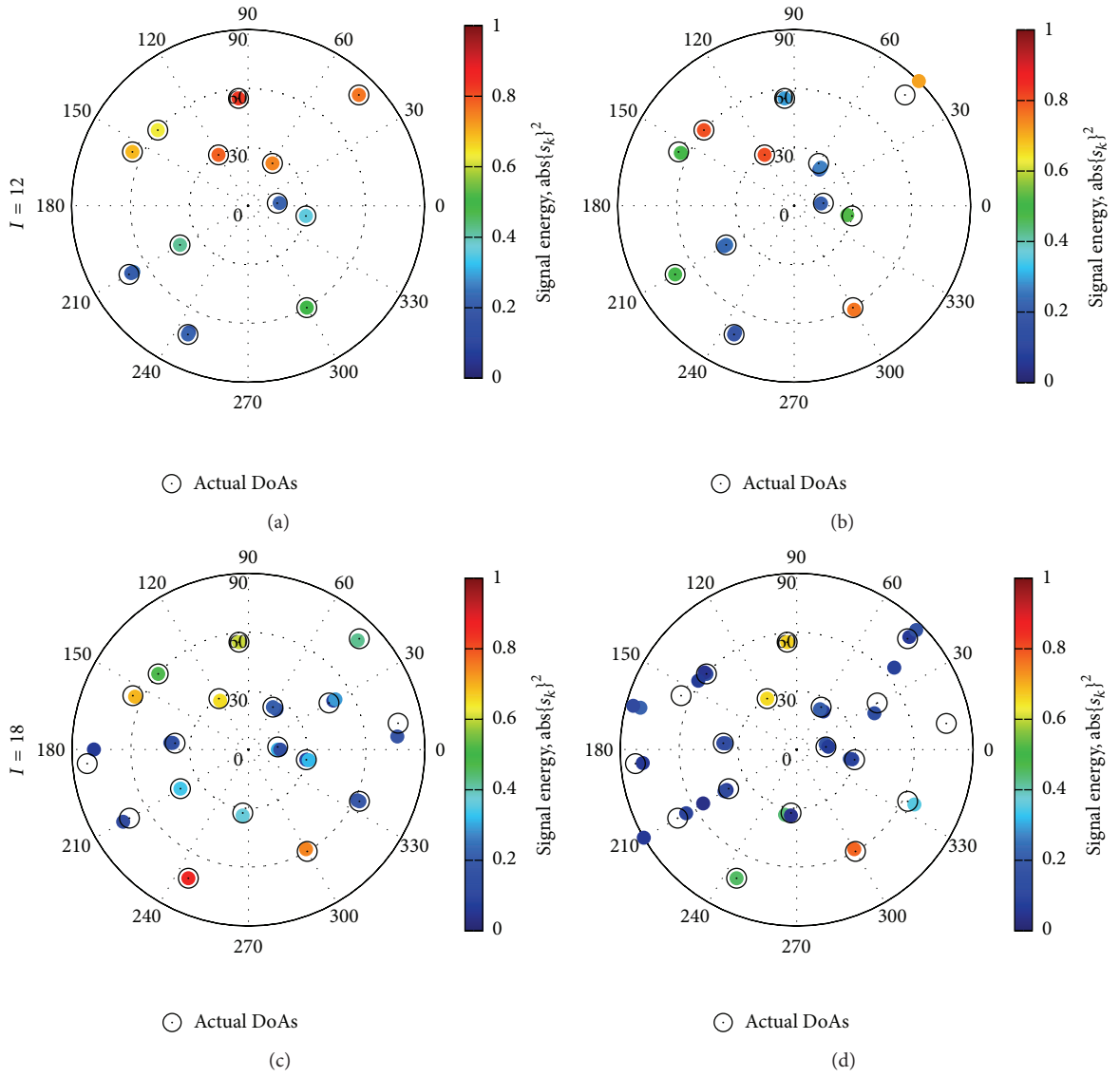

FIGURE 7: Fully populated array—($N = 25$; $d_x = d_y = 0.5\lambda$; $I = \{12, 18\}$; SNR = 10 dB; $T = 25$; $C = 50$)—plot of the best (left column) and worst (right column) estimations obtained by means of the MT-BCS among the C different noisy scenarios when (a) (b) $I = 12$ and (c) (d) $I = 18$.

measurements have been blurred with an additive Gaussian noise of variance σ^2 such that the resulting signal-to-noise ratio turns out to be

$$\text{SNR} = 10 \times \log \left[\frac{\sum_{n=1}^{N} \left| v_n^{\text{no-noise}} \right|^2}{N\sigma^2} \right], \tag{11}$$

with $v_n^{\text{no-noise}}$ ($n = 1, \ldots, N$) being the voltage measured at the nth array element in the noiseless case. The angular observation domain (Figure 1) has been partitioned with a uniform grid characterized by a sampling step equal to $\Delta\theta = 1.25^\circ$ and $\Delta\phi = 1.25^\circ$ along the elevation and azimuthal direction, respectively. The energy threshold has been set to $\chi = 0.95$ according to [24].

In order to quantify the reliability and the effectiveness of the DoA estimation, the following indexes have been computed. For each ith signal, the location index [13] is defined as

$$\xi_i = \xi\left(\Psi_i, \widehat{\Psi}_i\right) \triangleq \frac{\Phi\left(\Psi_i, \widehat{\Psi}_i\right)}{\Phi^{(\max)}} \times 100, \tag{12}$$

where

$$\begin{aligned} \Phi\left(\Psi_i, \widehat{\Psi}_i\right) = \Big(&\left(\sin\theta_i \cos\phi_i - \sin\widehat{\theta}_i \cos\widehat{\phi}_i\right)^2 \\ &+ \left(\sin\theta_i \sin\phi_i - \sin\widehat{\theta}_i \sin\widehat{\phi}_i\right)^2 \\ &+ \left(\cos\theta_i - \cos\widehat{\theta}_i\right)^2 \Big)^{1/2} \end{aligned} \tag{13}$$

and $\Phi^{(\max)} = \max_{\Psi_i, \widehat{\Psi}_i}\{\Phi(\Psi_i, \widehat{\Psi}_i)\} = 2$ is the maximum admissible error in the DoA retrieval. Since the number of

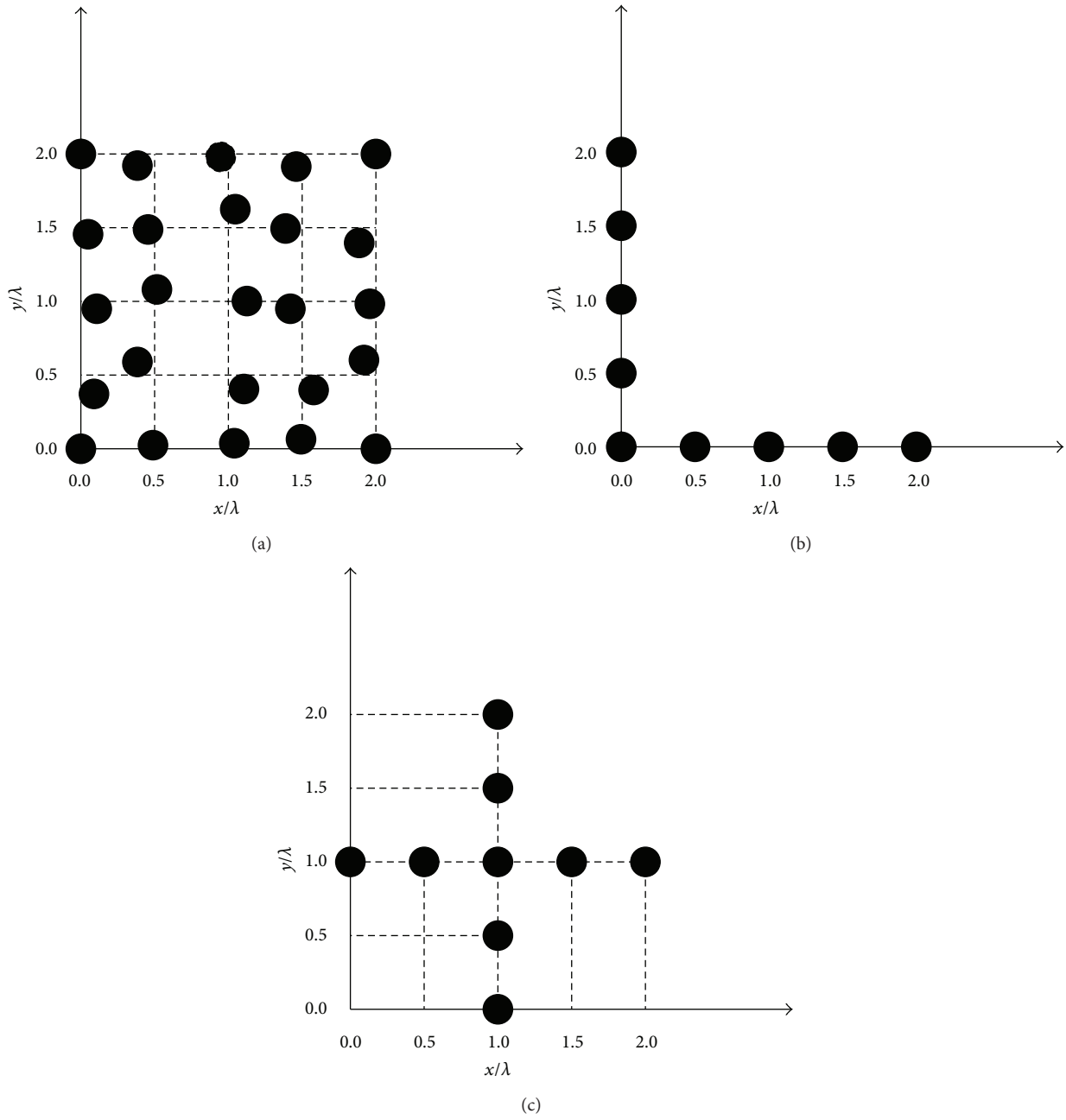

FIGURE 8: Array geometries comparison—geometries of the receiving (a) random ($N = 25$), (b) L-shaped ($N = 9$), and (c) cross-shaped ($N = 9$) arrays.

arriving signals $\widehat{I}$ is unknown and it is derived from the BCS processing, the global location index has been also evaluated [24]:

$$\xi = \begin{cases} \dfrac{1}{I}\left[\displaystyle\sum_{i=1}^{\widehat{I}} \xi\left(\Psi_i, \widehat{\Psi}_i\right) + \left(I - \widehat{I}\right)\xi^{(\text{penalty})}\right] & \text{if } \widehat{I} < I\,, \\ \dfrac{1}{I}\left[\displaystyle\sum_{i=1}^{I} \xi\left(\Psi_i, \widehat{\Psi}_i\right) + \sum_{i=I+1}^{\widehat{I}} \xi\left(\overline{\Psi}_i, \widehat{\Psi}_i\right)\right] & \text{if } \widehat{I} \geq I\,, \end{cases} \tag{14}$$

where $\xi^{(\text{penalty})} = \max_{\Psi_i, \widehat{\Psi}_i}\{\xi_i\} = 100$ is the maximum of (12) and $\overline{\Psi}_i = \arg\{\min_{i=I+1}[\xi(\Psi_i, \widehat{\Psi}_i)]\}$. Since it is preferred to detect all signals really present in the scenario, although overestimating their number then missing some of them, the penalty is considered only when $\widehat{I} < I$.

3.1. Single and Multiple Snapshot BCS-Based DoAs Estimation Techniques. Let us consider the fully populated array of Figure 2 with $N = N_x \times N_y = 25$ elements, with $N_x = N_y = 5$ being the number of elements along the x and y axes, collecting the data $\boldsymbol{v}(\tau)$. Several different electromagnetic

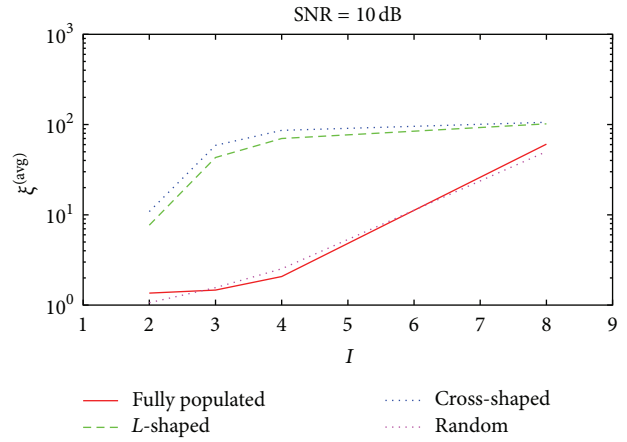

FIGURE 9: Array geometries comparison—($N = \{9, 25\}$; $d_x = d_y = 0.5\lambda$; $I \in [2 : 8]$; SNR = 10 dB; $T = 1$; $C = 50$)—behavior of the location index $\xi^{(ave)}$ averaged among C different noisy scenarios versus the number of arriving signals I when using the ST-BCS.

scenarios have been considered in which $I = 2$, $I = 4$, and $I = 8$ signals are supposed to impinge on the planar array from the directions indicated in Table 1. (In the numerical results, the actual DoAs are chosen lying on the sampling grid of the observation domain. Whether this condition does not hold true, off-grid compensation methods [29, 30], already proposed in the state-of-the-art literature, can be profitably used).

The power of the background noise has been set to yield SNR = 10 dB. In order to test the behavior of the ST-BCS and the MT-BCS, the simulation for each signal configuration has been repeated $C = 50$ times, while varying the noise samples on the data. The DoAs estimation error has been therefore evaluated through the average location index defined as

$$\xi^{(\text{avg})} = \frac{1}{C}\sum_{c=1}^{C}\xi^{(c)}, \tag{15}$$

with $\xi^{(c)}$ being computed as in (14).

As for the ST-BCS, a single snapshot has been processed each time ($T = 1$). Figure 3 shows the best (Figure 3—left column) and the worst (Figure 3—right column) solutions in terms of minimum ($\xi^{(\min)} = \min_{c=1,\ldots,C}\{\xi^{(c)}\}$) and maximum ($\xi^{(\max)} = \max_{c=1,\ldots,C}\{\xi^{(c)}\}$) location errors, respectively, among the $C = 50$ DoAs estimations carried out when $I = 2$ (Figures 3(a) and 3(b)), $I = 4$ (Figures 3(c) and 3(d)), and $I = 8$ (Figures 3(e) and 3(f)). In Figure 3, the actual DoAs are denoted with a point at the center of a circle, while the color points indicate the estimated signal locations and amplitudes. For the sake of clarity, the retrieved DoAs are also reported in Table 2 where the number of estimated signals $\widehat{I}$ is given, as well. As it can be observed, the strength of the estimated signals is different (Figure 3), even though they impinge on the antenna with the same energy because of the presence of the noise. On the other hand, the DoAs are predicted with a high degree of accuracy when $I = 2$ and $I = 4$ as confirmed by the values of the location error (Table 3). As a matter of fact, the error values are low also for the worst solutions among the C trials (i.e., $\xi^{(\max)}|_{I=2} = 3.80\%$ and $\xi^{(\max)}|_{I=4} = 3.89\%$). It is worth also noting that for $I = 2$ the location error is small even though the numbers of detected signals are greater than the actual ones ($\widehat{I}^{(\text{wst})}|_{I=2} = 3$) because two signals have very close DoAs (as compared to the sampling steps $\Delta\theta$ and $\Delta\phi$). However, if the ST-BCS shows being robust and accurate in such scenarios ($I = 2$ and $I = 4$), it is not able to correctly locate the actual DoAs when the number of signals increases to $I = 8$ (Figures 3(e) and 3(f)—Table 2). Indeed, the location error significantly increases as indicated by the indexes in Table 3.

As for the computational efficiency, the ST-BCS is able to perform the DoAs estimation in a limited CPU time ($t^{(\text{avg})} < 2.0$ [sec]—Table 3) (the simulations have been run using a standard processing unit (i.e., 2.4 GHz PC with 2 GB of RAM) with a nonoptimized code) also thanks to the single-snapshot processing. In order to investigate the effects of the SNR on the DoAs estimation capabilities of the ST-BCS, the SNR has been varied from −5 dB up to 30 dB with a step of 5 dB, while keeping the same DoAs of Table 1. In Figure 4, the values of the average location index are reported. As it can be noticed, the location index $\xi^{(\text{avg})}$ for $I = 2$ and $I = 4$ monotonically decreases, as one should expect, with the increment of the SNR. However, the ST-BCS estimates when $I = 8$ turn out to be still nonreliable also for higher SNR confirming the difficulty of dealing with such a complex scenario just processing one snapshot.

Let us now analyze the MT-BCS behavior. Firstly, the same problems addressed by means of the ST-BCS in Figure 3 are considered by taking into account only $T = 2$ snapshots. The best and worst MT-BCS results are reported in Figure 5, and the corresponding DoAs are given in Table 4. Unlike the ST-BCS (Table 2) the number of impinging signals is always correctly identified in the best case (Figure 5—left column), while in the worst case (Figure 5—right column), $\widehat{I} = I$ only when $I = 2$ and $I = 4$ signals. As a matter of fact, the average location error when $I = 8$ is still high ($\xi^{(\text{avg})}|_{I=8} = 18.1\%$). The use of only $T = 2$ snapshots does not guarantee reliable performance also with the MT-BCS, even though the advantages in terms of accuracy of the MT-BCS over the ST-BCS are nonnegligible as pointed out by the values in Table 3. On the opposite, the computational cost of the MT-BCS is higher than that of the ST-BCS (Table 3).

More reliable MT-BCS estimations can be yielded when processing a larger number of snapshots. Figure 6 shows that, also for complex electromagnetic scenarios (i.e., $I = 8$—Table 1), the average location error gets lower when T increases. By considering SNR = 10 dB as a representative example, one can observe that $\xi^{(\text{avg})}$ reduces almost one order of magnitude from $\xi^{(\text{avg})}|_{I=8} = 18.1\%$ ($T = 2$) to $\xi^{(\text{avg})}|_{I=8} = 2.20\%$ ($T = 5$). As expected, more accurate estimations arise with even more data (i.e., $\xi^{(\text{avg})}|_{I=8} = 1.23\%$ when $I = 10$, and $\xi^{(\text{avg})}|_{I=8} = 0.95\%$ when $I = 25$—Figure 6). The benefits from the correlation of the information coming from different time instants thanks to the MT-BCS are also highlighted by the behavior of the plots

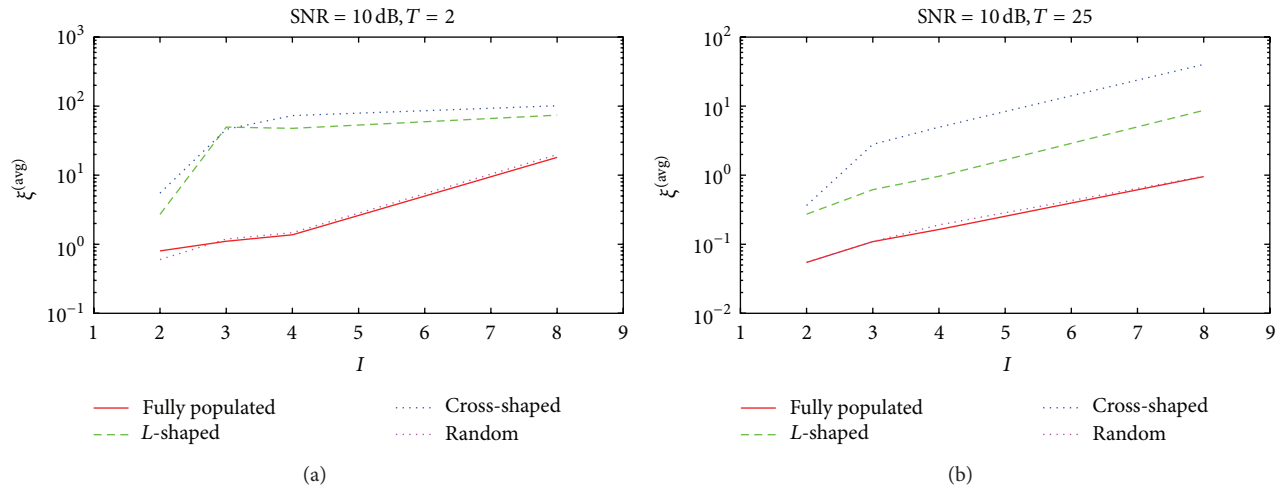

FIGURE 10: Array geometries comparison—($N = \{9, 25\}$; $d_x = d_y = 0.5\lambda$; $I \in [2 : 8]$; SNR = 10 dB; $T = \{2, 25\}$; $C = 50$)—behavior of the location index $\xi^{(\text{ave})}$ averaged among C different noisy scenarios versus the number of arriving signals I when using the MT-BCS with (a) $T = 2$ snapshots and (b) $T = 25$ snapshots.

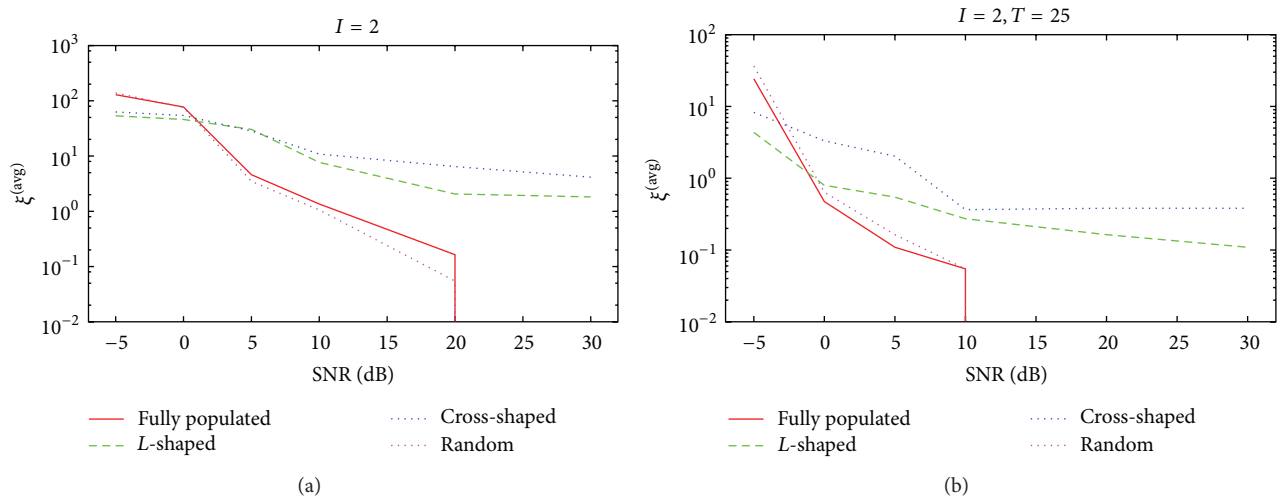

FIGURE 11: Array geometries comparison—($N = \{9, 25\}$; $d_x = d_y = 0.5\lambda$; $I = 2$; SNR = 10 dB; $T = \{1, 25\}$; $C = 50$)—behavior of the location index $\xi^{(\text{ave})}$ averaged among C different noisy scenarios versus the SNR when using (a) the ST-BCS with $T = 1$ snapshot and (b) the MT-BCS with $T = 25$ snapshots.

in Figure 6: $\xi^{(\text{avg})}$ more rapidly decreases for higher values of T when the quality of the data improves (i.e., higher SNR).

As long as the applications at hand do not require the fast or real-time identification of the DoAs, and there is the possibility to collect the data at consecutive time instants, the robust estimation of a larger number of impinging signals is allowed. In this context, Figure 7 shows the results obtained with the MT-BCS when $I = 12$ (Figures 7(a) and 7(b)) and $I = 18$ (Figures 7(c) and 7(d)) (SNR = 10 dB). As for the case $I = 12$, the DoAs are estimated with a good degree of accuracy also in the worst case within the C experiments (Figure 7(b)—$\xi^{(\text{max})}|_{I=12} = 1.77\%$), while the average location error amounts to $\xi^{(\text{avg})}|_{I=12} = 1.04\%$. Differently, the average error is $\xi^{(\text{avg})}|_{I=18} = 4.70\%$ and in the worst case (Figure 7(d)) is $\xi^{(\text{max})}|_{I=18} = 7.85\%$ when $I = 18$. For the sake of completeness, the best solutions are reported in Figures 7(a) and 7(c) when $I = 12$ and $I = 18$, respectively.

3.2. DoAs Estimation Performance for Different Array Geometries. In this section, the behavior of the BCS-based single-snapshot and multiple-snapshots DoAs estimators is analyzed for different array architectures. The three array geometries in Figure 8 are taken into account. As it can be noticed, the first array (Figure 8(a)) has the same number of elements of the fully populated one, but the sensors are randomly located on the antenna aperture. The other two arrays (Figures 8(b) and 8(c)) have less elements (i.e., $N = 9$) but same aperture length of the fully populated array along the two coordinate axes.

In the first example, the performance of the ST-BCS is assessed when changing the number of impinging signals from $I = 2$ up to $I = 8$, while keeping the noise level to SNR = 10 dB. Figure 9 shows the average location error ($C = 50$) obtained in correspondence with the three arrays. Unlike the fully populated arrangement enabling good estimation features especially until $I = 4$ ($\xi^{(\text{avg})}|_{I=2,3,4} < 2.00\%$), both the L-shaped array and the cross-shaped one do not allow reliable estimations also for the simplest scenario (i.e., $\xi^{(\text{avg})}|_{I=2}^{L\text{-Shaped}} = 7.69\%$ and $\xi^{(\text{avg})}|_{I=2}^{\text{Cross-Shaped}} = 10.87\%$). This is due, on the one hand, to the limited information collected from a single snapshot acquisition and, on other hand, to the fact that the number of sensors is one third the elements of the fully-populated configuration (i.e., $N^{\text{Fully-Populated}}/N^{L/\text{Cross-Shaped}} = 2.78$). As for the random array, the achieved performances are almost equal to those of the fully populated solution thus confirming the higher reliability when having at disposal a larger number of sensors. When using the MT-BCS, no significant improvements occur in comparison with the ST-BCS when $T = 2$, since average errors higher than $\xi^{(\text{avg})} = 2.00\%$ (Figure 10(a)) are obtained with both the L-shaped or cross-shaped array. Whether $T = 25$ snapshots are at disposal (Figure 10(b)), it turns out that the estimates from the L-shaped array present average location errors below $\xi^{(\text{avg})} = 2.00\%$ until $I = 5$. Differently, always worse performance is achieved with the cross-shaped array (Figure 10(b)).

In order to give some insight on the effects of the SNR, let us consider the case $I = 2$ as a representative example. The results from the ST-BCS and the MT-BCS are reported in Figures 11(a) and 11(b), respectively. The location error tends to reduce as the SNR increases for all array structures, even though the L-shaped array outperforms the cross-shaped one, and the random array behavior is always very close to that of the fully populated configuration.

4. Conclusions

The BCS method has been customized for the DoAs estimation of multiple signals impinging on planar arrays. Two different implementations, one requiring the data measured at a single snapshot and the other using the data collected at multiple snapshots, have been tested on a wide number of different scenarios as well as using different array arrangements. Likewise in the linear array case, the reported results have shown that:

(i) the two BCS-based implementations provide effective DoAs estimates just using as data the sensors output voltages without requiring the covariance matrix;

(ii) the joint estimation of the signals number and DoAs is enabled;

(iii) the correlation capability of the MT-BCS allows one to yield better results than the ST-BCS at the expenses of an increased computational burden.

As for the behavior of the two approaches versus the planar array geometry, it is possible to conclude that

(i) the fully populated and the random arrays give the best performance as compared to both the L-shaped and the cross-shaped arrays, but using a larger number of sensors;

(ii) under the assumption of the same number of elements, the L-shaped configuration always outperforms the precision from the cross-shaped arrangement.

References

[1] E. J. Candes and M. B. Wakin, "An introduction to compressive sampling: a sensing/sampling paradigm that goes against the common knowledge in data acquisition," *IEEE Signal Processing Magazine*, vol. 25, no. 2, pp. 21–30, 2008.

[2] W. U. Bajwa, J. Haupt, A. M. Sayeed, and R. Nowak, "Compressed channel sensing: a new approach to estimating sparse multipath channels," *Proceedings of the IEEE*, vol. 98, no. 6, pp. 1058–1076, 2010.

[3] A. Majumdar, R. K. Ward, and T. Aboulnasr, "Compressed sensing based real-time dynamic MRI reconstruction," *IEEE Transactions on Medical Imaging*, vol. 31, no. 12, pp. 2253–2266, 2012.

[4] J. Yang, J. Thompson, X. Huang, T. Jin, and Z. Zhou, "Random-frequency SAR imaging based on compressed sensing," *IEEE Transactions on Geoscience and Remote Sensing*, vol. 51, no. 2, pp. 983–994, 2013.

[5] G. Oliveri, P. Rocca, and A. Massa, "A bayesian-compressive-sampling-based inversion for imaging sparse scatterers," *IEEE Transactions on Geoscience and Remote Sensing*, vol. 49, no. 10, pp. 3993–4006, 2011.

[6] L. Poli, G. Oliveri, P. Rocca, and A. Massa, "Bayesian compressive sensing approaches for the reconstruction of two-dimensional sparse scatterers under TE illuminations," *IEEE Transactions on Geoscience and Remote Sensing*, vol. 51, no. 5, pp. 2920–2936, 2013.

[7] S. Ji, Y. Xue, and L. Carin, "Bayesian compressive sensing," *IEEE Transactions on Signal Processing*, vol. 56, no. 6, pp. 2346–2356, 2008.

[8] R. O. Schmidt, "Multiple emitter location and signal parameter estimation," *IEEE Transactions on Antennas and Propagation*, vol. 34, no. 3, pp. 276–280, 1986.

[9] R. Roy and T. Kailath, "ESPRIT—estimation of signal parameters via rotational invariance techniques," *IEEE Transactions on Acoustics, Speech, and Signal Processing*, vol. 37, no. 7, pp. 984–995, 1989.

[10] I. Ziskind and M. Wax, "Maximum likelihood localization of multiple sources by alternating projection," *IEEE Transactions on Acoustics, Speech, and Signal Processing*, vol. 36, no. 10, pp. 1553–1560, 1988.

[11] A. H. El Zooghby, C. G. Christodoulou, and M. Georgiopoulos, "A neural network-based smart antenna for multiple source tracking," *IEEE Transactions on Antennas and Propagation*, vol. 48, no. 5, pp. 768–776, 2000.

[12] M. Pastorino and A. Randazzo, "The SVM-based smart antenna for estimation of the directions of arrival of electromagnetic waves," *IEEE Transactions on Instrumentation and Measurement*, vol. 55, no. 6, pp. 1918–1925, 2006.

[13] M. Donelli, F. Viani, P. Rocca, and A. Massa, "An innovative multiresolution approach for DOA estimation based on a

support vector classification," *IEEE Transactions on Antennas and Propagation*, vol. 57, no. 8, pp. 2279–2292, 2009.

[14] J.-J. Fuchs, "On the application of the global matched filter to DOA estimation with uniform circular arrays," *IEEE Transactions on Signal Processing*, vol. 49, no. 4, pp. 702–709, 2001.

[15] D. Model and M. Zibulevsky, "Signal reconstruction in sensor arrays using sparse representations," *Signal Processing*, vol. 86, no. 3, pp. 624–638, 2006.

[16] A. C. Gurbuz, V. Cevher, and J. H. McClellan, "Bearing estimation via spatial sparsity using compressive sensing," *IEEE Transactions on Aerospace and Electronic Systems*, vol. 48, no. 2, pp. 1358–1369, 2012.

[17] D. Malioutov, M. Çetin, and A. S. Willsky, "A sparse signal reconstruction perspective for source localization with sensor arrays," *IEEE Transactions on Signal Processing*, vol. 53, no. 8, pp. 3010–3022, 2005.

[18] M. M. Hyder and K. Mahata, "Direction-of-arrival estimation using a mixed $\ell_{2,0}$ norm approximation," *IEEE Transactions on Signal Processing*, vol. 58, no. 9, pp. 4646–4655, 2010.

[19] H. Zhu, G. Leus, and G. B. Giannakis, "Sparsity-cognizant total least-squares for perturbed compressive sampling," *IEEE Transactions on Signal Processing*, vol. 59, no. 5, pp. 2002–2016, 2011.

[20] I. Bilik, "Spatial compressive sensing for direction-of-arrival estimation of multiple sources using dynamic sensor arrays," *IEEE Transactions on Aerospace and Electronic Systems*, vol. 47, no. 3, pp. 1754–1769, 2011.

[21] Z. Zhang and B. D. Rao, "Sparse signal recovery with temporally correlated source vectors using sparse Bayesian learning," *IEEE Journal on Selected Topics in Signal Processing*, vol. 5, no. 5, pp. 912–926, 2011.

[22] M. Carlin and P. Rocca, "A Bayesian compressive sensing strategy for direction-of-arrival estimation," in *Proceedings of the European Conference on Antennas and Propagation (EuCAP '12)*, pp. 1–2, Prague, Czech Republic, March 2012.

[23] M. Carlin, P. Rocca, G. Oliveri, and A. Massa, "Multi-task Bayesian compressive sensing for direction-of-arrival estimation," in *Proceedings of the IEEE International Conference on Wireless Information Technology and Systems (ICWITS '12)*, Maui, Hawaii, USA, November 2012.

[24] M. Carlin, P. Rocca, G. Oliveri, F. Viani, and A. Massa, "Directions-of-arrival estimation through Bayesian compressive sensing strategies," *IEEE Transactions on Antennas and Propagation*, 2013.

[25] G. Oliveri and A. Massa, "Bayesian compressive sampling for pattern synthesis with maximally sparse non-uniform linear arrays," *IEEE Transactions on Antennas and Propagation*, vol. 59, no. 2, pp. 467–481, 2011.

[26] M. E. Tipping, "Sparse Bayesian learning and the relevance vector machine," *Journal of Machine Learning Research*, vol. 1, no. 3, pp. 211–244, 2001.

[27] G. Oliveri, M. Carlin, and A. Massa, "Complex-weight sparse linear array synthesis by Bayesian Compressive Sampling," *IEEE Transactions on Antennas and Propagation*, vol. 60, no. 5, pp. 2309–2326, 2012.

[28] S. Ji, D. Dunson, and L. Carin, "Multitask compressive sensing," *IEEE Transactions on Signal Processing*, vol. 57, no. 1, pp. 92–106, 2009.

[29] E. T. Northardt, I. Bilik, and Y. I. Abramovich, "Spatial compressive sensing for direction of-arrival estimation with bias mitigation via expected likelihood," *IEEE Transactions on Signal Processing*, vol. 61, no. 5, pp. 1183–1106, 2013.

[30] Z. Yang, L. Xie, and C. Zhang, "Off-grid direction of arrival estimation using sparse Bayesian inference," *IEEE Transactions on Signal Processing*, vol. 61, no. 1, pp. 38–43, 2013.

Hindawi Publishing Corporation
Journal of Electrical and Computer Engineering
Volume 2013, Article ID 804615, 6 pages
http://dx.doi.org/10.1155/2013/804615

Research Article

Modeling and Processing L-Band Ground Based Radar Data for Landslides Early Warning

A. R. Laganà, M. T. Bevacqua, and T. Isernia

Dipartimento di Ingegneria dell'Informazione, delle Infrastrutture e dell'Energia Sostenibile,
Università Mediterranea di Reggio Calabria, Consorzio Nazionale Interuniversitario per le Telecomunicazioni (CNIT), Italy

Correspondence should be addressed to T. Isernia; tommaso.isernia@unirc.it

Received 26 May 2013; Accepted 19 June 2013

Academic Editor: Sandra Costanzo

Copyright © 2013 A. R. Laganà et al. This is an open access article distributed under the Creative Commons Attribution License, which permits unrestricted use, distribution, and reproduction in any medium, provided the original work is properly cited.

L-band radars have been proposed as possible way for monitoring landslides. In this paper, we examine and solve the principal difficulties arising in modeling and processing radar data, evidencing differences with more usual SAR imaging. Numerical examples in support of the proposed processing procedure are finally provided.

1. Introduction

Amongst the different possible ways to have a continuous monitoring of areas which may be subject to landslides, L-band radars offer the possibility to penetrate foliage while still being able to get some understanding of the evolution of the scenario by means of differential imaging techniques.

Differently from a large body of the literature, where imaging is performed by means of satellite-based radars (so that the movement of the satellite allows to rely on a synthetic aperture) the research activity considered in the following concern the exploitation of a fixed ground based radar, where the only eventually available movement of the sensor is achieved by a mechanical or electronic scanning of the antenna pattern.

Such a circumstance implies a number of interesting differences, which are discussed in the following, with respect to more usual radar imaging modeling and processing techniques.

In fact, a more detailed and difficult model is required for data simulation (which is useful to "tune" imaging procedure). Moreover, data processing requires more sophisticated techniques with respect to satellite-based imaging. On the other side, location on ground of the sensor allows a very simple deployment on those areas which are judged to have a risk of landslides. Also, the assumptions on "coherence" (see below), which are needed for differential imaging, are more easily verified with respect to differential interferometric SAR techniques.

For the sake of simplicity of explanation, most concepts regarding simulation and processing are explained with reference to a simple "2D geometry," that is, in a case where both fields and the scenario are invariant along one dimension, and the field is directed along such a direction. Such a simplifying assumption is then removed in Section 4.

In the following, Section 2 is concerned with the problem of accurately simulating scenarios of interest, and attention is paid to the need of developing models which take into account the fact that the radar antenna is supposed to be in the near zone of the scenario under test. Then, Section 3 presents the basic idea for monitoring possible deformations of the soil on the basis of a differential imaging technique. In particular, the need of solving such kind of inverse source problem is underlined, and a suitable processing technique is introduced and discussed.

Finally, the extension to the 3D case is discussed in Section 4, and results of processing (on simulated data) are presented in Section 5.

Conclusions and possible developments follow.

2. Modeling Radar Data

In order to provide whatever form of imaging technique, it is mandatory to get a deep understanding of the physical

mechanism underlying the process and to get a proper accurate mathematical modeling of this latter. In fact, this will allow a better comprehension of the phenomena at hand (possibly suggesting proper imaging techniques), and it will allow an accurate simulation of radar data, which is of course essential to properly tune imaging techniques.

The basic physical mechanism is the electromagnetic scattering [1]. In general case, backscattering is due to both a kind of reflection at the interface, as well as from the secondary field which is generated within the volume of interest.

By taking into account the values of permittivity and conductivity at the frequencies of our actual interest, the predominant mechanism is "surface scattering." In fact, as it can be deduced from Figure 1, the penetration depth, concerning the four kinds of soils described in [2], at the frequency range of interest is expected to be too small to be able to consider the mechanism of "volume scattering."

As no exact closed form, but only approximate solutions exist for the problem of scattering from a irregular surface [1], to derive a mathematical approximate expression of the scattered field, it is assumed a surface with gentle undulations [1], whose average horizontal dimension is large compared with the wavelength. This is a general case because if one wants to consider a rough surface, it is only necessary to add a term of roughness, according to "Clapps models" [3].

It is also assumed that the total field at any point on the surface can be computed as if the incident wave is impinging upon a infinite plane tangent to the point, according to the basic assumption of the Kirch off method [4–6] or "facets model" [1]. A mathematical statement of the scattered field, formulated by Stratton and Chu [4, 5] and modified by Silver [6], is as follows:

$$\mathbf{E_s} = K\widehat{\mathbf{n_s}} \times \int \left[\hat{\mathbf{n}} \times \mathbf{E} - \eta_s \widehat{\mathbf{n_s}} \times (\hat{\mathbf{n}} \times \mathbf{H})\right] e^{jk_s \mathbf{r}\cdot\widehat{\mathbf{n_s}}} dS, \quad (1)$$

where

(i) a time factor of the form $e^{j\omega t}$ is understood;

(ii) $K = -jk_s e^{jk_s R_0}/4\pi R_0$;

(iii) $\widehat{\mathbf{n_s}}$ is the unit vector in the scattered direction;

(iv) $\hat{\mathbf{n}}$ is the unit vector normal to interface;

(v) $\mathbf{r}$ is the vector that scans the points on the surface;

(vi) η_s and k_s are, respectively, the intrinsic impedance and wave number of the medium in which the scattered field is evaluated;

(vii) R_0 is the range from the center of the illuminated area to the point of observation;

(viii) $\mathbf{E}$ and $\mathbf{H}$ are the total electric and magnetic fields on the interface.

Equation (1) allows computeing the scattered field in far zone [7] as superposition of fields scattered by each point on the surface. On the other side, in the case of our interest the receiving antenna is in the near zone of the scenario at hand

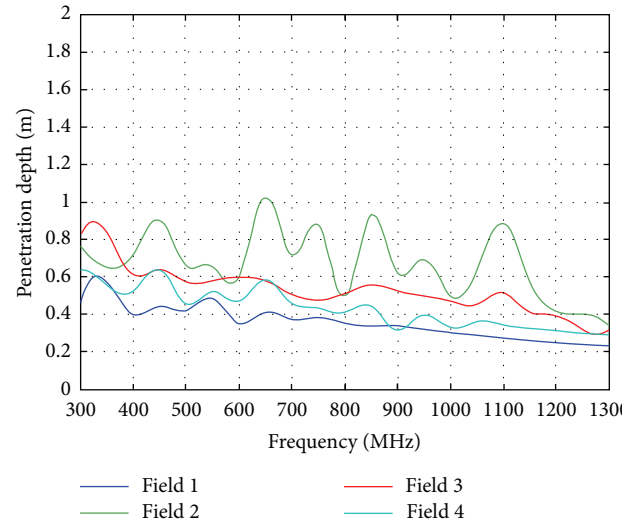

Figure 1: Penetration depth for soils described in [2].

(which acts as a source), so that (1) is noted as adequate to accurately modeling the radar data.

So, (1) has to be reformulated considering that some parameters, like the incident angle or the distance between the sensor and the scenario, change for each point on the surface. Accordingly, it is not possible to use the usual simplification for far-field region, that is, to approximate the distance factor in the denominator by R_0 and exploit a first-order approximation for the argument of the exponential.

Another basic difference with respect to SAR techniques concerns the kind of data which is collected.

Obviously, one needs some kind of data diversity to get an image after processing, and if a 2D image is the final goal, the raw data must be a function of two coordinates at least, which is commonly achieved in SAR systems by a translation of the platform and registering delays of the backscattered signals. In our scenario, the "platform" is fixed, and we would like to exploit monochromatic signals, which can allow a very simple data processing (see Section 3).

Hence, the needed diversity is achieved by a suitable 2D mechanical or electronic scanning of the antenna, so that our data will be a 2D function of (ϑ_p, φ_p), where such a couple denotes the direction where the radar antenna is pointing to.

By assuming a scenario (and incident fields) which is invariant along one direction, and assuming an incident field parallel to such a direction, the overall model becomes scalar, and the field collected at the radar position can be written as

$$E_s\left(\vartheta_p\right) = \frac{-jk_1}{4\pi} \int \left[\left(An_{sx} - Bn_{sz}\right)\right] \times \frac{e^{j2k_1|r-r_{tx}|}}{|r-r_{tx}|} h\left(\vartheta_p, \vartheta_a\right) dS, \quad (2)$$

where

$$A = \left(1 + R_{\text{perp}}\right)\left(-n_x\right) + \left(\hat{\mathbf{n}} \cdot \widehat{\mathbf{n}_\mathbf{i}}\right)\left(1 - R_{\text{perp}}\right)\left(-n_{sx}\right)$$
$$B = \left(1 + R_{\text{perp}}\right)\left(n_z\right) + \left(\hat{\mathbf{n}} \cdot \widehat{\mathbf{n}_\mathbf{i}}\right)\left(1 - R_{\text{perp}}\right)\left(n_{sz}\right), \quad (3)$$

where

(i) θ_p is the observation angle of the measuring sensor;

(ii) k_1 is the wave number of the medium;

(iii) R_{perp} is the Fresnel reflection coefficient;

(iv) h is the array factor of the sensor used for monitoring,

(v) $\widehat{\mathbf{n}_\mathbf{i}}$ is the unit vector that identifies the incident direction,

(vi) θ_a is the observation angle that scans the elementary areas on the surface (direction where the radar antenna is pointing to).

In (2), one can identify a factor depending on the antenna, a factor depending on the round-trip, and a factor depending on the scenario (shape of the interface and its electromagnetic characteristics).

A numerical simulator based on (2) has been developed successfully and tested in some canonical scenarios (flat and sinusoidally varying surfaces).

3. 2D Case Data Processing

3.1. The Basic Idea. In order to describe the strategy, it is convenient to rewrite the relation between the scattered electromagnetic field and the surface features, already described in (2), in a different form. In particular, the scattered electromagnetic field at the radar position when the radar antenna is pointing toward θ_p can be expressed by the following equation:

$$\begin{aligned} E_s\left(\theta_p\right) &= \int E_{s_\text{loc}}\left(\theta_a, \theta_p\right) d\theta_a \\ &= \int J_{\text{ind}}\left(\theta_a\right) \frac{e^{-jkR(\theta_a)}}{\sqrt{R\left(\theta_a\right)}} h_{\text{array}}\left(\theta_a, \theta_p\right) d\theta_a \\ &= \int f\left[R_{\text{perp}}\left(\theta_a\right)\right] e^{-j2k\Delta R(\theta_a)} \\ &\quad \times \frac{e^{-j2k\overline{R}(\theta_a)}}{\overline{R}\left(\theta_a\right)} h_{\text{array}}\left(\theta_a, \theta_p\right) d\theta_a, \end{aligned} \tag{4}$$

where:

(i) $E_{s_\text{loc}}(\theta_a)$ is the contribution to the overall received field due to each elementary area on the surface;

(ii) R is the generic distance between antenna and surface, in particular $R(\theta_a) = \overline{R}(\theta_a) + \Delta R(\theta_a)$, where $\overline{R}(\theta_a)$ is a "reference distance" and $\Delta R(\theta_a)$ is the amplitude corresponding to the surface deformation;

(iii) h_{array} is the array factor (in transmission and receiving case);

(iv) $f(R_{\text{perp}})e^{-j2k\Delta R(\theta_a)}$ is a function, called $\gamma(\theta_a)$, that depends on surface characteristics, that is, local reflection coefficient, roughness, and local height of the surface;

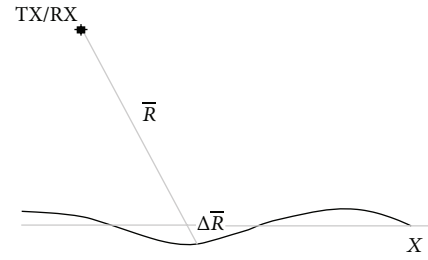

Figure 2: Reference scenario.

(v) $e^{-j2k\overline{R}(\theta_a)}/\overline{R}(\theta_a)$ is a term that depends on the round-trip path of the electromagnetic field.

Figure 2 shows the graphic representation of the reference scenario.

So, (4) can be rewritten as follows:

$$E_s\left(\theta_p\right) = \int \gamma\left(\theta_a\right) A\left(\theta_a, \theta_p\right) d\theta_a. \tag{5}$$

The processing used herein in order to locate possible surface deformations is based on differential interferometry [8], which works as follows. The phase of the reflectivity function contains information about the signal round-trip path. Therefore, a surface deformation causes a different length of round-trip path and consequently a phase displacement of the signal. Then, if $\gamma_1(\theta_a)$ and $\gamma_2(\theta_a)$ are reflectivity functions to two times t_1 and t_2, one can write:

$$\begin{aligned} \gamma_1\left(\theta_a\right) &= A_1 \varphi_1\left(\theta_a\right) e^{-jk2\Delta R_1(\theta_a)} \\ \gamma_2\left(\theta_a\right) &= A_2 \varphi_2\left(\theta_a\right) e^{-jk2\Delta R_2(\theta_a)}, \end{aligned} \tag{6}$$

where A_1 and A_2 are the maxim intensities of the two signals, the complex signals φ_1 and φ_2 take into account possible variations on the factor $f[R_{\text{perp}}(\theta_a)]$, and the exponential terms contain information about surface displacements. Then, "beating" the two signals, one achieves

$$\begin{aligned} &\gamma_1\left(\theta_a\right) \gamma_2\left(\theta_a\right)^* \\ &\quad = A_1 A_2 \left|\varphi_1\left(\theta_a\right) \varphi_2\left(\theta_a\right)\right| \\ &\qquad \times e^{j(\arg\varphi_1(\theta_a) - \arg\varphi_2(\theta_a))} e^{-jk2(\Delta R_1(\theta_a) - \Delta R_2(\theta_a))} \end{aligned} \tag{7}$$

Then, as long as the phase of $\varphi(\cdot)$ has not changed amongst the different instant times (e.g., under a "high correlation" assumptions), the phase of expression (7) gives back

$$2k\left(\Delta R_1\left(\theta_a\right) - \Delta R_2\left(\theta_a\right)\right), \tag{8}$$

which is obviously related to displacements. However, a last difficulty has to be tackled. In fact, the phase factor has an ambiguity of 2π (wrapped phase). So, a (possibly effective) phase unwrapping procedure is needed.

3.2. Extracting the Reflectivity Function. Traditional synthetic aperture radar (SAR) processing procedures heavily rely on the convolutional nature of the equation to be inverted [9].

In fact, such a circumstance is exploited to develop computationally effective codes based on fast Fourier transforms.

In our case, due to the expression of $A(\theta_a, \theta_p)$ and $\gamma(\theta_a)$ (a different choice would have been possibly by incorporating $e^{-j2k\overline{R}(\theta_a)}/\overline{R}(\theta_a)$ in the reflectivity, but then a much more cumbersome unknown $\widehat{\gamma}(\theta_a)$ has to be retrieved), one cannot rely any more on convolutions, so that different processing strategies have to be devised.

As in any integral equation with a smooth kernel, problem (5) is ill posed. (According to Hadamard definition, a problem is ill posed when its solution is not unique, or does not exist or does not depend continuously on the data.)

As a consequence, only an approximate version of the true reflectivity function can be found by looking for some kind of regularized solution.

Amongst the different possibilities, the well-known truncated singular-value decomposition (TSVD) [10] can be used. As a suitable alternative, a Tikhonov regularization [11] can be exploited, which is the suggested solution in case one has to deal with a very large number of unknowns.

3.3. The Phase Unwrapping Problem. As previously described, the phase factor in (8) has an ambiguity of 2π (wrapped phase) [12, 13]. The mathematical statement of the phase unwrapping problem can be expressed by

$$\varphi_{\text{unwrapped}} = \varphi_{\text{wrap}} + 2N\pi \tag{9}$$

and where the integer unknown N has to be determined for each point of the scenario.

Two-dimensional phase unwrapping is a classical problem encountered in several fields such as electromagnetic theory, optics and DInSAR data processing. For this reason, there is a large amount of research [14, 15] and solution approaches to both 1D and 2D phase unwrapping problem. Roughly speaking, solution approaches span from model-based procedures [14] to "total least squares" [15, 16]. Compressive sensing-based procedures have also been recently proposed [17].

4. Extension to the 3D Case

The approach previously described for the 2D geometry can be extended to the 3D case. In particular, it is possible to rewrite an equivalent approach in terms of open-circuit voltage [7] by

$$\begin{aligned} V_{\text{oc}}^{P}\left(\theta_p\right) &= \int_{\text{surface}} V_{\text{oc_loc}}^{P}\left(\theta_a, \theta_p\right) d\theta_a \\ &= \int_{\text{surface}} E_{\text{s_loc}}^{P}\left(\theta_a\right) \mathbf{h}_{\mathbf{rx}}^{\mathbf{P}}\left(\theta_a, \theta_p\right) d\theta_a \\ &= \int_{\text{surface}} \frac{e^{-j2k\overline{R}(\theta_a)}}{\overline{R}\left(\theta_a\right)^2} \mathbf{h}_{\mathbf{R}}^{\mathbf{P}}\left(\theta_a, \theta_p\right) \\ &\quad \times \gamma^{P}\left(\theta_a\right) \mathbf{h}_{\mathbf{T}}^{\mathbf{P}}\left(\theta_a, \theta_p\right) d\theta_a \\ &= \int_{\text{surface}} A^{P}\left(\theta_a, \theta_p\right) \gamma^{P}\left(\theta_a\right) d\theta_a, \end{aligned} \tag{10}$$

where

(i) $V_{\text{oc_loc}}^{P}$ is the open-circuit voltage induced by $E_{\text{s_loc}}^{P}$;

(ii) $\mathbf{h}_{\mathbf{R}}^{\mathbf{P}}$ is the array factor in transmission case;

(iii) $\mathbf{h}_{\mathbf{T}}^{\mathbf{P}}$ is the array factor in receiving case;

(iv) $\theta_a = (\vartheta_a, \varphi_a)$ corresponds to the polar coordinates of the points on the surface;

(v) $\theta_p = (\vartheta_p, \varphi_p)$ corresponds to the polar coordinates of the observation point of the measuring sensor;

(vi) P is a superscript that identifies the polarization channel.

In fact, in 3D case, one can consider four different types of transmission-reception setup [18]. Notably, for three of these four different "polarization channels," a different reflectivity function could be defined, but the signal processing required to get the unknown deformation would be exactly the same. Far from being a problem, such a circumstance could be exploited in order to improve accuracy in the deformation reconstruction and/or avoid possible ambiguities in the phase unwrapping step. On the other side, such an approach would need antennas able to work in both the two independent polarizations.

5. 2D Case Data Processing: Numerical Processor and Some Examples

Using contents as above, numerical simulators (for the 1D and 2D cases) have been developed first. Then, the different steps of the processors have also been developed in a MATLAB environment [19].

After validating the numerical simulator by examining results furnished by the codes in simple cases (flat surfaces, a single small deformation, and a sinusoidally varying, deformation), the processing chain has been tested.

The first example is aimed at displaying the reconstruction of a simple deformation, that is, a rigid shift. The working frequency is 2 GHz. The reference surface is the undulating surface shown in Figure 3. Assuming that at the time t_2 this surface is rigidly shifted of $\lambda/4$, the reconstruction is shown in Figure 4. The latter is obtained by the multiplication in (7). The unwrapping procedure used herein is the standard procedure of the MATLAB library. In correspondence to the nulls of the amplitudes of the functions $\gamma_1(\theta_a)$ and $\gamma_2(\theta_a)$, where there is a loss of information about the phase, a preprocessing, based on technique described in [15], has also been used. As it can be seen in Figure 4, the surface deformation is correctly indentified.

A second example considers a surface deformation forming by the overlapping between the undulating surface in Figure 3 and the deformation shown in Figure 5. The working frequency is 2 GHz.

The corresponding reconstruction is shown in Figure 6. As it can be seen also in this case, the deformation is correctly identified.

As it can be seen, one is able to retrieve deformations as small as a quarter of a wavelength. In all tests, the simulated

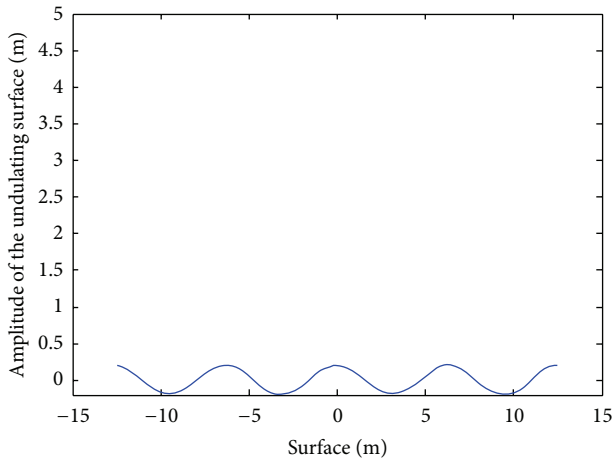

Figure 3: Undulating reference surface.

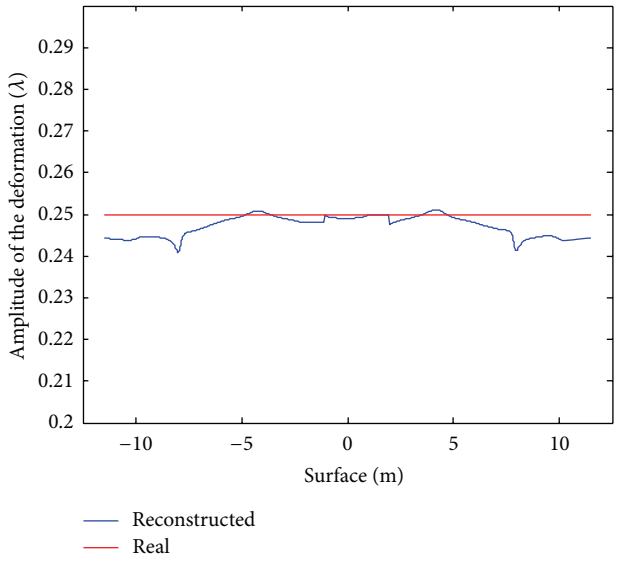

Figure 4: Surface deformation reconstructed (blue line), real surface deformation (red line).

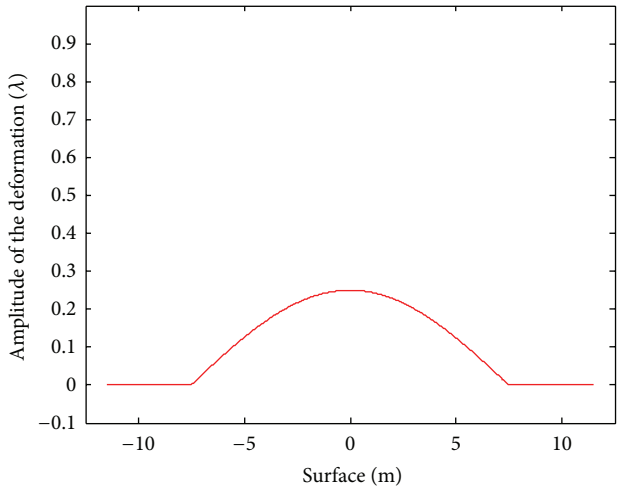

Figure 5: Example of deformation.

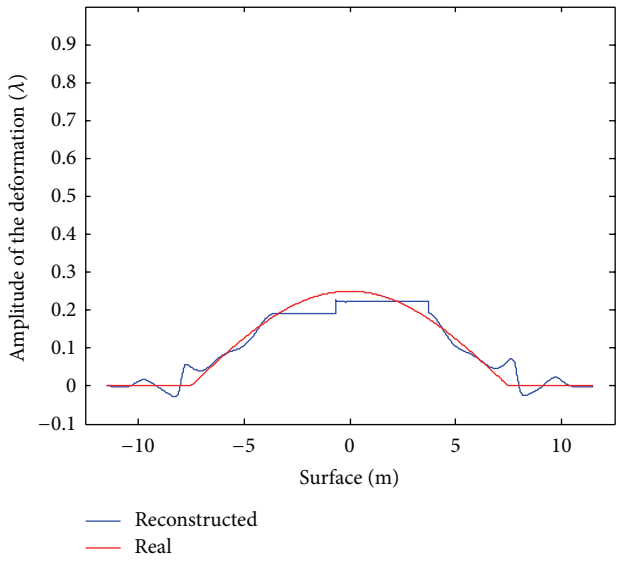

Figure 6: Surface deformation reconstructed (blue line), real surface deformation (red line).

data used for processing was affected by a simulated error with SNR = 20 dB.

Similar kinds of results are achieved in the preliminary test we are performing on the corresponding 3D processor.

6. Conclusions

In this paper, approaches commonly used in SAR for imaging of deformations have been generalized to the case of ground-based, nonsynthetic radars operating in the L band.

Such a case is indeed of interest in the applications, as it allows a very simple deployment of low-cost radar systems [20], and it allows to monitor regions which could not be easily accessible from satellites or airborne-based instrumentations. Moreover, the use of relatively low frequencies allows penetration of foliage. Last but not least, different from well-known DInSAR techniques, which requires multiple passages in slightly different orbits, the sensor is herein fixed, which allows a much more easy fulfillment of the coherence property recalled after (7).

On the other side, proper modeling and processing at these frequencies has required the development of both new simulators, as well as the development of the new processing techniques which have been introduced, discussed, and tested above.

Conflict of Interests

All authors state that the research herein described is not influenced by secondary interests (such as financial gain) and that they have no conflict of interests concerning all terms used in this paper.

Acknowledgment

This work has been carried out under the framework of PON 01_01503 National Italian Project "Landslides Early Warning," financed by the Italian Ministry of University and Research.

References

[1] F. T. Ulaby, R. K. Moore, and A. K. Fung, *Microwave Remote Sensing*, vol. III, chapter 11-12, Addison-Wesley, Boston, Mass, USA.

[2] N. R. Peplinski, F. T. Ulaby, and M. C. Dobson, "Dielectric properties of soils in the 0.3–1.3-GHz range," *IEEE Transactions on Geoscience and Remote Sensing*, vol. 33, no. 3, pp. 803–807, 1995.

[3] R. E. Clapp, "A theoretical and experimental study of radar ground return," Tech. Rep. 1024, MIT Radiation Lab, April 1946.

[4] J. A. Stratton, *Electromagnetic Theory*, McGraw-Hill, New York, NY, USA, 1941.

[5] J. A. Stratton and L. J. Chu, "Diffraction theory of electromagnetic waves," *Physical Review*, vol. 56, no. 1, pp. 99–107, 1939.

[6] S. Silver, *Microwave Antenna Theory and Design*, vol. 12 of *MIT Radiation Lab Series*, McGraw-Hill, New York, NY, USA, 1947.

[7] C. Balanis, *Antenna Theory: Analysis and Design*, John Wiley & Sons, New York, NY, USA, 2005.

[8] D. Massonnet and K. L. Feigl, "Radar interferometry and its application to changes in the earth's surface," *Reviews of Geophysics*, vol. 36, no. 4, pp. 441–500, 1998.

[9] G. Franceschetti and G. Schirinzi, "SAR processor based on two-dimensional FFT codes," *IEEE Transactions on Aerospace and Electronic Systems*, vol. 26, no. 2, pp. 356–366, 1990.

[10] M. Bertero and P. Boccacci, *Introduction to Inverse Problems in Imaging*, IOP, Bristol, UK, 1998.

[11] V. A. Tikhonov, *Methodes de Resolution de Problemes mal Poses*, Editions de Moscou, Traduction Française, Paris, France, 1976.

[12] O. M. Bucci and T. Isernia, "Electromagnetic inverse scattering: retrievable information and measurement strategies," *Radio Science*, vol. 32, no. 6, pp. 2123–2137, 1997.

[13] M. Costantini, "A novel phase unwrapping method based on network programming," *IEEE Transactions on Geoscience and Remote Sensing*, vol. 36, no. 3, pp. 813–821, 1998.

[14] Z.-P. Liang, "A model-based method for phase unwrapping," *IEEE Transactions on Medical Imaging*, vol. 15, no. 6, pp. 893–897, 1996.

[15] G. Fornaro, G. Franceschetti, R. Lanari, and E. Sansosti, "Robust phase-unwrapping techniques: a comparison," *Journal of the Optical Society of America A: Optics and Image Science, and Vision*, vol. 13, no. 12, pp. 2355–2366, 1996.

[16] G. Fornaro, A. Pauciullo, and E. Sansosti, "Phase difference-based multichannel phase unwrapping," *IEEE Transactions on Image Processing*, vol. 14, no. 7, pp. 960–972, 2005.

[17] M. Hosseini and O. Michailovich, "Derivative compressive sampling with application to phase unwrapping," in *Proceedings of European Signal Processing Conference (EUSIPCO '09)*, pp. 115–119, Glasgow, UK, August 2009.

[18] W.-M. Boerner, H. Mott, E. Lüneburg et al., "Polarimetry in radar remote sensing: basic and applied concepts," in *Principles and Applications of Imaging Radar*, F. M. Henderson and A. J. Lewis, Eds., vol. 2 of *Manual of Remote Sensing*, Chapter 5, pp. 271–357, John Willey & Sons, New York, NY, USA, 3rd edition, 1998.

[19] MATLAB, User's Guide, 2009, http://www.mathworks.it/.

[20] S. Costanzo, F. Spadafora, A. Borgia, O. H. Moreno, A. Costanzo, and G. Di Massa, "High resolution software defined radar system for target detection," in *Advances in Intelligent Systems and Computing*, vol. 206, pp. 997–1005, 2013.